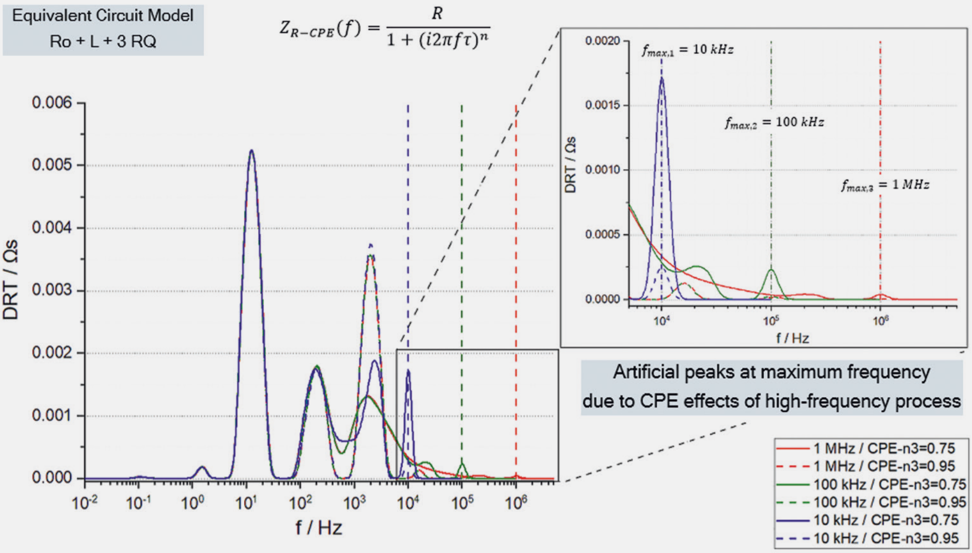

Distribution of Relaxation Times for Analysis of Solid Oxide Fuel Cell Stacks

Katharina Fitzek

Energie & Umwelt / Energy & Environment
Band / Volume 559
ISBN 978-3-95806-599-4

Mitglied der Helmholtz-Gemeinschaft

JÜLICH
Forschungszentrum

Schriften des Forschungszentrums Jülich
Reihe Energie & Umwelt / Energy & Environment Band / Volume 559

Forschungszentrum Jülich GmbH
Institut für Energie- und Klimaforschung
Elektrochemische Verfahrenstechnik (IEK-14)

Distribution of Relaxation Times for Analysis of Solid Oxide Fuel Cell Stacks

Katharina Fitzek

Schriften des Forschungszentrums Jülich
Reihe Energie & Umwelt / Energy & Environment Band / Volume 559

ISSN 1866-1793 ISBN 978-3-95806-599-4

Bibliografische Information der Deutschen Nationalbibliothek.
Die Deutsche Nationalbibliothek verzeichnet diese Publikation in der
Deutschen Nationalbibliografie; detaillierte Bibliografische Daten
sind im Internet über http://dnb.d-nb.de abrufbar.

Herausgeber und Vertrieb: Forschungszentrum Jülich GmbH
Zentralbibliothek, Verlag
52425 Jülich
Tel.: +49 2461 61-5368
Fax: +49 2461 61-6103
zb-publikation@fz-juelich.de
www.fz-juelich.de/zb

Umschlaggestaltung: Grafische Medien, Forschungszentrum Jülich GmbH

Druck: Grafische Medien, Forschungszentrum Jülich GmbH

Schriften des Forschungszentrums Jülich
Reihe Energie & Umwelt / Energy & Environment, Band / Volume 559

D 82 (Diss. RWTH Aachen University, 2021)

ISSN 1866-1793
ISBN 978-3-95806-599-4

Abstract

Electrochemical Impedance Spectroscopy (EIS) is a frequently used measurement technique to investigate the electrical and structural properties of electrochemical energy converters such as fuel cells and electrolyzers. Recently the Distribution of Relaxation Times (DRT) analysis became a promising method to increase the resolution of electrochemical processes on the relaxation time scale and to support the Equivalent Circuit Modelling (ECM) approach by an a priori estimation of the number of processes contributing to the total polarization loss. Among the possibilities to calculate the DRT function, the Tikhonov approach of regularized regression is a promising way to determine the DRT numerically. However, a main drawback of this method is the fact that a suitable regularization parameter has to be chosen that has a big impact on the shape of the DRT.

The aim of this thesis is to investigate the influence of constant phase element (CPE) behavior, inductive effects and EIS data structure on the accuracy and repeatability of the DRT with DRTtools. CPE behavior is observed in EIS measurements of fuel cells and leads to depressed semicircular arcs in the complex plane and a broadening of the relaxation time distribution. Inductive effects and measurement errors can originate from parasitic inductances in the test rig or the cables and lead to a disturbance of the impedance measurement especially in the high-frequency regime. For the simulation study conducted in this thesis, a theoretical impedance is calculated with an equivalent circuit model consisting of an ohmic resistor, an inductor and three parallel connections of an ideal resistor and a CPE (called RQ elements) in series to simulate three electrochemical processes in an SOFC which exhibit frequency dispersion behavior in different extents depending on the magnitude of the CPE exponent n. Additionally, simulation sets with different error structures and data point densities are simulated in varying frequency ranges to investigate their impact on the DRT calculated with DRTtools, as well as co-effects of the above mentioned parameters such as combined effects of parasitic inductances and high degrees of frequency dispersion. Subsequently, the results of the simulation study are verified on EIS measurements performed on a two-layer SOFC stack in F10 design of Forschungszentrum Jülich, highlighting the practical relevance of the simulation results. Furthermore, the numerical origin of the observed calculation artefacts is investigated and a method to remove the artefacts is proposed.

Kurzfassung

Die Elektrochemische Impedanzspektroskopie (EIS) ist eine häufig verwendete Messmethode zur Untersuchung von elektrischen und strukturellen Eigenschaften von elektrochemischen Energiewandlern, wie zum Beispiel Brennstoffzellen und Elektrolyseuren. Kürzlich wurde die Distribution of Relaxation Times (DRT) – Analysemethode zu einer vielversprechenden Methode, um die Auflösung der elektrochemischen Prozesse auf der Zeitskala der Relaxationszeiten zu erhöhen und für die Unterstützung des Equivalent Circuit Modelling (ECM) durch eine Vorabbestimmung der Anzahl von Prozessen. Unter den Möglichkeiten, die DRT-Funktion zu berechnen, ist die Tikhonov-Regularisierung ein vielversprechender Weg um die DRT-Funktion numerisch zu bestimmen. Ein großer Nachteil dieser Berechnungsmethode ist allerdings die Tatsache, dass ein geeigneter Wert für den Regularisierungsparameter ausgewählt werden muss, der einen großen Einfluss auf die From der DRT-Funktion hat.

Das Ziel dieser Arbeit ist die Untersuchung des Einflusses des constant phase element (CPE) Verhaltens, der Induktivität und der Datenstruktur auf die Richtigkeit und Wiederholbarkeit der DRT-Berechnung mittels DRTtools. CPE-Verhalten wird in EIS-Experimenten an Brennstoffzellen beobachtet und führt zu abgeflachten Halbkreisen in der komplexen Ebene und einer Verbreiterung der Relaxationszeitenverteilung. Induktive Effekte und Messfehler können auf parasitäre Induktivitäten im Messgerät oder der Verkabelung zurückgehen und führen zu einer Störung der Impedanzmessung, vor allem im Bereich hoher Frequenzen. Für die Simulationsstudie in dieser Arbeit wurden theoretische Impedanzen mittels eines Ersatzschaltmodells berechnet, das aus einem Ohm‘schen Widerstand, einer Induktivität und drei Parallelschaltungen aus einem Widerstand und einem CPE (RQ-Elemente genannt) in Serienschaltung zusammengesetzt ist, um elektrochemische Prozesse mit Frequenzdispersion in unterschiedlicher Ausprägung - abhängig vom CPE-Exponenten - zu simulieren. Zusätzlich wurden Testspektren mit unterschiedlichen Fehlerstrukturen und Datenpunktdichten sowie unterschiedlichen Frequenzbereichen simuliert, um deren Einfluss auf das Ergebnis der DRT-Berechnung mittels DRTtools zu untersuchen, sowie auch kombinierte Effekte der genannten Parameter, wie zum Beispiel kombinierte Effekte von parasitären Induktivitäten und stark ausgeprägten Frequenzdispersionseffekten. Anschließend wurden die Ergebnisse der Simulationsstude an EIS-Messungen, die an einem Zweizellenstack im F10-Design des Forschungszentrum Jülich durchgeführt wurden, verifiziert, um die praktische Relevanz der gezeigten Simulationsergebnisse zu unterstreichen.Weiters wurde der numerische Ursprung der Artefakte untersucht und eine Methode zur Entfernung dieser vorgeschlagen.

List of Abbreviations

AFC	Alkaline Fuel Cell
APU	Auxiliary Power Unit
ASC	Anode-Supported Cell
CNLS	Complex Nonlinear Least Squares
CPE	Constant Phase Element
CTE	Coefficient of Thermal Expansion
DRT	Distribution of Relaxation Times
ECM	Equivalent Circuit Model
EIS	Electrochemical Impedance Spectroscopy
FWHM	Full width at half-maximum
GOF	Goodness of Fit
GDC	Gadolinium Doped Ceria Oxide
LASSO	Least Absolute Shrinkage and Selection Operator
LSC	$La_xSr_{1-x}CoO_{3-\delta}$
LSCF	$La_xSr_{1-x}Co_yFe_{1-y}O_{3-\delta}$
MCFC	Molten Carbonate Fuel Cell
MIEC	Mixed Ionic and Electronic Conductor
MSC	Metal-Supported Cell
OCV	Open-circuit voltage
OLS	Ordinary Least Squares
ORR	Oxygen Reduction Reaction
PAFC	Phosphoric Acid Fuel Cell
PEMFC	Polymer Electrolyte Membrane Fuel Cell
RQ	Parallel connection of resistor and Constant Phase Element
SOC	Solid Oxide Cell
SOFC	Solid Oxide Fuel Cell
TPB	Triple-Phase Boundary
YSZ	Yttria stabilized Zirconia
ZARC	Circuit Element with Resistor and Constant Phase Element in Parallel

Contents

1. Introduction and goal of the work 1
2. Fundamentals and Literature 5
  - 2.1 Solid Oxide Fuel Cell (SOFC) 5
    - 2.1.1 Electrochemical Basics 5
    - 2.1.2 Cell and Stack Components 10
  - 2.2 Electrochemical Impedance Spectroscopy 15
    - 2.2.1 Basics 15
    - 2.2.2 Processes on AC stimulation 20
    - 2.2.3 Equivalent Circuit Modelling 27
    - 2.2.4 The Constant Phase Element 32
    - 2.2.5 Distribution of Relaxation Times 38
  - 2.3 Statement of Scientific Gap 47
3. Simulation Structure 50
  - 3.1 Equivalent Circuit Model 50
  - 3.2 Error models 51
  - 3.3 Parameter Variations 52
  - 3.4 DRT Settings 54
4. Results and Discussion 56
  - 4.1 Simulations with ideal EIS spectra 56
  - 4.2 Simulations with statistical error 80
    - 4.2.1 Simulations with error model 1 80
    - 4.2.2 Simulations with error model 2 111
    - 4.2.3 Simulations with ppd variation 140
    - 4.2.4 Simulations with variation of error level 151
    - 4.2.5 Simulations with variation of minimum frequency 161
  - 4.3 Summary of simulation results 166
  - 4.4 Verification of results on experiment 171
    - 4.4.1 Measurements at 650 °C 173
    - 4.4.2 Measurements at 700 °C 181
    - 4.4.3 Measurements at 800 °C 188
    - 4.4.4 Summary of Verification Results 195
5. Cross-chapter discussion 197
6. Summary 215

References 222

1. Introduction and goal of the work

Due to limited resources of fossil fuels and the rapidly advancing climate change, alternatives to replace fossil fuels and to produce energy from renewable resources has attracted a huge interest in recent years. One of the most promising alternatives to the combustion of fossil fuels in transportation and for energy conversion and storage is the use of hydrogen [1]. The principle of electrochemical energy conversion is therefore of great interest as the fuel cell is an electrochemical device which is able to convert chemical energy that is stored in the fuel gas into electrical energy directly without combustion process. With the so-called Solid Oxide Cells (SOCs), which are reversible electrochemical converters, both ways of energy conversion, namely conversion of chemical energy into electrical energy in the fuel cell mode and conversion of electrical energy into chemical energy in the electrolysis mode, can be realized in a single device, making them a promising choice for storing renewable energies such as solar or wind. Furthermore, the low temperature polymer fuel cell can be used to provide energy for electrical engines by the conversion of hydrogen.

According to the temperature at which fuel cells are operated, they are distinguished in:

1) Low Temperature Fuel Cells (60 °C to 120 °C) such as the Alkaline Fuel Cell (AFC) or the Polymer Electrolyte Membrane Fuel Cell (PEMFC)

2) Medium Temperature Fuel Cells (around 200 °C) such as the Phosphoric Acid Fuel Cell (PAFC) and

3) High Temperature Fuel Cells such as the Molten Carbonate Fuel Cell (MCFC) and the Solid Oxide Fuel Cell (SOFC), which are operated between 600 °C and 900 °C.

Among those the SOFC is a promising choice for stationary applications because it exhibits a high fuel flexibility, a high efficiency due to high operating temperatures and good reversibility, which makes it suitable for applications with combined fuel cell and electrolysis mode. Because the SOFC is manufactured mostly from ceramic components with brittle nature, it is most suitable for stationary applications. However, some effort is also put into the development of Metal- Supported Cells (MSCs) [2] [3] [4] for mobile applications such as Auxiliary Power Units (APUs).

Due to the high working temperatures in SOFCs, they suffer from material degradation, which has been subject of research for many years. Among the degradation mechanisms are structural changes of the anode material, such as the Nickel agglomeration in Nickel-YSZ Cermets, which reduces the active area for the electrochemical reaction and thereby leads to an increased polarization resistance [5]. Furthermore the conductivity of the electrolyte YSZ can be increased because of the formation of inhomogeneous composition phase boundaries [6]. Such degradation mechanisms can be studied in situ by means of DC and AC measurement techniques. Frequently used examples for DC techniques are the I-V-measurement and the current interruption method (iR measurement) with which the total polarization loss of the electrochemical cell can be determined. The drawback of both techniques is that the contributions from single loss mechanisms in the cell cannot be distinguished which makes a targeted material and design improvement rather difficult. In order to gain knowledge on the electrochemical loss mechanisms, the Electrochemical Impedance Spectroscopy (EIS), which is an AC measurement technique, has gained increasing popularity to study detailed electrochemical degradation mechanisms in SOFCs [7] [8]. The EIS analysis procedure in general includes the modelling of the electrical response of the investigated electrochemical system with an Equivalent Circuit Model (ECM) [9]. The theoretical impedance of this circuit is subsequently fitted against the experimental EIS data to calculate the characteristic physico-chemical parameters of the system such as polarization resistances, double layer capacitances and diffusion/adsorption coefficients. This fitting is usually realized with a Complex Non-linear Least Squares (CNLS) fitting algorithm. A major drawback of the ECM analysis method is the ambiguity of the equivalent circuits, as many different circuit models can result in precisely the same impedance response. Therefore, some prior knowledge about the investigated system is necessary to set up a physically-meaningful ECM. In order to overcome this limitation, the Distribution of Relaxation Times (DRT) analysis method has been proposed to identify the number of processes contributing to the total polarization loss of the fuel cell and their relaxation characteristics. The principle of this method is the deconvolution of the EIS data from the frequency domain into the time domain to visualize the characteristic relaxation time scales of the single electrochemical processes. As this task is a mathematically ill-posed problem due to a large number of unknowns [10], only numerical solutions of the distribution function are available. Several methods to solve this numerical problem have been proposed in literature – see chapter 2.2.5 - and each of them is vulnerable to numerical oscillations and inaccuracy, potentially leading to misinterpretations of the DRT result. In order to control the oscillations in the regularized regression approach, a suitable regularization parameter has to be chosen. The choice of this parameter is thereby always a trade-off between the closeness of the DRT to the experimental data and the suppression of numerical effects. Therefore the choice of this parameter is a crucial point in the deconvolution of the DRT. Measurement errors originating from the test rig and the measurement setup for example can lead to numerical instabilities in the DRT calculation. Another aspect that has not been paid much attention to yet, is the fact that also characteristic properties of the investigated electrochemical cell may cause numerical oscillations, such as the well-known frequency dispersion or constant phase element (CPE) behavior, which is leading to depressed semicircular arcs in the complex plane and which is causing a broadened distribution of relaxation times of the respective processes. As one of the purposes of the DRT analysis is the resolution of single electrochemical processes in terms of their relaxation time characteristics, broadened peaks may lead to an insufficient peak resolution or peak multiplication caused by numerical instabilities or over-regularization effects. Because the research in this field is quite rare, studies to investigate the influence of frequency dispersion and also its combination with measurement errors are needed to increase the knowledge on numerical weaknesses and limitations of the DRT analysis and thereby increase the awareness about the limitations to avoid misinterpretations of the DRT result. Another aspect has to be the proposal of strategies and recommendations to overcome the limitations and improve the reliability of the DRT analysis for SOFCs.

The goal of this work is to investigate the influence of frequency dispersion, inductances and EIS data properties on the accuracy and reliability of the DRT analysis by means of DRTtools [10] with simulation studies based on synthetic EIS spectra calculated with a suitable equivalent circuit model. The calculation of the DRT function in DRTtools is conducted by means of a combined discretization and regularized regression approach, where the latter is based on the Tikhonov approach of regularized regression. In the studies of this thesis, attention is also paid to an optimal choice of the regularization parameter, which is controlling the degree of numerical oscillation. The choice of DRTtools for conducting this study is based on the observation of artefacts in DRTs calculated with DRTtools from EIS spectra measured on SOFC stacks at the IEK-14 in a previous work [11]. The structured simulation study presented in this work should increase the knowledge on the link between physical properties of the SOFC together with the EIS data structure and the numerical behavior of the DRT analysis with DRTools. After discussion of the simulation results, a verification of those on experimental data from an SOFC stack with anode-supported cells (ASCs) in the Jülich F10-Design is presented, highlighting the practical relevance of the simulation study. Subsequently, the origin of the observed artefacts is analyzed and an approach to eliminate those from the DRT spectrum is proposed.

Outline

In ***Chapter 2***, the electrochemical basics of the Solid Oxide Fuel Cell, including the thermodynamic and kinetic description, as well as the description of physico-chemical processes which are governing the polarization loss, are presented. Furthermore, the theory behind the EIS measurement method and the calculation of the DRT are discussed in detail together with a discussion of the mathematical description and possible physical origins of the constant phase element.

In ***Chapter 3***, the structure and parametrization of the simulation model and the procedure of conducting the simulation study is described.

In ***Chapter 4***, the results of the simulation study are presented followed by a verification on experimental EIS data from SOFC stack measurements conducted at the Jülich Research Center.

In ***Chapter 5***, a cross-chapter discussion of the presented results is provided and a possible origin of the observed numerical artefacts is proposed. On this basis, a method to eliminate numerical artefacts is developed.

2. Fundamentals and Literature

2.1 Solid Oxide Fuel Cell (SOFC)

2.1.1 Electrochemical Basics

The Solid Oxide Fuel Cell (SOFC) is an electrochemical device which converts chemical energy into electrical energy by a controlled and separated electrochemical reaction of a fuel gas and an oxidant gas, taking place at high temperatures around 600 °C to 900 °C. Compared to other types of fuel cells, which are using liquid electrolytes - such as the Polymer Electrolyte Membrane Fuel Cell (PEMFC) - the electrolyte in the SOFC is a solid oxide material. In general, a fuel cell is composed of an anode, an electrolyte and a cathode. The oxidation reaction takes place at the anode, whereas the reduction takes places at the cathode. Besides providing a conductive path for ions which are formed in the half-cell reactions, the electrolyte acts as a separator of the fuel gas and oxidant gas to ensure the separation of the electrochemical half-cell-reactions and therefore prevent a direct reaction of the reactants. Two kinds of electrolytes can be used with either proton conducting or oxygen-ion conducting properties. The cells which are used for the experimental study in this thesis are composed of an oxygen-ion conducting electrolyte. Therefore the following description of the working principle and electrochemical basics are based on this kind of electrolyte, with H_2 as fuel gas and air as oxidant gas. As depicted in Figure 2.1.1, two half-cell-reactions take place at either electrode.

The half-cell-reaction at the fuel electrode (anode) is given by:

$$H_2 + O^{2-} \rightarrow H_2O + 2\,e^- \tag{1}$$

and the half-cell-reaction at the air electrode (cathode) is given by:

$$\frac{1}{2}O_2 + 2e^- \rightarrow O^{2-} \tag{2}$$

Combining the half-cell-reactions at both electrodes yields the overall electrochemical reaction as:

$$\frac{1}{2}O_2 + H_2 \rightarrow H_2O \tag{3}$$

When using biogas or methane as fuel gas, the following reactions take place in the anode:

$$CH_4 + H_2O \rightarrow CO + 3\,H_2 \tag{4}$$

with the water gas shift reaction taking place in parallel:

$$CO + H_2O \leftrightarrow CO_2 + H_2 \tag{5}$$

The O_2 at the air electrode is supplied by either an oxygen flow or an air flow and is reduced at the air electrode to O^{2-} ions, which are then transported via the electrolyte to the boundary of the fuel electrode, where they react with the fuel gas H_2 to form water and release two electrons. These electrons are transported via an external electrical circuit back to the cathode.

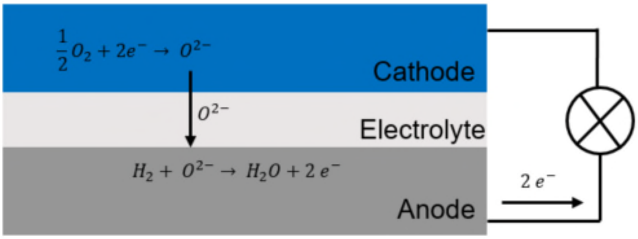

Figure 2.1.1. Working principle of an SOFC with an oxygen ion conductor and H_2 as fuel gas.

The driving force for the O^{2-} ions moving through the electrolyte is governed by the electrochemical potential, which is the sum of the chemical potential and a term dependent on the electrostatic potential φ. The chemical potential μ_i of species i is given by:

$$\mu_i = \mu_i^0 + RT \ln a_i \tag{6}$$

with μ_i^0 being the standard chemical potential and a_i being the activity of species i. This equation in general describes the energy that is needed to move one mole of the species i from infinity into the given mixture. In this regard, a species will move from areas with high chemical potential to areas with lower chemical potential. For moving one mole of species i with charge z_i into a mixture with potential φ, additional electrical work has to be raised, leading to the expression of the electrochemical potential:

$$\bar{\mu}_i = \mu_i + z_i F \varphi \tag{7}$$

with the electrostatic potential φ, Faraday's constant F and the charge of the species z_i. Two phases are in electrochemical equilibrium, if they have the same electrochemical potential.

In general the conversion of energy in the fuel cell obeys the basic thermodynamic equation

$$\Delta H = \Delta G + T\Delta S \tag{8}$$

with the enthalpy H, Gibb's energy G, temperature T and entropy S.

For fuel cells, the difference in Gibb's energy is the theoretical maximum electrical energy that the electrochemical cell can deliver. When the cell is in thermodynamic equilibrium, which means that no current is flowing, the theoretical cell voltage U_{th} can be calculated as

$$U_{th} = E_0 = -\frac{\Delta G}{zF} \tag{9}$$

with the Gibb's energy ΔG at constant temperature and pressure, the number of transferred electrons z, Faraday's constant F and the electromotive force E_0. For real systems, the cell voltage depends on the temperature and the concentrations or partial pressures of the reactants, as expressed in the Nernst equation

$$U_N(T) = E_o(T) + \frac{RT}{zF} \sum_i \ln\left(\frac{x_{i,P}^{\upsilon_{i,P}}}{x_{i,R}^{\upsilon_{i,R}}}\right) \tag{10}$$

with the gas constant R and the normalized partial pressures of the products and reactants $x_{i,P}$ and $x_{i,R}$ and the numbers of moles of products and reactants $\upsilon_{i,P}$ and $\upsilon_{i,R}$. This voltage is the cell voltage at a given temperature and partial pressures of the involved chemical species in the current-less state of the electrochemical cell, meaning under open-circuit voltage (OCV). For the system described above, with H_2 as fuel gas, the Nernst equation can be rewritten as

$$U_N(T) = E_0(T) + \frac{RT}{2F} \ln \left(\frac{x_{H_2O}}{x_{O_2}^{0.5} \; x_{H_2}} \right) \tag{11}$$

If a current is drawn from the cell, the voltage will drop due to polarization losses. These polarization losses are originating from the finite speed of the kinetics of the electrochemical reactions. They are generally distinguished into activation polarization η_{act} originating from the activation energy which is needed to overcome the activation barrier of the charge transfer mainly over the electrolyte-electrode interface, ohmic polarization η_{Ohm} originating from the limited electron and ion conductivity of the cell materials and the transport polarization η_{trans} which is due to finite diffusion and convection speed of reactant and product species. As indicated in Figure 2.1.2, the polarization- or I-V-curve of SOFCs shows almost no activation polarization behavior compared to a PEMFC. This is due to the high operating temperature of the SOFC which is decreasing the activation barrier for the charge transfer over the electrochemical interface.

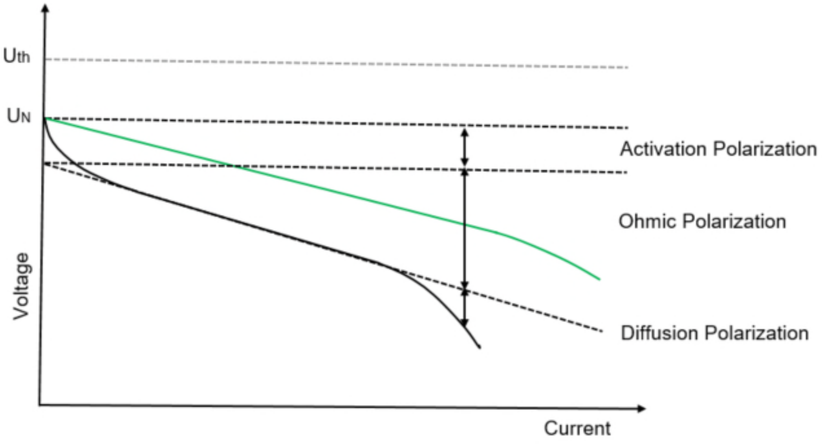

Figure 2.1.2. Exemplary polarization curves for an SOFC (green, humidified H_2) and a PEMFC (black).

Starting at low currents, the charge transfer between the electronic and ionic conductor leads to a drop of the cell voltage which can be seen at the beginning of the polarization curve. With increasing current, the conductivity of electrons and ions in the cell components becomes dominating leading to a linear correlation between the current and the voltage which is typical for ohmic conductors. At high currents, the electrochemical reaction and the charge transfer rates are so high that the diffusion of uncharged particles, such as reactants or products becomes the limiting factor for the speed of the electrochemical conversion.

A mathematical description of the reaction kinetics is given by the Butler-Volmer equation of electrochemical kinetics, which describes the current at each electrode-electrolyte interface in dependence of the activation polarization:

$$j = j_0 \left[\exp\left(\frac{\alpha_a zF\eta_{act}}{RT}\right) - \exp(-\frac{\alpha_C zF\eta_{act}}{RT})\right] \tag{12}$$

with the current density j, the exchange current density j_0, the anodic charge transfer coefficient α_a, the cathodic charge transfer coefficient α_c and the activation polarization η_{act}. The afore mentioned negligible activation polarization for SOFCs in comparison to PEMFC is due to the exponential relationship between the temperature and the current density. The exchange current density j_0 is proportional to the activation energy of the electrochemical process, the partial pressures of the reactants and the temperature [12]:

$$j_0 \propto j_{0,ref} \left(\frac{p_r}{p_{r,ref}}\right)^{\gamma} \exp\left[-\frac{E_C}{RT}\left(1 - \frac{T}{T_{ref}}\right)\right] \tag{13}$$

with the reference exchange current density $j_{o,ref}$, the partial pressure of reactants p_r, the reference pressure $p_{r,ref}$, a pressure dependency coefficient γ, the activation energy E_c and the temperature T.

The ohmic polarization results from the ionic and electronic conductivity in the electrolyte and the electrodes and is given by

$$\eta_{Ohm} = j \ \sum_i R_i \tag{14}$$

The diffusion polarization can be described by

$$\eta_{diff} = \frac{RT}{zF} \ln\left(\frac{c_{surf}}{c_{bulk}}\right) \tag{15}$$

with

$$c_{surf} = \frac{j_L - j}{j_L}\, c_{bulk} \tag{16}$$

and

$$j_L = \frac{zFDc_{bulk}}{l} \tag{17}$$

with the concentration of reactants at the electrode surface c_{surf}, the concentration of the reactant in the bulk c_{bulk}, the limiting current density j_L and the length of the diffusion area l. The limiting current density describes the current density at which the rate of the electrochemical reaction is that fast so that the concentration of the reactants at the electrode-electrolyte interface drops to zero.

Taking the mentioned polarization losses into account, the current-voltage relationship can be noted as follows:

$$U_r(j) = U_N - \eta_{act}(j) - \eta_{Ohm}(j) - \eta_{diff}(j) \tag{18}$$

2.1.2 Cell and Stack Components

As stated before, the SOFC is an electrochemical device which operates generally at high temperatures between 600 °C and 900 °C. Therefore it is necessary that the cell and stack materials have to exhibit good thermal and chemical stability at high temperatures. In Figure 2.1.3, the main components of a stack with anode-supported cells are shown schematically. The stack consists of the electrodes and the electrolyte, a current collector – such as nickel meshes with varying mesh sizes or Nickel sponges – and the interconnector plates, which are covered with a protective coating to prevent Cr evaporation from chromia-forming alloys and thereof the Cr-poisoning in the cathode [13] [14] [15]. The grooves in the interconnector plate serve as gas channels to ensure a uniform gas distribution over the cell area. There are different ways to define the groove structure of the interconnector, for example parallel straight channels - which are preferred in SOFCs - or meander-like channels. To separate the fuel gas and the air flow and prevent a direct reaction of those, a sealant layer is placed between the interconnector plate and the cell. Additionally, gas tightness of the electrolyte is needed to separate fuel and oxidant gas.

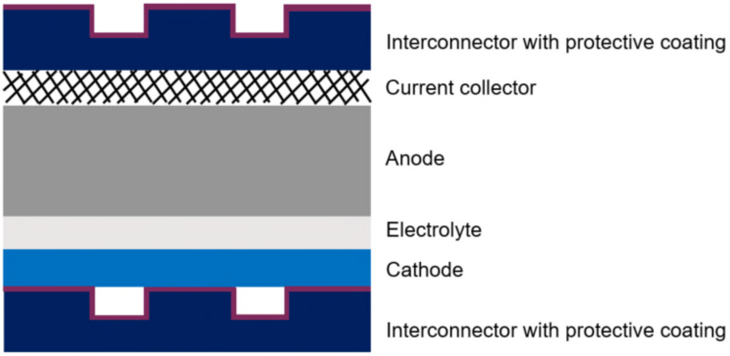

Figure 2.1.3. Schematic composition of an SOFC stack with ASCs.

The electrolyte should also exhibit good ionic conductivity and low thickness (exception: electrolyte-supported cells) to ensure low ohmic polarization loss as well as low electronic conductivity to prevent electrons moving over the electrolyte instead of moving over the external electrical circuit. Another requirement of the electrolyte is a good matching of the coefficient of thermal expansion (CTE) with both the cathode and anode material to prevent the evolution of stress gradients during temperature cycling, which can damage the interface region. The electrode materials should exhibit high thermal and chemical stability in oxidizing and reducing atmosphere. Additionally, the porous microstructure of the electrodes should be stable under operating conditions to ensure constant catalytic activity at the triple-phase boundary (TPB). The principle of this TPB is schematically shown in Figure 2.1.4. The ionic conductor delivers the oxygen ions from the electrolyte, the gas phase provides the fuel gas and removes the gaseous reaction product from the reaction site and the catalyst is needed to drive the electrochemical reaction and to transport the electrons to the current collector. Another important material property of the porous electrodes is the percolation of the ionic conductor and the catalyst, as isolated structures of only catalyst or ionic conductor are not contributing to the TPB length and are therefore electrochemically inactive parts of the cell. In the following sections, a short review of the requirements to the single parts of the SOFC stack and frequently used materials is given.

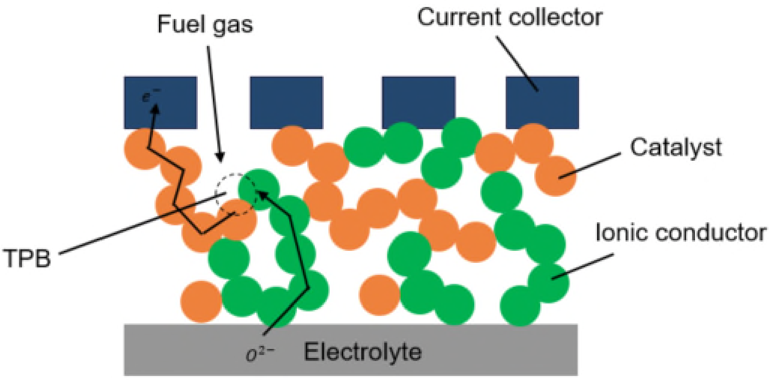

Figure 2.1.4. 2D-scheme of the triple-phase boundary (TPB) in the porous fuel electrode.

SOFC Materials

Typical electrolyte materials for SOFCs are based on zirconia, ceria and perovskites based on $LaGaO_3$. Among those, Yttrium stabilized zirconia (YSZ) is the material which is most commonly used in SOFCs. The substitution of Zr^{4+} with Y^{3+} increases the number of oxygen vacancies in the crystal lattice which leads to higher ionic conductivity as the mechanism is based on hopping events of oxygen atoms via vacancies in the lattice. Among the various YSZ materials, the one doped with 8 mol-% Y_2O_3 (8YSZ) exhibits the highest ionic conductivity with 0. 18 S cm^{-1} at 1000 °C [16] [17]. Ceria based electrolytes exhibit higher ionic conductivities than YSZ but develop appreciable electronic conductivity above 600 °C. A typical ceria based electrolyte is Gadolinium doped Cerium oxide (GDC). In $LaGaO_3$ materials, Lanthanum on the A-site can be replaced by Sr, Ca, Ba, Nd or Sm and Gallium on the B-site can be replaced by Mg, In, Al or Zn [18] [19]. It has been shown for $La_{0.8}Sr_{0.2}Ga_{0.83}Mg_{0.17}O_{3-\alpha}$ that high conductivities can be achieved [20].

At the cathode the oxygen reduction reaction (ORR) takes place. The electrons and the ions which are needed for the reduction have to be transported through the electrode to the triple-phase boundary, therefore the cathode material has to exhibit a sufficiently high electronic conductivity and ionic conductivity. Single materials with such properties are called Mixed Ionic Electronic Conductors (MIEC). Another important structural property of the cathode is a high porosity to ensure an efficient gas flow to the TPB. Materials based on $LaCoO_3$, such as $La_{1-y}Sr_yCo_{1-x}Fe_xO_3$ (LSCF) show high electronic and ionic conductivity over a large temperature range, which makes them a suitable cathode material. Because the doping with Fe reduces the ionic conductivity [21], $La_{1-x}Sr_xCoO_3$ (LSC) is considered to be a promising alternative cathode material for SOFCs.

At the anode, the oxidation of the fuel gas takes place. Similar to the reaction at the cathode, the oxidation of the fuel can only take place at the TPB. To increase this active area, the electrode has to exhibit a certain porosity. Especially for anode-supported cells (ASCs), in which the anode serves as the cell-stabilizing substrate, the mechanical stability has to be high although a high porosity is needed for a high electrochemical performance. The most commonly used catalyst towards hydrogen oxidation is Nickel because of its chemical stability against hydrogen and good catalytic activity [22]. As there is an appreciable CTE mismatch between pure Ni and the commonly used YSZ electrolyte, Ni-YSZ cermets with Ni contents of of 40 – 60 wt-% have been developed in the 1970s. These cermets are now the most commonly used anode materials in SOFCs due to their high electronic conductivity, good ionic conductivity and excellent catalytic activity [23]. Another advantage of using a Ni-YSZ cermets compared to pure Ni is the increase of the TPB length. For pure Ni the active area would be limited to the interface region with the electrolyte. When using the cermet, the oxygen conducting areas extend into the electrode and therefore lead to an increased TPB [24]. An important degradation mechanism of the Ni-YSZ cermet, which has to be considered for the operation at high temperatures, is the Nickel agglomeration [25]. By coarsening of the Ni particles, the active area is reduced and therefore the anodic reaction polarization is increased.

If other fuels than hydrogen, such as carbon or sulfur containing fuel gases are used, the Ni-YSZ cermet is prone to carbon deposition [26] or sulfur poisoning [27] which leads to a decrease in the catalytic activity of the anode. Several studies were conducted to overcome these degradation issues by adding additional components to the cermet. The addition of alumina (Al_2O_3) was proven to increase the coking resistance [28] and to improve the electrochemical performance due to preventing an overgrowth of NiO particles during the sintering procedure [29]. Also the addition of silver [30] or Nb_2O_5 [31] is discussed in literature for enhancement of the anode performance.

The interconnector serves as a conductor of current and heat between adjacent fuel cells in the stack, as well as a separator between reducing and oxidizing atmospheres of the anode and cathode of adjacent cells in the stack. Therefore the interconnector material has to provide thermal and chemical stability against dual-atmospheric environments at high temperatures and especially high electronic conductivity to reduce ohmic losses. Chromium containing ferritic steels such as Crofer 22 APU [32] are the material of choice because of their good conductivity at high temperatures and matching CTE to the cell components [33]. To prohibit the evaporation of Cr from the ferritic steel, the interconnector is usually coated with protective coatings such as materials based on manganese oxide with different dopants (Co, Fe, etc.) [34] [35].

2.2 Electrochemical Impedance Spectroscopy

2.2.1 Basics

The general approach of electrical measurements is to apply an electrical stimulus (current or voltage) to the electrodes and measure the response of the system under investigation. In Electrochemical Impedance Spectroscopy (EIS) the electrochemical system is stimulated with a single-frequency AC voltage (or current) of the form

$$V(t) = V_0 \sin(\omega \mathrm{t}) \tag{19}$$

with angular frequency

$$\omega = 2\pi f \tag{20}$$

and the phase shift (Θ) and amplitude (I_0) of the resulting current (or voltage)

$$I(t) = I_0 \sin(\omega t + \theta) \tag{21}$$

is measured. This stimulation is repeated for all frequencies in the desired frequency range of the measurement, which is normally between 1 mHz and 1 MHz. The mathematical relations between the input voltage and the resulting current are quite complex in the time domain and a system of differential equations has to be solved to calculate the impedance function. The use of Fourier transformation allows to simplify the mathematical treatment by transforming the relations from the time domain into the frequency domain, in which the voltage-current relation can be described as:

$$I(i\omega) = \frac{V(i\omega)}{Z(i\omega)} \tag{22}$$

which is similar to the form of ohm's law for DC current. The complex quantity Z (iω) is called the impedance function and its value is the impedance of the investigated circuit at a particular angular frequency ω. In a more general form, which can be applied to any electrical system, the impedance function in the frequency domain can be denoted as

$$Z(i\omega) = \frac{F\{V(t)\}}{F\{I(t)\}} \tag{23}$$

with the operator F { } representing a Fourier transform.

The impedance can be plotted as a complex number in the so-called Argand diagram, which can be found in Figure 2.2.1, on the basis of the general notation of complex numbers:

$$Z(\omega) = Z' + iZ'' \tag{24}$$

with Z' and Z'' denoting the real and imaginary part of the impedance, which are frequently denoted as Re (Z) and Im (Z) as well.

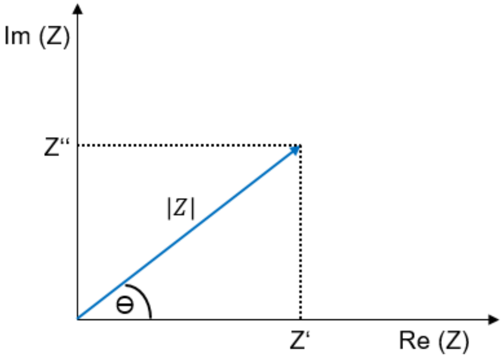

Figure 2.2.1. Argand diagram of the impedance Z (ω)

Based on Figure 2.2.1, the equations for the real and imaginary part can be derived:

$$Re(Z) = Z' = |Z|\cos(\theta) \tag{25}$$

$$Im(Z) = Z'' = |Z|\sin(\theta) \tag{26}$$

with the phase angle

$$\theta = tan^{-1}\left(\frac{Z''}{Z'}\right) \tag{27}$$

and the modulus of the impedance

$$|Z| = \sqrt{(Z')^2 + (Z'')^2} \tag{28}$$

An important constriction to the above mentioned mathematical simplifications in the frequency domain is that are only valid under the condition of

a) linearity: linear voltage-current relationship
b) causality: the resulting phase shift and amplitude have to be directly related to the physico-chemical processes of the investigated system
c) stationarity: the investigated system has to be time-invariant

In general, electrochemical systems show strong nonlinear current-voltage behavior when electrical currents or voltages are high. To ensure a linear relationship between voltage and current, the amplitude of the input voltage V_0 has to be less than the thermal voltage at the operating temperature [36]

$$V_T = \frac{kT}{e} \tag{29}$$

with Boltzmann's constant k, temperature T and elementary charge e. For standard operation temperatures of SOFCs (~700 °C) this value is around 84 mV.

Typical physico-chemical processes taking place on the electrical stimulus are the transport of electrons through electronic conductors, the transfer of electrons over the electrolyte-electrode-interface or the flow of charged species via defects or vacancies in the electrolyte. The flow rate (=current) of charged species thereby depends on the one hand on the ohmic resistance of the electrodes and the electrolyte and on the other hand on the reaction rates of the electrochemical reactions at the triple-phase boundary.

In general two kinds of properties can be derived from EIS measurements:

a) Those originating from the material itself, such as electronic and ionic conductivity, dielectric constants, charge mobilities, diffusion coefficients, etc.
b) Those originating from the electrode-electrolyte interface, such as reaction rates, double-layer capacitances, adsorption rates, etc.

The measured impedance response can be visualized by means of Nyquist or Bode diagrams as shown in Figure 2.2.2. From the Nyquist diagram, the ohmic resistance can be estimated from the intersection with the x-axis at high frequencies. The intersection at low frequencies is related to the total resistance of the electrochemical system. By subtracting the ohmic resistance from the total resistance, the polarization resistance of the cell can be obtained. For calculating single process polarization resistances, a modelling approach is needed. This can be done by means of equivalent circuit modelling in combination with a complex non-linear least squares (CNLS) fitting method, which is described in detail in the next section.

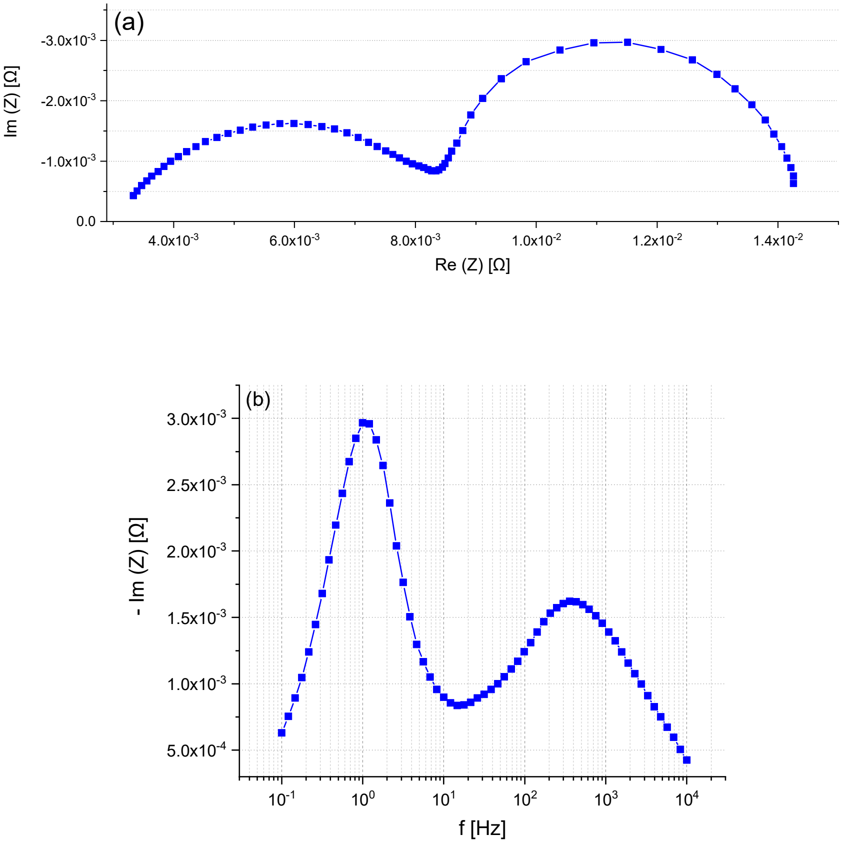

Figure 2.2.2. Exemplary Nyquist (a) and Bode (b) diagram.

Kramers-Kronig Transforms

As EIS measurements can suffer from statistical or systematic measurement errors, a validation of the impedance data before proceeding with the data analysis is recommended [37] [38]. The Kramers - Kronig validity test is based on the following equations, which were first proposed in a slightly different form by Kramers and Kronig [39] [40]:

$$Z_{Re}(\omega) = \frac{2}{\pi}\int_0^\infty \frac{\omega' Z_{Im}(\omega')}{\omega^2-\omega'^2}d\omega' \tag{30}$$

$$Z_{Im}(\omega) = -\frac{2}{\pi}\int_0^\infty \frac{\omega Z_{Re}(\omega')}{\omega^2-\omega'^2}d\omega' \tag{31}$$

The main statement of the above equations is that the real and imaginary part of the impedance are not independent from each other, but related by the Kramers-Kronig relations. This means that in ideal cases the real part can be calculated from the imaginary part and vice versa. This gives rise to the possibility to validate experimental EIS data by calculating the real part from the imaginary part and comparing the result with the measured real part and vice versa.

As the integrals above have to be solved from zero to infinity and frequency data cannot be available from the experiment in this range, the calculation of the Kramers-Kronig residuals (KKR) needs to be done numerically. Several methods for solving the equations have been proposed in literature [41] [42]. In the present work, the Linear KK-Tool developed by the Karlsruhe Institute of Technology (KIT) [43] [44] is used for estimation of the KKR. In this tool, the impedance is modeled with a series connection of an ohmic resistor and M parallel connections of a resistor and a capacitor (RC element), giving the expression for the model impedance response as:

$$\hat{Z}(\omega) = \hat{R}_{Ohm} + \sum_{k=1}^{M}\frac{\hat{R}_k}{1+j\omega\tau_k} \tag{32}$$

A procedure of how to define the most suitable number of RC elements automatically can be found in [43] and is implemented in the Linear KK-tool. To overcome the problem of nonlinearity due to unknown time constants τ_k of the RC elements, those are set to $\tau_k = (\omega_k)^{-1}$. The sum over N experimental frequencies to be minimized is therefore the following:

$$S = \sum_{i=1}^{N}\left[\frac{Z_{Re}(\omega_i)-\hat{Z}_{Re}(\omega_i)}{|Z(\omega_i)|}\right] + \left[\frac{Z_{Im}(\omega_i)-\hat{Z}_{Im}(\omega_i)}{|Z(\omega_i)|}\right] \tag{33}$$

The calculated KK residuals, which are presented in this thesis, are then defined by

$$KKR_{Re}\,(\omega) = \frac{Z_{Re}(\omega) - \hat{Z}_{Re}(\omega)}{|Z(\omega)|} \tag{34}$$

$$KKR_{Im}\,(\omega) = \frac{Z_{Im}(\omega) - \hat{Z}_{Im}(\omega)}{|Z(\omega)|} \tag{35}$$

As a general reference point, KKR below 1 % can be assumed to ensure an acceptable EIS data quality [45]. Nevertheless the KKR have also to be judged in terms of their shape, meaning that randomly distributed residuals point towards a valid measurement whereas pronounced bias in the KKR points towards systematic effects that are due to violations of the linearity or causality principle [46].

2.2.2 Processes on AC stimulation

This chapter should give an overview on typical physico-chemical processes that are taking place if an electrochemical system as a fuel cell is perturbed with an AC current. The main processes can be summarized as follows:

a) Conductivity in the electrolyte
b) Gas diffusion in the porous electrodes and current collector
c) Charging of interfaces
d) Charge transfer at electrolyte-electrode interface

These processes can be investigated with EIS measurements. By modelling these physical processes with electrical analogs (see chapter 2.2.3), the respective properties of the electrochemical system can be determined by means of a fitting approach.

Conductivity in the electrolyte

If an electric field is applied to a conducting material as an electrolyte, the charges will move along the gradient of the electric field. The relationship between the charge density and the gradient of the electric field is given by Poisson's equation:

$$\nabla^2 \Phi = -\frac{\rho}{\varepsilon_s \varepsilon_0} \tag{36}$$

with the electric potential Φ, the charge density ρ and the dielectric constants ε.

For the interior of the electrolyte, electro-neutrality is assumed. The flux of species i is governed by the characteristic mobility u_i and the gradient in the electrochemical potential $\bar{\mu}_i$

$$j_i = -c_i u_i \nabla \bar{\mu}_i \tag{37}$$

This equation needs to be extended with a term for electrochemical potential gradients arising from other species k – if present - which may also have an influence on the driving force for the movement of species i.

If only one electrolyte species is mobile, as in solid electrolytes used in SOFCs, and no concentration gradients are present as this is the case for an electrolyte with reversible electrodes, the current density can be described as

$$j = -F^2 \sum_i c_i z_i^2 u_i \nabla \Phi \tag{38}$$

with the conductivity term

$$-F^2 \sum_i c_i z_i^2 u_i = \sigma \tag{39}$$

From the above equations, it is visible that under the mentioned circumstances the conductivity of the electrolyte obeys Ohm’s law. The polarization which is arising from this limited conductivity can be observed in the high frequency regime of the EIS spectrum. The electrical analogue that is commonly used for modelling the conductivity of the electrolyte is an ideal resistor. In case of a simple ion hopping process with no long range interactions, the conductivity should be independent of frequency. However, it is possible in solid electrolytes that there are interactions between defect species which will lead to a frequency-dependent conductivity. This frequency dependency leads to a constant phase element behavior, which is described in detail in section 2.2.4.

Diffusion in the porous electrodes and current collector

If an AC voltage is applied to the electrochemical cell, concentration gradients will build up due to the consumption of reactants and formation of products in the electrochemical reaction. Figure 2.2.3 should give an overview of concentration gradients building up in an SOFC under operation. For simplicity reasons, the location where the electrochemical reaction takes place is assumed to be at the electrolyte-electrode interface for the discussion. In reality the reaction takes place along entire triple-phase boundary which is spreading into the electrodes, as described in the previous chapter.

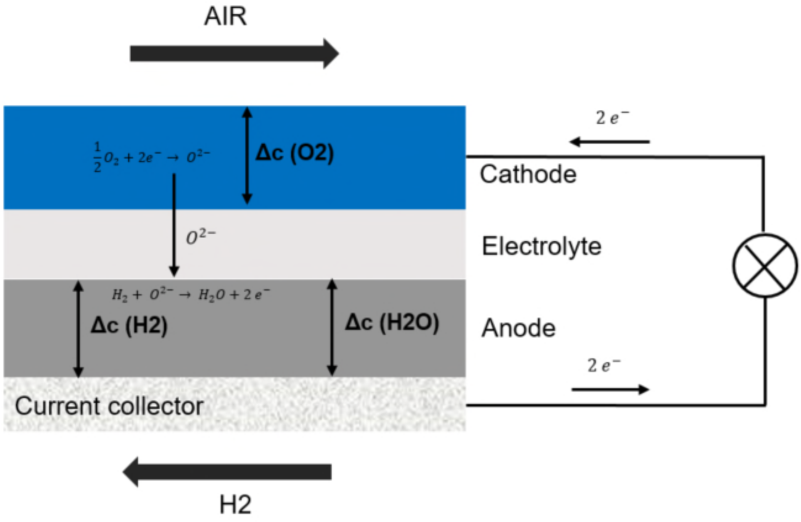

Figure 2.2.3. Concentration gradients which are present on applying voltage to an SOFC.

Under open circuit condition and constant gas flow in the SOFC stack, a uniform gas distribution is assumed in the electrodes. Once a current is drawn from the cell, O_2 will be reduced at the electrochemical interface and the oxygen ions will move through the electrolyte. To ensure a constant fuel cell mode during the EIS measurement, usually the AC current is superimposed on a constant DC current. At the anode side, H_2 moves to the electrolyte interface and is oxidized with the oxygen ions from the electrolyte forming water vapor which is transported back to the gas channel. Therefore, the concentration of H_2 is lower at the electrode-electrolyte interface and the H_2O concentration is higher, respectively. These concentration differences are the main driving force for the diffusion of the uncharged reactant and product species. The impedance arising from a diffusion limitation, can be written as

$$Z(i\omega) = \frac{\frac{dE}{dc}(\omega^{-0.5} - i\omega^{-0.5})}{zF\sqrt{2D}} \tag{40}$$

with the diffusion constant D.

The diffusion-related impedance is therefore proportional to the square root of the angular frequency ω, which leads to a straight line in the Nyquist plot inclined with π/4 (45 °).

At high frequencies and small AC amplitudes, there is no significant depletion of reactants at the electrochemical interface. Therefore diffusion limitation polarization is visible in the low-frequency range of the EIS spectrum. The electrical equivalents to model the diffusion related impedance are the infinite-length and the finite-length Warburg elements [47]. For more details on the mathematical description of the related impedance response refer to chapter 2.2.3.

Of course the assumption of ideal uniform gas distribution is only valid if the porosity of the electrodes and the gas flows are sufficiently high and the geometry of the gas channels can provide a uniform distribution over the interconnector plate area. Improving the gas distribution over the cell area and inside the electrodes is a matter of material engineering for electrode materials and of interconnector plate design. Analyzing the diffusion-related impedance is therefore a useful method to improve the material and stack properties of SOFC stacks.

Charging of interfaces

On applying a voltage to an electrochemical system, the interface between the electrode and the electrolyte will be charged due to an excess of charge carriers at the electrode surface. This distribution of charge leads to the formation of a so-called electrochemical double layer which electrically behaves like a parallel plate capacitor. The length to which the concentration perturbation extends into the electrolyte in general depends on the dielectric constant, the temperature and the bulk concentration of charges and is called Debye length L_D.

The higher the charge concentration in the electrolyte, the thinner the electrochemical double layer will be. Describing this layer as an ideal parallel plate capacitor is based on the assumptions that the charges are point charges, the dielectric constant is constant throughout the electrolyte material, the boundary between the electrode and electrolyte is sharp and that there are no charge screening effects present. While for solid-liquid interfaces, the interface capacitance can be described well by the Gouy-Chapman equation, experimental studies and the mathematical description of solid-solid interfaces are not straightforward as there is often a non-ideal frequency dispersion observed [36].

As discussed in chapter 2.2.1, the electrodes used for SOFCs are made of porous materials and cermets with mixed electronic and ionic conductivity. For such systems, the interface between electrode and electrolyte is extending into the electrode and is present at the entire triple-phase boundary length. It has to be emphasized though that the sharpness of the boundary mentioned before is meant on the atomic scale in terms of the electronic wave function, which should not extend beyond the geometrical plane of the interface. In real materials there will be defects and property distributions in space which can potentially lead to a non-ideal capacitive behavior which is frequently modeled by using the constant phase element and leads to the observation of frequency dispersion effects in EIS measurements. For more details refer to chapter 2.2.4.

Charge Transfer at the Electrolyte-Electrode Interface

The following mathematical description of the current-voltage relationship at the electrochemical interface is based on chapter 2.1.4 in [36].

The reaction rate of a heterogeneous charge transfer reaction of the form

$$O + ne \ \rightarrow R \tag{41}$$

in general is described by

$$-i_F = nF\left[k_f c_O - k_b c_R\right] \tag{42}$$

with the faradaic current density i_F, the forward and backward reaction rate constants $k_{f,b}$ and the concentrations of the reactants and products c_O and c_R at the interface. In general, this current is composed of a DC part governed by the mean DC potential V and the mean concentrations at the interface c_O and c_R and an AC part (Δi_F) arising from the perturbation potential ΔV and the concentration fluctuations Δc_i. The faradaic impedance can therefore be expressed as:

$$Z_F = \frac{\{\Delta V\}}{\{\Delta i_F\}} \tag{43}$$

with { } denoting the Laplace transform operator.

In general the electric field at the interface has an impact on the energies of various species approaching the interface, which leads to a dependency of the activation energy barrier on the potential difference across the interface. This dependency of the rate constants can be expressed as:

$$k_f = k_0 \exp(\frac{-\alpha(V-V_0)nF}{RT}) \tag{44}$$

$$k_b = k_0 \exp(\frac{(1-\alpha)nF(V-V_0)}{RT}) \tag{45}$$

where k$_0$ is the rate constant at the formal potential E$_0$ and α is the charge transfer coefficient. The term (V-V$_0$) is denoted as overpotential η in what follows. The AC part of the faradaic impedance can be expressed in dependency on the concentrations and the electrode potential as:

$$\Delta i_F = \sum \left(\frac{\partial i_F}{\partial c_i}\right) \Delta c_i + \left(\frac{\partial i_F}{\partial V}\right) \Delta V + hihger\ order\ terms \tag{46}$$

Based on the above considerations, the faradaic impedance can be described as:

$$Z_F = \left(\frac{\partial i_F}{\partial V}\right)^{-1} \left[1 - \sum_i \left(\frac{\partial i_F}{\partial c_i}\right) \frac{\{\Delta c_i\}}{\{\Delta i_F\}}\right] \tag{47}$$

The first term is the charge transfer resistance and the second term expresses the influence of the mass transport to and from the electrode on the impedance. The term {Δc$_i$}/{Δi$_F$ } could be expressed as a solution of the diffusion equation. At equilibrium the concentrations c$_O$ and c$_R$ at the interface are equal to the bulk concentrations c$_O$* and c$_R$* which are related through the Nernst equation

$$\frac{c_O^*}{c_R^*} = exp \frac{nF}{RT} \eta \tag{48}$$

which simplifies the expression ∂i$_F$/ ∂V to:

$$\frac{\partial i_F}{\partial V} = \frac{n^2F^2}{RT} k_0 exp \left[-\frac{\alpha nF}{RT} \eta c_0^*\right] \tag{49}$$

The charge transfer resistance can therefore be described as:

$$R_{ct} = \frac{RT}{nFi_0} \tag{50}$$

with the exchange current density i_0. When mass transfer to the electrode is not relevant, the well-known Butler-Volmer equation describes the faradaic current density:

$$i_F = i_0 \left[\exp\left(\frac{\alpha nF}{RT}\eta\right) - \exp\left(-\frac{(1-\alpha)nF}{RT}\eta\right)\right] \tag{51}$$

A major assumption which is made in the theory presented here is that the faradaic current is decoupled from the non-faradic current. In terms of equivalent circuit modelling this means that the double-layer capacitance is placed in parallel to the faradaic impedance because

$$i = i_F + i_{NF} \tag{52}$$

However, in general the non-faradic current is also a function of the concentration of reactive species. For solid-liquid systems, the decoupling can be achieved via making the concentration of electroactive species very small compared to the inactive ones which are doing most of the double-layer charging. Of course this is not possible in solid electrolytes, where the electroactive species is the only charge carrier in most of the cases. Therefore there is a coupling between the faradic current and the double-layer charging.

To describe such systems, an alternative equation has been proposed [48]

$$i = i_0 \left[1 + \frac{C_{dl}\eta}{|q| - \Delta V C_{dl}}\right] \exp\frac{nF}{RT}\alpha\,\eta \tag{53}$$

where q is the charge density of anions in the inner double layer.

This concept can be extended to reactions with more than one step or reactions including adsorbed species by coupling the reaction steps and mass transport relations accordingly. A few examples are the Gerischer impedance [49] or the impedance models proposed by Armstrong and Henderson [50]. The impact of specific adsorption will not be put in more detail in this thesis.

2.2.3 Equivalent Circuit Modelling

The analysis of impedance data generally can be done by means of two modelling approaches, namely the physico-chemical modelling or the equivalent circuit modelling. In physico-chemical modelling, the model is based on theoretical physico-chemical relations from which the theoretical impedance can be calculated. This theoretical impedance is then fitted by means of a CNLS approach and the fitting parameters can be calculated to characterize the system under investigation. An example for a physico-chemical fuel cell model is the Kulikovsky impedance model for the PEMFC [51].

In equivalent circuit modelling, the impedance of the system is modeled with a combination of ideal electrical circuit elements such as resistors, capacitors and inductors. The impedance of the equivalent circuit model $Z_{eq}(\omega)$ is then fitted against the experimental impedance parametrize the circuit elements and thus estimate the physico-chemical properties of the cell such as bulk conductivities, diffusion constants or electrochemical reaction rates. The relationship between ideal circuit elements and physico-chemical properties could be shown in early works [52] [53].

In an equivalent circuit model, resistors represent conductive paths such as the bulk conductivity of the electrodes or the electrolyte or a charge transfer resistance at the interface where the electrochemical reaction takes place [54] [55]. Capacitors can be associated with space charge polarization regions in the vicinity of the electrochemical interface or with specific adsorption at this interface. Based on the theoretical considerations regarding the faradaic and non-faradaic impedance presented in chapter 2.2.2, an electrochemical process step at an interface can therefore be modeled as a parallel connection of a resistor and a capacitor with the resistor representing the charge transfer resistance of the electrochemical reaction and the capacitor representing the double-layer capacity at the electrode-electrolyte interface. Furthermore, inductors can be used to model parasitic inductive effects in SOFC test rigs or the cabling between the test rig and the EIS measurement tool.

The theoretical impedance of a pure resistor and capacitor is given by:

$$Z_R(\omega) = R \tag{54}$$

$$Z_C(\omega) = \frac{1}{i\omega C} \tag{55}$$

The theoretical impedance of an inductor is given by:

$$Z_L(\omega) = i\omega L \tag{56}$$

When combining circuit elements as parallel connections, the total impedance Z_{sum} can be calculated as:

$$\frac{1}{Z_{sum}(\omega)} = \sum_n \frac{1}{Z_n(\omega)} \tag{57}$$

For series connections of circuit elements, the following expression is used to calculate the total impedance of the circuit:

$$Z_{sum}(\omega) = \sum_n Z_n(\omega) \tag{58}$$

The total impedance of an ideal RC (R and C in parallel) element is given by:

$$Z_{RC}(\omega) = \frac{R}{1+i\omega RC} \tag{59}$$

The corresponding characteristic relaxation time τ_{RC} of the electrochemical process is

$$\tau_{RC} = RC \tag{60}$$

The relaxation time is frequently transformed into a relaxation frequency by $f_{RC} = 2\pi/\tau_{RC}$. This relaxation frequency is higher for transfer rates of electrons over the electrode-electrolyte interface (1 kHz to 10 kHz) and low for diffusion processes of uncharged species through the electrodes (0. 1 – 10 Hz) [56].

A major disadvantage of using equivalent circuit models is that they are often ambiguous. That means that many different equivalent circuits can yield exactly the same Z_{eq}. For choosing a physically-meaningful ECM, at least some knowledge about the electrochemical processes in the investigated system is necessary. To account for this problem, the Distribution of Relaxation Times analysis is helpful to get an approximation of the number of processes contributing to the overall polarization loss and their respective relaxation time characteristics. This method is described in detail in section 2.2.4.

Another complication arises from the fact that ordinary circuit elements such as resistors or capacitors describe ideal electrical behavior. However, real electrochemical systems are of finite size and the properties of their individual parts are distributed in space. In general two kinds of distributions can be distinguished, namely the ones originating from non-local processes such as diffusion and convection and the ones arising from a distribution of material properties over the cell area. Diffusion processes are commonly modeled by using Warburg elements. They can be split up into the infinite-length Warburg element and the finite-length Warburg element [47], which appeared first for supported systems in the work of Llopis and Colon [57] and for unsupported systems in the work of Macdonald regarding space charge polarization effects [58] [59] and effects on small-signal frequency AC response [60] [61] [62]. To model chemical reactions of electroactive species in the bulk, another distributed element, the Gerischer element [63], is commonly used. This element is also used to describe electrochemical reactions which include adsorption of reactive species at the electrode interface. In order to account for distributed material properties as well as for non-ideal electrical properties in general, the so-called constant phase element (CPE) is frequently used for modeling processes exhibiting non-ideal effects. Details on its physical origins are given in chapter 2.2.4.

The theoretical impedance of a CPE is given by:

$$Z_{CPE}(\omega) = \frac{1}{(i\omega)^n Q} \tag{61}$$

with the CPE exponent n and the CPE constant Q.

The parallel connection of an ideal resistor and a CPE is called ZARC or RQ element and is mathematically described by the following expression:

$$Z_{RQ}(\omega) = \frac{R}{1+R\frac{1}{(i\omega)^n Q}} \tag{62}$$

with the relaxation time τ_{RQ} of the associated electrochemical process

$$\tau_{RQ} = \sqrt[n]{RQ} \tag{63}$$

Combining the latter two formulas yields an alternative way of describing the RQ element in terms of resistance and relaxation time

$$Z_{RQ}(\omega) = \frac{R}{1+(i\omega\tau)^n} \tag{64}$$

Compared to the ideal RC element, the RQ element results in a depressed semicircle in the Nyquist diagram, as shown in Figure 2.2.3 with the degree of depression increasing with a decreasing value of the CPE exponent n.

The impedance of a fuel cell is typically modeled with an equivalent circuit model consisting of a series connection of a resistor and various distributed elements such as an RQ, Warburg or Gerischer elements, as depicted in Figure 2.2.4. The Warburg element is used for modelling diffusion processes and the Gerischer element models combined adsorption-reaction processes.

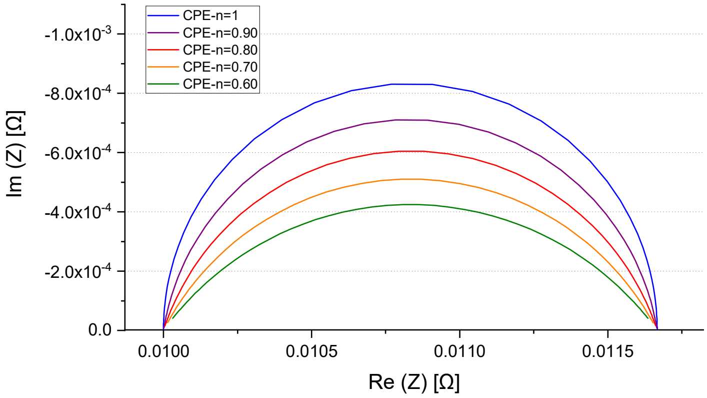

Figure 2.2.3. Exemplary Nyquist plot of an electrochemical process exhibiting CPE behavior with different values of the CPE exponent n.

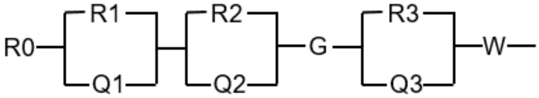

Figure 2.2.4. Typical ECM for modelling the response of a fuel cell with distributed circuit elements (G=Gerischer element, W=Warburg element, R0-R3= resistor, Q1-Q3=Constant Phase Element)

Once the ECM is built up, the theoretical impedance of the given circuit is fitted against the experimental impedance by using a complex non-linear least squares method [64]. The advantage of CNLS-fitting compared to Nonlinear Least Squares (NLLS) fitting is that both the real and imaginary part can be used simultaneously to estimate the fitting parameters of the model. The general approach of CNLS fitting is to minimize the sum of squares of the difference between the theoretical and the experimental value which is given by

$$S = \sum_{k=1}^{N}\left[W_{k,R}\left(Z'_{exp}(\omega_k) - Z'_{eq}(\omega_k, \boldsymbol{P})\right)^2 + W_{k,I}\left(Z''_{exp}(\omega_k) - Z''_{eq}(\omega_k, \boldsymbol{P})\right)^2\right] \quad (65)$$

with the matrix **P** containing the set of fitting parameters of the model and optional W_k representing the weighting parameters of the real and imaginary part. Usually a Levenberg-Marquardt (LM) algorithm [65] [66] [67] is used for solving the minimization of S numerically. Starting with a set of estimated fitting parameters, the minimum of the sum of squares is found via iterations with incremental changes of the fitting parameters. Usually this procedure is done with at least two distinct sets of starting values to ensure that the solution which is found is not a local minimum of the optimization problem. The goodness of fit (GOF) is frequently visualized in the Nyquist or Bode diagram by plotting the experimental data and the calculated model impedance. When using ideal circuit elements, the physical interpretation of the fitting parameters R and C are quite straightforward and represent the charge transfer resistance and the double-layer capacitance of the associated electrochemical process. As soon as distributed elements such as the CPE are used, the interpretation of the fitting parameters becomes more puzzling. Therefore, a thorough investigation on the origin of constant phase behavior is needed which is discussed in the subsequent chapter.

As a summary, the general workflow of an EIS analysis is illustrated in Figure 2.2.5. The method of Distribution of Relaxation Times is described in detail in section 2.2.5.

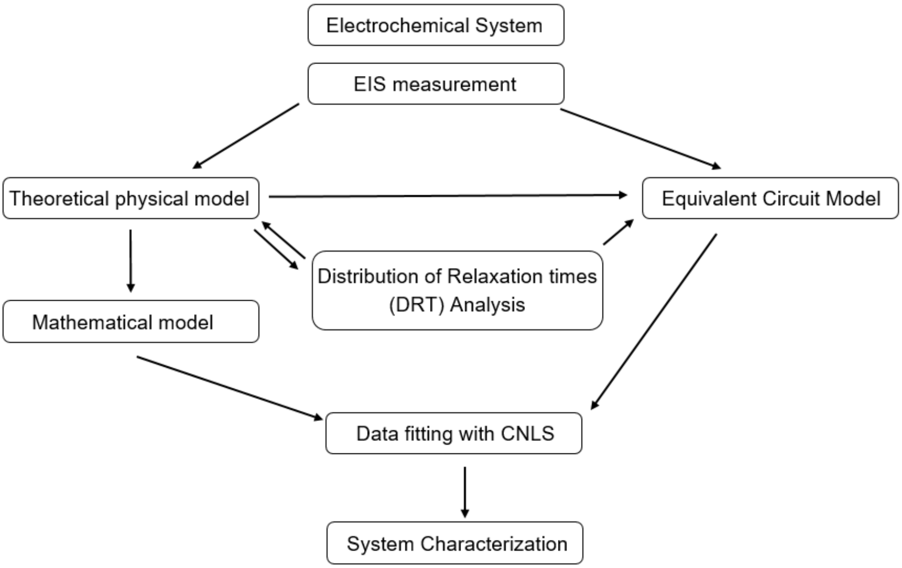

Figure 2.2.5. Flow diagram of EIS data analysis for the characterization of electrochemical systems

2.2.4 The Constant Phase Element

Although the constant phase element is ubiquitous in equivalent circuit modelling for various electrochemical systems, there is still a lack of understanding in the physical origin of this impedance behavior. The first appearance of the CPE was at the investigation of dielectric relaxation processes in solid crystalline materials and polar liquids [36]. One of the first approaches to model the dielectric relaxation in polar media was to describe the process of dipole relaxation with a single time constant, as proposed by Debye in 1929 [68]. However, studies on crystalline polar solids showed more than one relaxation time in the material [69]. Therefore it was attempted to extend the Debye model to describe relaxation processes with more than one relaxation time resulting in a distribution of relaxation times. The generalized expression for the distribution of the dielectric function is given by:

$$\varepsilon - \varepsilon_\infty = \int_0^\infty \frac{(\varepsilon_s - \varepsilon_\infty)G(\tau)d\tau}{1+p\tau} \tag{66}$$

with the high frequency dielectric constant or refractive index ε_∞, the static dielectric constant ε_s, the complex frequency variable p and the distribution of relaxation times G(τ), which represents the fraction of (ε_s-ε_∞) made up of processes having relaxation times between τ and τ + dτ. Furthermore this distribution should be normalizable as

$$\int_0^\infty G(\tau)d\tau = 1 \qquad (67)$$

Several distributions fulfilling the above mathematical requirements have been stated to describe the phenomenon of depressed semicircular arcs in complex permittivity, for example the Cole-Cole distribution [70] with a symmetrical distribution around a center value τ_0 or the Cole-Davidson distribution [71], which is an asymmetrical distribution. This approach of studying the broadening of the response of dielectric materials is stated to be the origin of the constant phase elements that are seen in impedance studies of solid electrolytes and solid-solid interfaces as depressed semicircular arcs in the complex plane [36].

The concepts which have been elaborated for polar liquids and solids subsequently have been extended to conducting liquids and solids. Corresponding to the early concepts of Onsager [72] [73], Debye and Falkenhagen [74], the physical origin of a frequency dependent conductivity in solid conductive materials is the interaction between different defects in the crystal lattice or the presence of additional phases. Those inhomogeneities in the material are leading to a non-uniform potential profile across the conductive path thus resulting in multiple activation energies for the ion hopping process, which is governing the overall electrical conductivity of solid materials.

Noticeable work in this field has been done by Jonscher [75] [76], who showed that many different types of conductors exhibit a CPE behavior causing a frequency-dependent conductivity. Corresponding to his work, the origin of frequency dispersion is the relaxation of the ionic atmosphere after the movement of a charged particle from one lattice position to another. In a model stated by Funke [77] it is assumed that after the hopping of an ion to the next lattice site with a new minimum in the local lattice potential, this ion is still away from the minimum of the total potential energy, which includes contributions from other mobile defects as well. On this theoretical basis, the Concept of Mismatch and Relaxation (CMR) has been proposed [78] [79], which is frequently used to describe the ionic conductivity of disordered materials, for example in [80].

The above presented concepts were the basis for the investigation of CPE behavior in various electrochemical systems such as electrode-electrolyte systems with solid-liquid and solid-solid interfaces. In general, it can be distinguished between three origins causing the CPE behavior, namely material properties and related processes

a) Inside the electrolyte, such as crystal orientation, crystallinity, grain boundaries, defects or a distribution of resistivity within the material
b) At the electrode-electrolyte interface, such as interface roughness, atomic surface or 3D irregularity, defects at the interface, non-uniform current and/or potential distributions or effects due to specific adsorption leading to a distribution of rate constants
c) In the electrode, such as porosity, pore size distribution and inner surface roughness, anomalous diffusion in porous structures or electrode geometry in general

These potential physical origins are discussed in more detail in the following sections.

Electrolyte

Abouzari [80] investigated the ionic conductivity of quartz glass and lithium borate glass with impedance spectroscopy to study the influence of the crystal structure and surface roughness on the degree of frequency dispersion governed by the CPE exponent n. In the study it was found that the CPE exponent is close to unity for the crystalline quartz glass and appreciably lower for the lithium borate glass, but for both materials independent of the surface roughness. As a conclusion it was stated that the CPE behavior in the glass is correlated to the forward-backward correlation of elementary hopping processes of the mobile ions, as described in the ‘Concept of Mismatch and Relaxation’ (CMR) by Funke that was mentioned before.

Heterogeneous grain boundary properties in solid polycrystalline electrolytes have also been stated as the origin of CPE behavior [81]. Such grain size effects were subject of research works regarding the solid oxide electrolyte material YSZ [82]. It could be shown that the exponent of the CPE exhibits a linear relationship with the standard deviation of conductivity distributions due to grain boundary property distributions in solid conductors. Hirschorn linked the constant phase element behavior to resistivity distributions in films and proposed models to calculate the resistivity by means of the CPE parameters Q and n [83] [84]. Another model to calculate resistivity distribution along the film thickness by means of the CPE parameters was proposed by Córdoba-Torres [85] [86].

Electrode-Electrolyte-Interface

Another origin of CPE behavior are non-ideal double layer capacitances which are especially observed to occur at solid-solid polarizable interfaces, as shown in early works by Bottelberghs [87] and Raistrick [88]. Further studies also led to the proposal that the CPE behavior at the electrode-electrolyte interface is arising from a capacitance distribution across the electrode surface and models have been proposed correlating the CPE parameters to the effective double layer capacitance [89] [90]. More recently it could be shown with finite-element simulations of disk electrodes that surface heterogeneity arising from non-uniform capacitance causes frequency dispersion effects in the frequency range above 1 kHz [91].

Additional to surface distributions of capacitances, also normal-to-surface distributions of time constants were proposed to cause CPE-behavior [92] and mathematical models to determine the film thickness from CPE parameters were proposed. Also the coupling of faradaic and charging currents at the electrochemical interface was found to correlate with CPE effects [93]. The effects described there are most relevant for systems in which the charge carriers can accumulate at the interface and therefore lead to a charging of the electrochemical double layer.

Roughness of the electrode-electrolyte interface was stated as the most probable origin of the constant phase element for a long time. One of the first models correlating macroscopic electrode roughness with frequency dispersion was proposed by de Levie [94]. It was also proposed that the CPE exponent n is directly reflecting the roughness of the solid electrode and is independent of the material [95]. Wang showed that the CPE - n decreases with increasing roughness of the interface between a solid electrolyte and a blocking metal electrode and with an increasing temperature [96]. Kerner proposed that the frequency dependence of the capacitance is due to atomic scale inhomogeneities rather than to macroscopic aspect of roughness [97] [98]. More recently, Córdoba-Torres proposed that CPE behavior of interfaces is more related to energetic than to geometric heterogeneity [99].

Special emphasis was also put on the correlation between electrode geometry and constant phase element behavior. It is stated in literature that the electrode geometry can cause current and potential distributions which are then causing the frequency dispersion effects seen in the impedance response of the investigated systems. Alexander performed finite-element simulations for disk electrodes to show that the surface geometry profile of the electrodes, simulated as V - shaped grooves on the electrode surface, induces current distributions which are causing the frequency dispersion in the high frequency range [100]. Córdoba-Torres performed an experimental study on the current and potential distribution on disk electrodes and showed the effect of geometry-induced distributions on the impedance response in the high frequency range [101]. Hsu [102] suggested a simple equation to calculate the interfacial capacitance from the fitting parameters of the CPE with

$$C_{CPE} = R^{\frac{1-n}{n}} Q^{\frac{1}{n}} \tag{68}$$

with CPE exponent n, CPE parameter Q and resistance R. Although this formula is widely used, it does not give a physical interpretation of the parameters Q and n and is only valid if n or RQ is close to unity [103]. However, the CPE exponent can be found around 0.8 for example for LSM/YSZ systems used in SOFCs [104]. Another equation for the interface capacitance was theoretically derived from the analytic capacitance distribution that yields a perfect CPE behavior [90] and is given by:

$$C_{CPE} = [Q(R_e^{-1} + R_{ct}^{-1})^{n-1}]^{1/n} \tag{69}$$

There the electrolyte resistance R_e is taken into account as well. This equation has been widely used to determine interfacial capacitance and in some case the active surface area from CPE parameters [105] [106]. In a theoretical study on the geometry-induced current and potential distributions, it could be shown that equation (69) leads to the best estimate of the interfacial capacitance [107]. For discussion of the calculation of active area from CPE parameters refer to [108].

J.R. Macdonald proposed a distribution of relaxation times in the impedance response of dielectric and conductive systems due to exponential and Gaussian distributions of activation energies [109]. More recently, also distributions in rate constants of reactions coupled by an adsorbed intermediate at the electrode-electrolyte interface were proposed to cause frequency dispersion [110]. The characteristic frequency range in which the dispersion occurs is stated to be dependent on the parameters of the faradaic impedance. On the other hand, it could be shown that surface distribution of reactivity for a single-step reaction did not cause a CPE behavior [111].

A further origin of the Constant Phase Element is stated to be a time-constant distribution due to frequency dependence of the capacitance and the ohmic resistance resulting in a complex ohmic resistance. Newman showed that the complex character of the ohmic resistance is a function of the electrode geometry, the interfacial impedance and the electrolyte conductivity [112]. Further investigation on the origin of the complex ohmic impedance showed that this phenomenon is related to contributions of radial current distributions to the local current densities on the electrode [113]. Based on 3D finite-element simulations, a model relating the electrode geometry, the interface capacitance and electrode conductivity with the maximum possible frequency for the impedance measurement to avoid frequency dispersion effects in the high frequency range, was proposed. This means that the electrode geometry limits the maximum frequency in the impedance measurement that can be measured without facing complex ohmic impedance effects [114]. Gharbi investigated the ohmic contribution in the high frequency range for capacitive and faradaic electrochemical responses [115].

Although studies on frequency dispersion effects caused by the non-ideal interfacial response in SOFCs are currently missing, the above discussed general physical origins of the CPE behavior, such as non-uniform current and potential distributions over the cell area or macroscopic and atomic roughness of the interface, could potentially also be present in the SOFC.

Electrode

Studies on porous electrodes have been conducted to correlate the CPE behavior to an inner surface capacity [116] arising from the fact that the electrode-electrolyte interface is spreading into the porous electrode or to the pore size (-distribution) of the electrode material [117] [118] [119]. Furthermore, anomalous diffusion mechanisms inside the porous network have been proposed to be the origin of frequency dispersion effects [120].

The studies that are published so far were mostly conducted on disk electrodes or solid-liquid systems. Although detailed studies on the physical origin of CPE behavior related to the SOFC are quite rare [121], it is ubiquitous in equivalent circuit modelling for SOFCs [122] [123] [124] as it is in general seen as a commonly acknowledged behavior in the impedance response of the electrode-electrolyte-interface [125]. Niya [126] investigated the dependence of the CPE exponent on operating conditions in Proton Exchange Membrane Fuell Cells and showed that there is no dependence of CPE-n on the temperature but only on the change of current densities. As a summary, material properties and their distribution inside the electrolyte, at the electrode-electrolyte-interface or inside the electrodes, as well geometry-induced potential and current distributions over the cell area can in principle lead to the observation of CPE behavior in the impedance response of different electrochemical systems.

Electrochemical processes that exhibit CPE behavior in the electrical response do not exhibit a single relaxation time but have to be described with a distribution of relaxation times. To analyze electrochemical processes which exhibit this kind of relaxation behavior, the method of Distribution of Relaxation Times was developed and will be discussed in detail in the next chapter.

2.2.5 Distribution of Relaxation Times

As discussed in the chapters before, the origin of the Distribution of Relaxation Times was the observation of frequency-dependent electrical properties of polar and conductive materials, such as permittivity and conductivity, and the resulting need to describe the relaxation of electrochemical processes with more than one relaxation time. For typical Debye processes with a single relaxation time, the DRT function is a delta function at the characteristic relaxation time. For electrochemical processes with distributed relaxation times, the DRT function is distributed around a characteristic relaxation time τ_0, as shown in Figure 2.2.6.

In recent years the DRT analysis method became of high interest to investigate the characteristic time scales on an EIS experiment and to achieve a higher resolution of processes compared to Nyquist and Bode plotting [127] [128] [129]. Another great advantage of the DRT is the fact that in principle no prior knowledge about the number of processes is needed, compared to the ECM approach described above. Furthermore, the problem of ambiguous equivalent circuits is potentially overcome, according to Macdonald [130]. Therefore the DRT method can act as an alternative method in EIS data interpretation [131] or assist the ECM based data analysis [8].

The calculation of the characteristic time scales in an EIS experiment by means of the DRT is done via a transformation of the impedance data from the frequency domain into the relaxation time domain, which is based on the following expression:

$$Z_{DRT}(f) = R_O + \int_0^\infty \frac{g(\tau)}{1+i2\pi f\tau} d\tau \tag{70}$$

with the ohmic resistance R_O and distribution function of relaxation times $g(\tau)$. This equation expresses a typical Voigt circuit, which consists of an ohmic resistor in series with the sum of an infinite number of RC elements.

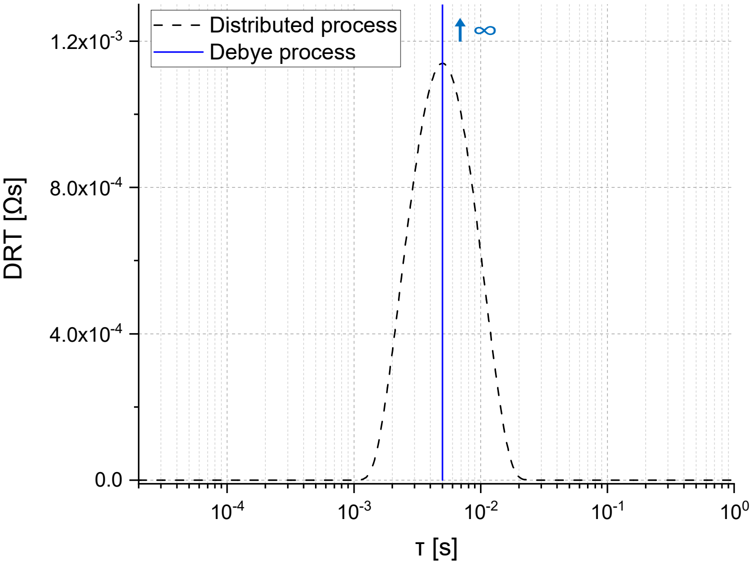

Figure 2.2.6. Comparison of the principal DRT shape for a Debye process with a single relaxation time (blue solid line) and a distributed process with Gaussian shape (black dashed line).

As the frequency data is often collected on the logarithmic scale, the above equation can be rewritten as:

$$Z_{DRT}(f) = R_O + \int_{-\infty}^{\infty} \frac{\gamma(ln\tau)}{1+i2\pi f\tau} dln\tau \qquad (71)$$

Determining the function γ (ln τ) is done by means of fitting Z_{DRT} with the experimental data Z_{exp}, which is a mathematically ill-posed problem due to the large number of unknowns. Many methods for calculating the γ (ln τ) have been proposed in literature, such as the evolutionary programming techniques of Tsur and co-workers [132] [133] [134], Monte Carlo methods developed by Tuncer and McDonald [135] [136], Fourier-filtering by Tiffée and co-workers and Boukamp [45] [137] or the Maximum entropy method by Hörlin [138]. In this thesis, the regularized regression approach [139] [140] [141] [142] plays an important role as it is used in DRTtools by Wan [10] that is used for performing the simulation in this study. Therefore, the regularized regression approach is discussed in more detail in the following sections.

Regularized regression approaches

In general, regression methods are used to estimate the parameters of a mathematical model that is best fitting the sample data by minimizing the deviations between the model function and the data points. In the simplest case, this is done via minimizing the squared deviations between the data points and the respective values of the model function at the given x-values in the so-called Ordinary Least Squares (OLS) approach. Extending the OLS by introducing a penalty to the coefficients and their error terms leads to regularized regression approaches like the Ridge regression, which was first introduced by Hoerl and Kennard [143] and the Least Absolute Shrinkage and Selection Operator (LASSO) regression method [144]. Both are special cases of the general Tikhonov regularization approach. In general, the regularized regression method is based on the minimization of the following sum:

$$\sum_{n=1}^{N}[y_n - g(x_1, x_2, \dots x_n, f_n)]^2 + \lambda P(x_1, x_2, \dots x_n) \tag{72}$$

for N data points y_n taken at f_n, the fitting function g and the penalization term P, which is weighted with the regularization parameter λ.

The Ridge regression is used for solving continuous problems when the number of unknown parameters exceeds the number of experimental data points or if the data set exhibits collinearity, which means that there are correlations between the unknown parameters. In this method, a so- called L2 penalty is added, which is the sum of squared magnitudes of the unknown parameters x times a differentiation matrix Γ, which leads to a penalty function like

$$P(\boldsymbol{x}) = \|\boldsymbol{\Gamma x}\|_2^2 \tag{73}$$

With $\| \ \|_2$ denoting the Euclidian norm as:

$$\|\boldsymbol{x}\|_2 = \sqrt{\sum_{n=1}^{N} x_n^2} \tag{74}$$

The strength of the penalty is controlled by the regularization parameter λ. If this parameter is set to zero, the Ridge regression equals the OLS. If λ = ∞, all parameters of the model function are shrunk to zero. With this Ridge penalty, both a minimization of the sum of regression errors, which describes how well the model fits the data, and the sum of numerical derivatives, which describes how much the regressed data is oscillating, are realized. This leads to the fact that increasing the regularization parameter to suppress numerical oscillations will also add more penalty on the derivatives which lowers the closeness between the model and the actual data. Therefore, the choice of the regularization parameter is always a trade-off between the model accuracy and the degree of numerical oscillations.

In the LASSO regression method, the coefficients are penalized by an L1 penalty of the form

$$P(\boldsymbol{x}) = \|\boldsymbol{x}\|_1 \tag{75}$$

with

$$\|x\|_1 = \sum_{n=1}^{N} |x_n| \tag{76}$$

which equals the sum of absolute values of the coefficients which leads to the fact that for high regularization parameters many coefficients are exactly zero, which is not possible in Ridge regression. Therefore the LASSO regression is more suitable for solving discrete problems [127].

For solving the ridge regression problem numerically, quadratic programming algorithms can be used which in general find a coefficient vector **x** to minimize quadratic problems with n variables and m constraints like [145]

$$\min_{x} \frac{1}{2} \boldsymbol{x}^{\boldsymbol{T}} \boldsymbol{Q} \boldsymbol{x} + \boldsymbol{c}^{T} \boldsymbol{x} \tag{77}$$

subject to the condition

$$\boldsymbol{Ax} \leq \boldsymbol{b} \tag{78}$$

with a real-valued n-dimensional vector **c**, an n x n-dimensional matrix **Q**, an m x n-dimensional matrix **A** and an m-dimensional matrix **b** giving the (linear) constraints for the coefficients in **x**.

For the solution of this minimization problem in MATLAB, the so-called interior-point-convex algorithm can be used, which is performing the following steps [146]:

- Pre-solve: The algorithm is removing redundancies and simplifying constraints. For details be referred to Gould [147].
- Generate initial point: The initialization is done with a vector of ones with n rows. In a first predictor step, the initial point is placed closer to the central path [148].

- Predictor-Corrector steps: The algorithm tries to find a point where the Karush-Kuhn-Tucker (KKT) conditions hold. In first place, a step from the Newton-Raphson formula is predicted followed by the computation of a corrector step, which attempts to better enforce the constraints. After calculating the corrected step, the algorithm performs more calculations to prepare for better subsequent steps. For more details on the algorithm basics be referred to Mehrotra [149] and Gondzio [150].
- Stopping Conditions: The predictor-corrector algorithm iterates until it reaches a point that satisfies the constraints within the given tolerances and where the step sizes are small.
- Post-solve: After reaching the stopping criterion, the original problem before the Pre-solve step is reconstructed by undoing the pre-solve operations.

DRT deconvolution with DRTtools

In DRTtools, the DRT function is determined in two steps, namely the discretization of γ (ln τ) with a sum of convenient basis functions followed by the calculation of the weighting parameters by means of the Ridge regression method. The choice of a convenient basis function is of great importance to reduce the approximation error [151]. The first approach for choosing a suitable basis function was using piece-wise linear (PWL) functions [127] [152] assuming that γ (ln τ) is linear between each consecutive timescale. In [10] the use of radial basis functions (RBFs) instead of PWL functions was proposed to increase the estimation quality of the DRT. An RBF is a symmetric function depending on the distance from a given center value, as:

$$RBF = \mathit{\Phi}_{\mu}(|(x - c|) \tag{79}$$

centered at x=c. The shape factor μ governs the full width at half maximum (FWHM) of the radial basis function. The advantage of using RBFs is that they can achieve a spectral accuracy which means that the approximation error decreases exponentially with an increasing number of discretization points [153] [154] . Furthermore RBF approximations can help to avoid oscillations at the edges of an interval during high degree polynomial interpolation (Runge effects) and do not require any special distribution of collocation points which makes their application more flexible [155]. As stated above, the calculation of the DRT consists of two steps: the discretization and the regularized regression, which are described in more detail in the following sections.

Discretization

The discretization in general can be done by building up the DRT model as a Voigt circuit consisting of N RC elements, which can be modeled as a sum of Dirac distributions δ centered at N characteristic times $\tau_1 \ldots \tau_N$

$$\gamma\ (\ln\tau) = \sum_{n=1}^{N} x_n \delta(\ln\tau - \ln\tau_n) \tag{80}$$

Where x_n are unknown fitting parameters which have to be determined via the regularized regression method. However, this approach is only suitable for discrete DRT functions. In real systems which frequently exhibit CPE behavior, the DRT has to be a continuous function and therefore the basis functions have to be continuous as well. Rewriting the above equation with usage of RBF yields:

$$\gamma\ (\ln\tau) = \sum_{n=1}^{N} x_n \Phi_\mu(|\ln\tau - \ln\tau_n|) \tag{81}$$

with N being the number of RC elements or single RBFs. An example for a simple RBF is the Gaussian function, which is also used for DRT calculation in this thesis and is mathematically defined by:

$$\Phi_\mu(x) = \exp(-(\mu x)^2) \tag{82}$$

In Figure 2.2.7, the modelling of DRT peaks as a sum of single RBFs, each representing an RC element, is shown graphically. Once the discretization is done, the estimation of the DRT function by calculating the fitting coefficients x_n of the single RBFs is done via regularized regression. Mathematical details can be found in the following chapter.

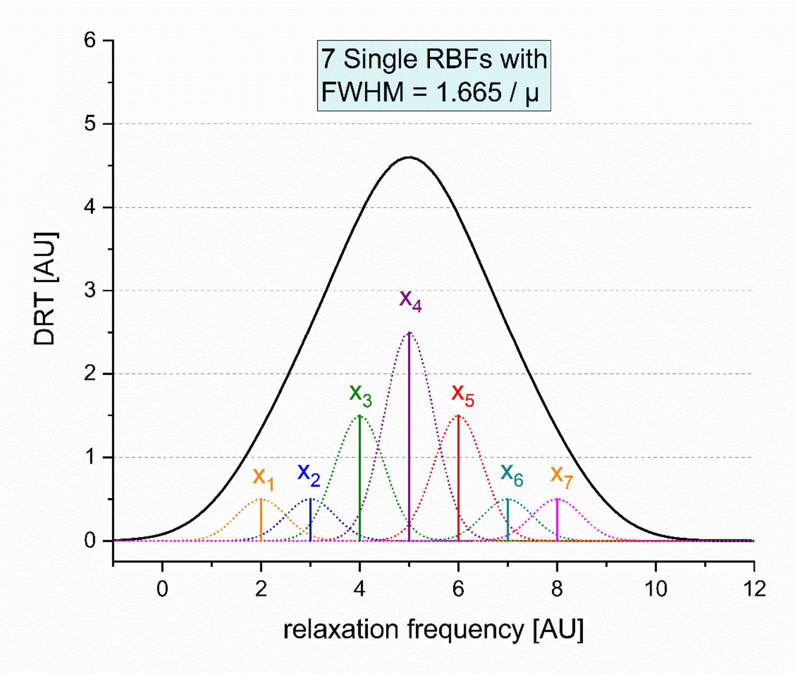

Figure 2.2.7. Graphical representation of the discretization of the DRT function with single RBFs each representing a single RC element with a characteristic relaxation frequency. The DRT is given as the sum of the RBFs, weighted by the fitting coefficients x_n. The FWHM of the single RBFs is governed by the shape factor μ.

Estimation of DRT function

The calculation of the DRT is done by fitting the DRT model Z_{DRT} against the experimental impedance data Z_{exp}. This fitting is realized with a least squares fit via minimizing the following sum:

$$S = \sum_{m=1}^{M} \left\{ w_m^{'} \left[Z_{DRT}^{'}(f_m) - Z_{exp}^{'}(f_m) \right]^2 + w_m^{''} \left[Z_{DRT}^{''}(f_m) - Z_{exp}^{''}(f_m) \right]^2 \right\} \qquad (83)$$

Inserting the impedance model for Z_{DRT} and putting equation (84) in a matrix form, one obtains the sum as a function of the coefficient matrix **x** [10]:

$$S\,(\boldsymbol{x}) = \left\| \boldsymbol{\Omega}^{'} (R_\infty \mathbf{1} + \boldsymbol{A}^{'} \boldsymbol{x} - \boldsymbol{Z}_{exp}^{'}) \right\|^2 + \left\| \boldsymbol{\Omega}^{''} (\boldsymbol{A}^{''} \boldsymbol{x} - \boldsymbol{Z}_{exp}^{''}) \right\|^2 \qquad (84)$$

The derivation of expressions of **A’/A’’** and **Ω’/ Ω’’** can be found in the Appendix. This problem is ill-posed due to the fact that the number of unknowns is bigger than the number of experimental data points and therefore only numerical solutions to the optimization problem are available. The suppression of the resulting numerical oscillations can be done with adding an extra L2 penalty term like:

$$\lambda \boldsymbol{x}^{\boldsymbol{T}} \boldsymbol{M} \boldsymbol{x} \tag{85}$$

Adding this penalty term to (85), one obtains the entire sum to be minimized as:

$$S\ (\boldsymbol{x}) = \left\| \boldsymbol{\Omega}^{'} (R_{\infty} \mathbf{1} + \boldsymbol{A}^{'} \boldsymbol{x} - \boldsymbol{Z}^{'}_{exp}) \right\|^2 + \left\| \boldsymbol{\Omega}^{''} (\boldsymbol{A}^{''} \boldsymbol{x} - \boldsymbol{Z}^{''}_{exp}) \right\|^2 + \lambda \boldsymbol{x}^{\boldsymbol{T}} \boldsymbol{M} \boldsymbol{x} \tag{86}$$

The expression of the matrix **M** can again be found in the Appendix. The minimization of S (**x**) is the well-known Tikhonov regularization problem [156] [157] [158]. The oscillations in the DRT are therein controlled by regularization parameter λ. Important to be mentioned is the fact that the minimization of S (**x**) gets more vulnerable to oscillations if the number of RC elements N is much bigger than the number of experimental frequencies M [159]. This means that the regularization parameter needs to increase as the ratio N/M increases. Additionally, it has to be noted that the matrices **A’** and **A’’** themselves strongly depend on the shape factor μ. This parameter is related to the FWHM of the underlying RBF used for discretization by FWHM = 1.665/μ. Small μ values can again lead to flattening of the DRT function and thus loss of physical information.

The fact that the regularization parameter λ is governing the degree of oscillations and therefore the number of peaks present leads to the problem of finding the optimal λ to suppress unwanted oscillations without losing physical information. Several methods were proposed in literature which should optimize the regularization parameter to achieve the above mentioned requirements, such as the Re-Im-Cross-validation [160], The Re-Im-Discrepancy method by Morozov [161], self - consistency methods [157] or the L-curve criterion method [162]. In the Re-Im-cross validation, the following term is minimized to find the optimal λ

$$ReImCV\ (\lambda) = \left\| Z^{'}_{exp} - A^{'} x^{''} \right\|^2 + \left\| Z^{''}_{exp} - A^{''} x^{'} \right\|^2 \tag{87}$$

Similarly, in the Re-Im-discrepancy method, the term

$$ReImDisc(\lambda) = \left\| \gamma_\lambda^{'} - \gamma_\lambda^{''} \right\|^2 \tag{88}$$

is minimized to find the optimal regularization parameter.

Another interesting method is an extension of the Re-Im-Cross-validation, namely the n-fold cross - validation [144] [163]. In this method, the solution is computed from several subsets of the data – the so-called training sets – and the obtained value is compared with other subsets, the so-called test sets [164]. It has also been proposed to use a vector of regularization parameters rather than a single value to account for specific relaxation time distributions on different time scales [165]. Schlüter et al. proposed an optimization routine based on repetitive DRT calculations based on EIS data sets generated with data resampling and subsequent DRT variance investigation [166]. Although there are a lot of methods proposed to determine the optimal regularization parameter, they have weaknesses when it comes to analysis of EIS data. For example the noise level in the EIS experiment is not known a priori, convergence of the mentioned methods is not guaranteed [167], many local minima may arise [168] or the error structure may violate the normality hypothesis [169]. Especially when it comes to frequency dispersion effects leading to CPE behavior of the impedance response, different kinds of problems with finding the optimal λ have to be considered, such as the characteristic peak broadening in the DRT which could potentially lead to oscillations or misinterpretations on the number of processes present due to peak overlapping.

The next section gives a statement of the scientific gap which is addressed in this thesis.

2.3 Statement of Scientific Gap

As mentioned in chapter 2.2.5, many methods for finding an optimal regularization parameter to calculate the DRT function have been presented in literature. Most of them are mainly based on the error structure of the underlying EIS data and use the cross-validation of the real and imaginary part based on the Kramers-Kronig relationship [40] [39]. By using the Tikhonov regularization method implemented in DRTtools, the DRT function γ (ln τ) is discretized with radial basis functions such as the Gaussian function leading to distributions of relaxation times around a characteristic value τ_0. As discussed in section 2.2.4, the distribution of relaxation times becomes broader with decreasing CPE exponent n, as shown in Figure 2.3.1. The physical origin of this broadening may be the distribution of material and electrical properties in the electrochemical cell leading to a greater number of relaxation times of a single process. Note the oscillations at low relaxation times in the figure below which is already arising from the simulated frequency dispersion by means of the CPE.

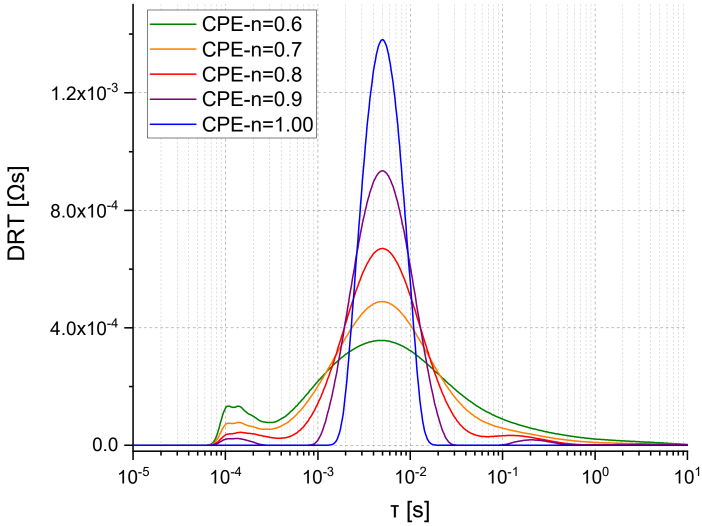

Figure 2.3.1. DRT functions based on the simulation of an electrochemical process with different values of the CPE exponent n, calculated with DRTtools.

As stated in the literature, the DRT analysis should help to identify electrochemical processes that are overlapping in the complex plane and should give an answer to the question how many distinct electrochemical processes are contributing to the total polarization loss of the cell. The separation of peaks in the DRT analysis is stated to be successful, if the characteristic relaxation times are separated by more than one order of magnitude. This might be true for electrochemical processes with no or less frequency dispersion, but is not investigated so far for systems exhibiting one or more processes with significant CPE behavior and therefore peak broadening for all peaks present in the worst case. As stated by Gavriluk et al. [170], at present state no thorough investigation on the interplay of significant CPE behavior and numerical stability of the Tikhonov regularization algorithm and the choice of an optimal regularization parameter has been conducted so far.

As CPE behavior can potentially be observed for EIS measurements on SOFC stacks due to distributed material properties, gas concentration distributions over the cell area and temperature gradients as well as current distributions, the principal behavior of DRT calculation in response to frequency dispersion and measurement errors has to be investigated to proof the accuracy and reliability of DRT results and to gain knowledge on the numerical behavior of the DRT calculation for such systems. It was also found in stack measurements at the Jülich Research Center, that the test rig and the cabling to the EIS measurement tool may give rise to parasitic inductive effects which may potentially influence the DRT calculation [11].

The approach in the present work is turning around the usual work flow of conducting a DRT study to identify the number of processes and their relaxation time characteristics with a subsequent CNLS fit with a suitable ECM derived from the findings of the DRT. Therefore, an ECM with three distinct transport and electrochemical processes modeled by three RQ elements with different CPE exponents is used to calculate the theoretical EIS spectrum which is then analyzed by DRTtools to investigate the discrepancy between the expected DRT results and the actual result dependent on the magnitude of the CPE exponent, the inductance, the error structure of the EIS spectrum, which was analyzed with the Kramers - Kronig validity test. Furthermore, the influence of EIS sampling rates (points per decade) and the available frequency range on the DRT result are investigated.

Following the theoretical study, the findings are verified on experimental EIS measurements conducted on SOFC stacks at the Jülich Research Center to highlight the practical relevance of the simulation results in the electrochemical characterization of SOFC stacks. In a subsequent cross - chapter analysis and discussion, a possible origin of the observed numerical effects is proposed together with an alternative choice of the regularization parameter in DRTtools to overcome the numerical weaknesses.

3. Simulation Structure

In the following chapter the mathematical details on the models which have been used to conduct the EIS and DRT simulation study, will be provided. Additionally, an overview on the performed parameter variation is given.

3.1 Equivalent Circuit Model

The EIS spectra which are analyzed with DRTtools are simulated by using an equivalent circuit model which is shown in Figure 3.1. It consists of a series connection of an ideal ohmic resistor (R1), an inductor (L1) and three parallel connections of a resistor (R2-R4) and a constant phase element (CPE1-3), which are referred to as 'RQ elements' in this thesis. The ohmic resistor represents the resistance of the solid electrolyte and contact loss between the interconnector plates and the cells in a stack, the inductance is built in to simulate parasitic inductive effects originating from the test rig and the cabling of the EIS measurement tool. The three RQ elements represent transport and electrochemical processes in the cathode or anode of the SOFC. The parametrization of the model is given in Table 3.1. The choice of parameters is done on the basis of observed values for anode - supported SOFCs [11]. The calculation of the EIS spectra is performed in MATLAB ®.

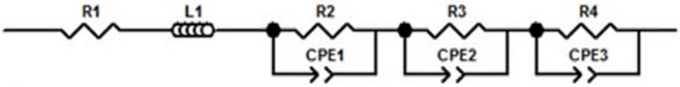

Figure 3.1. Equivalent Circuit Model used for the simulation of EIS spectra for the DRT study.

For simulations in different frequency ranges, the absolute number of data points used for simulation of EIS spectra was adapted to the number of decades to obtain a constant points per decade (ppd) value throughout the simulation. Additionally, a parameter study with purposely varying ppd values between 7 and 70 was performed to investigate the influence of the data point density on the accuracy of the DRT analysis. The details of the parameter variations are given in chapter 3.3.

Table 3.1. Parameters which are used to simulate synthetic EIS spectra for subsequent DRT analysis. The parameters marked with a star are part of the parameter study, all others are kept constant throughout the study.

Parameter	Value
Minimum frequency	10 mHz – 100 mHz*
Maximum frequency	10 kHz – 1 MHz*
Points per decade	7 - 70*
τ_1 / f_1	0. 08 s / 12. 5 Hz
τ_2/ f_2	0. 005 s / 200 Hz
τ_3 / f_3	0. 0005 s /2000 Hz
Ratio R2:R3:R4	3:1:2
Polarization resistances	2 – 20 mΩ*
Ohmic resistance	2 – 20 mΩ*
Inductance	$1*10^{-9}$ – $2*10^{-7}$ H*

3.2 Error models

In order to study the influence of measurement errors on the accuracy and repeatability of the DRT analysis, two different error models are used to simulate a statistical measurement error in the EIS data. The mathematical description of the error models is given in Table 3.2. The aim of error model 1 is to achieve an independent error structure of real and imaginary part especially in the high frequency range to simulate the influence of high frequency distortions of the measurement signal that were observed in EIS measurements on SOFC stacks in a previous work of the IEK-14 of the Jülich Reasearch Center [11]. Error model 2 has been taken from literature [127] directly and describes a comparable error structure and level of the real and imaginary part by scaling the error of the real and imaginary part with the modulus of the impedance. The motivation to use two different error models is to determine if there is a dependency of the DRT result not only on the error magnitude but also on the error structure. The value of ε_0 is also part of the parameter study and has been varied in the range between 0. 01 % and 0. 5 %. For details on the parameter variations refer to chapter 3.3. The variables η' and η'' describe independent random numbers with a mean value of zero and a variance of one, which are generated with the MATLAB® *randn* built-in function.

Table 3.2. Mathematical structure of error models used for EIS simulations

	Error model 1	Error model 2
Real part	$Re^*(f) = Re(f) + \varepsilon_0 \cdot \lvert Re(f)\rvert \cdot \eta'$	$Re^*(f) = Re(f) + \varepsilon_0 \cdot \lvert Z(f)\rvert \cdot \eta'$
Imaginary Part	$Im^*(f) = Im(f) + \varepsilon_0 \cdot \lvert Im(f)\rvert \cdot \eta''$	$Im^*(f) = Im(f) + \varepsilon_0 \cdot \lvert Z(f)\rvert \cdot \eta''$ with $\lvert Z(f)\rvert = \sqrt{Re(Z)^2 + Im(Z)^2}$

3.3 Parameter Variations

In order to perform the simulation study in a well-structured way, it has been split into simulation series consisting of 10 simulation sets each. While one of the parameters is varied in the given range, all others are kept constant within one simulation set. The structure of an exemplary simulation series is shown in Table 3.3. In set 1 the polarization resistance is varied between 2 mΩ and 20 mΩ with 2 mΩ increments, while the inductance and the CPE exponents are kept constant at 1. 00 and 1*10^{-9} H respectively. This means that every simulation set contains ten EIS spectra which are analyzed by DRTtools subsequently. Originally the variation of the ohmic resistance and the single polarization resistances were intended to be included in the entire simulation study. As there was no influence of those seen on the numerical stability of the DRT, they have been omitted from the subsequent parameter study leaving the CPE-n and L as the only ECM parameters to be varied.

In order to take differences due to the available frequency range into account, every simulation series was repeated three times in the frequency ranges 100 mHz to 10 kHz, 100 mHz to 100 kHz and 100 mHz to 1 MHz. In the main simulation study, the minimum frequency and the number of points per decade was kept constant at 100 mHz and 14 ppd, respectively. In case of erroneous EIS spectra, the value of ε_0 is chosen to be 0. 5 % as default value. In a distinct simulation series, EIS spectra have been simulated with ε_0 values of 0. 2 %, 0. 1 % and 0. 01 % and ppd values between 7 and 70. Every EIS spectrum is subsequently analyzed with 16 different regularization parameter values between 10^{-6} and 8*10^{-3}.

For the main simulations this means that three simulation studies for ideal EIS, EIS with error model 1 and EIS with error model 2 were performed. Each of them consists of four different simulation series with variation of CPE-n1 to CPE-n3 and L, which themselves consist of ten simulation sets each. Adding up all these EIS spectra one comes up with 400 EIS spectra per simulation set and 1200 per simulation series. Taking the variation of frequency range into account, the outcome for the main simulations are therefore 3600 EIS spectra, each analyzed with 16 different regularization parameters in the DRT analysis which gives 57 600 DRT spectra in total. Due to this high number of DRT spectra, the variation of the number of points per decade, the minimum frequency and the error level were performed on a representative sample of the main simulations. Based on the preliminary results of the main simulations, the simulation series with variation of the CPE exponent of process 3 at 2000 Hz was chosen as the representative sample, because this CPE – n3 was found to have a major influence on the numerical fluctuations in the DRT. The polarization resistance was fixed to 10 mΩ and the inductance was chosen to be $2*10^{-9}$ H. For every simulation experiment, two simulation sets with CPE exponents of process 1 and 2 fixed to 0, 95 and 0. 75 were performed.

It has to be emphasized that only a representative part of the results is presented in the course of this thesis. This is justified as during the analysis of the DRT spectra it turned out that a small sample can sufficiently represent the important results due to high qualitative similarities. The results of those simulations will be presented in chapter 4. Attempts to define an accuracy of the DRT result in a quantitative way by means of the calculation of relaxation times and polarization resistances as well as comparisons with the theoretical ideal DRT were not successful and therefore omitted in the course of this study. A brief description of the occurred problems is given in the Appendix/Part A.

In case of simulations with erroneous EIS spectra, a repeatability study was performed to evaluate the observed differences in the DRT which are seen in the parameter study and to assess the repeatability of the DRT analysis as a numerical stability criterion depending on the EIS properties, such as the points per decade, the frequency range, the inductance and the CPE behavior.

Table 3.3: Exemplary simulation series for variation of the polarization resistance between 2 mΩ and 20 mΩ.

Set no.	R_{pol}/R_{Ω} [mΩ]	L [H]	CPE-n1 []	CPE-n2 []	CPE-n3 []
1	[2;20]	$1*10^{-9}$	1.00	1.00	1.00
2	[2;20]	$2*10^{-9}$	0.95	0.95	0.95
3	[2;20]	$4*10^{-9}$	0.90	0.90	0.90
4	[2;20]	$8*10^{-9}$	0.85	0.85	0.85
5	[2;20]	$1*10^{-8}$	0.80	0.80	0.80
6	[2;20]	$2*10^{-8}$	0.75	0.75	0.75
7	[2;20]	$4*10^{-8}$	0.70	0.70	0.70
8	[2;20]	$8*10^{-8}$	0.65	0.65	0.65
9	[2;20]	$1*10^{-7}$	0.60	0.60	0.60
10	[2;20]	$2*10^{-7}$	0.55	0.55	0.55

3.4 DRT Settings

To analyze the high number of EIS spectra, the code of the program DRTtools [10] was adapted to achieve a fast generation of DRT spectra with different values of the regularization parameter λ. For all DRT calculations which were performed in this thesis, Gaussian functions have been used as RBFs in the discretization. In DRTtools, there is the option to add an inductor to the DRT fitting model, resulting in a Voigt circuit with an additional inductor in series, which is shown as the option "Fitting with Inductance" in the GUI. This option was used for all DRT calculations which are presented in this work. The reason for choosing this option lies in the fact that the inductance is included in the ECM used for EIS simulation and should therefore also be included in the DRT model. The addition of the inductance term leads to the following impedance model:

$$Z_{DRT}(f) = i2\pi fL + R_O + \int_0^{\infty} \frac{g(\tau)}{1+i2\pi f\tau} d\tau \tag{89}$$

Additionally, the real and imaginary part of the EIS data were used simultaneously for calculation. The settings for the shape factor and the derivation used were set to the default values, except for one simulation series, in which the shape factor was varied between one and four to check its influence on the numerical oscillations. In Table 3.4, the regularization parameter set which is used for the DRT calculations in the present study can be found.

Table 3.4: Regularization Parameters for DRT calculation with DRTtools

No.	**λ**	**No.**	**λ**	**No.**	**λ**	**No.**	**λ**
1	$1*10^{-6}$	**5**	$1*10^{-5}$	**9**	$1*10^{-4}$	**13**	$1*10^{-3}$
2	$2*10^{-6}$	**6**	$2*10^{-5}$	**10**	$2*10^{-4}$	**14**	$2*10^{-3}$
3	$4*10^{-6}$	**7**	$4*10^{-5}$	**11**	$4*10^{-4}$	**15**	$4*10^{-3}$
4	$8*10^{-6}$	**8**	$8*10^{-5}$	**12**	$8*10^{-4}$	**16**	$8*10^{-3}$

4. Results and Discussion

In the following chapters the results of the simulation study are presented. In first place, the results based on ideal EIS spectra without statistical error are presented. There the polarization resistance, the inductance, the CPE exponents of the RQ elements and the maximum frequency was varied. In the following part, the results based on EIS spectra with statistical error added by means of error model 1 and 2 are presented. In the simulations with erroneous EIS spectra only the inductance, the CPE exponents and the maximum frequency was varied based on the results of the ideal EIS simulations. Furthermore, the number of points per decade, the minimum frequency and the error magnitude ε_0 was investigated and a repeatability study was performed for both error models. Afterwards, a comparison between the simulations with and without statistical error will be given together with a summary of the findings of the simulation study.

At the end of this chapter, the findings of the simulation study are verified on experimental EIS spectra which are measured at an SOFC stack at IEK-14 of the Jülich Research Center, emphasizing the practical relevance of the findings.

4.1 Simulations with ideal EIS spectra

In the following chapter the results of the simulations based on ideal EIS spectra are presented. Figure 4.1.1 shows the dependency of the DRT result on the magnitude of the total polarization resistance (with R2: R3: R4 = 3: 1: 2 as shown in Table 3.1) and the inductance. The CPE exponents are kept constant at 0. 95 for all electrochemical processes and the maximum frequency is 100 kHz. In Figure 4.1.1 the corresponding Nyquist diagrams of the simulated EIS spectra for the variation of the total polarization resistance and the inductance can be found.

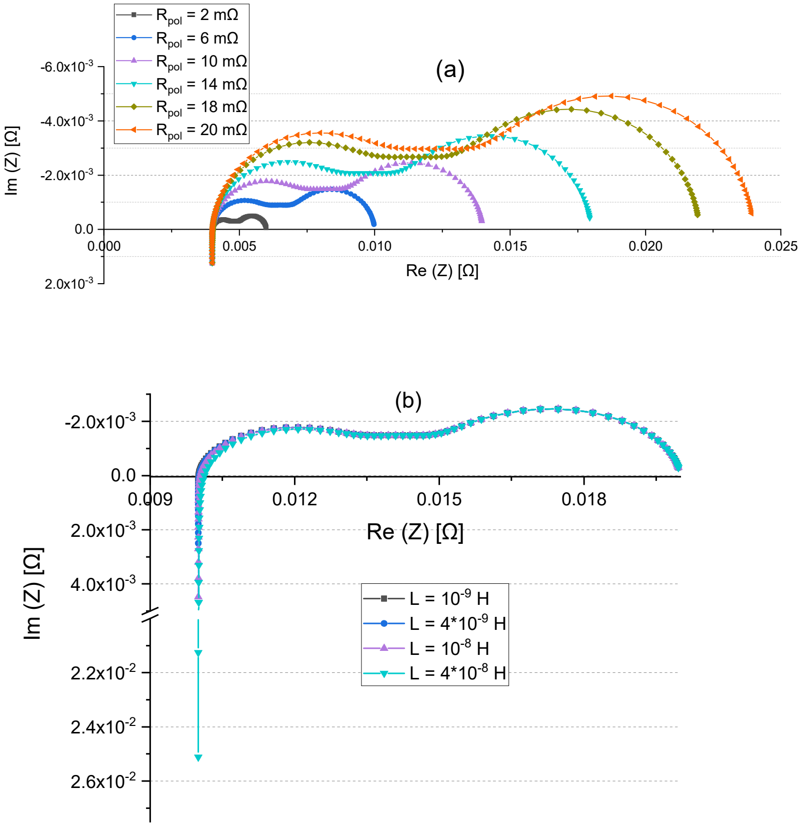

Figure 4.1.1. Nyquist diagrams of the simulated EIS spectra for variation of the total polarization in (a) and the inductance in (b). The CPE exponents of all electrochemical processes are 0. 95. In (b), the total polarization resistance is 10 mΩ. (100 mHz – 100 kHz, 14 ppd). Remark: In (b) he x- and y-axis scales are not linked 1:1 for better visibility of the semicircles.

In Figure 4.1.2 (a), where the DRT results can be found, the influence of the total polarization resistance can be stated as being only of quantitative nature as the peak height of the undesired oscillations increases in the same extent as the peak height of the simulated electrochemical processes. It has to be emphasized that the peak height of the artificial peaks is very low in comparison to the simulated peaks, which lowers the risk of interpreting them as electrochemical processes in the practical application of the DRT analysis. Nevertheless the peak height would most probably show changes when operation parameters, e.g. hydrogen flow, air flow, water content of fuel gas or temperature are changed. This could potentially lead to misinterpretations of the changes in the properties of the artificial peaks. Figure 4.1.2 (b) shows that an ideal inductance does not cause numerical oscillations in the DRT calculation if the inductance is included in the DRT fitting model, as implemented for this study. This means that the inductance itself is in principle not causing numerical artefacts. Of course this finding has to be proven on EIS spectra with statistical errors to also investigate the indirect impact of inductive effects via enhancing measurement errors in the high-frequency range. These results are shown in a later chapter of this thesis.

Because there is no influence of the total polarization resistance and the ideal inductance seen on the numerical stability of the DRT calculation, further results achieved with different maximum frequencies in the EIS data set are not presented here. The emphasis is put on the variation of the exponents of the constant phase elements.

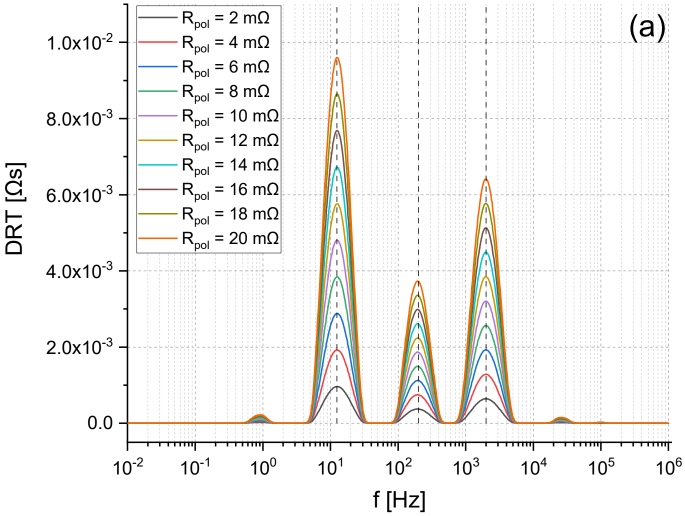

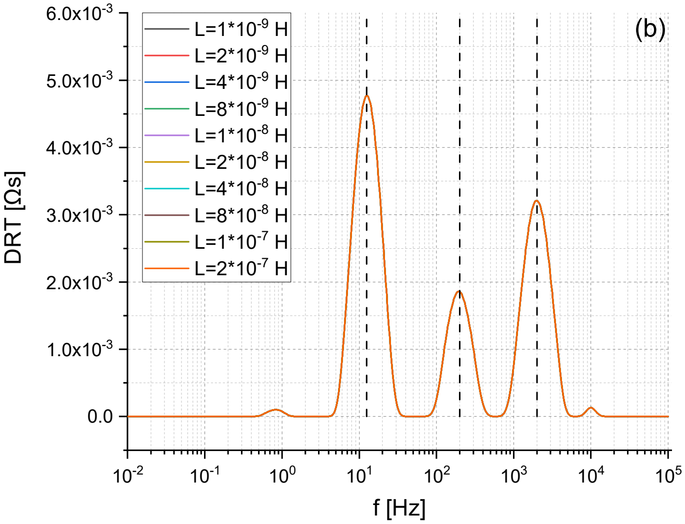

Figure 4.1.2. DRT spectra calculated from EIS data sets with total different polarization resistances (R2+R3+R4) in (a) and inductance values in (b). All curves are overlapped in (b).The regularization parameter for the DRT calculation is λ=10^{-4}. All CPE exponents are 0. 95. The total polarization resistance is 10 mΩ. (100 mHz – 100 kHz, 14 ppd).

For the variation of the CPE exponents, which are a measure of the extent of frequency dispersion of the respective electrochemical process, the simulation sets with a total polarization resistance of 10 mΩ and inductance of $2*10^{-9}$ H were chosen to be presented in this section. Because there was an influence of the frequency range seen on the results of the DRT function, the results for different maximum frequencies of 10 kHz, 100 kHz and 1 MHz are shown. In Figure 4.1.3, an exemplary Nyquist diagram is shown for the simulation set with varying CPE-n1 while the remaining CPE exponents are fixed to 0. 95. It can be observed there that with decreasing CPE – n1 the overlapping with the mid-frequency process is more pronounced.

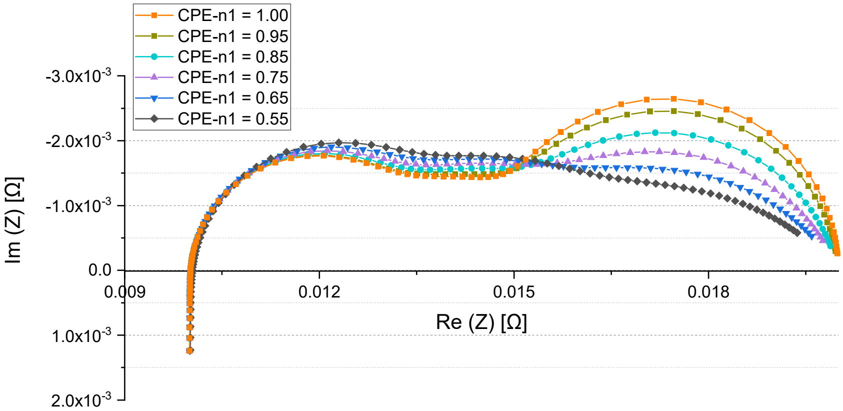

*Figure 4.1.3. Nyquist diagram for simulated EIS spectra with varying CPE-n1 values while the CPE exponents of the remaining processes are fixed to 0. 95. L = 2*10-9 H and the total polarization resistance is 10 mΩ. (100 mHz – 100 kHz, 14 ppd).*

In Figure 4.1.4, the DRT results for the variation of the CPE exponent for the 12. 5 Hz process (CPE - n1) is shown for the EIS simulation in the frequency range from 100 mHz to 100 kHz with a data point density of 14 points per decade. In graph (a) and (c) the value of the remaining two CPE exponents is 0. 95 whereas in graph (b) and (d) the value of the remaining two CPE exponents is 0. 75. The reason for choosing these two simulation sets is to show how the oscillations and the peak overlapping are enhanced if more than one CPE exponent is significantly lower than one thus deviating from the ideal RC behavior. This deviation is increasing with decreasing CPE exponents of the processes, which justifies the usage of only two simulation sets as representatives of the whole simulation series.

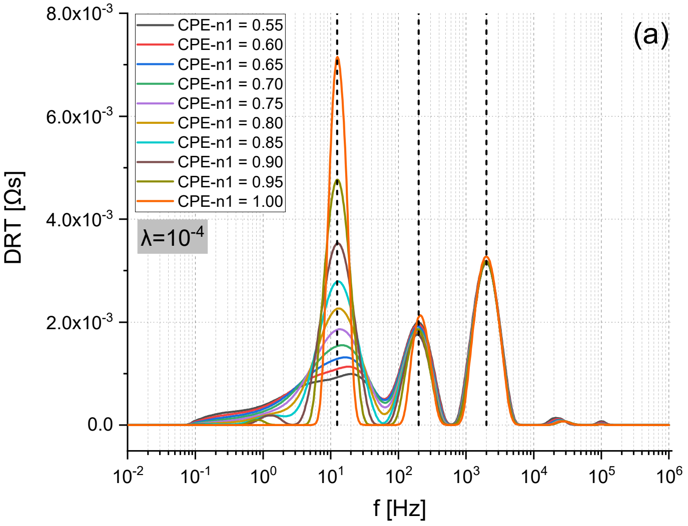
(a)
DRT [Ωs]
f [Hz]
8.0x10-3
6.0x10-3
4.0x10-3
2.0x10-3
0.0
10-2
10-1
100
101
102
103
104
105
106
CPE-n1 = 0.55
CPE-n1 = 0.60
CPE-n1 = 0.65
CPE-n1 = 0.70
CPE-n1 = 0.75
CPE-n1 = 0.80
CPE-n1 = 0.85
CPE-n1 = 0.90
CPE-n1 = 0.95
CPE-n1 = 1.00
λ=10-4

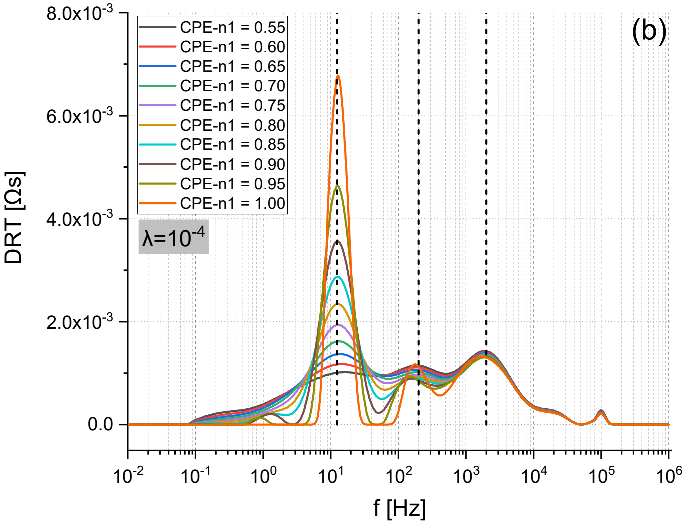
(b)
DRT [Ωs]
f [Hz]
8.0x10-3
6.0x10-3
4.0x10-3
2.0x10-3
0.0
10-2
10-1
100
101
102
103
104
105
106
CPE-n1 = 0.55
CPE-n1 = 0.60
CPE-n1 = 0.65
CPE-n1 = 0.70
CPE-n1 = 0.75
CPE-n1 = 0.80
CPE-n1 = 0.85
CPE-n1 = 0.90
CPE-n1 = 0.95
CPE-n1 = 1.00
λ=10-4

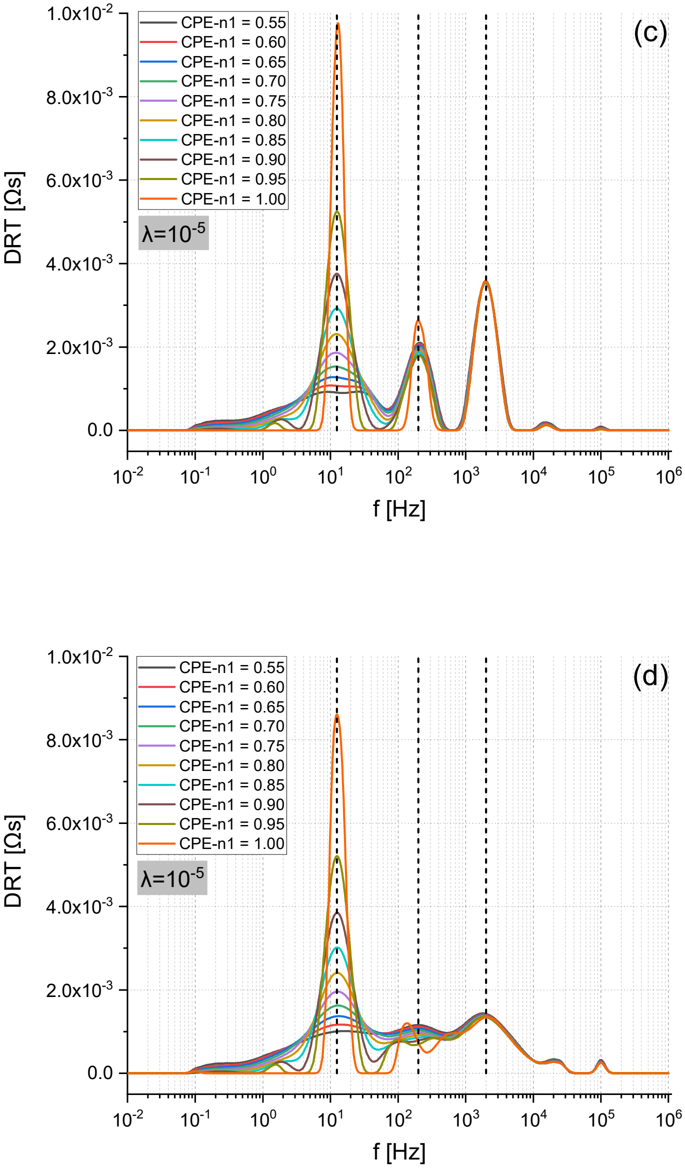

Figure 4.1.4. DRT plots based on ideal EIS spectra for variation of the CPE exponent of the electrochemical process at a relaxation frequency of 12. 5 Hz. In (a) and (c) the CPE exponents of the other processes are 0. 95. In (b) and (d) the CPE exponents of the other processes are 0. 75. The Regularization parameter λ=10^{-4} in (a) and (b), and λ=10^{-5} in (c) and (d). L=$2*10^{-9}$ H and the total polarization resistance is 10 mΩ. (100 mHz – 100 kHz, 14 ppd)

The influence of a low value of CPE-n1 is mostly confined to the low frequency range of the DRT, in which the respective process is located. Additionally, a combined effect with a lower CPE exponent of the mid frequency process (CPE-n2) can be observed, resulting in a more pronounced peak overlapping of the 12. 5 Hz process and the 200 Hz process. If both CPE exponents in the low and mid frequency area are well below one, the peak resolution of the two processes becomes insufficient, especially for high regularization parameters. Unwanted multiplication of the low-frequency peak is only beginning to become visible for CPE exponents as low as 0. 60 and a regularization parameter of 10^{-5}. Furthermore, the peak multiplication seems to be more favorable if the CPE exponent of the adjacent process is closer to one, which becomes visible when graph (c) and (d) are compared. From these results it can be concluded that low values of the CPE exponent in the low-frequency range are only causing unwanted peak multiplication for CPE-n values around 0. 60 or lower in combination with low λ values. Furthermore, increasing values of CPE – n1 are causing the evolution of shoulders beginning at the low-frequency peak and reaching into the direction of the low-frequency edge of the DRT spectrum. Apparently the high-frequency area of the DRT is rather unaffected by the variation of the CPE – n1.

In Figure 4.1.5, the results of the combined variation of the CPE exponent of the 12. 5 Hz process (CPE - n1) and the maximum frequency of the EIS data set are shown. The CPE exponents of the remaining processes are 0. 95 respectively. In (a) the entire frequency range is shown, while in (b) only the frequency range starting from 5 kHz is shown. It can be observed that there is almost no influence of the CPE-n1 on the oscillations in the high-frequency range. The differences between the spectra simulated for different maximum frequencies are confined to the high - frequency range of the DRT spectrum and the CPE exponent of the 12. 5 Hz process mainly influences the low- and mid-frequency region of the DRT. From this it can be concluded that there is no interplay between CPE - n1 and the maximum frequency of the underlying EIS spectrum. Anyhow it can be observed that numerical artefacts are located at the maximum frequency of the EIS data set and for simulations to higher frequencies, additional peaks between the 2000 Hz process and the maximum frequency occur. Those artefacts will be analyzed in the further course of this thesis.

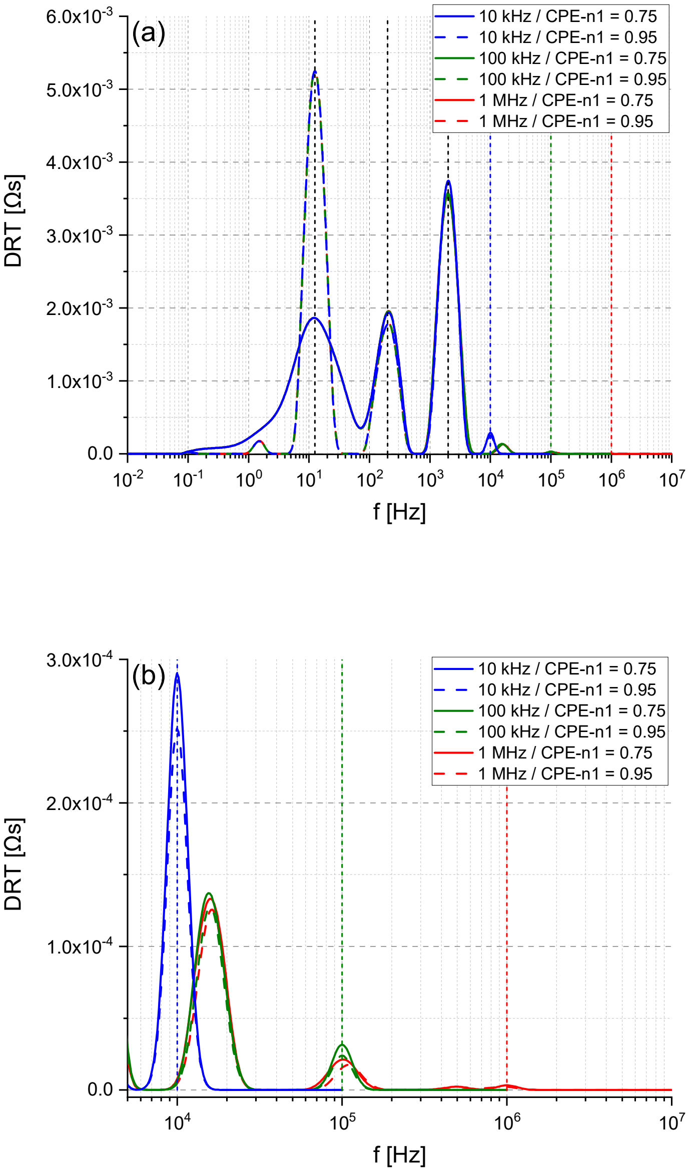

Figure 4.1.5. Comparison of DRT spectra based on the simulation of different frequency ranges together with a variation of CPE-n1 for the entire frequency range in (a) and zoomed into the high frequency range starting at 5 kHz in (b). Regularization parameter $\lambda=10^{-5}$. The remaining CPE exponents are fixed to 0. 95. $L = 2*10^{-9}$ H. The total polarization resistance is 10 mΩ. (14 ppd)

When the CPE exponent of the mid-frequency process at 200 Hz relaxation frequency (CPE - n2) is varied between 0. 55 and 1. 00, a similar trend can be observed as for the simulations shown before. An exemplary Nyquist diagram for the variation of CPE – n2 can be found in Figure 4.1.6 with the remaining CPE exponents fixed to 0. 95. It can be observed that with decreasing CPE – n2 the mid-frequency peak becomes less visible.

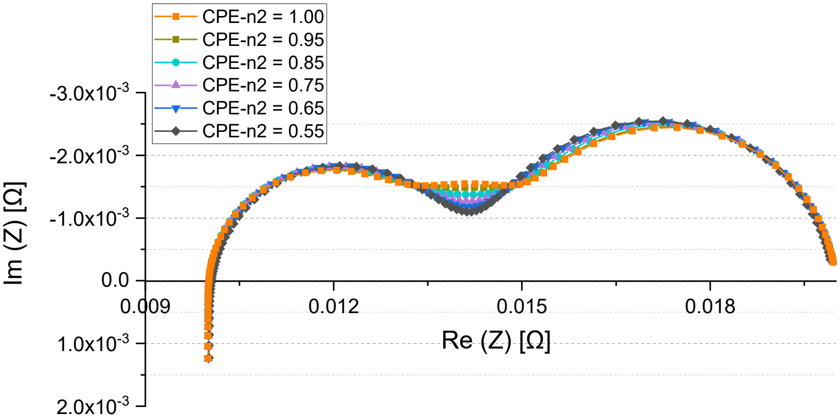

*Figure 4.1.6. Nyquist diagram for simulated EIS spectra with varying CPE-n2 values while the CPE exponents of the remaining processes are fixed to 0. 95. L = 2*10-9 H and the total polarization resistance is 10 mΩ. (100 mHz – 100 kHz, 14 ppd).*

The results of the DRT calculation can be found in Figure 4.1.7. Again all DRT spectra are shown for regularization parameters of 10^{-4} and 10^{-5} and with CPE exponents of the remaining processes fixed to 0. 95 in (a), (c) and (e) and 0. 75 in (b) and (d). The differences between the DRT spectra for varying CPE - n2 can be found mostly in the mid-frequency range, in which the variation of the frequency dispersion has been implemented in the EIS model. This behavior was observed before for the simulations with different CPE – n1, where the effects are mostly confined to the low-frequency regime.

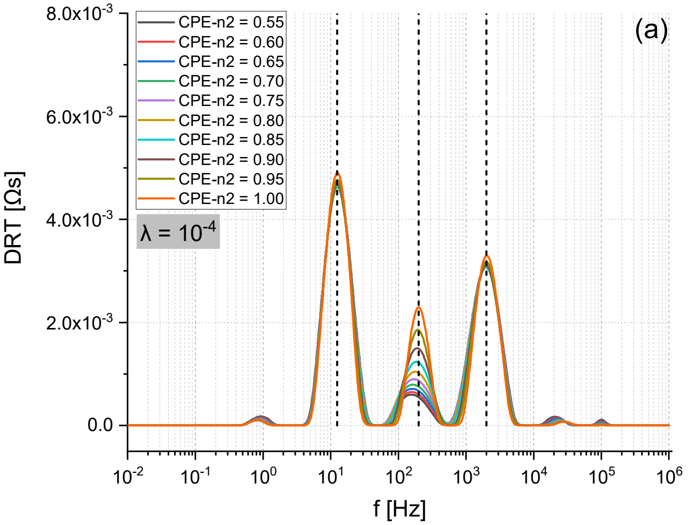
(a)
DRT [Ωs]
f [Hz]
8.0x10^-3
6.0x10^-3
4.0x10^-3
2.0x10^-3
0.0
10^-2
10^-1
10^0
10^1
10^2
10^3
10^4
10^5
10^6
CPE-n2 = 0.55
CPE-n2 = 0.60
CPE-n2 = 0.65
CPE-n2 = 0.70
CPE-n2 = 0.75
CPE-n2 = 0.80
CPE-n2 = 0.85
CPE-n2 = 0.90
CPE-n2 = 0.95
CPE-n2 = 1.00
λ = 10^-4

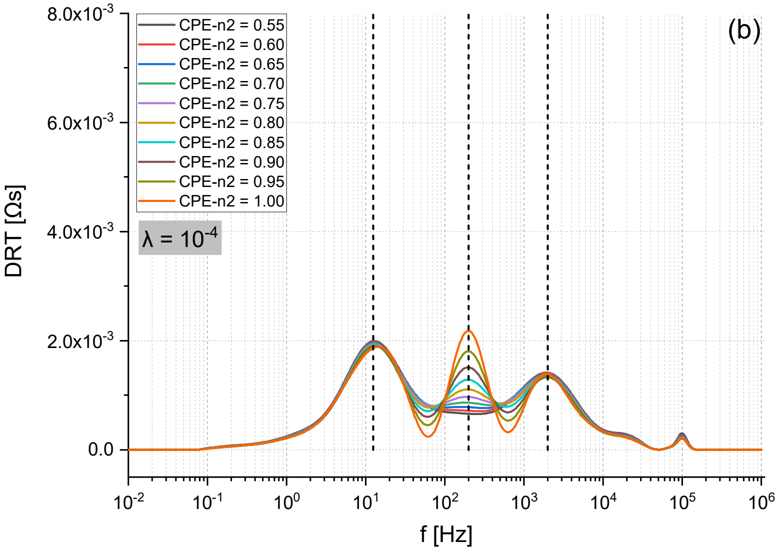
(b)
DRT [Ωs]
f [Hz]
8.0x10^-3
6.0x10^-3
4.0x10^-3
2.0x10^-3
0.0
10^-2
10^-1
10^0
10^1
10^2
10^3
10^4
10^5
10^6
CPE-n2 = 0.55
CPE-n2 = 0.60
CPE-n2 = 0.65
CPE-n2 = 0.70
CPE-n2 = 0.75
CPE-n2 = 0.80
CPE-n2 = 0.85
CPE-n2 = 0.90
CPE-n2 = 0.95
CPE-n2 = 1.00
λ = 10^-4

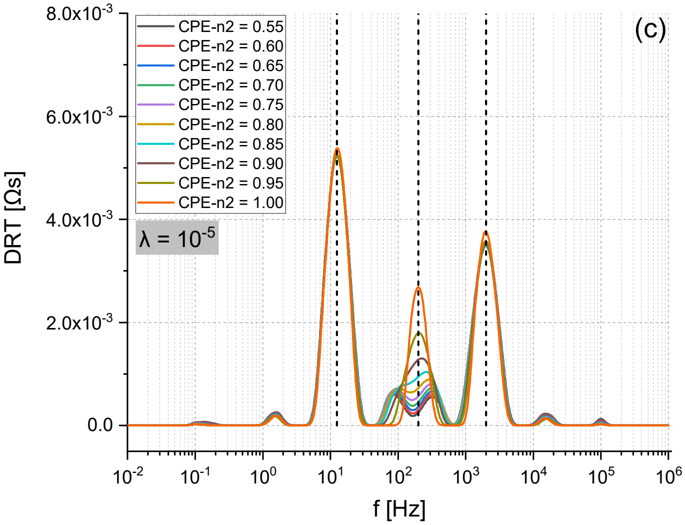

(c)
DRT [Ωs]
8.0x10^{-3}
6.0x10^{-3}
4.0x10^{-3}
2.0x10^{-3}
0.0
f [Hz]
10^{-2}
10^{-1}
10^{0}
10^{1}
10^{2}
10^{3}
10^{4}
10^{5}
10^{6}
CPE-n2 = 0.55
CPE-n2 = 0.60
CPE-n2 = 0.65
CPE-n2 = 0.70
CPE-n2 = 0.75
CPE-n2 = 0.80
CPE-n2 = 0.85
CPE-n2 = 0.90
CPE-n2 = 0.95
CPE-n2 = 1.00
λ = 10^{-5}

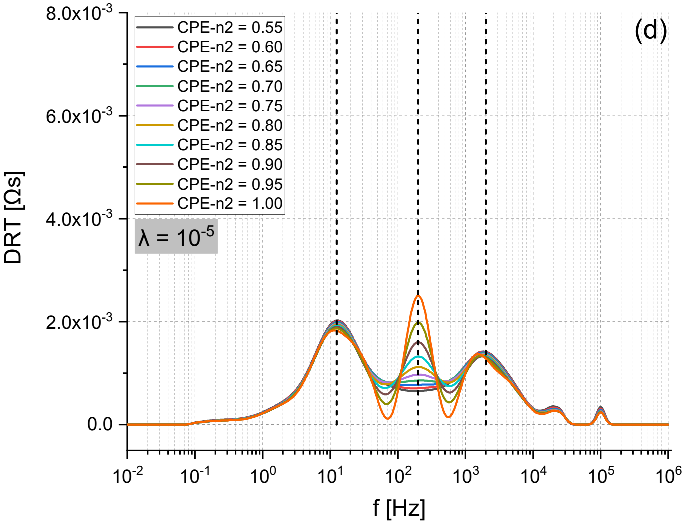

(d)
DRT [Ωs]
8.0x10^{-3}
6.0x10^{-3}
4.0x10^{-3}
2.0x10^{-3}
0.0
f [Hz]
10^{-2}
10^{-1}
10^{0}
10^{1}
10^{2}
10^{3}
10^{4}
10^{5}
10^{6}
CPE-n2 = 0.55
CPE-n2 = 0.60
CPE-n2 = 0.65
CPE-n2 = 0.70
CPE-n2 = 0.75
CPE-n2 = 0.80
CPE-n2 = 0.85
CPE-n2 = 0.90
CPE-n2 = 0.95
CPE-n2 = 1.00
λ = 10^{-5}

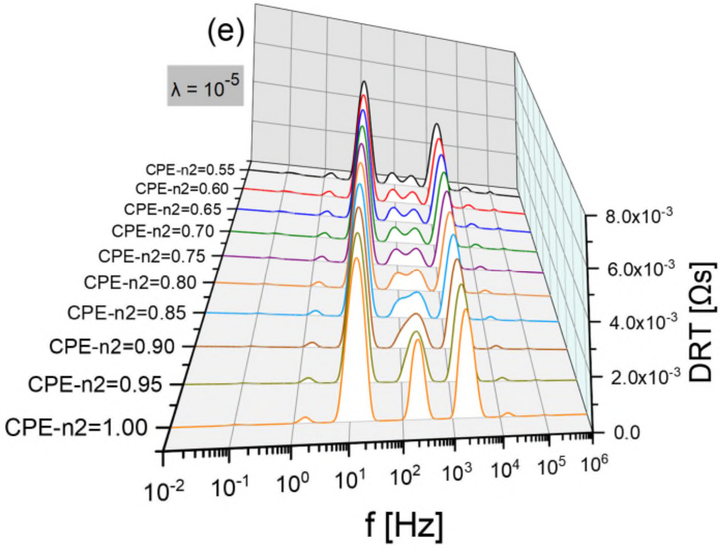

Figure 4.1.7. DRT plots based on ideal EIS spectra for variation of the CPE exponent of the electrochemical process at a relaxation frequency of 200 Hz. In (a) and (c) the CPE exponents of the other processes are 0. 95. In (b) and (d) the CPE exponents of the other processes are 0. 75. The Regularization parameter $\lambda=10^{-4}$ *in (a) and (b), and* $\lambda=10^{-5}$ *in (c) and (d).* $L=2*10^{-9}$ *H. (100 mHz – 100 kHz, 14 ppd). In (e), the data from (c) are shown as 3D plot.*

In comparison to the results shown before for the low-frequency process, here an unwanted peak multiplication of the 200 Hz process already takes place for CPE - n2 values as low as 0. 85 if the regularization parameter is chosen to be 10^{-5} or lower, even in cases in which the CPE exponents of the remaining processes are fixed to 0. 95, as shown in Figure 4.1.7 (c) and (e). Interestingly this effect does not occur if the CPE exponents of the adjacent processes are decreased to 0. 75. Then the mid-frequency peaks is more depressed with decreasing values of CPE – n2, which is also matching the observations made in the simulations with varying CPE – n1. Based on these results, there is a potential risk of misinterpreting the mid-frequency electrochemical process as two distinct ones if the regularization parameter is chosen wrongly. In case of low CPE exponents of the remaining two processes are decreased there is the risk of losing the information about the mid-frequency peak, especially for high values of the regularization parameter. This observation is quite interesting as it demonstrates the interplay of CPE effects of the different processes with each other.

If only the mid-frequency process exhibits significant CPE behavior, this peak is multiplied with decreasing CPE exponents. If the adjacent peaks exhibit low CPE exponents as well, the mid frequency peak disappears with decreasing CPE - n2, which means a significant qualitative difference and will potentially lead to different interpretations of the DRT result.

In comparison to the results for the variation of CPE- n1, the variation of CPE - n2 already exhibits a slight influence on the high-frequency artefacts, as shown in Figure 4.1.8, in which the DRT results for EIS simulations to different maximum frequencies are shown. In (a) the entire frequency range is shown, whereas in (b) only the high-frequency range starting at 5 kHz is plotted. It can be observed that the peak height of the artificial peaks located at the respective maximum frequency is increasing with a decreasing value of CPE – n2. Besides the artefacts at the maximum frequency, additional artificial peaks appear between the real 2000 Hz process and the respective f_{max} for simulations to 100 kHz and 1 MHz which also show an increasing trend with decreasing CPE – n2. This means that CPE behavior of electrochemical processes with relaxation frequencies in the range of 200 Hz can already affect the DRT function in the high-frequency regime.

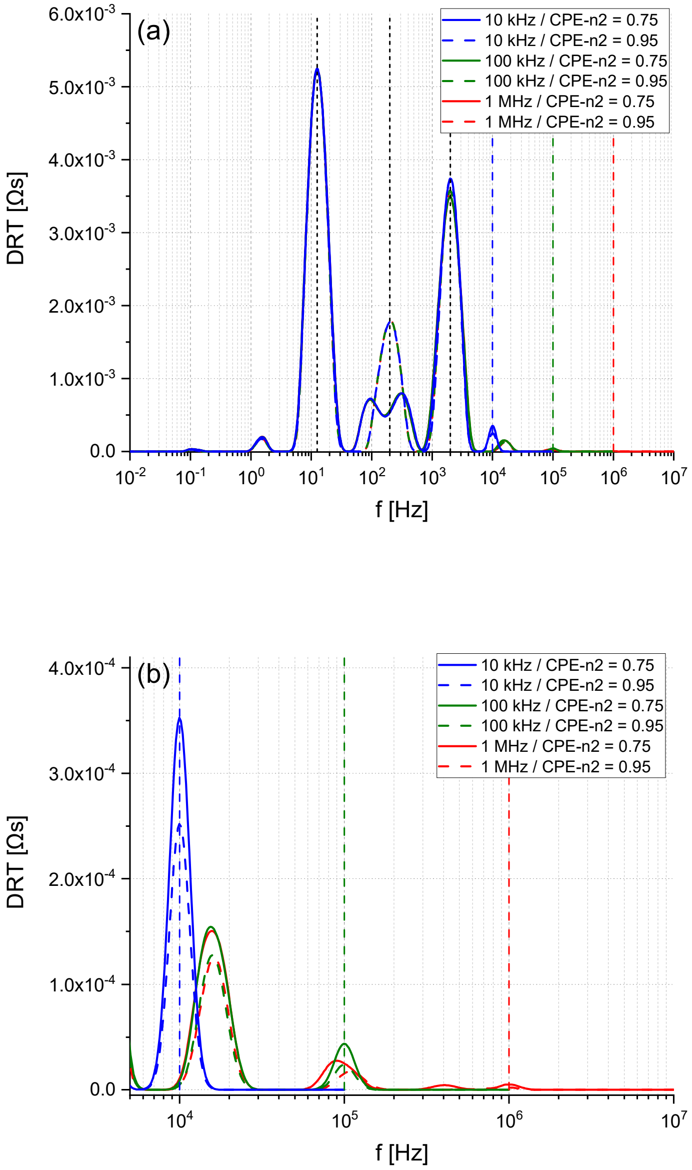

Figure 4.1.8. Comparison of DRT spectra based on the simulation of different frequency ranges together with a variation of CPE-n2 for the entire frequency range in (a) and zoomed into the high frequency range starting at 5 kHz in (b). Regularization parameter $\lambda=10^{-5}$*. The remaining CPE exponents are fixed to 0. 95.* $L = 2*10^{-9}$ *H. The total polarization resistance is 10 mΩ. (14 ppd).*

Lastly, an exemplary Nyquist diagram for the variation of the CPE-n3 can be found in Figure 4.1.9. The CPE exponents of the remaining processes are fixed to 0. 95. It can be seen that with decreasing CPE – n3 the intersection with the x-axis is shifted to higher values of the Re (Z).

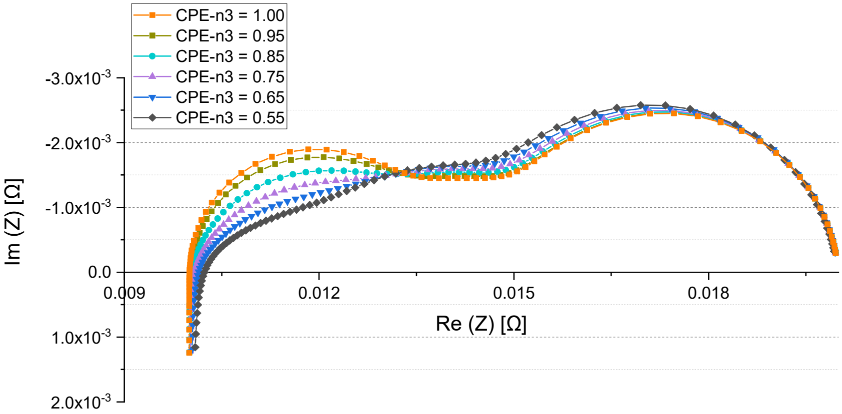

*Figure 4.1.9. Nyquist diagram for simulated EIS spectra with varying CPE-n3 values while the CPE exponents of the remaining processes are fixed to 0. 95. L = 2*10^{-9} H and the total polarization resistance is 10 mΩ. (100 mHz – 100 kHz, 14 ppd).*

The DRT results of the variation of the CPE exponent for the high-frequency process (CPE – n3) with a relaxation frequency of 2000 Hz are shown in Figure 4.1.10 based on EIS simulations in the frequency range 100 mHz to 100 kHz. As observed before for the low- and mid-frequency processes, the influence of the CPE - n3 is mostly confined to the high frequency area and the impact on the mid- and low-frequency area is fairly low. Again the peak overlapping with the 200 Hz process is favored if the CPE exponent of the latter is decreased as well. For the variation of CPE - n3, a significant influence on the numerical oscillations in the high frequency range can be observed, especially on the artificial sharp peak at the maximum frequency that also was observed before in stack measurements on anode-supported SOFC stacks at the IEK-14 of the Jülich Research Center [11]. If the regularization parameter is decreased to 10^{-5}, the second artificial peak located around 20 kHz relaxation frequency gets detached from the 2000 Hz process. This artefact is again also increasing with decreasing CPE – n3. Based on this results, there is evidence that the CPE behavior of electrochemical processes with high relaxation frequencies is responsible for the formation of high-frequency artefacts in the DRT spectrum. This trend is nicely observable especially in Figure 4.1.10 (c) and (e).

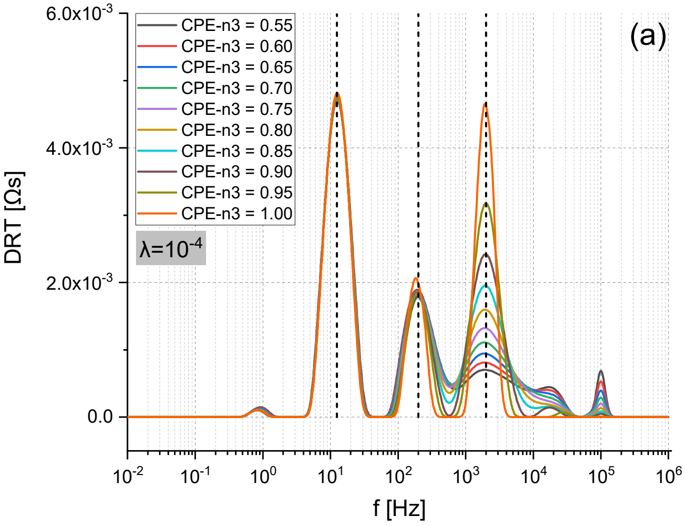
(a)
CPE-n3 = 0.55
CPE-n3 = 0.60
CPE-n3 = 0.65
CPE-n3 = 0.70
CPE-n3 = 0.75
CPE-n3 = 0.80
CPE-n3 = 0.85
CPE-n3 = 0.90
CPE-n3 = 0.95
CPE-n3 = 1.00
λ=10^{-4}
DRT [Ωs]
6.0x10^{-3}
4.0x10^{-3}
2.0x10^{-3}
0.0
10^{-2}
10^{-1}
10^{0}
10^{1}
10^{2}
10^{3}
10^{4}
10^{5}
10^{6}
f [Hz]

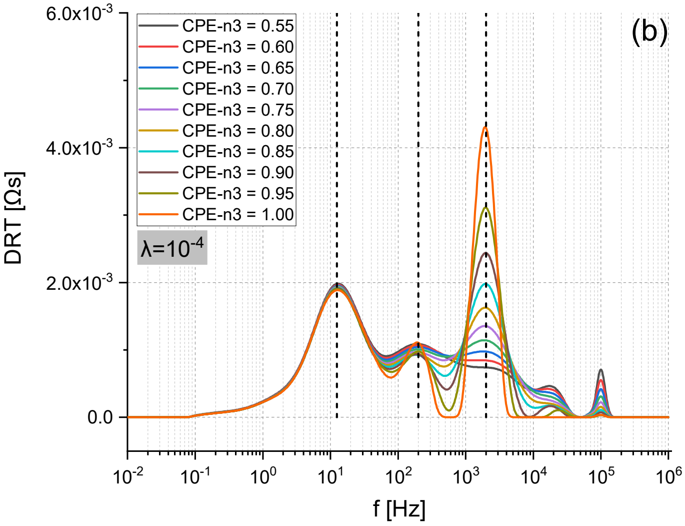
(b)
CPE-n3 = 0.55
CPE-n3 = 0.60
CPE-n3 = 0.65
CPE-n3 = 0.70
CPE-n3 = 0.75
CPE-n3 = 0.80
CPE-n3 = 0.85
CPE-n3 = 0.90
CPE-n3 = 0.95
CPE-n3 = 1.00
λ=10^{-4}
DRT [Ωs]
6.0x10^{-3}
4.0x10^{-3}
2.0x10^{-3}
0.0
10^{-2}
10^{-1}
10^{0}
10^{1}
10^{2}
10^{3}
10^{4}
10^{5}
10^{6}
f [Hz]

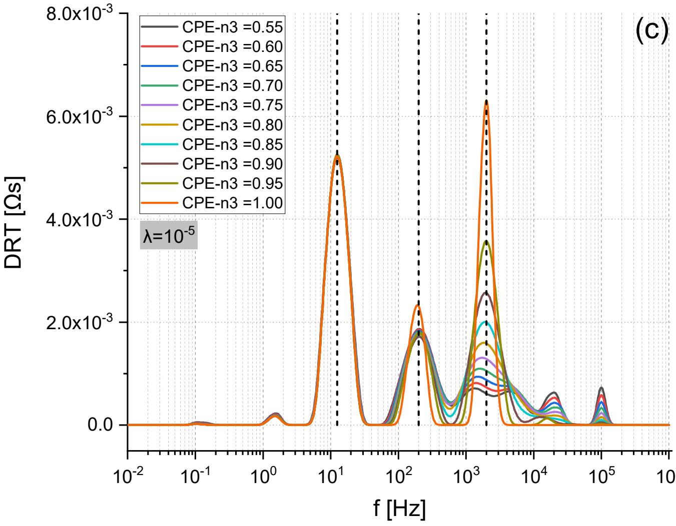
(c)
DRT [Ωs]
f [Hz]
λ=10^-5
CPE-n3 =0.55
CPE-n3 =0.60
CPE-n3 =0.65
CPE-n3 =0.70
CPE-n3 =0.75
CPE-n3 =0.80
CPE-n3 =0.85
CPE-n3 =0.90
CPE-n3 =0.95
CPE-n3 =1.00
8.0x10^-3
6.0x10^-3
4.0x10^-3
2.0x10^-3
0.0
10^-2
10^-1
10^0
10^1
10^2
10^3
10^4
10^5
10^6

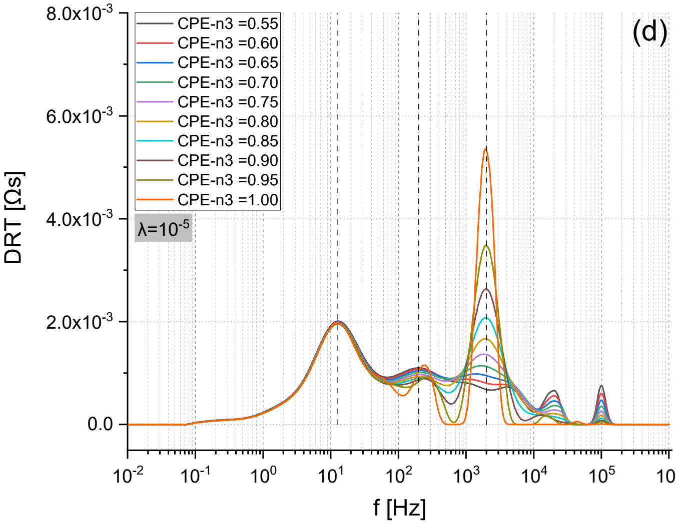
(d)
DRT [Ωs]
f [Hz]
λ=10^-5
CPE-n3 =0.55
CPE-n3 =0.60
CPE-n3 =0.65
CPE-n3 =0.70
CPE-n3 =0.75
CPE-n3 =0.80
CPE-n3 =0.85
CPE-n3 =0.90
CPE-n3 =0.95
CPE-n3 =1.00
8.0x10^-3
6.0x10^-3
4.0x10^-3
2.0x10^-3
0.0
10^-2
10^-1
10^0
10^1
10^2
10^3
10^4
10^5
10^6

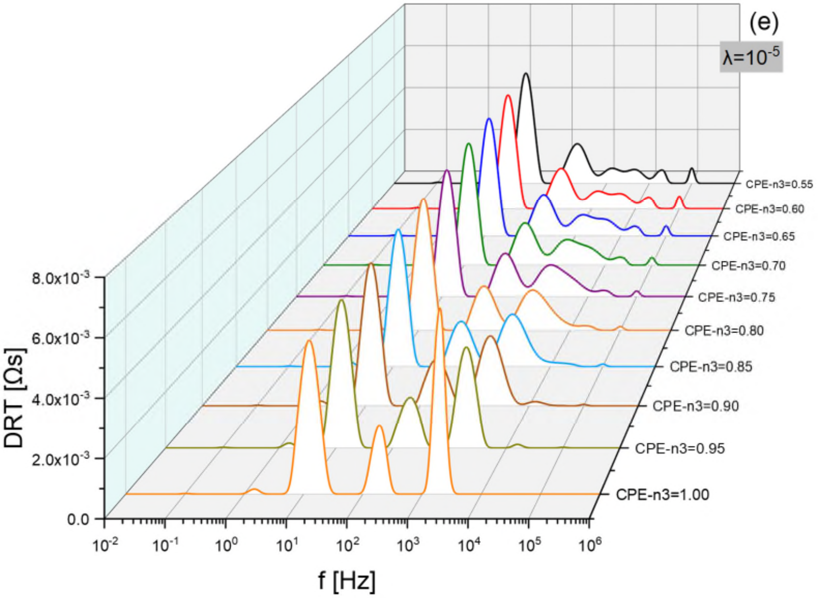

Figure 4.1.10. DRT plots based on ideal EIS spectra for variation of the CPE exponent of the electrochemical process at a relaxation frequency of 2000 Hz. In (a) and (c) the CPE exponents of the other processes are 0. 95. In (b) and (d) the CPE exponents of the other processes are 0. 75. The Regularization parameter $\lambda=10^{-4}$ *in (a) and (b), and* $\lambda=10^{-5}$ *in (c) and (d).* $L=2*10^{-9}$ *H and the total polarization resistance is 10 mΩ. (100 mHz – 100 kHz, 14 ppd). In (e), the data from (c) are shown as 3D plot.*

Together with the results from the variation of the inductance, the findings are pointing against the assumption that high inductance values are responsible for the observed artefacts in the high-frequency regime. In practice of course the inductance is causing an additional measurement error to the EIS spectrum which could still have an influence on the oscillations. This factor has to be checked by simulating the variation of the inductance together with an error model, which is shown later in this thesis. While for λ-values of 10^{-4}, as implemented in Figure 4.1.10 (a) and (b), no unwanted peak multiplication of the 2000 Hz process is visible, for $\lambda= 10^{-5}$, as implemented in Figure 4.1.10 (c) and (d), a multiplication is visible for CPE-n3 values below 0. 70. This result emphasizes the importance of a thoughtful choice of the regularization parameter in case of significant frequency dispersion effects are present.

In Figure 4.1.11 the combined variation of the maximum frequency and CPE – n3 is shown. It is clearly visible that the CPE exponent of the high-frequency process has a major influence on the artefacts in the high-frequency range of the DRT spectrum and especially on the expression of the artificial peaks at the maximum frequency. With decreasing CPE exponent, the peak height of these characteristic artificial peaks increases significantly. For the simulation to 100 kHz, the peak only appears for a CPE exponent of 0. 75 and is not visible for the spectrum with CPE exponent 0. 95. If the EIS is simulated up to 1 MHz, the peak is almost not visible, also for CPE-n3 of 0. 75. The fact that this artificial peak is located at the maximum frequency offers the possibility to identify this peak as an artefact in experimental DRT analysis. However, with decreasing CPE-n3, additional artificial peaks between the maximum frequency and the simulated 2000 Hz process appear in the DRT spectrum, which will be prone to misinterpretation as electrochemical processes. This finding leads to the proposal that EIS measurements with different maximum frequencies at the same operation point should be analyzed with DRT to verify the high-frequency electrochemical processes because the real process should not follow the frequency variation while the artificial peaks will shift due to a change in the maximum frequency.

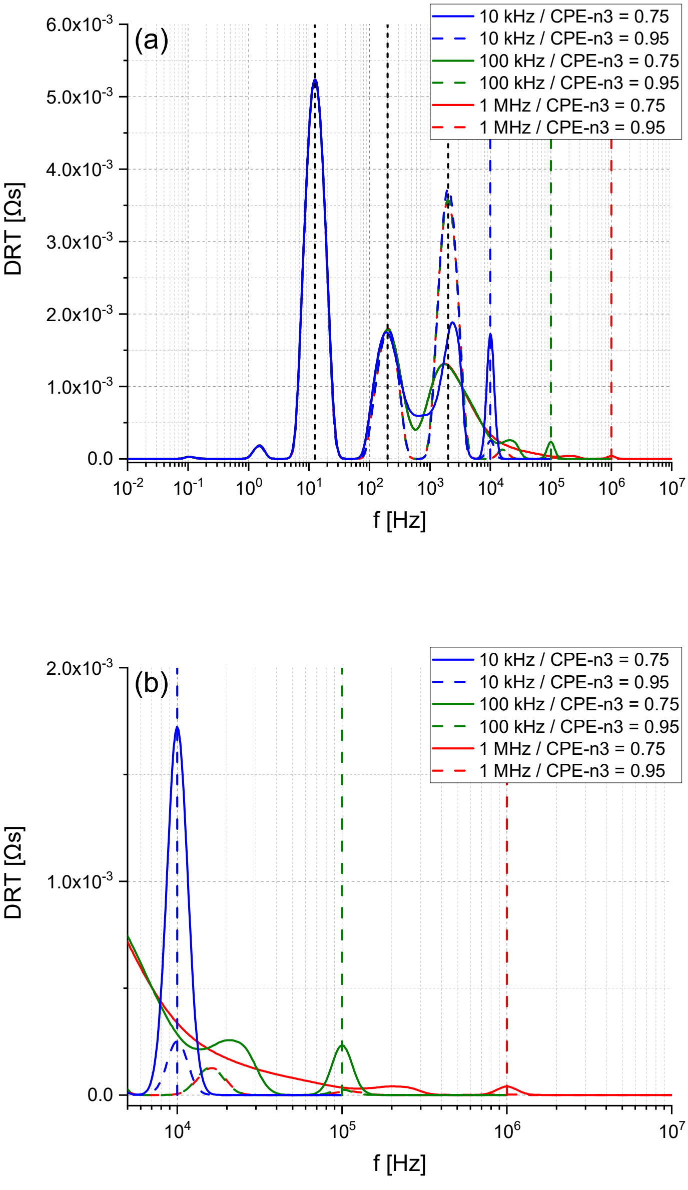

Figure 4.1.11. Comparison of DRT spectra based on the simulation of different frequency ranges together with a variation of CPE-n3 for the entire frequency range in (a) and zoomed into the high frequency range starting at 5 kHz in (b). Regularization parameter $\lambda=10^{-5}$. The remaining CPE exponents are fixed to 0. 95. $L = 2*10^{-9}$ H. The total polarization resistance is 10 mΩ. (14 ppd)

In Figure 4.1.12, the variation of the CPE – n3 for EIS simulations to maximum frequencies of 10 kHz in (a) and 1 MHz in (b) are shown to show the interplay of the CPE – n3 and the maximum frequency for CPE exponents between 0. 55 and 1. 00 systematically. It can be observed that the peak height of the artificial maximum frequency peak is more pronounced if the distance on the frequency scale between the simulated high-frequency process and the maximum frequency is smaller. This means that the maximum frequency artefact in the present case is less pronounced when the maximum frequency is increased. If the EIS spectrum is simulated up to 1 MHz, the artefact exhibits a small peak height, but additional artefacts appear between the simulated process at 2000 Hz and 1 MHz. As shown before, the shoulder in the high-frequency range that can be observed in Figure 4.1.12 (b) will be detached from the 2000 Hz process when the value of the regularization parameter is decreased which will lead to the expression of multiple artificial peaks between 2000 Hz and 1 MHz that can then become subject of misinterpretations.

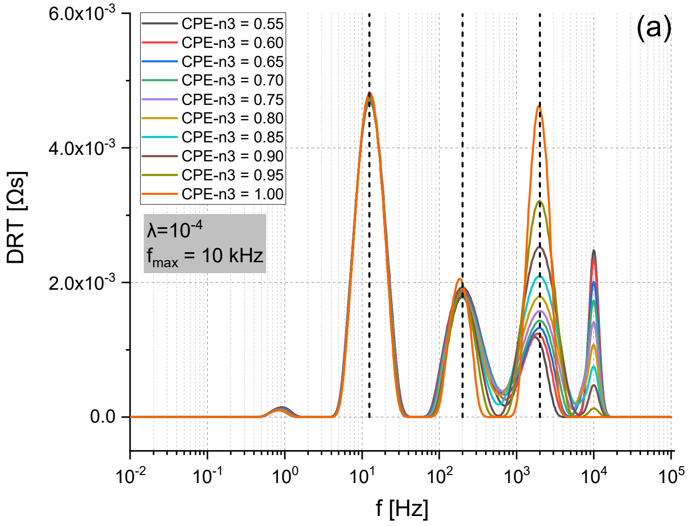

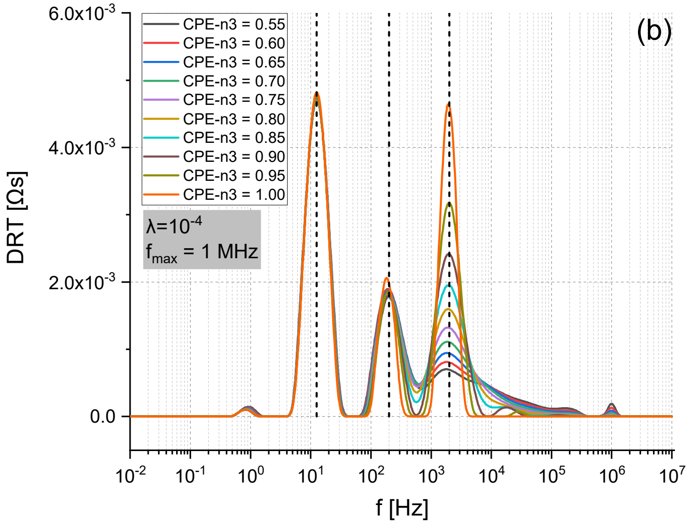

Figure 4.1.12. Graphical depiction of the combined influence of CPE – n3 and the maximum frequency of the underlying EIS spectrum, which is 10 kHz in (a) and 1 MHz in (b). The regularization parameter is 10^{-4} for both, the CPE exponents of the remaining processes are 0. 95 $L=2*10^{-9}$ H and the total polarization resistance is 10 mΩ. (14 ppd)

The conclusions that can be drawn from the analysis of ideal synthetic EIS spectra are the following:

- The CPE exponent influences the DRT result mostly in the frequency range of the associated electrochemical process.
- Frequency dispersion of processes at the frequency edges has a significant influence on the numerical oscillations arising there. This is especially true for the high-frequency range.
- In case of a combined frequency dispersion behavior of adjacent electrochemical processes, sufficient peak resolution is hardly possible even in case of separation of the relaxation frequencies by one decade.
- The DRT result is depending on the maximum frequency of the EIS data set.
- The sharp high frequency artificial peak is located precisely at the maximum frequency of the EIS data set and shows an increasing peak height with decreasing CPE exponent of the high- frequency process and to a lower extent with decreasing CPE exponent of the mid- frequency process.
- In addition to the sharp high-frequency artificial peak, further artefacts appear between the maximum frequency and the simulated 2000 Hz process in case of simulations up to 100 kHz and 1 MHz, which can lead to misinterpretation of those as electrochemical processes and their expression is increasing with decreasing values of the CPE – n2 and CPE – n3 as well.
- The peak height of the artefacts decreases with an increasing maximum frequency or generally speaking with an increased distance between the real high-frequency process and the maximum frequency.
- The polarization resistance only shows a negligible effect on the numerical stability.
- An ideal inductance does not have any influence on the DRT result if it is included in the DRT model via the option “Fitting with inductance” in DRTtools.
- In general, EIS data sets measured up to different maximum frequencies should be analyzed with DRT to verify the high-frequency electrochemical processes.

The choice of simulation series which are repeated with additional statistical error is based on the results shown for ideal EIS spectra. The variation of the polarization resistance was omitted because it was not expected to gain any more knowledge on conducting these simulations. Therefore the next simulations have been confined to variations of the inductance, the CPE exponents and the maximum frequency. The results are presented in the following chapter 4.2.

4.2 Simulations with statistical error

In the following chapter the results of the EIS simulations with added statistical error are presented. Because there were two different error models used, the chapter is separated into two parts. Following these results, the simulation study to investigate the influence of the data point density in terms of the points per decade, the minimum frequency and the error magnitude are presented at the end of this chapter. The latter simulations were performed on one representative simulation series. In order to investigate the impact of the simulated error structure, compare the error models and link the error to the DRT result, Kramers - Kronig validity tests were performed with the freely available Linear KK-Tool developed by the Karlsruhe Institute of Technology (KIT) [43] [44].

4.2.1 Simulations with error model 1

In comparison to the DRT spectra shown in chapter 4.1 based on ideal EIS spectra, in this chapter all DRT spectra are shown with higher values of the regularization parameter λ to suppress the oscillations which are caused by the added noise.

In Figure 4.2.1, the Kramers - Kronig residuals (called KKR in what follows) are shown for the real and imaginary part of the EIS spectrum simulated with CPE - n1 = 0. 75 and the remaining CPE exponents set to 0. 95. The inductance value is fixed to $2*10^{-9}$ H and the total polarization resistance (R2+R3+R4) is 10 mΩ. The residuals of the real part are randomly distributed over the entire frequency range and mostly within the limit of 1 %. The residuals of the imaginary part show a small bias, especially in the frequency range from 1 kHz to 1 MHz and are much smaller compared to the residuals of the real part, which is due to the fact that the error of the imaginary part scales with the absolute amount of Im (Z) and the real part scales with the absolute amount of Re (Z), whereas the magnitude of Im (Z) is roughly one order of magnitude smaller than Re (Z).

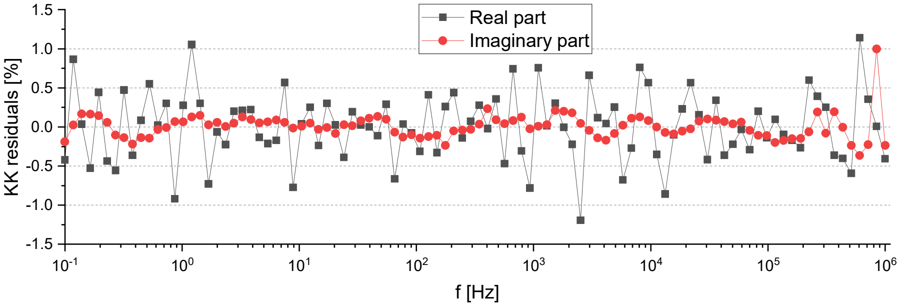

Figure 4.2.1. Kramers-Kronig residuals of the real and imaginary part of the impedance simulated with error level $\varepsilon_0 = 0.5$ *% and CPE - n1 = 0. 75 /CPE-n2, 3 = 0. 95 for the frequency range from 100 mHz to 1 MHz with 14 ppd. The inductance value is L=* $2 \cdot 10^{-9}$ *H. The total polarization resistance is 10 mΩ.*

By applying error model 1 to the EIS data, a distinct error nature of the real and imaginary part can be achieved, which is probably more close to the experimental EIS recording as the signal-to-noise ratio will be different for the real and imaginary parts in the experiment. Furthermore, an increasing error level on the imaginary part by increasing inductive effects can be simulated, which is also visible in Figure 4.2.1 at high frequencies.

In order to check the influence of the CPE exponents on the KKR, the values were compared for different simulation series in which the CPE exponent of the respective process is decreased to 0. 75 and the inductance is increased by one order of magnitude compared to the default value $2^{*}10^{-9}$ H. The results are shown in Figure 4.2.2 (a) for the real part and in (b) for the imaginary part. From the observation there it can be concluded that the value of the CPE exponent does not have a systematic influence on the KKR of neither the real nor the imaginary part. Therefore the oscillations in the DRT calculation which are caused by the CPE are most probably a weakness of the deconvolution method itself. Furthermore, an increase of the inductance from $2^{*}10^{-9}$ H to $2^{*}10^{-8}$ H value does not show a clear impact on the KKR of the imaginary part in the high-frequency range. Regarding the imaginary part of the KKR, the increasing values for increasing frequency are visible very clearly in Figure 4.2.2 (b). This kind of behavior was intended to simulate the influence of parasitic inductances in the high-frequency range while keeping the KKR low in the remaining frequency range.

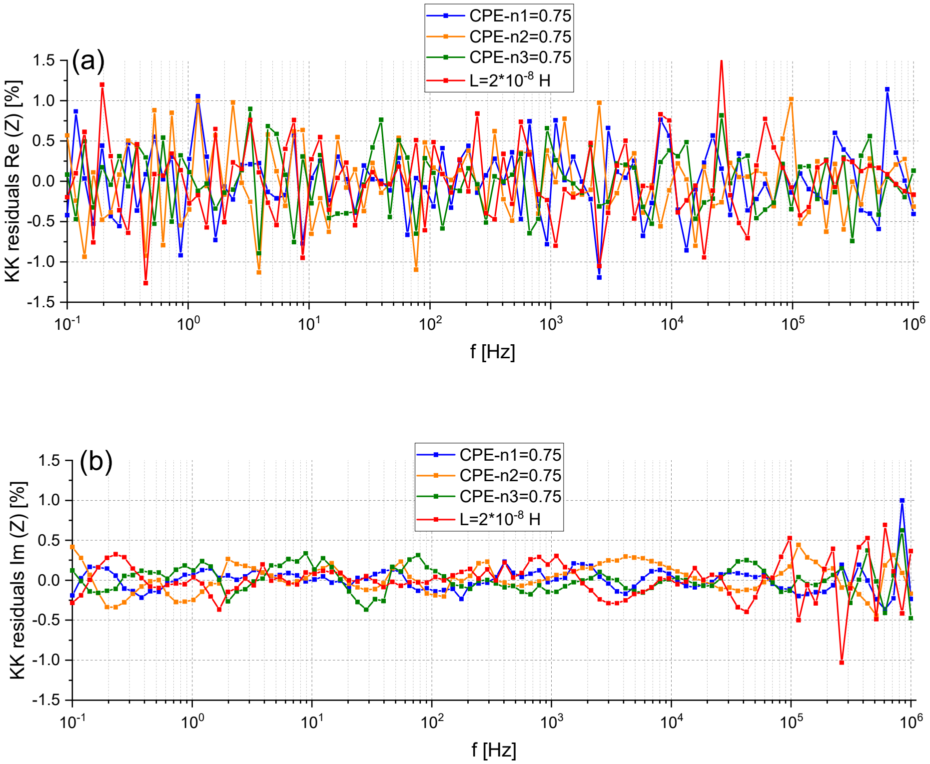

*Figure 4.2.2. Comparison of Kramers-Kronig residuals for the real (a) and imaginary (b) part of the impedance for EIS simulation in the frequency range 100 mHz to 1 MHz with 14 ppd and error model 1. The inductance for the CPE variations is set to L=2*10^{-9} H. The total polarization resistance is 10 mΩ.*

In Figure 4.2.3, an exemplary Nyquist diagram for the variation of the CPE-n1 can be found. The CPE exponent of the remaining processes are thereby 0. 95. It can be observed that the expression of the low-frequency arc in the complex plane is becoming more depressed with a decreasing value of the CPE exponent for the 12. 5 Hz process. Furthermore, a low value of CPE – n1 also covers the mid-frequency process in the Nyquist diagram.

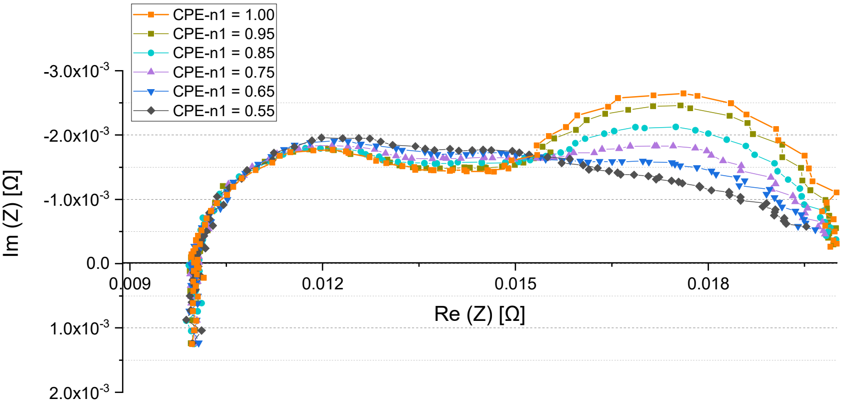

*Figure 4.2.3. Nyquist diagram for simulated EIS spectra (+ error model 1) with varying CPE-n1 values while the CPE exponents of the remaining processes are fixed to 0. 95. L = 2*10*$^{-9}$ *H and the total polarization resistance is 10 mΩ. (100 mHz – 100 kHz, 14 ppd).*

In Figure 4.2.4, the DRT results for the variation of the CPE exponent of the 12. 5 Hz process (CPE – n1) are shown for two representative simulation series in which the CPE exponents of the remaining two electrochemical processes are fixed to 0. 95 and 0. 75 respectively. The results with CPE – n2 and CPE – n3 being 0. 95 correspond to the Nyquist diagram shown before. In principle the trend of increasing number of peaks in the low-frequency range with decreasing value of the CPE exponent and the confinement of the oscillations to the frequency range where the CPE behavior occurs is the same as for simulations without error, with an increased level of numerical oscillation due to the error leading to the need of higher regularization parameters for the DRT calculation. While for calculation of the DRT from EIS without error also λ values of 10^{-5} still give reasonable results, it is necessary to choose roughly ten times higher values of λ for DRT calculation of EIS spectra with error model 1 and ε_0 = 0. 5 %. Therefore, the DRT spectra calculated with $\lambda = 10^{-3}$ and $\lambda = 10^{-4}$ are presented throughout this chapter.

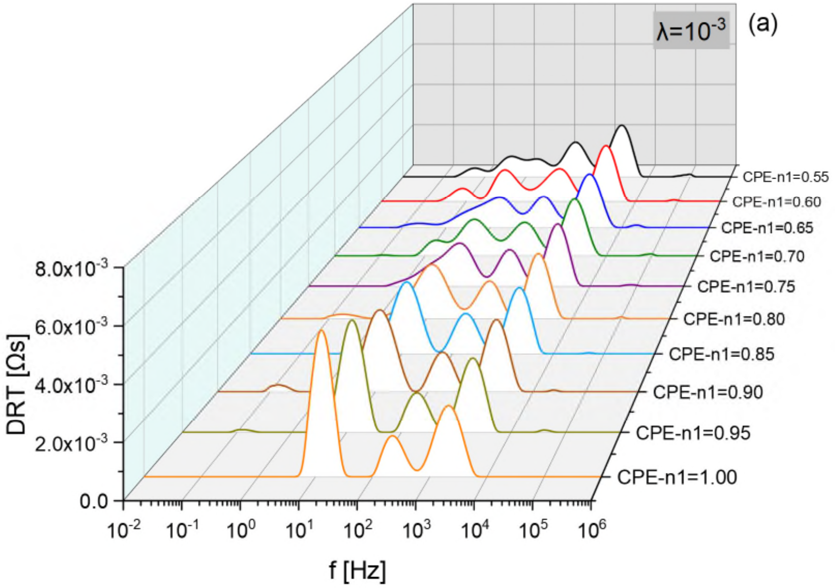
λ=10^{-3}
(a)
DRT [Ωs]
8.0x10^{-3}
6.0x10^{-3}
4.0x10^{-3}
2.0x10^{-3}
0.0
10^{-2}
10^{-1}
10^{0}
10^{1}
10^{2}
10^{3}
10^{4}
10^{5}
10^{6}
f [Hz]
CPE-n1=0.55
CPE-n1=0.60
CPE-n1=0.65
CPE-n1=0.70
CPE-n1=0.75
CPE-n1=0.80
CPE-n1=0.85
CPE-n1=0.90
CPE-n1=0.95
CPE-n1=1.00

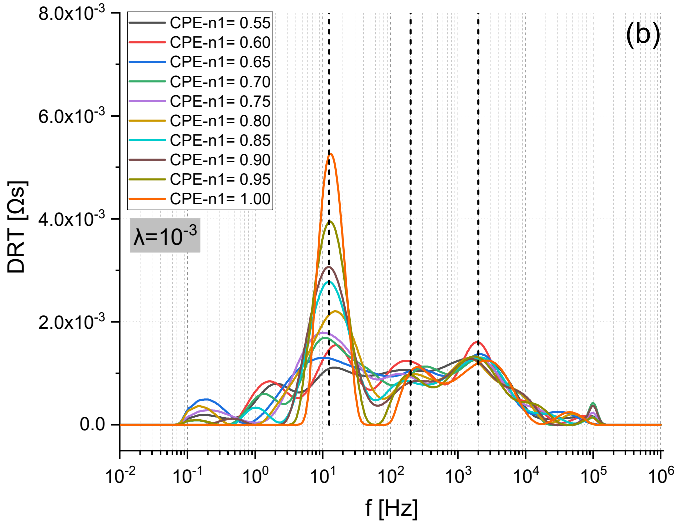
8.0x10^{-3}
6.0x10^{-3}
4.0x10^{-3}
2.0x10^{-3}
0.0
DRT [Ωs]
CPE-n1= 0.55
CPE-n1= 0.60
CPE-n1= 0.65
CPE-n1= 0.70
CPE-n1= 0.75
CPE-n1= 0.80
CPE-n1= 0.85
CPE-n1= 0.90
CPE-n1= 0.95
CPE-n1= 1.00
λ=10^{-3}
(b)
10^{-2}
10^{-1}
10^{0}
10^{1}
10^{2}
10^{3}
10^{4}
10^{5}
10^{6}
f [Hz]

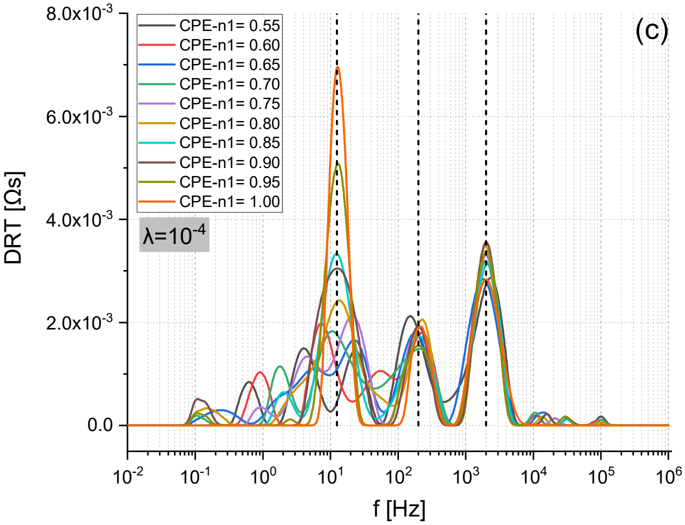

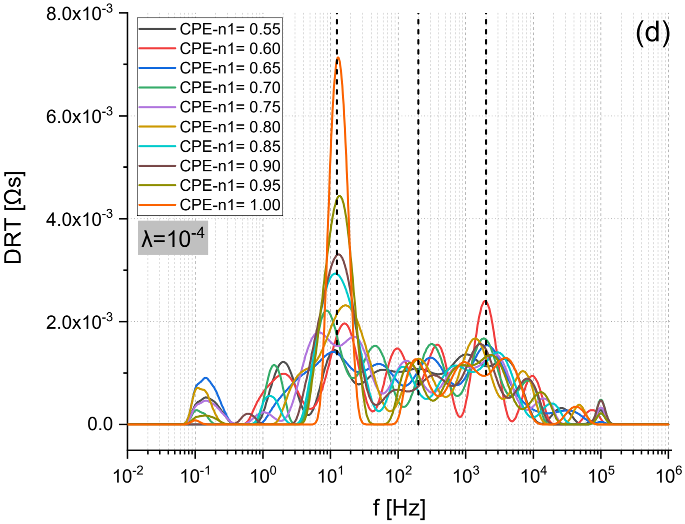

*Figure 4.2.4. DRT plots for variation of the CPE exponent of the electrochemical process at a relaxation frequency of 12. 5 Hz. In (a) and (c) the CPE exponents of the other processes are 0. 95. In (b) and (d) the CPE exponents of the other processes are 0. 75. Regularization parameter for DRT calculation is λ=10^{-3} for (a) and (b) and λ=10^{-4} for (c) and (d). L=2*10^{-9} H and the total polarization resistance is 10 mΩ. (100 mHz – 100 kHz, 14 ppd)*

The trend to an increasing peak multiplication in the low-frequency range with decreasing CPE – n1 can be clearly observed in Figure 4.2.4 (a), where the remaining CPE exponents are 0. 95 respectively. Comparing these results for a regularization parameter of 10^{-3} with the ones shown in Figure 4.2.4 (c) with 10^{-4}, the increase of numerical stability through a combined effect of measurement error and low regularization parameters becomes obvious, as the numerical oscillations in the low-frequency range become very pronounced. In case of low CPE exponents of all electrochemical processes, as shown in Figure 4.2.4 (b) and (d), the numerical oscillations are already very prominent for regularization parameters as high as 10^{-3} and lead to an extremely noisy DRT spectrum for values of 10^{-4}, which already cannot be interpreted anymore.

An important finding from these simulations is that there is evidence that the statistical error only enhances the numerical instability of the DRT which is caused by low CPE exponents, while the areas of the DRT spectrum without significant CPE behavior still give low oscillation levels although the statistical error is present there as well. In reverse this means that electrochemical systems which do not exhibit high degrees of frequency dispersion are more robust to measurement errors in terms of a reliable DRT analysis.

In Figure 4.2.5, a comparison of the DRT spectra based on EIS simulations to different maximum frequencies are shown for the variation of CPE – n1. In (a) the entire frequency range is shown, whereas in (b) the DRT is zoomed into the high-frequency range starting at 5 kHz. Regarding the low-frequency regime, there is no systematic impact of the different maximum frequencies seen. The differences are most probably due to the statistical error. Looking into the high-frequency range, there is no systematic impact of the CPE – n1 on the location and expression of the artificial peaks observable.

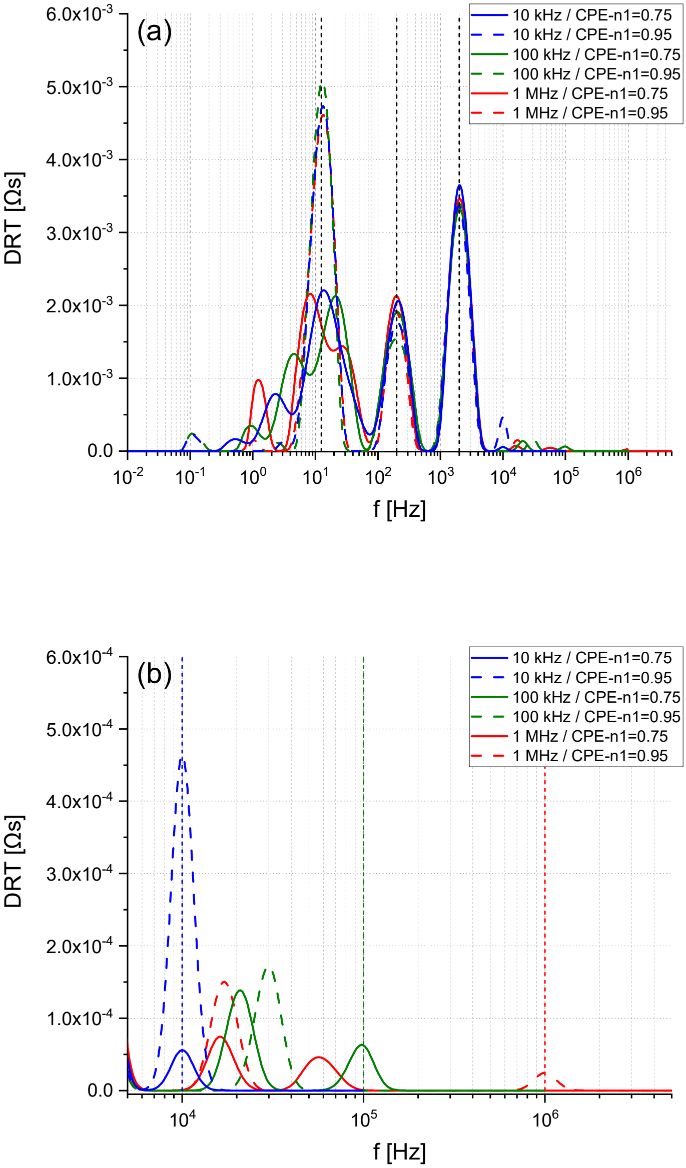

Figure 4.2.5. Comparison of DRT spectra for simulation of different frequency ranges and variation of CPE exponent in the low- frequency range (CPE-n1) for the entire frequency range in (a) and zoomed into the high frequency range in (b) for error model 1. Regularization parameter $\lambda=10^{-4}$. The CPE exponents of the other processes are 0. 95. $L = 2*10^{-9}$ H and the total polarization resistance is 10 mΩ. (14 ppd)

The results from ideal EIS simulations which showed that the-low frequency numerical oscillations are enhanced by CPE behavior of low-frequency electrochemical processes, is also achieved for simulations with error model 1. The oscillations at the high-frequency edge of the DRT are due to the statistical error in combination with CPE – n2 and CPE – n3 of 0. 95 and therefore show no systematic relationship with the CPE – n1. This statement can be confirmed if the variation of CPE – n1 is decoupled from the mid- and low-frequency CPE behavior by setting the CPE exponents of those two to one, as shown in Figure 4.2.6. In that case almost no high frequency artefacts are observed for all maximum frequencies and CPE – n1 of 0. 95 and 0. 75.

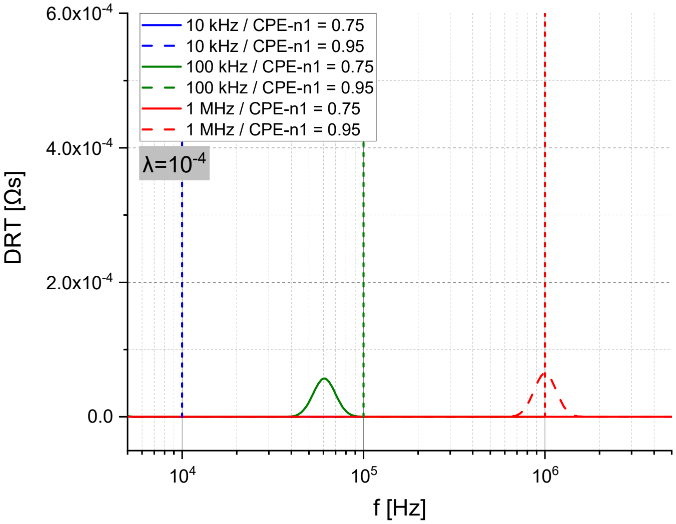

*Figure 4.2.6. Comparison of DRT spectra for simulation of different frequency ranges and variation of CPE exponent in the low- frequency range (CPE-n1). Regularization parameter λ = 10^{-4}. The CPE exponents of the other processes are 1. 00. L = 2*10^{-9} H and the total polarization resistance is 10 mΩ. (14 ppd)*

In Figure 4.2.7, an exemplary Nyquist diagram for the variation of the CPE-n2 is shown. The CPE exponents of the remaining processes are 0. 95. Here the decreasing value of CPE – n2 leads to a vanishing semicircle in the mid-frequency range.

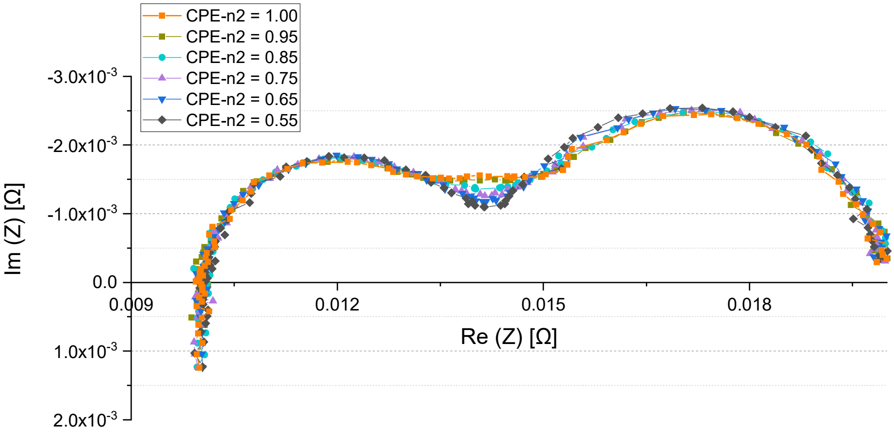

*Figure 4.2.7. Nyquist diagram for simulated EIS spectra (+ error model 1) with varying CPE-n2 values while the CPE exponents of the remaining processes are fixed to 0. 95. L = 2*10^{-9} H and the total polarization resistance is 10 mΩ. (100 mHz – 100 kHz, 14 ppd).*

In Figure 4.2.8, the DRT results of the variation of the CPE exponent of the 200 Hz process (CPE – n2) are shown for two simulation series with the CPE exponents of the remaining processes fixed to 0. 95 and 0. 75 respectively. The results with CPE – n1 and CPE – n3 are 0. 95 correspond to the Nyquist diagram shown in Figure 4.2.7. From the qualitative point of view, the results are comparable with the ones from the simulations without error as well if the regularization parameter is chosen roughly one magnitude higher compared to the analysis of ideal EIS spectra. Again the oscillations at the frequency edges are at a low level if only the CPE exponent of the mid-frequency process is decreased well below one. In addition there is no systematic influence of CPE-n2 seen on the peak height of the low-frequency artefacts. The observed differences are due to random errors applied to the EIS data. This confirms the result of the simulations without error that CPE behavior of low- or high-frequency processes is more likely to cause numerical oscillations at the frequency edges of the DRT, compared to frequency dispersion in the mid-frequency area.

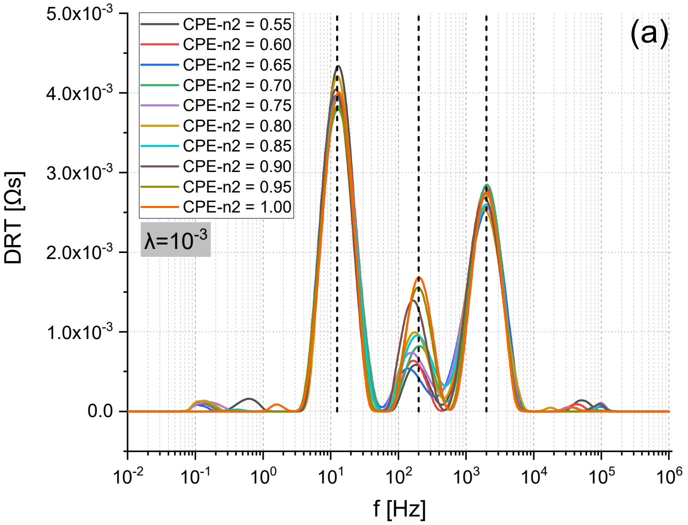
(a)
CPE-n2 = 0.55
CPE-n2 = 0.60
CPE-n2 = 0.65
CPE-n2 = 0.70
CPE-n2 = 0.75
CPE-n2 = 0.80
CPE-n2 = 0.85
CPE-n2 = 0.90
CPE-n2 = 0.95
CPE-n2 = 1.00
λ=10^-3
DRT [Ωs]
5.0x10^-3
4.0x10^-3
3.0x10^-3
2.0x10^-3
1.0x10^-3
0.0
f [Hz]
10^-2
10^-1
10^0
10^1
10^2
10^3
10^4
10^5
10^6

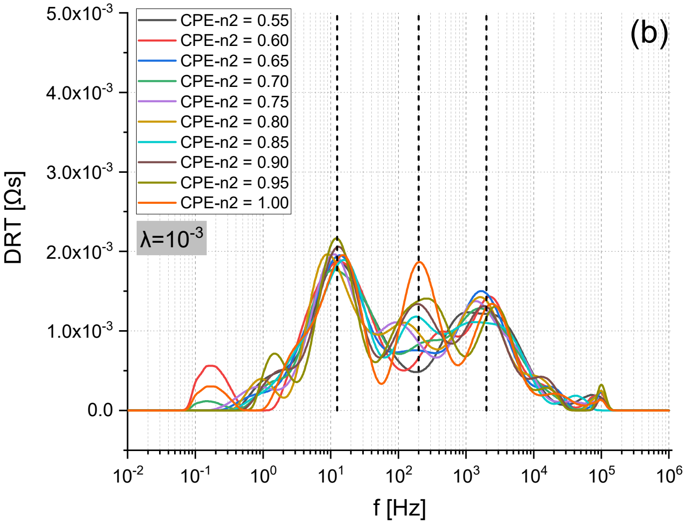
(b)
CPE-n2 = 0.55
CPE-n2 = 0.60
CPE-n2 = 0.65
CPE-n2 = 0.70
CPE-n2 = 0.75
CPE-n2 = 0.80
CPE-n2 = 0.85
CPE-n2 = 0.90
CPE-n2 = 0.95
CPE-n2 = 1.00
λ=10^-3
DRT [Ωs]
5.0x10^-3
4.0x10^-3
3.0x10^-3
2.0x10^-3
1.0x10^-3
0.0
f [Hz]
10^-2
10^-1
10^0
10^1
10^2
10^3
10^4
10^5
10^6

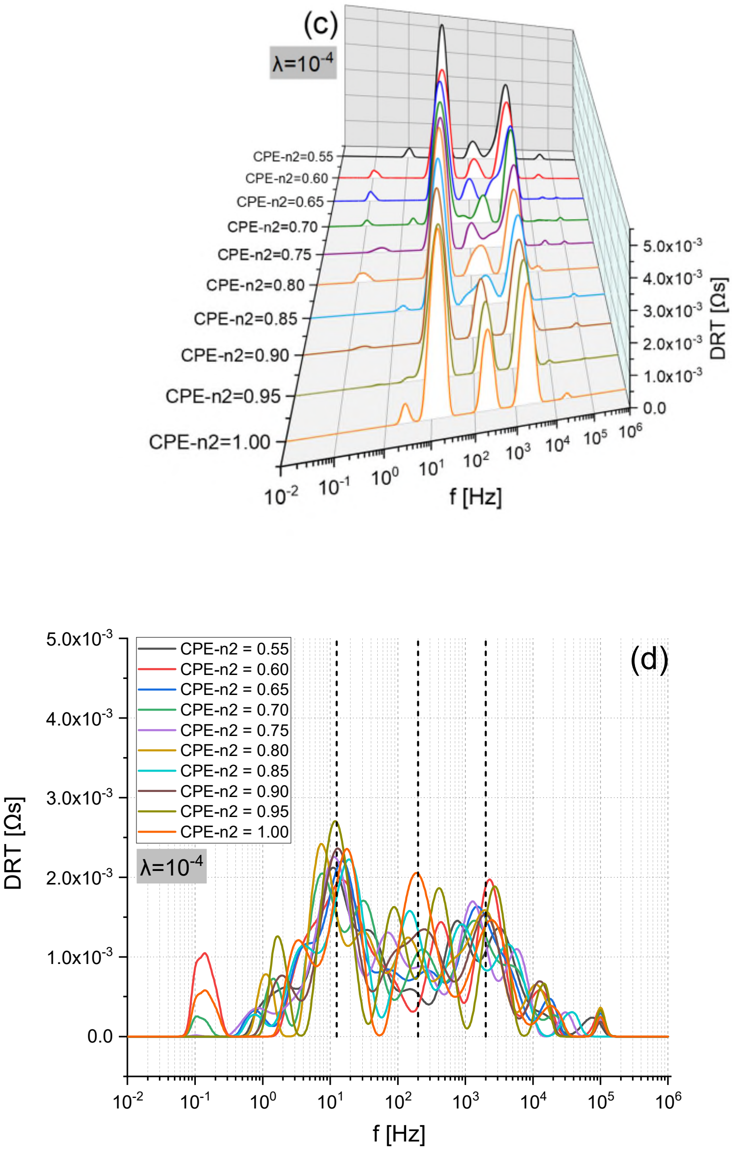

Figure 4.2.8. DRT plots for variation of the CPE exponent of the electrochemical process at relaxation frequency 200 Hz. In (a) and (c) the CPE exponents of the other processes are 0. 95. In (b) and (d) the CPE exponents of the remaining processes are 0. 75. Regularization parameter for DRT calculation is $\lambda=10^{-3}$ for (a) and (b) and $\lambda=10^{-4}$ for (c) and (d). $L = 2*10^{-9}$ H and the total polarization resistance is 10 mΩ. (100 mHz – 100 kHz, 14 ppd)

Especially in Figure 4.2.8 (c), the additional impact of the error on the expression of the correct number of peaks in the mid-frequency range is clearly visible, as the extent of peak multiplication is not strictly following the magnitude of the CPE - n2 as shown for ideal EIS spectra (compare Figure 4.1.7). In graph (d), the combined effect of low CPE – n of all processes in combination with statistical error is visualized where distinct electrochemical processes cannot be clearly identified anymore. As observed in the simulations with different CPE – n2, also in the current case the statistical error acts as an enhancer of numerical instabilities caused by the CPE. This is especially obvious in Figure 4.2.8 (a), where the CPE exponents of process 1 and 3 are 0. 95 and the frequency edges only exhibit slight numerical oscillations.

In Figure 4.2.9, a comparison of the maximum frequencies for the variation of CPE – n2 is shown. The over-regularization in the mid-frequency range appears in the same extent for CPE exponents as low as 0. 75, regardless of the simulated maximum frequency. Furthermore, the influence of the CPE behavior of the mid-frequency process on the high-frequency oscillations is slightly visible due to more pronounced artificial peaks for CPE-n2 = 0. 75. The influence on the low-frequency artefacts is somehow more elusive with a slight trend to enhancement with decreasing CPE – n2. Important to state is the fact that in case of simulation up to 100 kHz and 1 MHz, the additional artefacts located between the 2000 Hz process and the maximum frequency are more pronounced compared to the maximum frequency artefact and are even at a similar position for the 100 kHz and 1 MHz simulation, which would potentially cause a misinterpretation of this artefact as an electrochemical process. In such cases, more EIS spectra at the same operation point can potentially help to verify the real high-frequency electrochemical processes.

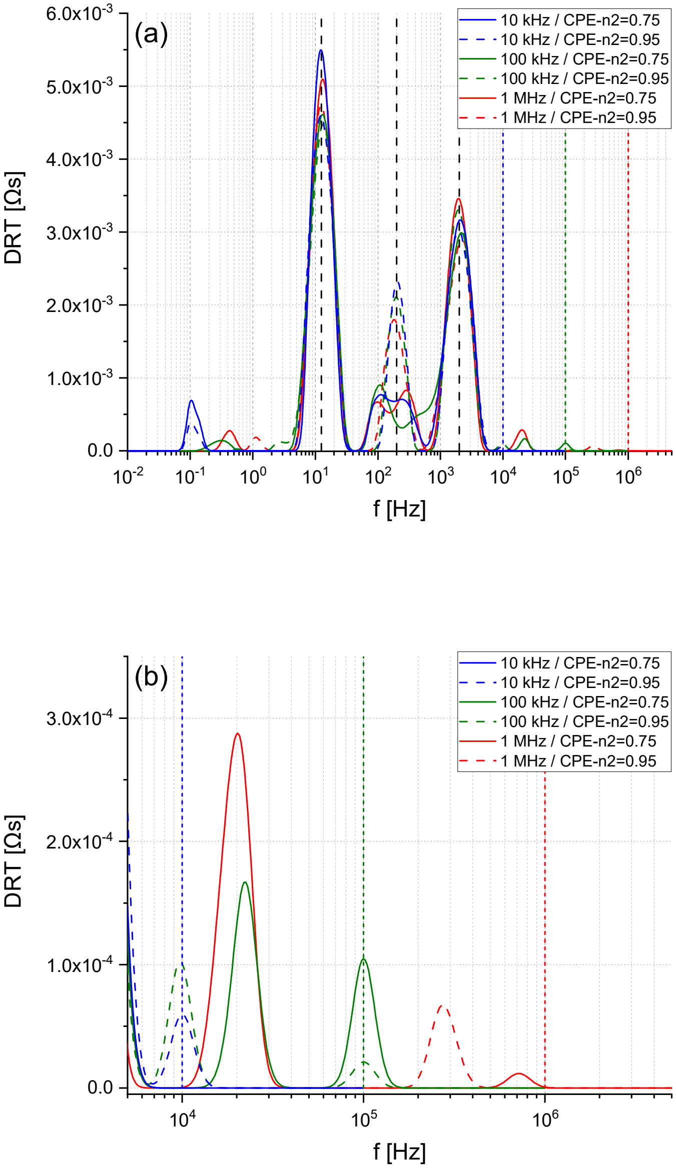

*Figure 4.2.9. Comparison of DRT spectra for simulation of different frequency ranges and variation of CPE exponent for the 200 Hz process for the entire frequency range in (a) and zoomed into the high frequency range in (b). Regularization parameter λ=10^{-4}. The CPE exponents of the remaining two processes are fixed to 0. 95. L = 2*10^{-9} H and the total polarization resistance is 10 mΩ. (14 ppd)*

In order to prove the influence of CPE – n2 on the high-frequency numerical artefacts, the maximum frequency comparison for the case in which CPE –n1 and CPE – n3 are both set to one, is shown in Figure 4.2.10. Comparing this result with the one in Figure 4.2.9 when CPE – n3 is 0. 95, it can be stated that the CPE – n2 alone does not cause systematic effects in the high frequency range and that it is only enhancing the effects caused by CPE – n3.

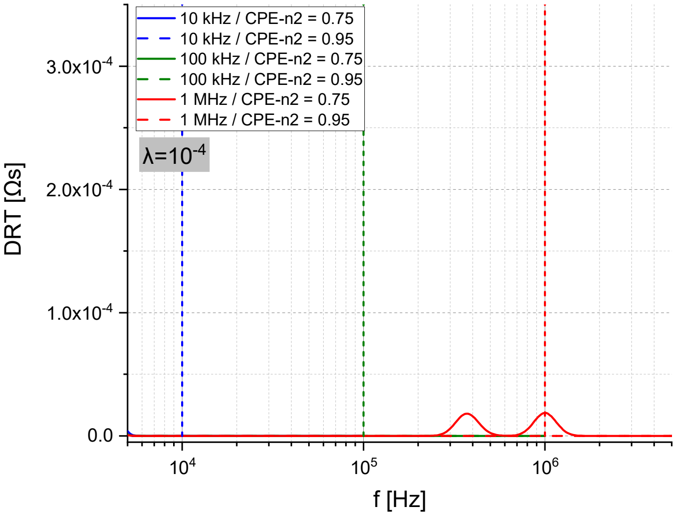

Figure 4.2.10. Comparison of high-frequency DRT spectra for simulation of different frequency ranges and variation of CPE exponent in the mid- frequency range (CPE-n2). Regularization parameter $\lambda=10^{-4}$*. The CPE exponents of the other processes are 1. 00. L = 2*10*$^{-9}$ *H and the total polarization resistance is 10 mΩ. (14 ppd)*

In Figure 4.2.11, an exemplary Nyquist diagram for the variation of the CPE-n3 is shown. The CPE exponents of the remaining processes are 0. 95. Here the decreasing value of CPE – n3 is causing an increased depression of the semicircular arc in the high-frequency range and also a shift of the x-axis intersection to higher values of Re (Z) with decreasing CPE exponent.

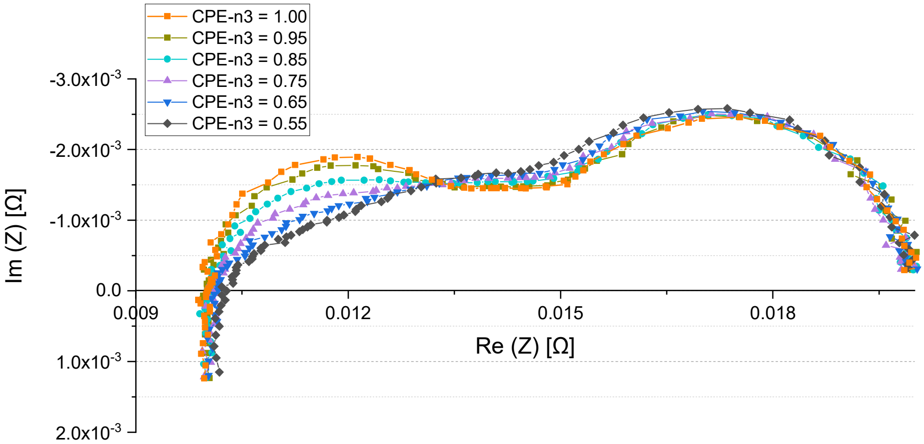

*Figure 4.2.11. Nyquist diagram for simulated EIS spectra (+ error model 1) with varying CPE-n3 values while the CPE exponents of the remaining processes are fixed to 0. 95. L = 2*10^{-9} H and the total polarization resistance is 10 mΩ. (100 mHz – 100 kHz, 14 ppd).*

In Figure 4.2.12 the DRT results of the variation of the CPE exponent of the 2000 Hz process (CPE – n3) are shown for the two representative simulation series with remaining CPE exponents fixed to 0. 95 and 0. 75 respectively. The results with CPE – n1 and CPE – n2 are 0. 95 correspond to the Nyquist diagram that was shown in Figure 4.2.11. As already observed in the simulation of ideal EIS spectra, the CPE exponent of the 2000 Hz process has a significant influence on the high-frequency artefacts. In comparison to the DRT results of the ideal EIS spectra, here the peak height of the artificial sharp peak at the maximum frequency is not following the decreasing value of the CPE exponent exactly, as can be observed in Figure 4.2.12 (a).

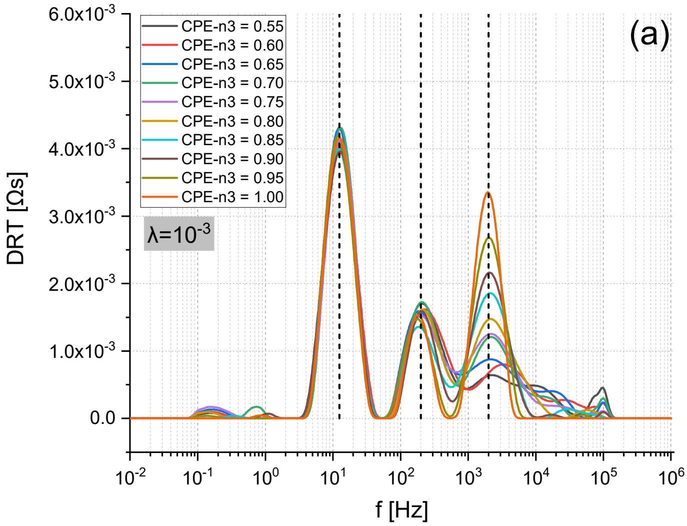
(a)
CPE-n3 = 0.55
CPE-n3 = 0.60
CPE-n3 = 0.65
CPE-n3 = 0.70
CPE-n3 = 0.75
CPE-n3 = 0.80
CPE-n3 = 0.85
CPE-n3 = 0.90
CPE-n3 = 0.95
CPE-n3 = 1.00
λ=10^{-3}
DRT [Ωs]
6.0x10^{-3}
5.0x10^{-3}
4.0x10^{-3}
3.0x10^{-3}
2.0x10^{-3}
1.0x10^{-3}
0.0
f [Hz]
10^{-2}
10^{-1}
10^{0}
10^{1}
10^{2}
10^{3}
10^{4}
10^{5}
10^{6}

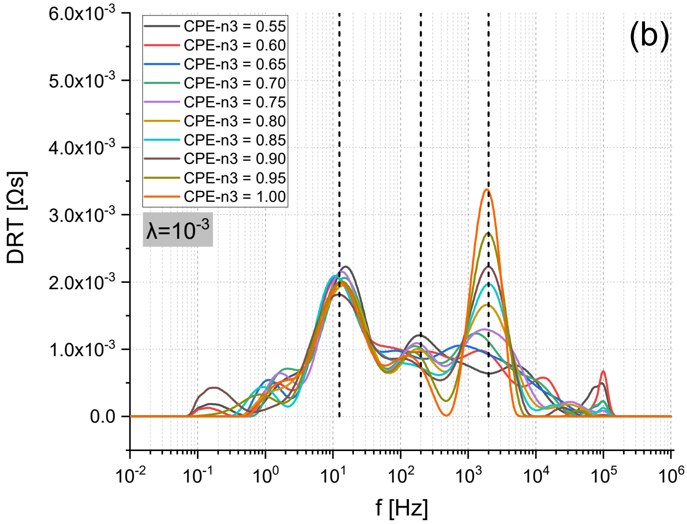
(b)
CPE-n3 = 0.55
CPE-n3 = 0.60
CPE-n3 = 0.65
CPE-n3 = 0.70
CPE-n3 = 0.75
CPE-n3 = 0.80
CPE-n3 = 0.85
CPE-n3 = 0.90
CPE-n3 = 0.95
CPE-n3 = 1.00
λ=10^{-3}
DRT [Ωs]
6.0x10^{-3}
5.0x10^{-3}
4.0x10^{-3}
3.0x10^{-3}
2.0x10^{-3}
1.0x10^{-3}
0.0
f [Hz]
10^{-2}
10^{-1}
10^{0}
10^{1}
10^{2}
10^{3}
10^{4}
10^{5}
10^{6}

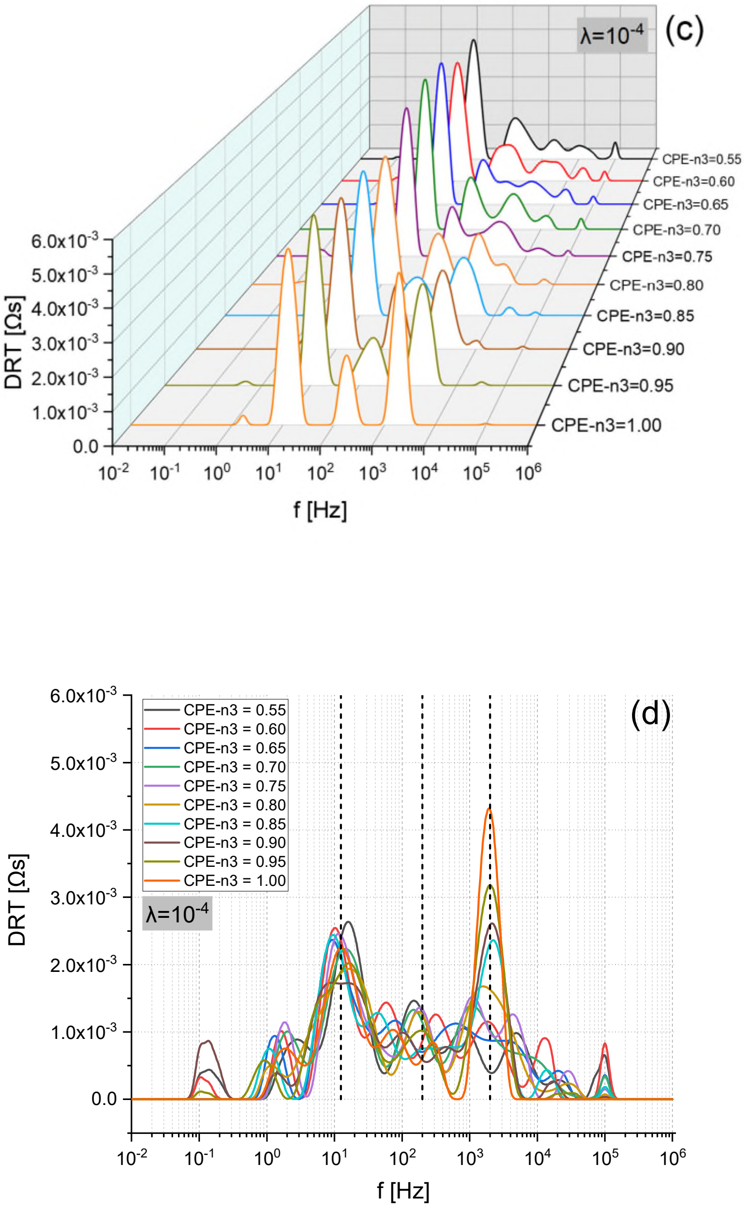

*Figure 4.2.12. DRT plots for variation of the CPE exponent of the electrochemical process at a relaxation frequency of 2000 Hz. In (a) and (c) CPE exponents of the other processes are 0. 95. In (b) and (d) the CPE exponents of the other processes are 0. 75. Regularization parameter for DRT calculation is λ=10^{-3} for (a) and (b) and λ=10^{-4} for (c) and (d). L = 2*10^{-9} H and the total polarization resistance is 10 mΩ. (100 mHz – 100 kHz, 14 ppd)*

However, there is a clear trend to an increasing peak height of the artefacts seen for lower values of the regularization parameter in Figure 4.2.12 (c). This is another hint that the noise has an additional contribution to the expression of high-frequency artefacts. Because of the fact that the error structure will give rise to different expressions of the high-frequency oscillations, simulations with a different error model are presented in the next chapter together with a comparison of the results from error model 1 and 2. In case of high degrees of frequency dispersion for all three electrochemical processes, as shown in Figure 4.2.12 (b) and (c), the oscillations spread also to the mid-frequency range with the high-frequency edge as starting point when the regularization parameter is decreased. Again it has to be pointed out that the low-frequency area of the DRT is very accurate if no or less CPE behavior is present in this frequency range, as can be observed in Figure 4.2.12 (a) and (c). Again low CPE exponents of all processes together with statistical error and low values of the regularization parameter cause severe oscillations in the entire frequency range, especially visible in Figure 4.2.12 (d).

The comparison of the maximum frequencies together with varying CPE – n3, which is shown in Figure 4.2.13, confirms the observation from the ideal EIS simulations that the CPE exponent of the high-frequency process is the main contributor to the high-frequency artefacts. Additionally, it is clearly seen that the expression of the sharp high-frequency peak is more pronounced if the maximum frequency is 10 kHz and gets less expressed with increasing maximum frequency. It has to be emphasized also that the sharp artificial peak is not always observable if EIS data are available up to 1 MHz, as the probability of observing the peak decreases with increasing maximum frequency, which was shown before for simulation of ideal EIS spectra. For the simulations to 100 kHz and 1 MHz the artefacts between the 2000 Hz process and the maximum frequency are clearly pronounced at roughly 12 kHz and 20 kHz for CPE - n3 = 0. 75. In comparison to the results based on ideal EIS spectra, the impact of the statistical errors is evident as an influence of it on the position and peak height of the artefacts between 2000 Hz and f_{max} and the probability of the appearance of the artefact at the maximum frequency for the simulation up to 1 MHz.

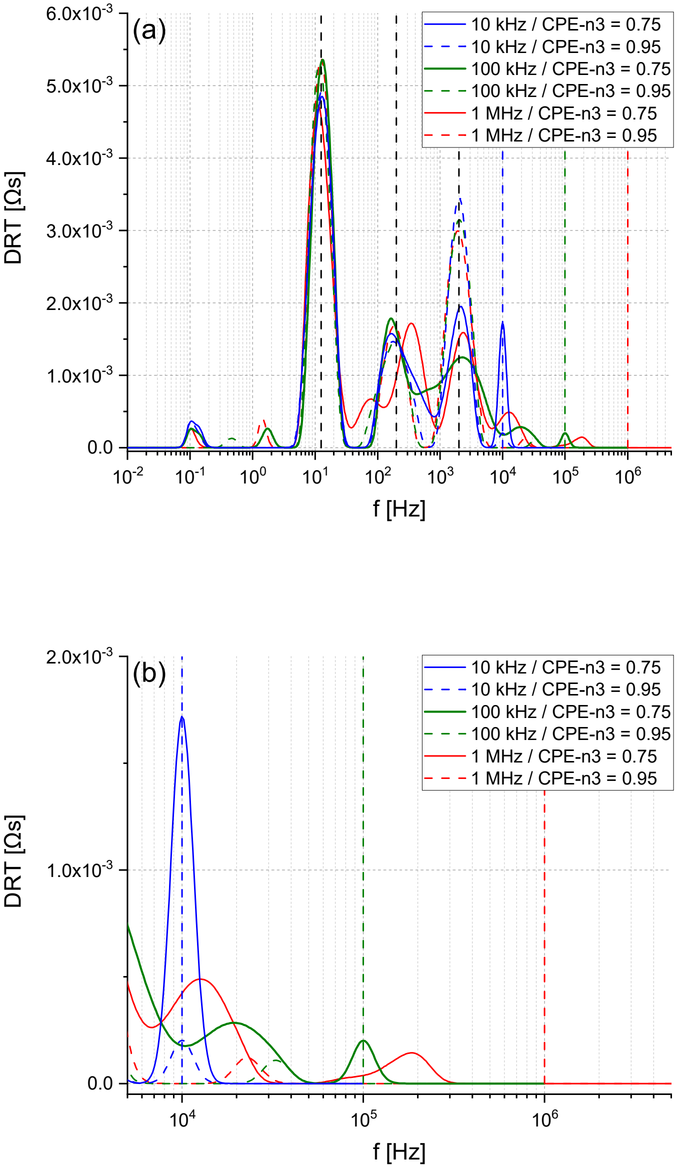

Figure 4.2.13. Comparison of DRT spectra for simulation of different frequency ranges and variation of CPE exponent for the 2000 Hz process (CPE-n3) for the entire frequency range in (a) and zoomed into the high frequency range in (b). Regularization parameter $\lambda=10^{-4}$. The CPE exponents of the remaining two processes are fixed to 0. 95. $L = 2*10^{-9}$ H and the total polarization resistance is 10 mΩ. (14 ppd)

In Figure 4.2.14, a Nyquist diagram of simulated EIS spectra with different values of the inductance can be found. The CPE exponents of all electrochemical processes are 0. 95 and the total polarization resistance is 10 mΩ. Here only inductances up to 4*10^{-8} H are graphically depicted, as higher values cover the entire range of negative imaginary parts. Nevertheless, with further increasing inductance values, the inductive tail at positive imaginary parts of the impedance reaches very high values.

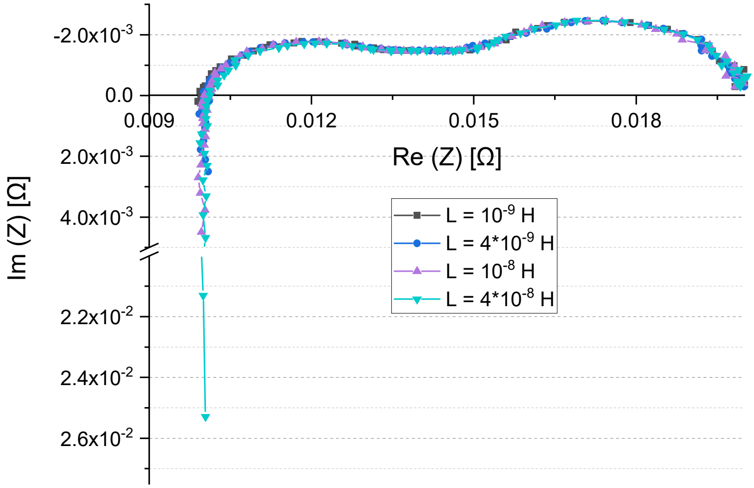

Figure 4.2.14. Nyquist diagram for simulated EIS spectra (+ error model 1) with varying inductance values while the CPE exponents of all processes are fixed to 0. 95. The total polarization resistance is 10 mΩ. (100 mHz – 100 kHz, 14 ppd). Remark: The x- and y-axis scales are not linked 1:1 for better visibility of the semicircles.

When the DRT results for different values of the inductance between 10^{-9} H and 2*10^{-7} H are analyzed, as shown in Figure 4.2.15, it can be observed that there is no systematic impact of the inductance on the oscillations in the high-frequency range. Only the spectra for L as high as 10^{-7} H and 2*10^{-7} H show a slight increase of the peak height of the characteristic artificial peak if the regularization parameter is 10^{-5} and the CPE exponents are decreased to 0. 75. From comparison of the graphs in Figure 4.2.15 (a) and (b) with the graphs in (c) and (d), the major impact of the CPE exponent on numerical oscillation is evident. In case of CPE-nx = 0. 95, there is no influence of the inductivity seen at all.

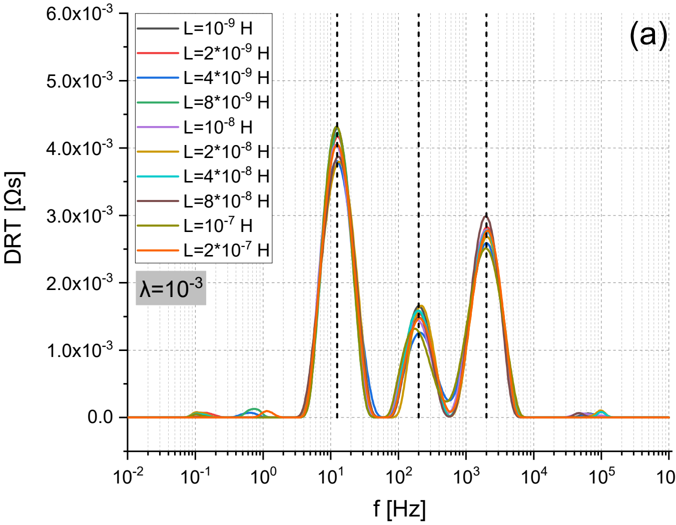
(a)
DRT [Ωs]
f [Hz]
6.0x10^-3
5.0x10^-3
4.0x10^-3
3.0x10^-3
2.0x10^-3
1.0x10^-3
0.0
10^-2
10^-1
10^0
10^1
10^2
10^3
10^4
10^5
10^6
L=10^-9 H
L=2*10^-9 H
L=4*10^-9 H
L=8*10^-9 H
L=10^-8 H
L=2*10^-8 H
L=4*10^-8 H
L=8*10^-8 H
L=10^-7 H
L=2*10^-7 H
λ=10^-3

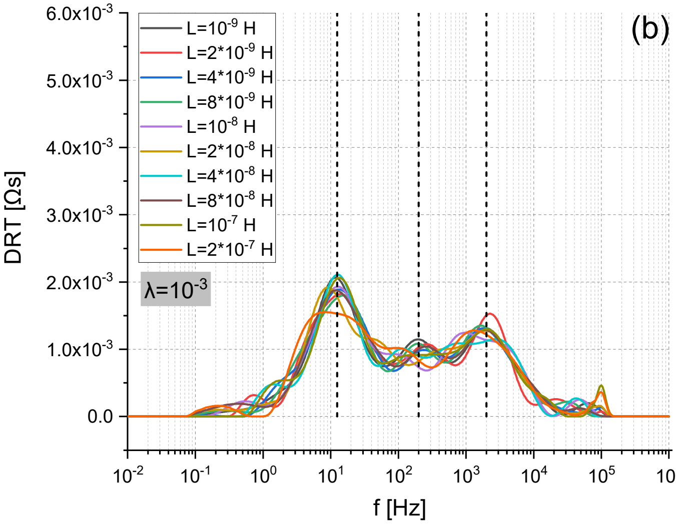
(b)
DRT [Ωs]
f [Hz]
6.0x10^-3
5.0x10^-3
4.0x10^-3
3.0x10^-3
2.0x10^-3
1.0x10^-3
0.0
10^-2
10^-1
10^0
10^1
10^2
10^3
10^4
10^5
10^6
L=10^-9 H
L=2*10^-9 H
L=4*10^-9 H
L=8*10^-9 H
L=10^-8 H
L=2*10^-8 H
L=4*10^-8 H
L=8*10^-8 H
L=10^-7 H
L=2*10^-7 H
λ=10^-3

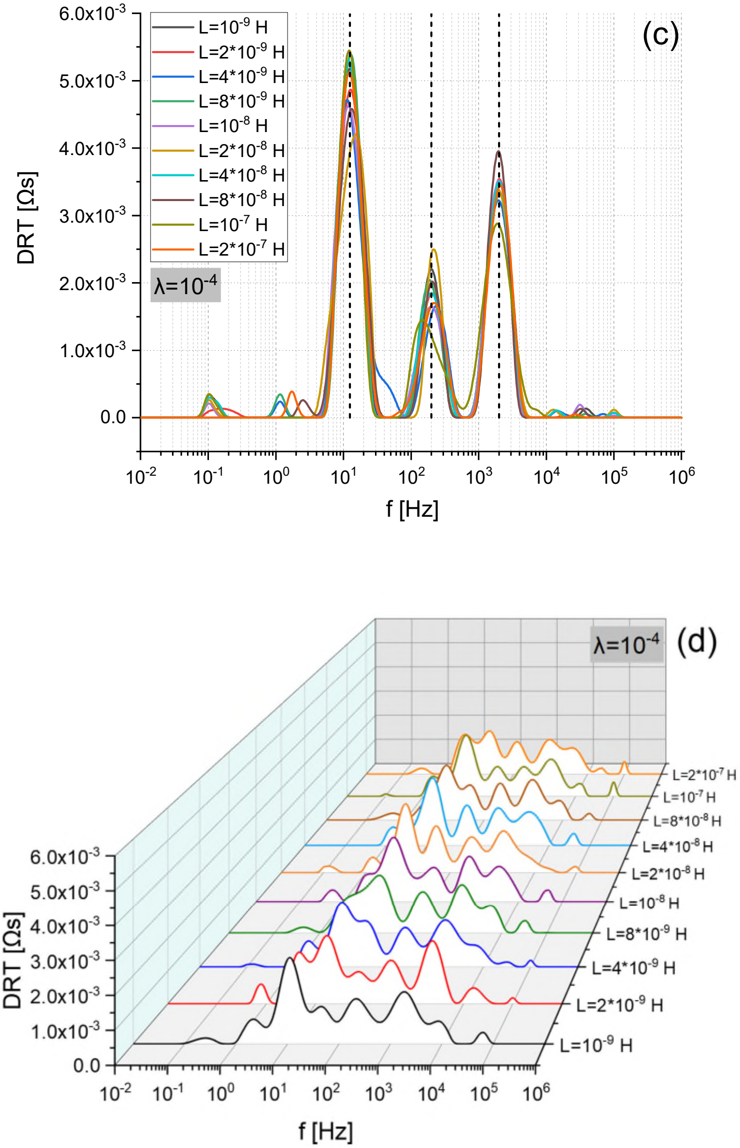

Figure 4.2.15. DRT plots for variation of the inductance. In (a) and (c) the CPE exponents of the electrochemical processes are 0. 95. In (b) and (d) the CPE exponents of electrochemical processes are 0. 75. Regularization parameter for DRT calculation is $\lambda=10^{-3}$ for (a) and (b) and $\lambda=10^{-4}$ for (c) and (d). $L = 2*10^{-9}$ H and the total polarization resistance is 10 mΩ. (100 mHz – 100 kHz, 14 ppd)

In order to confirm the statement that inductances are not causing the observed high-frequency numerical artefacts, a variation of the inductance for the case in which all CPE exponents are one is shown in Figure 4.2.16. It can be observed that no artefacts are present neither in the low- nor in the high-frequency range if no CPE effects are simulated. In such cases, also inductance values as high as $2*10^{-7}$ H do not cause numerical oscillations. Comparing this results with the Nyquist diagram shown in Figure 4.2.14, it can be stated that also tremendously high inductance values do not cause problems in the DRT calculation. This means that the inductance is potentially only contributing to numerical artefacts via causing measurement errors in the high-frequency range. As stated before, this enhancement of numerical oscillation is also only occurring if CPE effects are present. The fact that CPE effects are necessary for the formation of numerical artefacts is also evident when looking at Figure 4.2.16, as there are no artefacts or peak multiplications seen at all, although the EIS spectra are simulated with statistical errors.

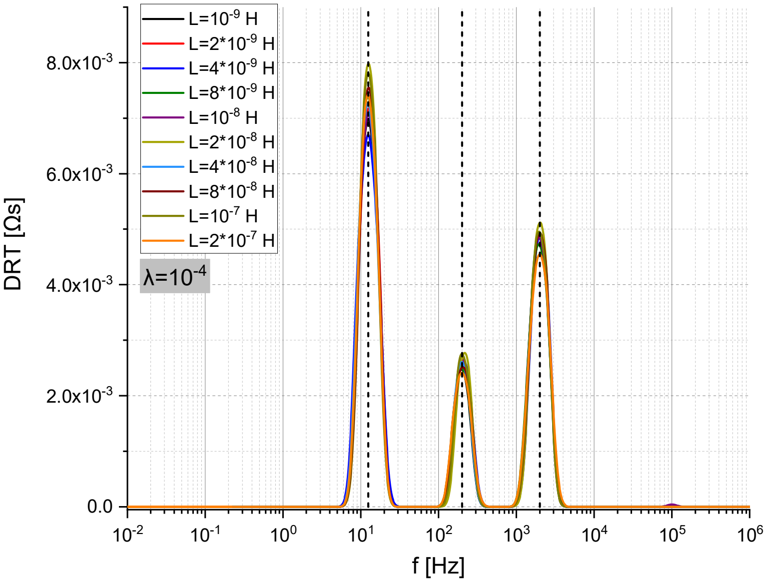

Figure 4.2.16. Comparison of different values of the inductance for the case in which all CPE exponents are one thus representing ideal RC elements. The regularization parameter is 10^{-4}. The total polarization resistance is 10 mΩ. (100 mHz – 100 kHz, 14 ppd)

A similar result is also achieved if the option “Fitting without inductance” is chosen in DRTtools. The results of the DRT calculation with this settings are shown in Figure 4.2.17. Here a peak shift of the 2000 Hz peak and to a smaller extent of the 200 Hz peak is seen with increasing values of the inductance. From this result it has to be recommended that in case of the presence of experimental inductive effects, the option “Fitting with inductance” should be chosen to achieve a higher accuracy regarding the peak positions. It also means that in principle the addition of an inductor to the DRT model is not the root cause for the observed high-frequency artefacts. By analyzing EIS spectra with different values of CPE – n3 combined with the option “Fitting without inductance”, as shown in Figure 4.2.17, this statement can be proven as the peak height of the numerical artefacts still follows the decreasing value of the CPE exponent.

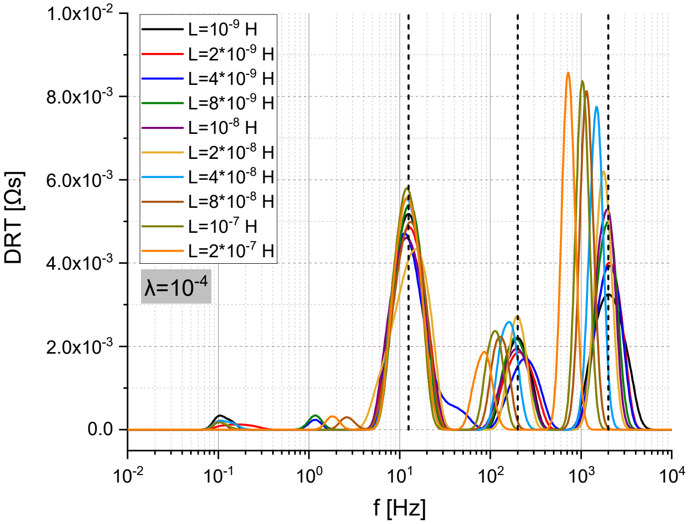

Figure 4.2.17. DRT plots with varying inductance and CPE exponents of the electrochemical processes set to 0. 95. The regularization parameter λ is 10^{-4}. For the calculation in DRTtools, the option “Fitting without inductance” was chosen for calculating the DRT. The total polarization resistance is 10 mΩ. (100 mHz – 10 kHz, 14 ppd)

Besides the proof that the handling of the inductance in DRTtools is not changing the CPE effects on the DRT, another interesting effect can be seen in Figure 4.2.18, namely that in case that the maximum frequency is only 10 kHz, the peak height of the artefact is now following the decreasing value of CPE – n3 exactly, which was not observed for simulations in the frequency range from 100 mHz to 100 kHz.

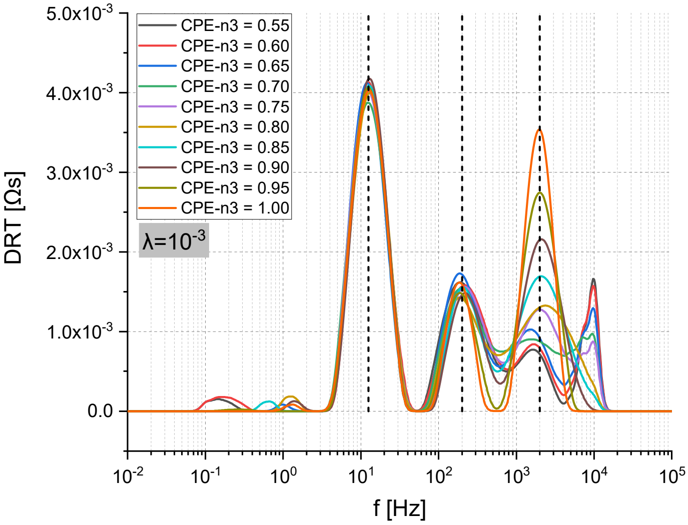

*Figure 4.2.18. DRT plots with varying the CPE exponent of the 2000 Hz process with other CPE-n fixed to 0. 95 and an inductance of 2*10^{-9} H calculated with a regularization parameter of λ=10^{-3}. For the calculation in DRTtools, the option "Fitting without inductance" was chosen. L=2*10^{-9} H and the total polarization resistance is 10 mΩ. (100 mHz – 100 kHz, 14 ppd)*

As expected from the analysis shown so far, there is no systematic contribution from the inductance seen for different maximum frequencies, as shown in Figure 4.2.19.

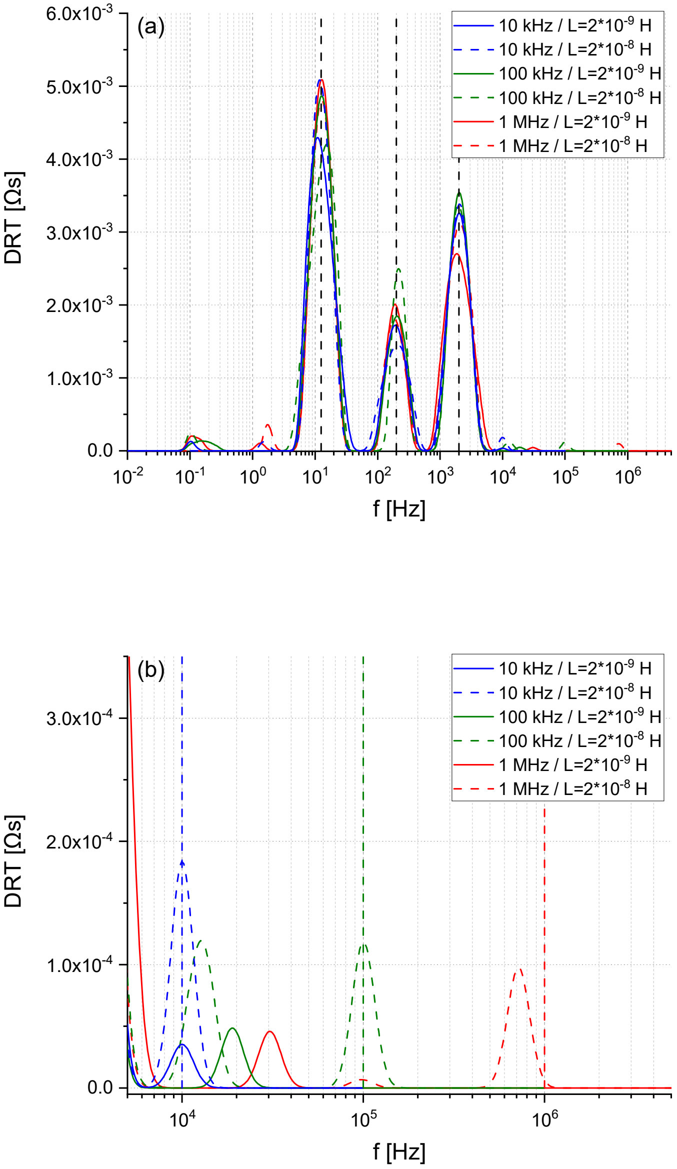

Figure 4.2.19. Comparison of DRT spectra for simulation of different frequency ranges and variation of the inductance for the entire frequency range in (a) and zoomed into the high frequency range in (b). Regularization parameter λ=10^{-4}. The CPE exponents of the remaining two processes are fixed to 0. 95. The total polarization resistance is 10 mΩ. (14 ppd). Remark: "Fitting with inductance" was chosen for DRT calculation.

The artificial peaks that are observed in the high-frequency range are due to the effect of CPE – n3 of 0. 95 which is enhanced by the statistical error. The trend to more pronounced artefacts with L = $2*10^{-8}$ H is most probably due to the higher level of statistical error on the imaginary part in the high-frequency range because of the increase of the positive imaginary parts of the impedance with increasing inductance values, as this error is scaling with the value of the imaginary part directly as $Im^* (Z) = Im (Z) + \varepsilon_0 |Im (Z)| \eta''$ (see Section 3.2).

Repeatability study error model 1

To investigate the influence of the error on the repeatability of the DRT calculation with DRTtools, a repeatability study was performed on a representative simulation set which was chosen on the basis of the results shown before in this chapter. For this study, five EIS spectra were simulated with identical parametrization of the equivalent circuit model and noise with error model 1 was added. Afterwards the EIS spectra were analyzed with DRTtools by using different values of the regularization parameter.

Table 4.2.1 contains the information about the parameters of the ECM which was used for the study. The simulation set with variation of CPE - n3 was chosen because of the high impact on the high - frequency region that has been confirmed before.

Table 4.2.1. ECM parameters for the EIS simulation of the repeatability study with error model 1

Parameter	Value
Polarization/ Ohmic resistance	10 mΩ
Inductance	$2*10^{-9}$ H
CPE exponent 12,5 Hz process	0. 95
CPE exponent 200 Hz process	0. 95
CPE exponent 2000 Hz process	0. 75
ε0	0. 5 %
points per decade	14

Figure 4.2.20 shows the DRT spectra for two different values of the maximum frequency of 10 kHz in (a) and (b) and 100 kHz in (c) and (d) with regularization parameters of $\lambda=10^{-3}$ and $\lambda=10^{-4}$.

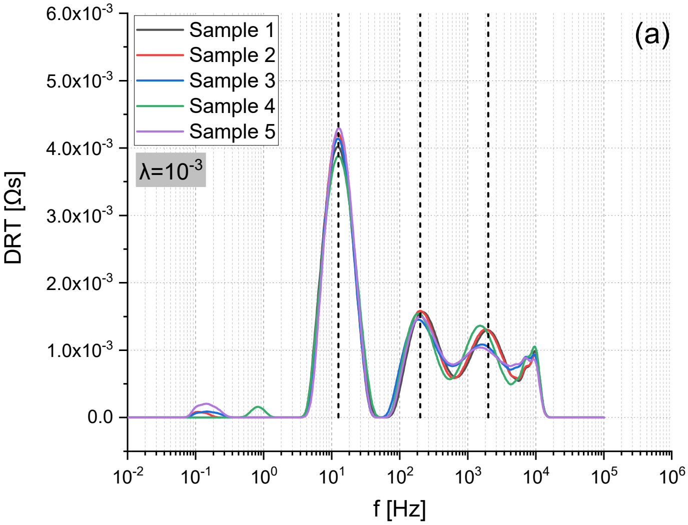
(a)
Sample 1
Sample 2
Sample 3
Sample 4
Sample 5
λ=10^-3
DRT [Ωs]
6.0x10^-3
5.0x10^-3
4.0x10^-3
3.0x10^-3
2.0x10^-3
1.0x10^-3
0.0
10^-2
10^-1
10^0
10^1
10^2
10^3
10^4
10^5
10^6
f [Hz]

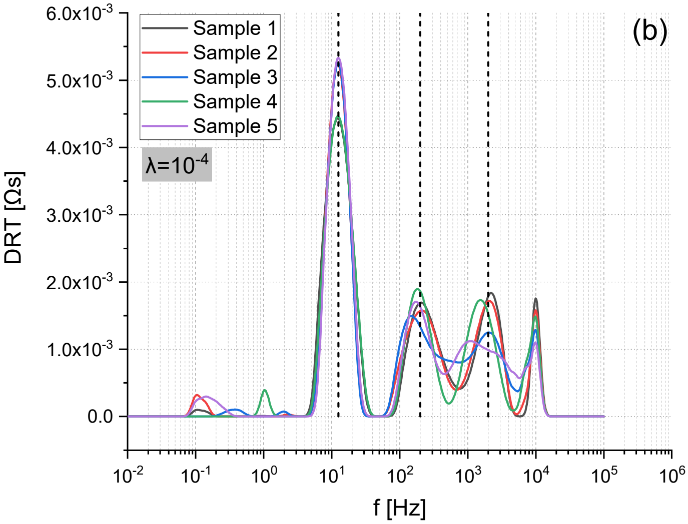
(b)
Sample 1
Sample 2
Sample 3
Sample 4
Sample 5
λ=10^-4
DRT [Ωs]
6.0x10^-3
5.0x10^-3
4.0x10^-3
3.0x10^-3
2.0x10^-3
1.0x10^-3
0.0
10^-2
10^-1
10^0
10^1
10^2
10^3
10^4
10^5
10^6
f [Hz]

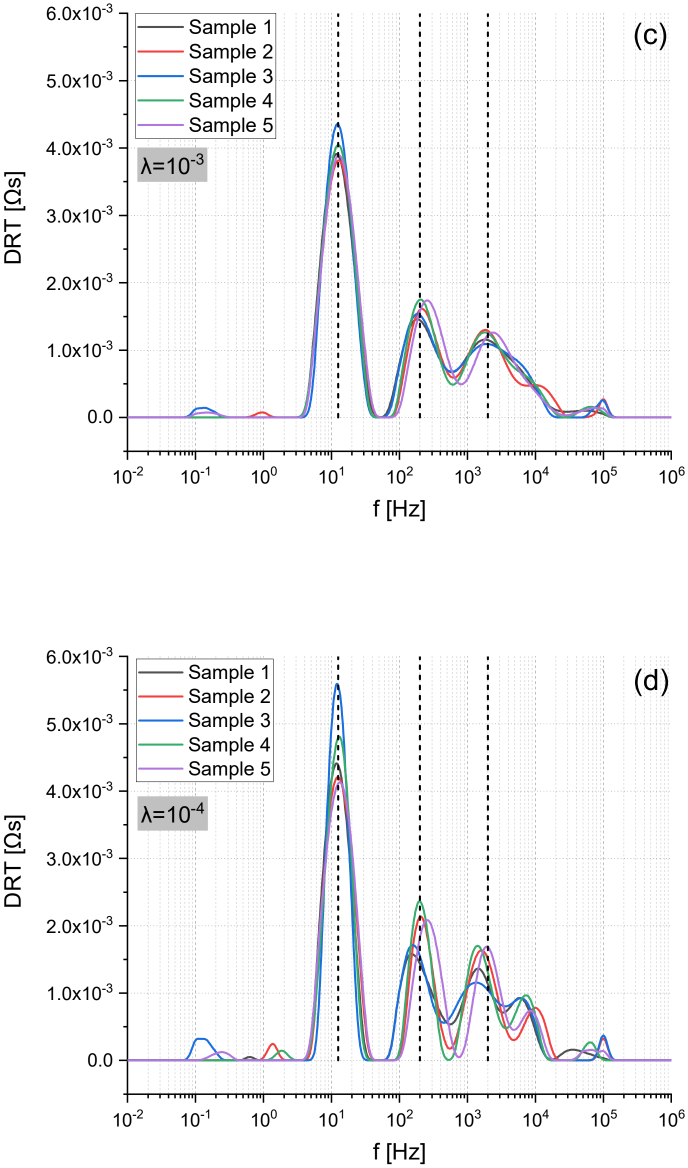

Figure 4.2.20. DRT spectra of the repeatability study for maximum frequencies of 10 kHz in (a) and (b) and 100 kHz in (c) and (d). The regularization parameter is $\lambda=10^{-3}$ *for (a) and (c) and* $\lambda=10^{-4}$ *for (b) and (d).* $L = 2*10^{-9}$ *H and the total polarization resistance is 10 mΩ. (14 pdd). All samples were simulated with identical parametrization of the ECM and statistical error according to error model 1 was added.*

The conclusion that can be drawn from these results is that the repeatability of the DRT calculation is in principle independent of the maximum frequency but strongly dependent on the regularization parameter. Another important finding is that the artefacts are influenced in an unsystematic way by the random error, which means that they are subject of changes although the parameters of the electrical model are constant. However, these differences are minimized if the value of the regularization parameter is increased, which leads to the conclusion that even from EIS measurements with significant noise level accurate DRT functions can be calculated if more than one EIS data set is available for the optimization procedure proposed by Schlüter [166], which is based on a minimization of the variance between DRT functions calculated from different EIS data sets at the same operation point. The results also confirm the statement based on the simulations shown so far for error model 1, that statistical errors can influence the appearance of high-frequency artefacts caused by the CPE.

The main conclusions that can be drawn from the simulations with error model 1 are the following:

- For DRT calculation based on EIS spectra with error model 1, roughly one magnitude higher regularization parameters have to be chosen compared to EIS simulations without statistical error to suppress the oscillations.
- Statistical errors, applied via error model 1, act as an enhancer of numerical oscillations caused by CPE behavior.
- If no CPE effects are present, the level of numerical oscillations in the DRT is very low, also for appreciable noise in the EIS spectrum
- Regarding the high-frequency artificial peaks, the statistical error influences the peak position and peak height especially for the artefacts that are located between the 2000 Hz process and the maximum frequency. This will complicate the identification of artefacts as such
- Inductive effects that increase the error on the imaginary part in the high-frequency regime do not cause numerical oscillations, even for values of L as high as $2*10^{-7}$ H. They only can act as an enhancer of CPE-based oscillations due to their impact on the error level in the high-frequency range.
- In case of choosing the option “Fitting without inductance” in DRTtools, the high-frequency peak is shifted to lower relaxation frequencies with increasing values of the inductance, but no additional artefacts are observed.

4.2.2 Simulations with error model 2

In the following chapter, the results of EIS simulations with error model 2 are presented. For this error model, the noise for both the real and imaginary part scales with the modulus of the impedance. It is frequently used in EIS simulations which can be found in the literature, for example in [127]. In comparison to the DRT calculations for ideal EIS spectra, the regularization parameter was roughly one magnitude higher to suppress the numerical oscillations caused by the simulated noise.

In Figure 4.2.21, the Kramers-Kronig residuals for the EIS simulation in the frequency range 100 mHz to 1 MHz are shown with the CPE exponent for the 12.5 Hz process is set to 0. 75 while the remaining CPE exponents are 0. 95. Compared to error model 1, the residuals for the real and imaginary part are comparable from a qualitative and quantitative point of view and are randomly distributed over the entire frequency range. Because there is no difference between different maximum frequencies seen, only the result for the simulation from 100 mHz to 1 MHz is shown. A big difference to the KKR of error model 1 is that there is no bias in the KKR of the imaginary part visible.

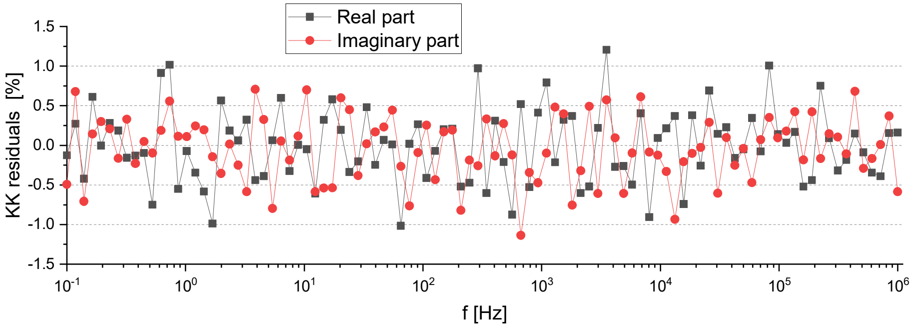

Figure 4.2.21.Kramers-Kronig residuals of the real and imaginary part of the impedance simulated with error level $\varepsilon_0 = 0.5$ *% and CPE - n1 = 0. 75 /CPE-n2, 3 = 0. 95 for the frequency range from 100 mHz to 1 MHz with 14 ppd. The inductance value is L=* $2*10^{-9}$ *H. The total polarization resistance is 10 mΩ.*

In Figure 4.2.22 (a) and (b) the KKR for the real and imaginary part are compared for the different CPE exponents of the electrochemical processes at 12. 5 Hz, 200 Hz and 2000 Hz and a higher inductance value of $2*10^{-8}$ H. As observed before in the simulations with error model 1, no influence of the CPE exponents or the inductance on the KKR for neither the real part nor the imaginary part can be observed. Interestingly, the higher inductance value does not have a significant impact on the KKR in the high-frequency range for both the real and the imaginary parts.

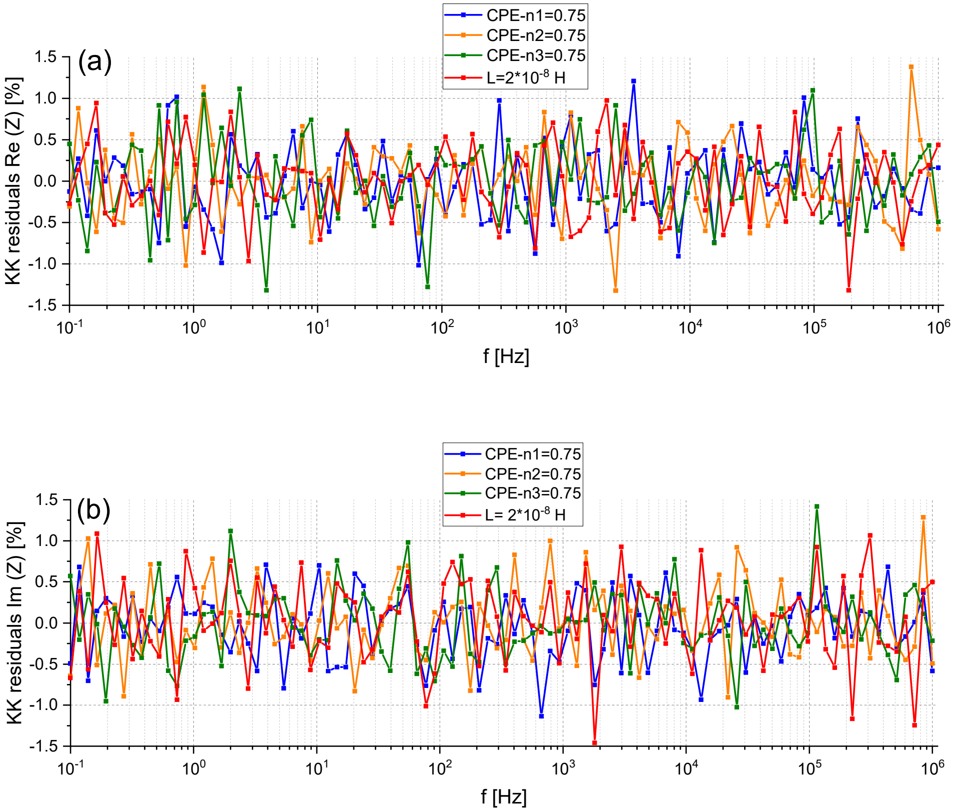

Figure 4.2.22. Comparison of Kramers-Kronig residuals for the real part in (a) and the imaginary part in (b) for simulation with different CPE exponents and inductance values in the frequency range from 100 mHz to 1 MHz with error model 2. The inductance for the CPE variations is set to $L=2*10^{-9}$ *H. The total polarization resistance is 10 mΩ. (14 ppd)*

In Figure 4.2.23, an exemplary Nyquist diagram for the variation of the CPE-n2 can be found. The CPE exponents of the remaining processes are 0. 95. Compared to the simulations with error model 1, the higher level of distortion in the EIS data is clearly visible. This is due to the fact that the KKR of the imaginary part are higher for error model 2. It can be observed that a decreasing value of the CPE – n1 leads to an increased depression of the semicircular arc in the low-frequency regime.

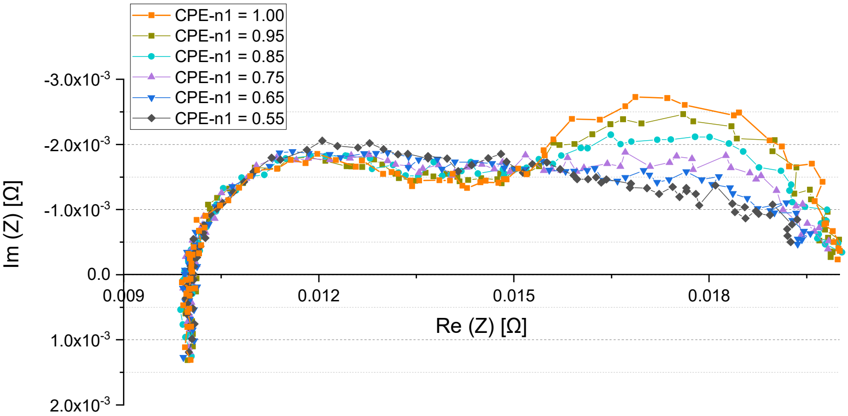

*Figure 4.2.23. Nyquist diagram for simulated EIS spectra (+ error model 2) with varying CPE-n1 values while the CPE exponents of the remaining processes are fixed to 0. 95. L = 2*10^{-9} H and the total polarization resistance is 10 mΩ. (100 mHz – 100 kHz, 14 ppd).*

In Figure 4.2.24, the DRT results for simulation of different values of the CPE exponent of the 12. 5 Hz process (CPE – n1) are shown for a frequency range from 100 mHz to 100 kHz of the underlying EIS data set. As already observed for the simulations with error model 1, the numerical oscillations are mostly confined to the frequency range of the process exhibiting a low value of the CPE exponent. It is also obvious that low regularization parameters of 10^{-4} are not able to suppress numerical oscillations in a sufficient manner to achieve reasonable DRT results. In the extent to which the CPE exponents decrease from one, the numerical oscillations increase as well. From this it can be concluded that with decreasing CPE exponent, the value of the regularization parameter has to be increased to achieve a low oscillation level.

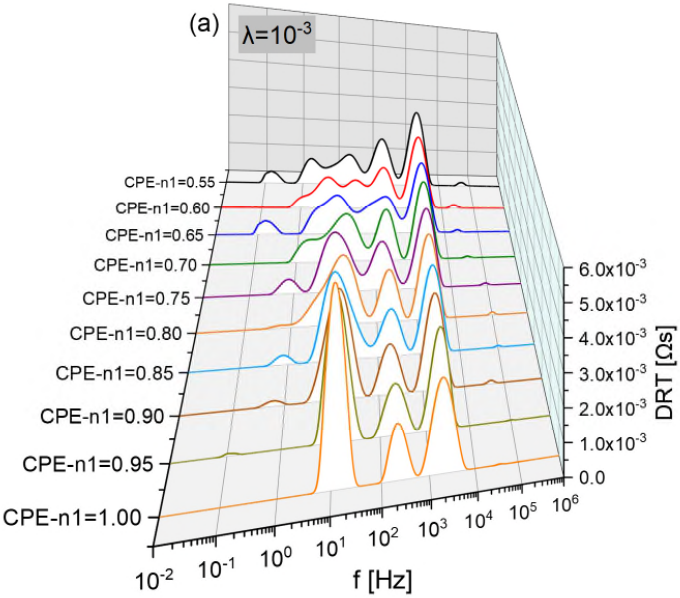
(a)
λ=10^{-3}
CPE-n1=0.55
CPE-n1=0.60
CPE-n1=0.65
CPE-n1=0.70
CPE-n1=0.75
CPE-n1=0.80
CPE-n1=0.85
CPE-n1=0.90
CPE-n1=0.95
CPE-n1=1.00
6.0x10^{-3}
5.0x10^{-3}
4.0x10^{-3}
3.0x10^{-3}
2.0x10^{-3}
1.0x10^{-3}
0.0
DRT [Ωs]
10^{-2}
10^{-1}
10^{0}
10^{1}
10^{2}
10^{3}
10^{4}
10^{5}
10^{6}
f [Hz]

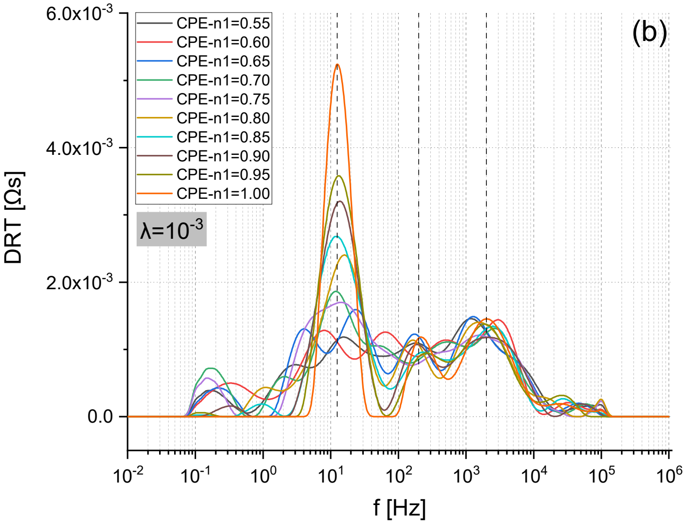
(b)
CPE-n1=0.55
CPE-n1=0.60
CPE-n1=0.65
CPE-n1=0.70
CPE-n1=0.75
CPE-n1=0.80
CPE-n1=0.85
CPE-n1=0.90
CPE-n1=0.95
CPE-n1=1.00
λ=10^{-3}
6.0x10^{-3}
4.0x10^{-3}
2.0x10^{-3}
0.0
DRT [Ωs]
10^{-2}
10^{-1}
10^{0}
10^{1}
10^{2}
10^{3}
10^{4}
10^{5}
10^{6}
f [Hz]

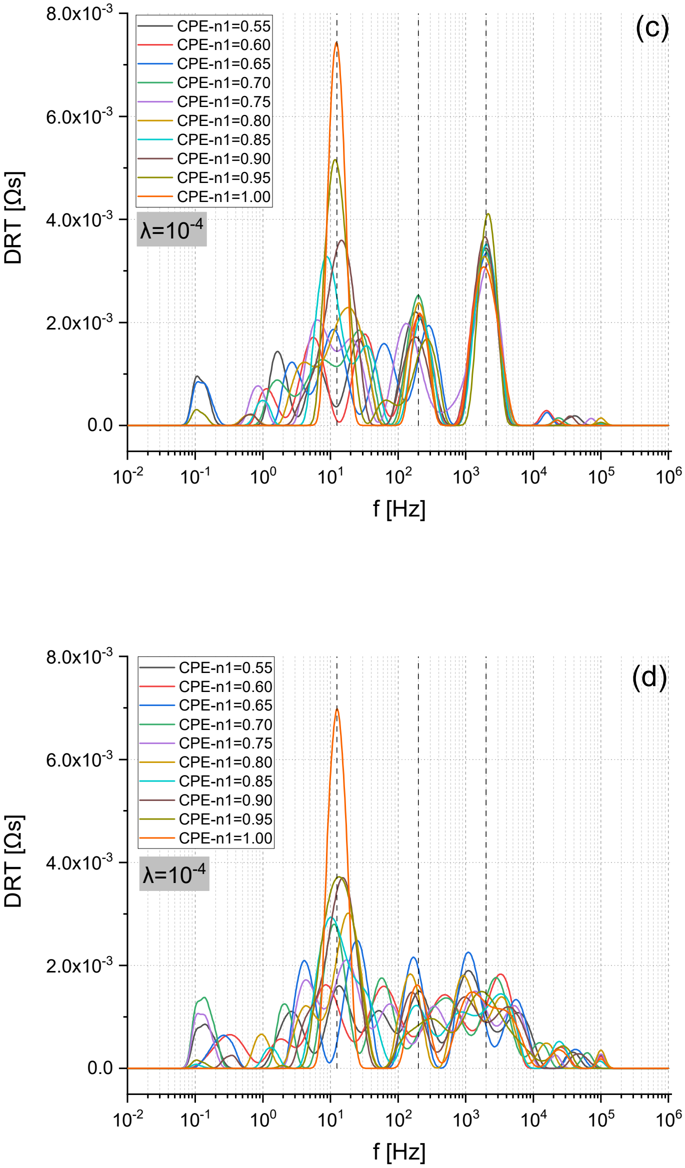

Figure 4.2.24. DRT plots for variation of the CPE exponent of the electrochemical process at a relaxation frequency of 12. 5 Hz. In (a) and (c) the CPE exponents of the other processes are 0. 95. In (b) and (d) the CPE exponents of the other processes are 0. 75. Regularization parameter for DRT calculation is $\lambda=10^{-3}$ *for (a) and (b) and* $\lambda=10^{-4}$ *for (c) and (d).* $L=2*10^{-9}$ *H and the total polarization resistance is 10 mΩ. (100 mHz – 100 kHz, 14 ppd)*

As observed in the simulations based on ideal EIS spectra and EIS spectra with error model 1, the oscillations spread more into the adjacent frequency regimes if the regularization parameter is reduced, which can be observed in Figure 4.2.24 (a) and (c). Regarding the higher degree of peak multiplication in the low-frequency range with a decreasing CPE – n1, the results show the same trend as the simulations with no error and error model 1, meaning an increased tendency for peak multiplication with a decreasing CPE exponent. Furthermore, low values of all CPE exponents especially in combination with low regularization parameters lead to severe numerical oscillations, as can be observed in Figure 4.2.24 (d).

Looking at the results for different maximum frequencies and CPE exponents for the 12. 5 Hz process, no systematic correlation between the maximum frequency and the value of CPE – n2 can be seen, as shown in Figure 4.2.25. As stated before, the decreased CPE exponent of the low-frequency process is causing numerical oscillation and resulting peak multiplication in the low-frequency regime but no systematic impact on the high-frequency oscillations can be observed.

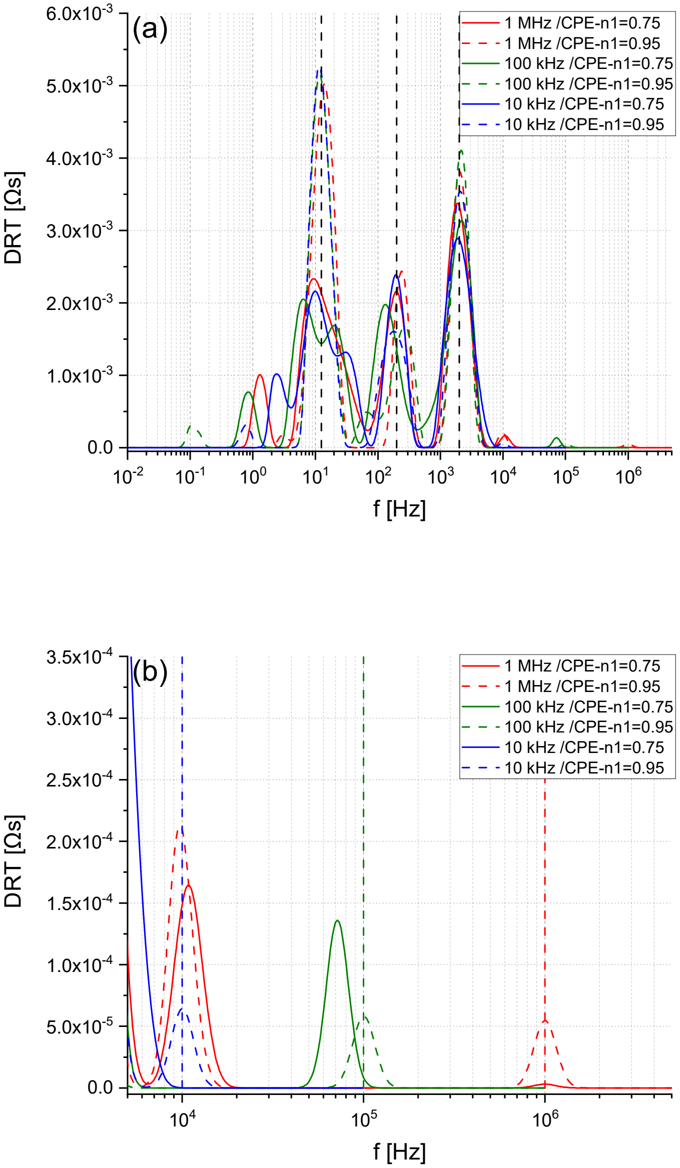

Figure 4.2.25. Comparison of DRT spectra for simulation of different frequency ranges and variation of CPE exponent for the 12. 5 Hz process (CPE-n1) for the entire frequency range in (a) and zoomed into the high frequency range in (b). Regularization parameter $\lambda=10^{-4}$. The CPE exponents of the remaining two processes are fixed to 0. 95. $L = 2*10^{-9}$ H and the total polarization resistance is 10 mΩ. (14 ppd)

In order to underpin this statement, the DRT was also calculated for the case in which all remaining CPE exponents are one. The result is shown in Figure 4.2.26. In this case only one artificial peak at 1 MHz can be observed with a very small peak height only.

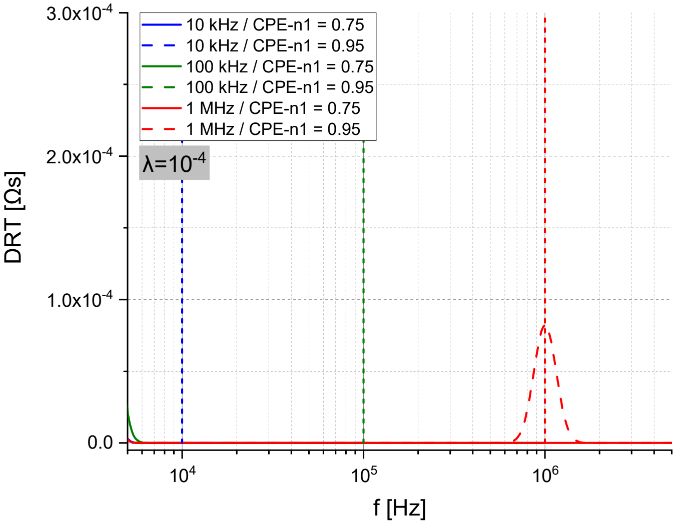

*Figure 4.2.26. Comparison of DRT spectra for simulation of different frequency ranges and variation of CPE exponent in the low- frequency range (CPE-n1). Regularization parameter λ=10^{-4}. The CPE exponents of the other processes are 1. 00. L = 2*10^{-9} H and the total polarization resistance is 10 mΩ. (14 ppd)*

In Figure 4.2.27, the Nyquist diagram for EIS simulated with different values of the CPE-n2 are shown. The CPE exponents of the remaining processes are 0. 95. Again the degree of data distortion is higher compared to error model 1. The decreasing CPE – n2 causes a covering of the mid-frequency process in the complex plane.

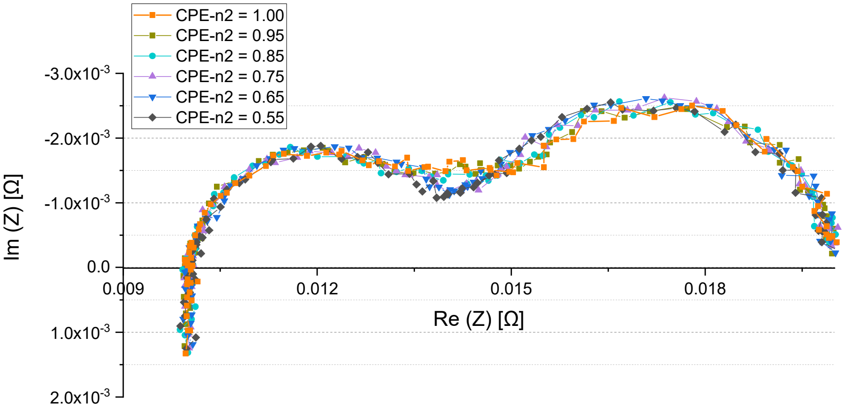

*Figure 4.2.27. Nyquist diagram for simulated EIS spectra (+ error model 2) with varying CPE-n2 values while the CPE exponents of the remaining processes are fixed to 0. 95. L = 2*10^{-9} H and the total polarization resistance is 10 mΩ. (100 mHz – 100 kHz, 14 ppd).*

In Figure 4.2.28, where the DRT results for the variation of CPE – n2 are shown, it is observable that comparable results to ideal EIS simulations and simulations with error model 1 are achieved. Oscillations, peak depression and peak multiplication effects are mostly confined to the frequency range around the relaxation frequency of the 200 Hz process with small impact to the high-frequency artefacts. The tendency for numerical instability is increasing with increasing number of processes with noticeable CPE behavior, as can be observed in Figure 4.2.28 (b) and (d) with the CPE exponents of the remaining processes are decreased to 0. 75. As observed in the simulations with error model 1, the error enhances the CPE effects. Again the degree of peak multiplication in the 200 Hz range is not following the decreasing CPE – n2 exactly.

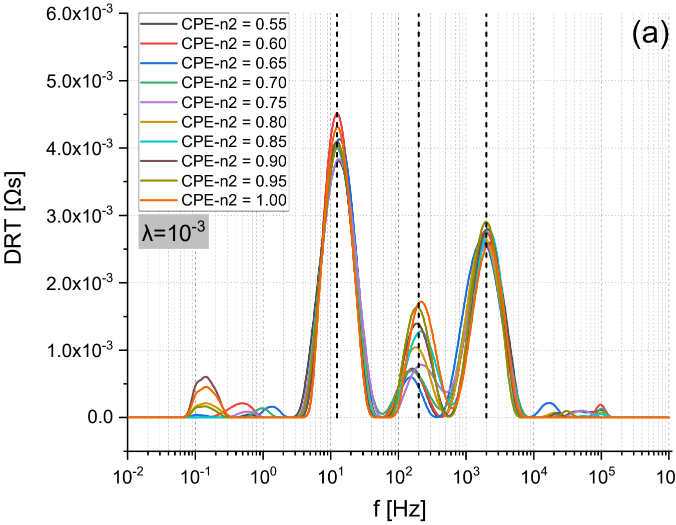
6.0x10^{-3}
5.0x10^{-3}
4.0x10^{-3}
3.0x10^{-3}
2.0x10^{-3}
1.0x10^{-3}
0.0
DRT [Ωs]
CPE-n2 = 0.55
CPE-n2 = 0.60
CPE-n2 = 0.65
CPE-n2 = 0.70
CPE-n2 = 0.75
CPE-n2 = 0.80
CPE-n2 = 0.85
CPE-n2 = 0.90
CPE-n2 = 0.95
CPE-n2 = 1.00
λ=10^{-3}
(a)
10^{-2}
10^{-1}
10^{0}
10^{1}
10^{2}
10^{3}
10^{4}
10^{5}
10^{6}
f [Hz]

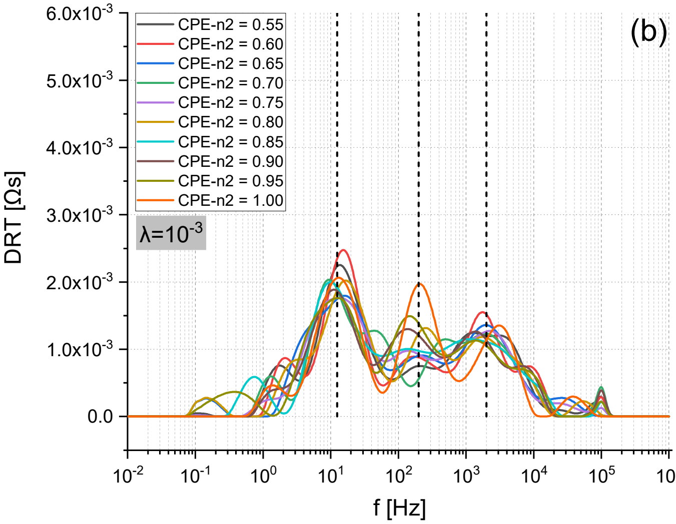
6.0x10^{-3}
5.0x10^{-3}
4.0x10^{-3}
3.0x10^{-3}
2.0x10^{-3}
1.0x10^{-3}
0.0
DRT [Ωs]
CPE-n2 = 0.55
CPE-n2 = 0.60
CPE-n2 = 0.65
CPE-n2 = 0.70
CPE-n2 = 0.75
CPE-n2 = 0.80
CPE-n2 = 0.85
CPE-n2 = 0.90
CPE-n2 = 0.95
CPE-n2 = 1.00
λ=10^{-3}
(b)
10^{-2}
10^{-1}
10^{0}
10^{1}
10^{2}
10^{3}
10^{4}
10^{5}
10^{6}
f [Hz]

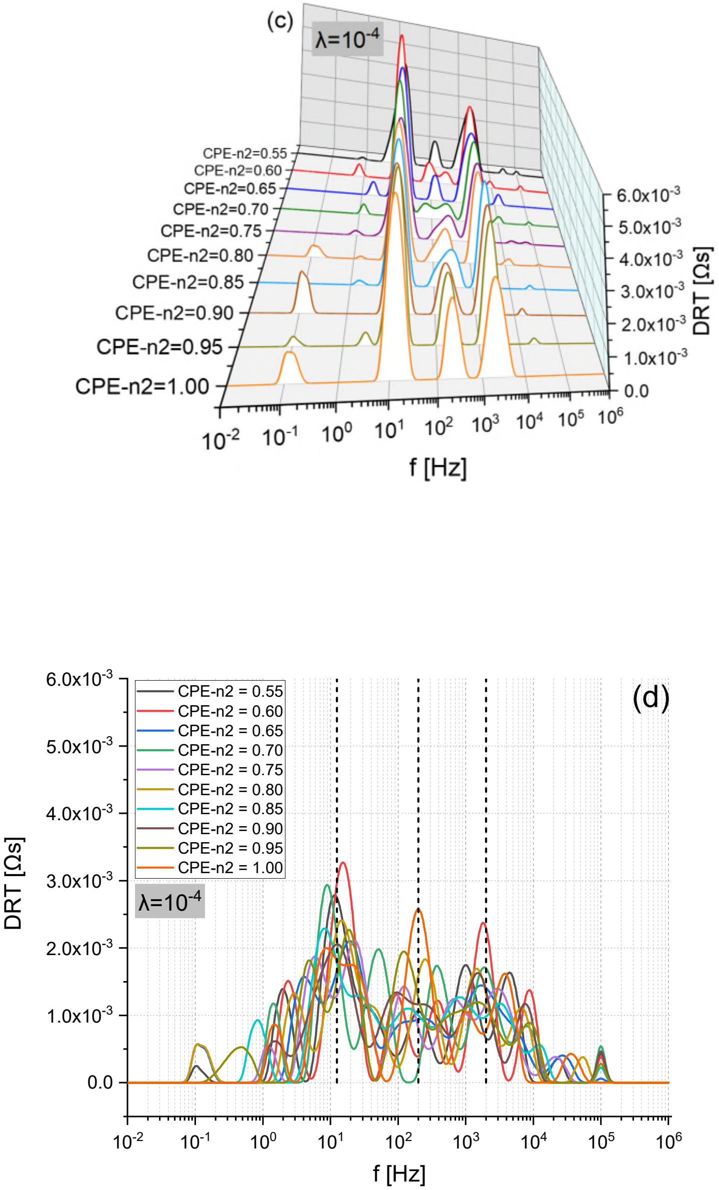

Figure 4.2.28. DRT plots for variation of the CPE exponent of the electrochemical process at a relaxation frequency of 200 Hz. In (a) and (c) the CPE exponents of the other processes are 0. 95. In (b) and (d) the CPE exponents of the other processes are 0. 75. Regularization parameter for DRT calculation is $\lambda=10^{-3}$ *for (a) and (b) and* $\lambda=10^{-4}$ *for (c) and (d).* $L=2*10^{-9}$ *H and the total polarization resistance is 10 mΩ. (100 mHz – 100 kHz, 14 ppd)*

Regarding the effect of CPE - n2 together with the maximum frequency of the underlying EIS data set on the expression of high-frequency artefacts, which is shown in Figure 4.2.29, there is no systematic relationship of the CPE – n2 with the maximum frequency observable. As shown in the simulation with error model 1, there is no systematic impact of the CPE – n2 on the high-frequency artefacts. For higher maximum frequencies, additional artificial peaks between f_{max} and the 2000 Hz process are seen, which exhibit the potential of misinterpretation as real electrochemical processes in experimental studies. These results point at an impact of the statistical error on the expression of the artificial peaks by shifting them to a frequency between the highest electrochemical relaxation process and the maximum frequency, which emphasizes the importance of high-quality EIS data for performing a reliable DRT analysis.

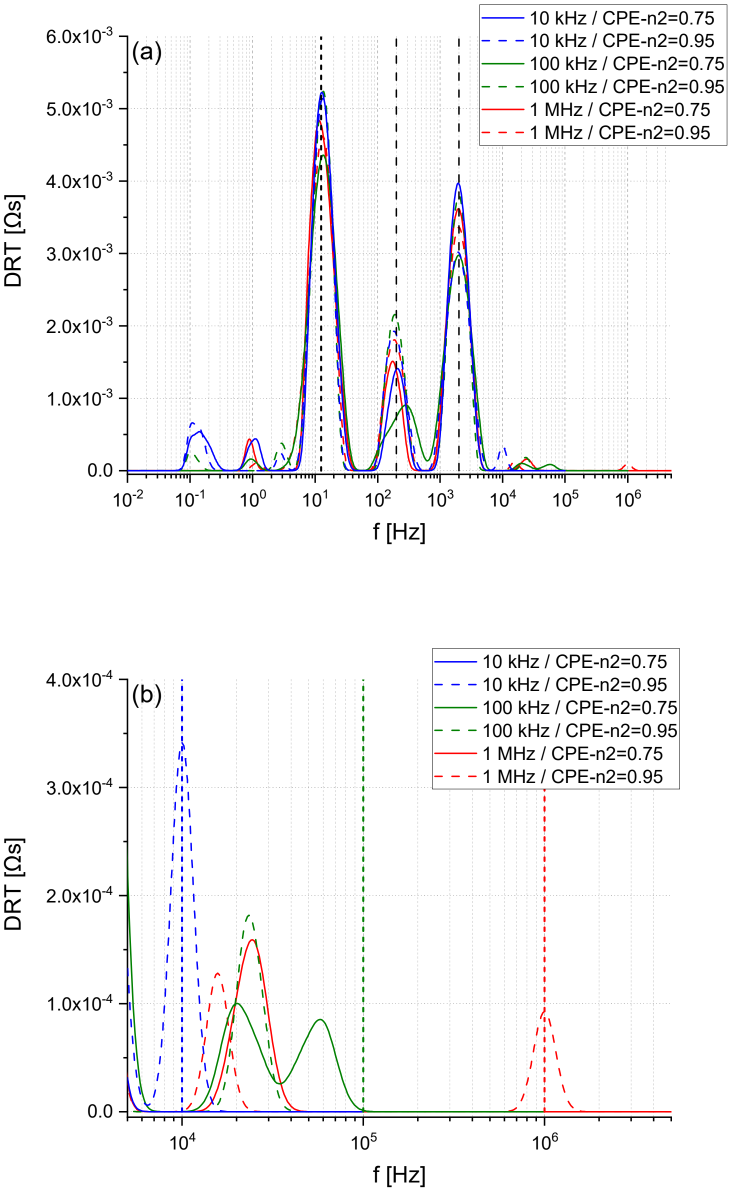

Figure 4.2.29. Comparison of DRT spectra for simulation of different frequency ranges and variation of CPE exponent for the 200 Hz process for the entire frequency range in (a) and zoomed into the high frequency range in (b). Regularization parameter $\lambda=10^{-4}$*. The CPE exponents of the remaining two processes are fixed to 0. 95.* $L = 2*10^{-9}$ *H and the total polarization resistance is 10 mΩ. (14 ppd)*

In order to check the interplay of CPE – n2 with CPE – n3 regarding the high-frequency artificial peaks, the combinations of maximum frequency and CPE – n2 in case that the remaining CPE exponents are one, is shown in Figure 4.2.30. Compared with the results for the variation of CPE – n1, there are fairly more artefacts visible in the DRT underlining the finding from before that the CPE – n2 has a greater influence on the high-frequency artefacts compared to CPE – n1. A comparison with the results from the simulations with error model 1, it can be stated that with error model 2 - which exhibits a higher level of KKR due to the scaling with the modulus of the impedance – the artefacts in the high frequency regime are more pronounced. This can be due to the additional higher error on the imaginary part, which also points into the direction that parasitic inductances can potentially cause oscillations in the high-frequency regime indirectly via increasing the measurement error. Although there is a trend to a higher degree of numerical oscillation in the high-frequency range for CPE – n2 lower than one compared to CPE – n1 are lower than one, it is evident from Figure 4.2.30, that the effect is not of systematic nature.

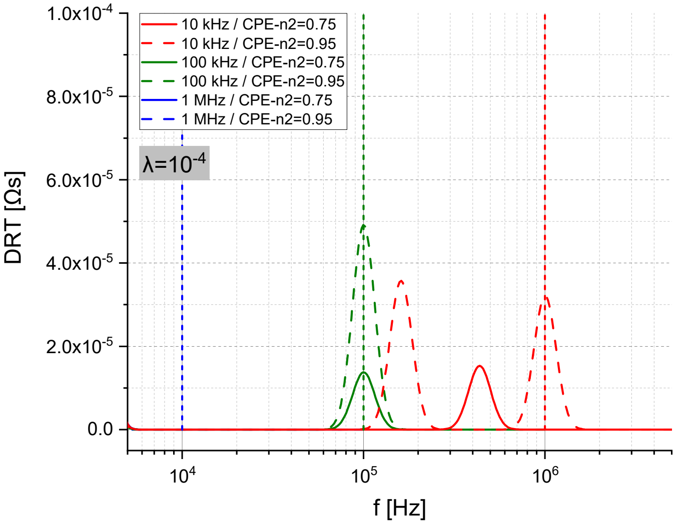

*Figure 4.2.30. Comparison of DRT spectra for simulation of different frequency ranges and variation of CPE exponent in the mid- frequency range (CPE-n2) zoomed into the high frequency range. Regularization parameter λ=10^{-4}. The CPE exponents of the other processes are 1. 00. L = 2*10^{-9} H and the total polarization resistance is 10 mΩ. (14 ppd)*

In Figure 4.2.31, the simulation results based on EIS spectra simulated from 100 mHz to 10 kHz with different values of the CPE - n2, are shown. It can be observed that the maximum frequency artefact shows a slight tendency to increase with decreasing CPE exponent of the 200 Hz process. Comparing these results with the simulations based on ideal EIS spectra, a clear impact of the statistical error on the expression of the artefacts can be stated, based on the fact that for ideal EIS spectra the peak height is following the decreasing CPE – n2 perfectly, whereas with statistical error the correlation is not that clear anymore. The oscillations which are visible in the low-frequency range show no systematic correlation to the magnitude of the CPE – n2.

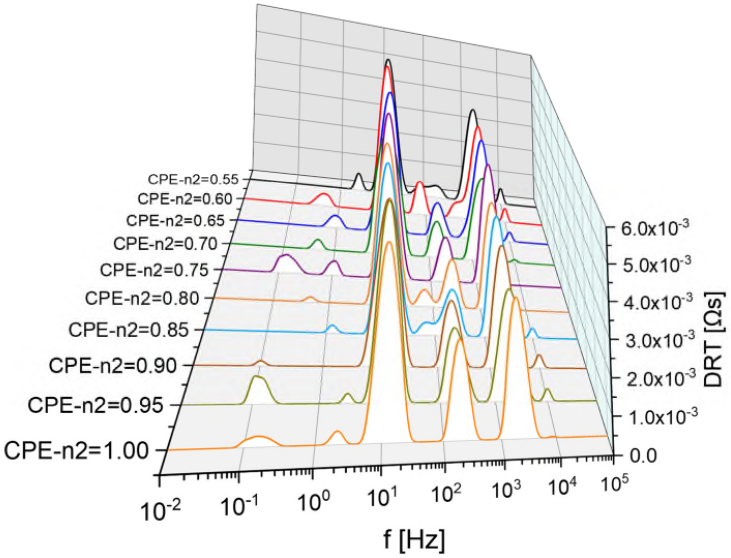

Figure 4.2.31. DRT plots for the variation of CPE-n2 and simulation in the frequency range 100 mHz to 10 kHz. The regularization parameter is 10^{-4}. CPE exponents of the remaining processes are fixed to 0. 95 and the inductance is L= $2*10^{-9}$ H. The total polarization resistance is 10 mΩ. (14 ppd).

In Figure 4.2.32, the Nyquist diagram for simulated EIS spectra with different values of the CPE exponent of the 2000 Hz process (CPE-n3) are shown. The CPE exponents of the remaining processes are 0. 95. Here, the increasing degree of depression of the semicircular arc in the high-frequency regime with decreasing value of CPE – n3 can be observed. Additionally, lower CPE exponents of the 2000 Hz process lead to an increased value of the x-axis intersection.

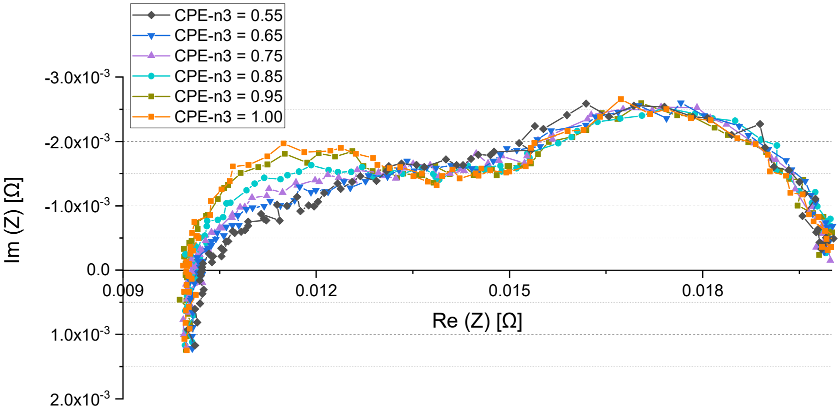

*Figure 4.2.32. Nyquist diagram for simulated EIS spectra (+ error model 2) with varying CPE-n3 values while the CPE exponents of the remaining processes are fixed to 0. 95. L = 2*10^{-9} H and the total polarization resistance is 10 mΩ. (100 mHz – 100 kHz, 14 ppd).*

In Figure 4.2.33, the DRT results for the simulation series with varying the CPE exponent of the 2000 Hz process (CPE – n3) are shown for EIS simulations in the frequency range from 100 mHz to 100 kHz. The impact of this frequency dispersion on the characteristic high-frequency artificial peak is fairly obvious, but the peak height is not following the CPE exponent exactly, as already shown in the simulations with error model 1, underlining the impact of the statistical error. However, it can be observed that the statistical error alone, in cases in which the CPE – n3 is one, is not causing numerical oscillations. This again emphasizes the fact that the origin of the high-frequency artificial peaks is the frequency dispersion behavior of electrochemical processes exhibiting a high relaxation frequency. As shown in the simulations with error model 1, the numerical oscillations are mostly confined to the frequency range in which processes with noticeable CPE behavior are located. If more than one process exhibits significant CPE behavior, the oscillations spread over the entire frequency range, which can be observed in Figure 4.2.33 (b) and (d).

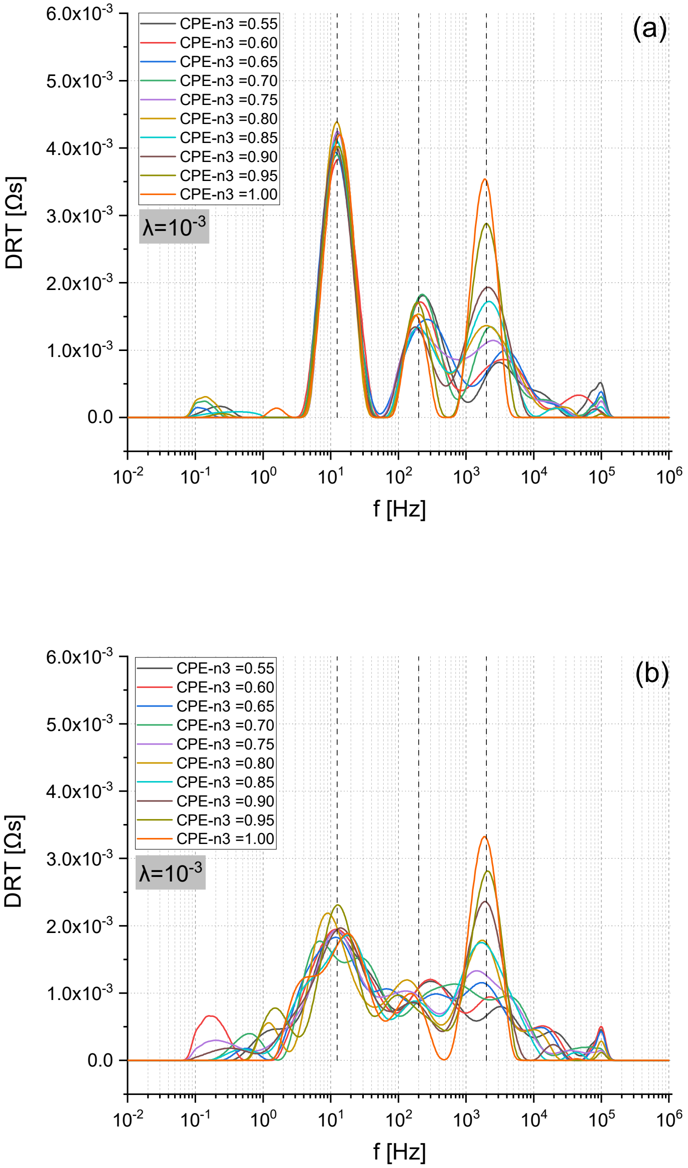
(a)
(b)
CPE-n3 =0.55
CPE-n3 =0.60
CPE-n3 =0.65
CPE-n3 =0.70
CPE-n3 =0.75
CPE-n3 =0.80
CPE-n3 =0.85
CPE-n3 =0.90
CPE-n3 =0.95
CPE-n3 =1.00
λ=10^-3
DRT [Ωs]
0.0
1.0x10^-3
2.0x10^-3
3.0x10^-3
4.0x10^-3
5.0x10^-3
6.0x10^-3
f [Hz]
10^-2
10^-1
10^0
10^1
10^2
10^3
10^4
10^5
10^6

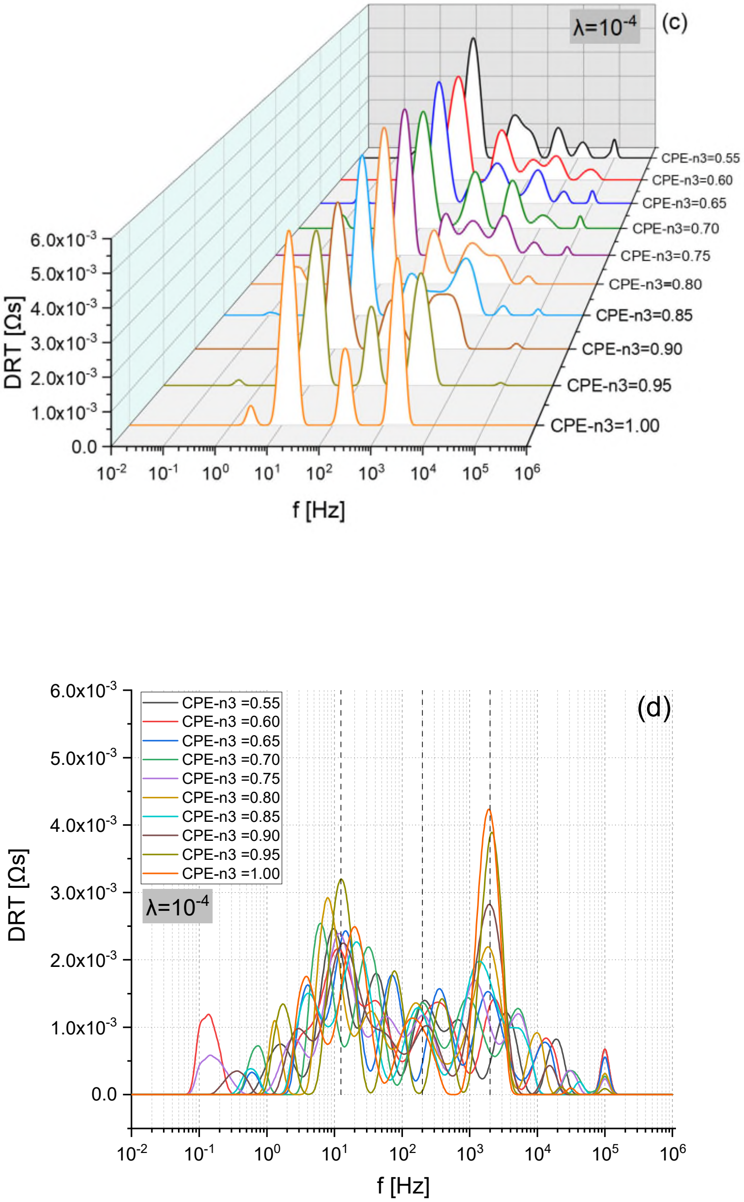

Figure 4.2.33. DRT plots for variation of the CPE exponent of the electrochemical process at a relaxation frequency of 2000 Hz. In (a) and (c) the CPE exponents of the other processes are 0. 95. In (b) and (d) the CPE exponents of the other processes are 0. 75. Regularization parameter for DRT calculation is $\lambda=10^{-3}$ *for (a) and (b) and* $\lambda=10^{-4}$ *for (c) and (d).* $L=2*10^{-9}$ *H and the total polarization resistance is 10 mΩ. (100 mHz – 100 kHz, 14 ppd)*

When the EIS simulation is conducted in the frequency range from 100 mHz to 10 kHz, the peak height of the characteristic peak is following the value of the CPE exponent exactly, as shown in Figure 4.2.34. Furthermore, an increasing peak multiplication with decreasing CPE – n3 is evident. Combining these results with the ones shown before for the variation of CPE - n2, it can be concluded that the higher the maximum frequency or the greater the frequency distance between the high frequency electrochemical process and the maximum frequency, the higher is the potential influence of the statistical error on the high frequency artefacts. This means that experimental EIS measurements starting from higher frequencies are no guarantee for a reliable DRT analysis as they are more heavily affected by measurement errors.

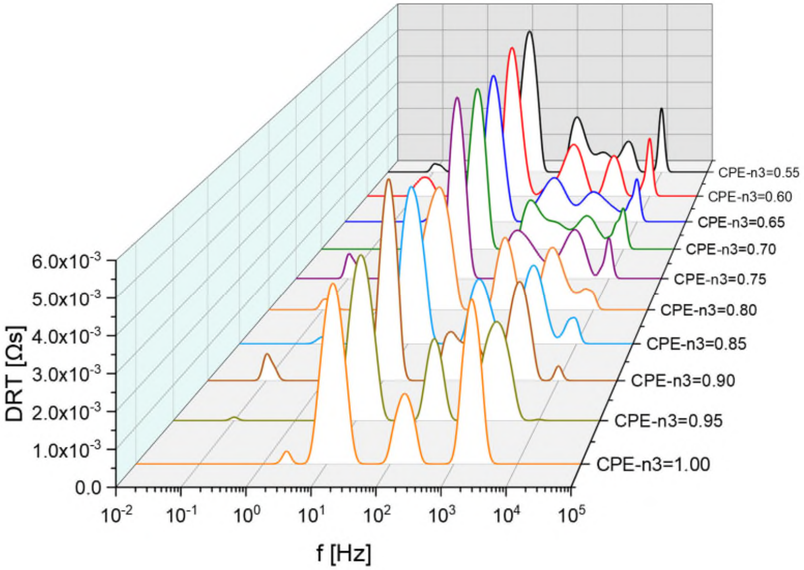

Figure 4.2.34. DRT plots for the variation of CPE-n3 and simulation in the frequency range 100 mHz to 10 kHz. The regularization parameter is 10^{-4}. CPE exponents of the remaining processes is fixed to 0, 95 and the inductance is L= $2*10^{-9}$ H. The total polarization resistance is 10 mΩ. (14 ppd).

Comparing the DRT spectra for variation of the maximum frequency in the EIS spectrum together with CPE - n3, as shown in Figure 4.2.35, a similar result as for the simulations with error model 1 is obtained, namely a systematic correlation of the characteristic high-frequency artefact with the maximum frequency and the frequency dispersion of the 2000 Hz process.

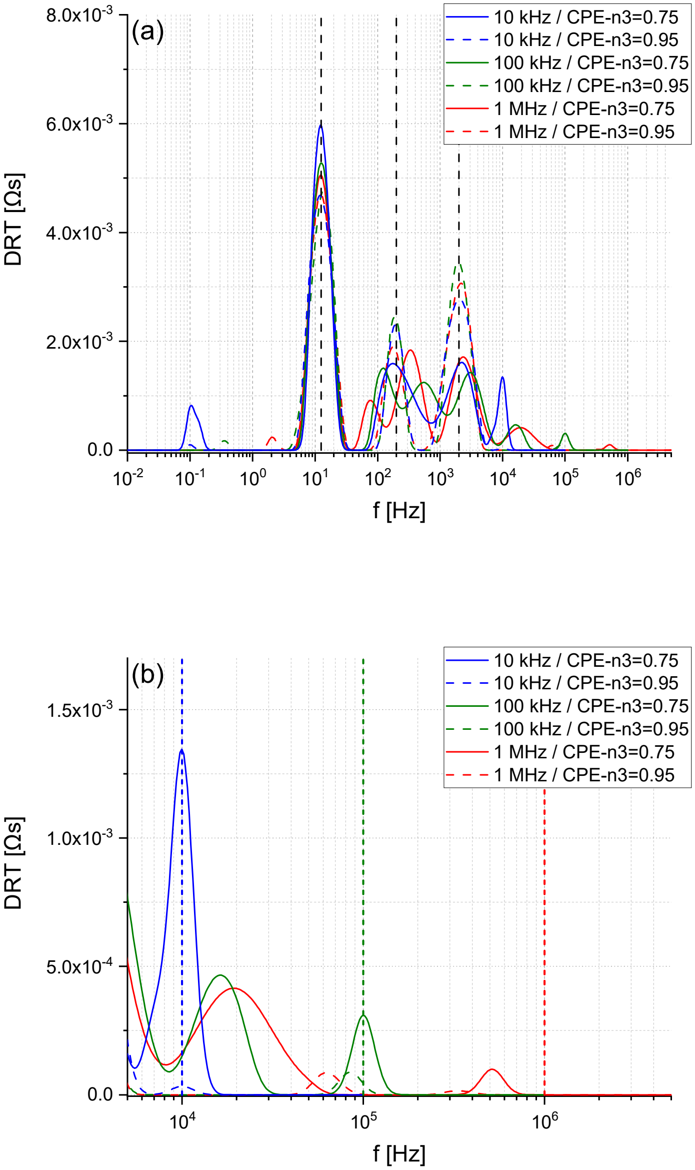

*Figure 4.2.35. Comparison of DRT spectra for simulation of different frequency ranges and variation of CPE exponent for the 2000 Hz process for the entire frequency range in (a) and zoomed into the high frequency range in (b). Regularization parameter λ=10^{-4}. The CPE exponents of the remaining two processes are fixed to 0. 95. L = 2*10^{-9} H and the total polarization resistance is 10 mΩ. (14 ppd)*

However, if the maximum frequency is 100 kHz or 1 MHz, additional artefacts between the electrochemical process and the artefact arise which bear the risk of being interpreted as real electrochemical processes. The peak height of those additional artefacts is correlating with a decreasing CPE – n3.

Finally in Figure 4.2.36, the Nyquist plot for simulated EIS spectra with different values of the inductance are shown. The CPE exponents of all electrochemical processes is 0. 95. Only inductance values up to 4*10^{-8} H are shown, as higher values of the inductance would cover the data in the range of negative imaginary parts of the impedance. Based on this figure, it can be seen that very high values of the inductance were simulated in the present study.

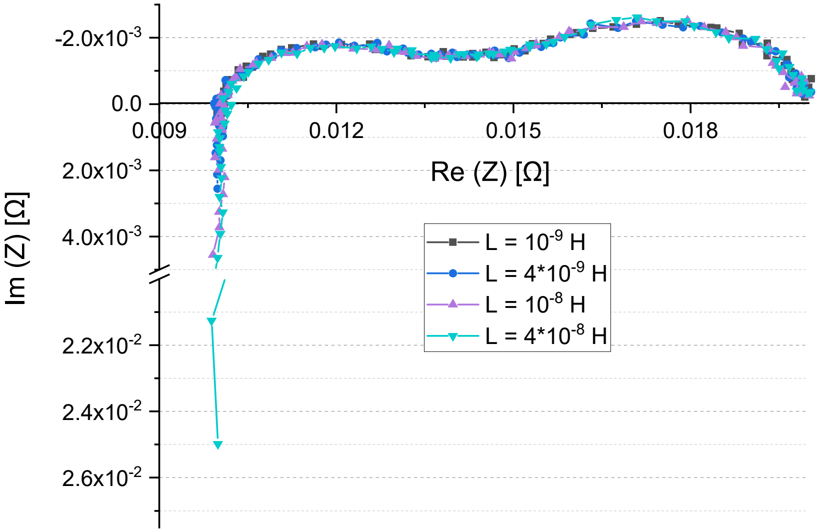

Figure 4.2.36. Nyquist diagram for simulated EIS spectra (+ error model 1) with varying inductance values while the CPE exponents of all processes are fixed to 0. 95. The total polarization resistance is 10 mΩ. (100 mHz – 100 kHz, 14 ppd). Remark: The x- and y-axis scales are not linked 1:1 for better visibility of the semicircles.

In Figure 4.2.37, the DRT results for the simulation series with varying inductance values are shown for EIS simulations with error model 2.

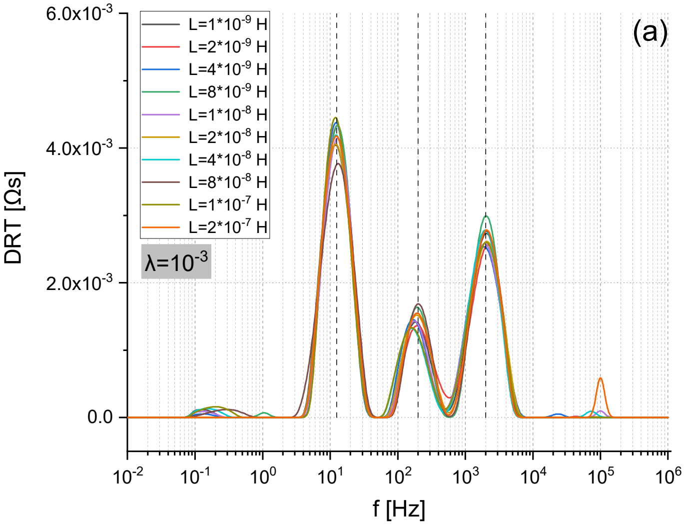
(a)
DRT [Ωs]
6.0x10^{-3}
4.0x10^{-3}
2.0x10^{-3}
0.0
f [Hz]
10^{-2}
10^{-1}
10^{0}
10^{1}
10^{2}
10^{3}
10^{4}
10^{5}
10^{6}
L=1*10^{-9} H
L=2*10^{-9} H
L=4*10^{-9} H
L=8*10^{-9} H
L=1*10^{-8} H
L=2*10^{-8} H
L=4*10^{-8} H
L=8*10^{-8} H
L=1*10^{-7} H
L=2*10^{-7} H
λ=10^{-3}

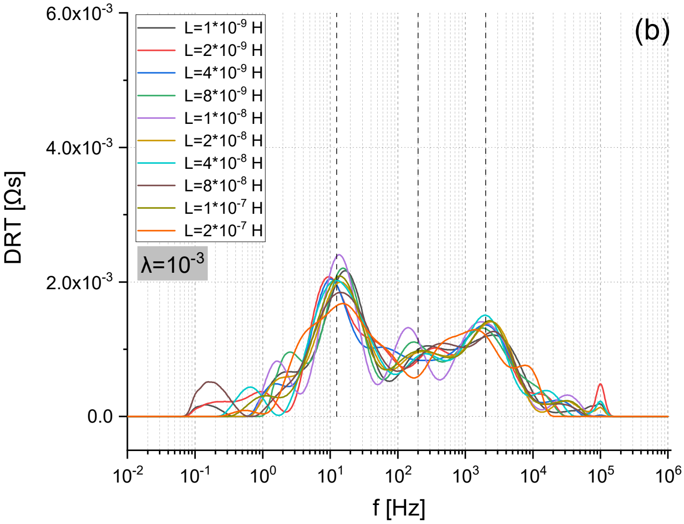
(b)
DRT [Ωs]
6.0x10^{-3}
4.0x10^{-3}
2.0x10^{-3}
0.0
f [Hz]
10^{-2}
10^{-1}
10^{0}
10^{1}
10^{2}
10^{3}
10^{4}
10^{5}
10^{6}
L=1*10^{-9} H
L=2*10^{-9} H
L=4*10^{-9} H
L=8*10^{-9} H
L=1*10^{-8} H
L=2*10^{-8} H
L=4*10^{-8} H
L=8*10^{-8} H
L=1*10^{-7} H
L=2*10^{-7} H
λ=10^{-3}

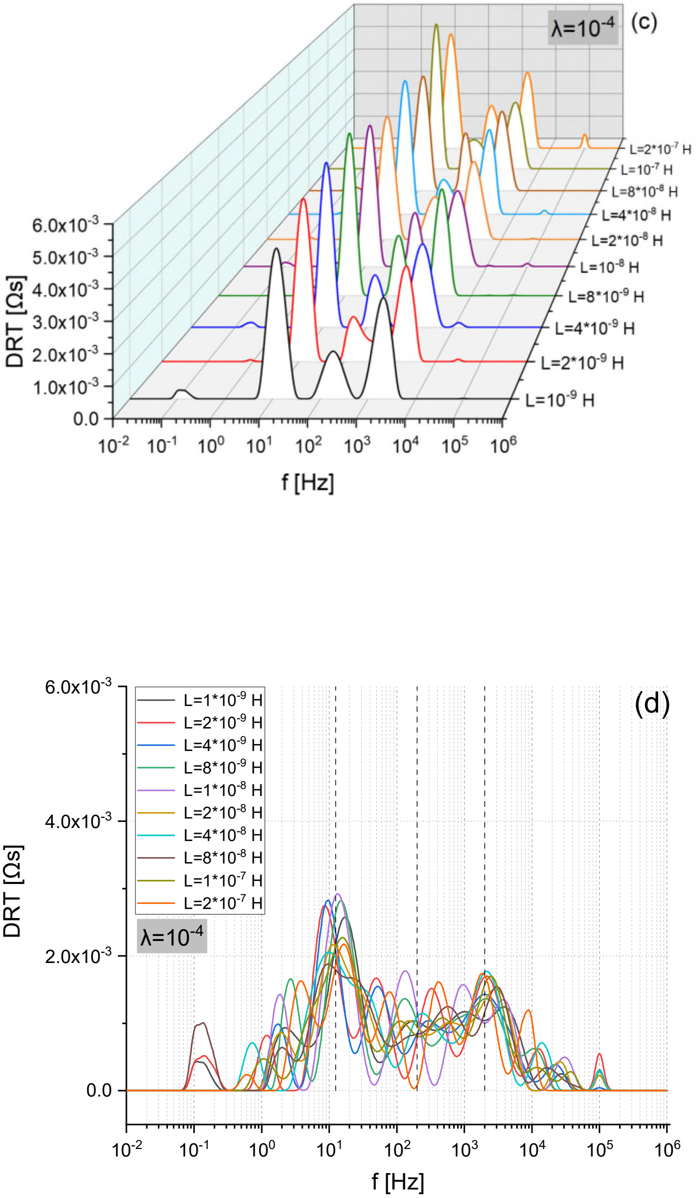

*Figure 4.2.37. DRT plots for variation of the inductance. In (a) and (c) the CPE exponents of the electrochemical processes are 0. 95. In (b) and (d) the CPE exponents of electrochemical processes are 0. 75. Regularization parameter for DRT calculation is λ=10^{-3} for (a) and (b) and λ=10^{-4} for (c) and (d). L = 2*10^{-9} H and the total polarization resistance is 10 mΩ. (100 mHz – 100 kHz, 14 ppd)*

It can be observed that there is no systematic influence of the inductance on the high-frequency range of the DRT, as already observed in the simulations with error model 1. It seems that the error (-structure) has a greater impact on the high- frequency region than the inductance itself. This can be confirmed by comparing the results for the inductance variation for error model 1 and error model 2. While for simulations with error model 1 with low noise level on the imaginary part, the high frequency artificial peaks have low peak height, the peaks are more pronounced in the simulations with error model 2, in which the noise level of the imaginary part is significantly higher.

The statement of a low impact of the inductance on the numerical instability in the high-frequency range of the DRT function can be proven if the CPE exponents of all electrochemical processes are fixed to one and the inductance is varied, as shown in Figure 4.2.38. From these results it is clearly seen that the CPE is the origin of the oscillations and that high inductance values can only enhance the numerical effects caused by the frequency dispersion by means of an increasing measurement error in the high-frequency regime.

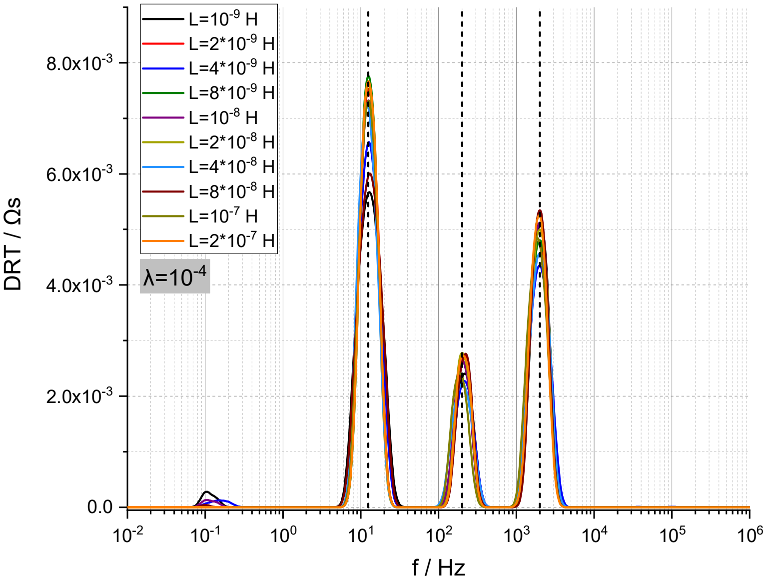

Figure 4.2.38. Comparison of different values of the inductance for the case in which all CPE exponents are one. The regularization parameter is 10^{-4}. The total polarization resistance is 10 mΩ. (100 mHz – 100 kHz, 14 ppd).

Looking at the comparison of different maximum frequencies for L =2*10^{-9} H and 2*10^{-8} H in Figure 4.2.39, the statement that the inductance is not systematically contributing to the high frequency oscillations is confirmed. Interestingly the maximum frequency artefact for the simulations up to 1 MHz is quite pronounced, which is again most probably due to the statistical errors. In general it can be assumed that parasitic inductances originating from the test rig and the cabling are potentially causing noise in the high-frequency regime on the real and imaginary part of the impedance and therefore have an indirect impact on the numerical oscillations observed in the high-frequency range of the DRT. However, based on the current study, there need to be CPE effects present to lead to the expression of numerical artefacts. This means that the inductance and the statistical errors can only act as enhancers of the numerical instabilities caused by the CPE, which is a major finding of this thesis.

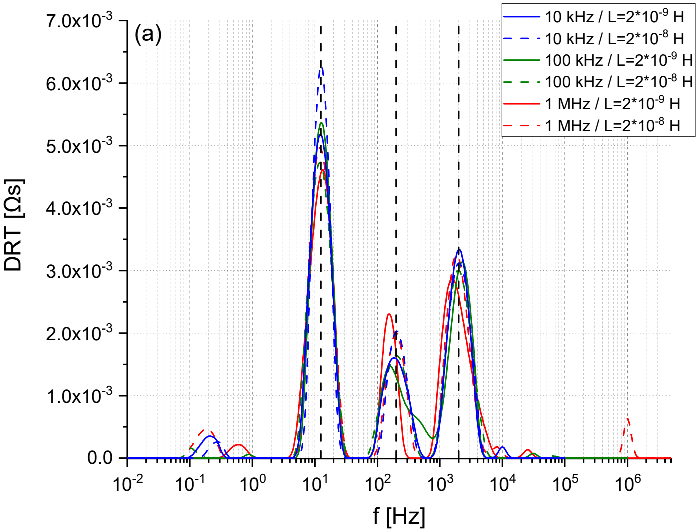

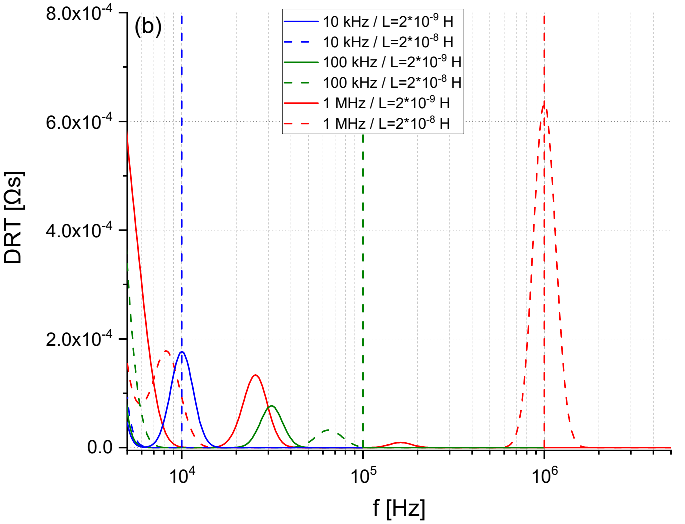

Figure 4.2.39. Comparison of DRT spectra for simulation of different frequency ranges and variation of the inductance value for the entire frequency range in (a) and zoomed into the high frequency range in (b). Regularization parameter λ=10^{-4}. The CPE exponents of the electrochemical processes are fixed to 0. 95. The total polarization resistance is 10 mΩ. (14 ppd)

Repeatability study for error model 2

As for error model 1, a simulation study was performed to investigate the repeatability of the DRT calculation in principle without any variation of the electrochemical parameters in the underlying ECM. This is necessary for evaluation of the impact of the model parameters on the DRT result. The results for error model 2 are not differing much from those received for error model 1 though, see Figure 4.2.40. The repeatability is increasing with an increasing value of the regularization parameter and CPE exponents approaching values of one. Additionally, the repeatability is comparable for simulations to 10 kHz and 100 kHz, with a slight tendency to a higher repeatability for simulations to 10 kHz. This fits the observations from before which showed a greater impact of the errors for simulations to higher maximum frequencies. For simulation to 10 kHz, the main contributor to the artificial peaks is the CPE – n3. For higher f_{max}, there is a combined effect of CPE – n3 and the error, potentially leading to a higher variance between subsequent simulations. An important fact to point out is that the peak height of the characteristic peak is almost constant throughout the samples which affirms the finding that the CPE exponent of the high-frequency electrochemical process is the main contributor to this artefact. Additionally, the level of numerical oscillation in the low- and mid-frequency range is fairly low also for low λ-values of 10^{-4} if no significant frequency dispersion is simulated in this frequency regime. From this it can be concluded that noise can even be suppressed with low values of the regularization parameters if the electrochemical processes show no significant CPE behavior. In reverse this means that for a reasonable choice of the correct regularization parameter for DRT analysis in case of significant oscillation or peak overlapping, at least a rough estimation of the CPE exponent of the contributing electrochemical process of the investigated system has to be available. This information could be provided from a CNLS fit of the EIS data. As stated in chapter 4.2.1, the differences of the DRT curves are minimized with increasing regularization parameter values which offers a possibility for an optimization of λ via minimizing those differences in the DRT spectra. A proposal of using this approach for optimization of the regularization parameter was given by Schlüter [166].

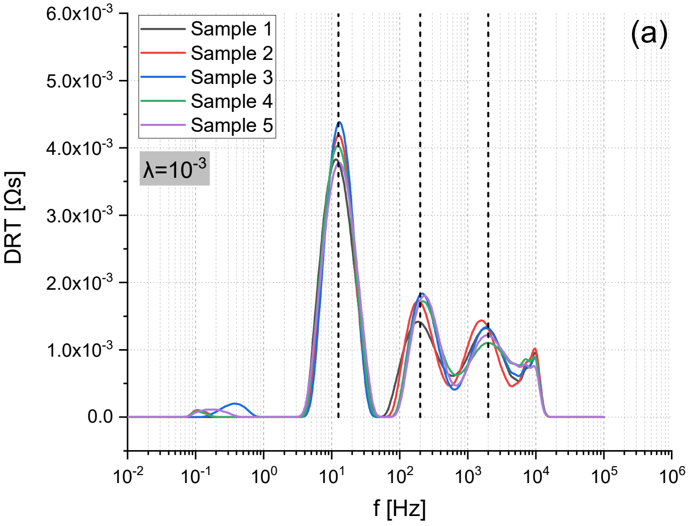
(a)
Sample 1
Sample 2
Sample 3
Sample 4
Sample 5
λ=10^-3
DRT [Ωs]
6.0x10^-3
5.0x10^-3
4.0x10^-3
3.0x10^-3
2.0x10^-3
1.0x10^-3
0.0
10^-2
10^-1
10^0
10^1
10^2
10^3
10^4
10^5
10^6
f [Hz]

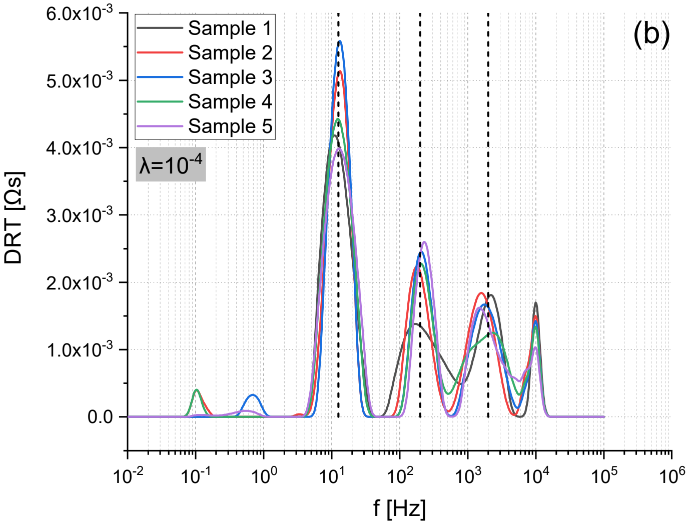
(b)
Sample 1
Sample 2
Sample 3
Sample 4
Sample 5
λ=10^-4
DRT [Ωs]
6.0x10^-3
5.0x10^-3
4.0x10^-3
3.0x10^-3
2.0x10^-3
1.0x10^-3
0.0
10^-2
10^-1
10^0
10^1
10^2
10^3
10^4
10^5
10^6
f [Hz]

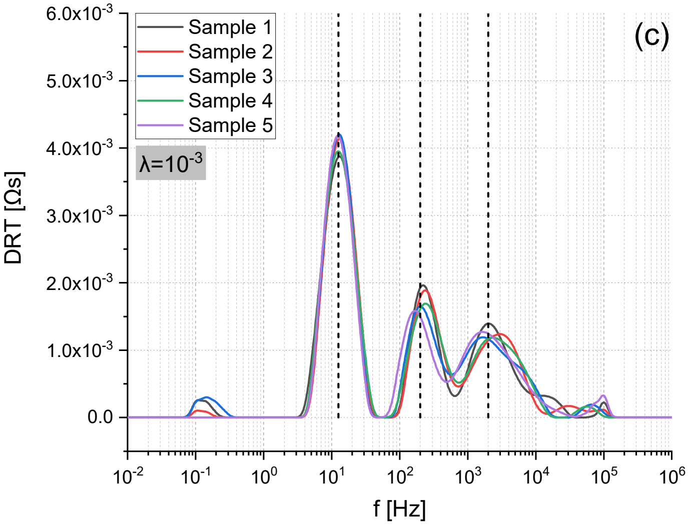

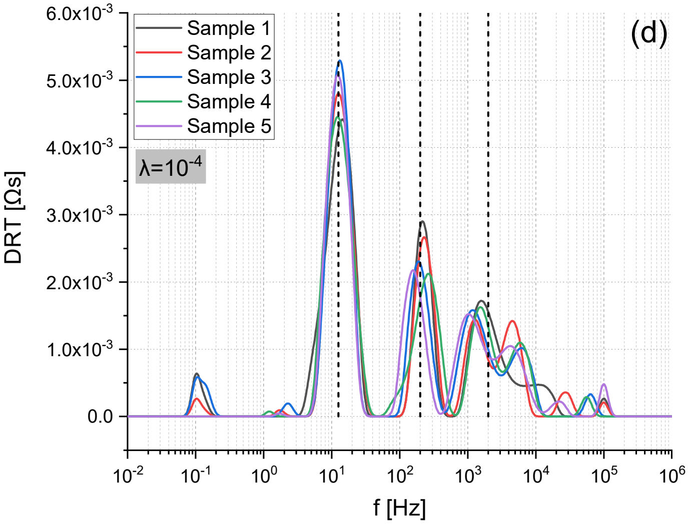

Figure 4.2.40. DRT spectra of the repeatability study on error model 2 for maximum frequencies of 10 kHz (a) and (b) and 100 kHz (c) and (d). The regularization parameter is λ=10^{-3} for (a) and (c) and λ=10^{-4} for (b) and (d). The total polarization resistance is 10 mΩ. (14 ppd). The parametrization of the ECM is identical for Samples 1-5 and statistical error according to error model 2 is added.

In the following chapters, a more detailed analysis on the influence of the points per decade, the error level and the minimum frequency in combination with CPE effects is provided. The simulations were performed on a representative part of the simulation series which is chosen on the basis of the results shown in the chapters before.

The main conclusions that can be drawn from the simulations with error model 2 are the following:

- Compared to EIS simulations with error model 1, the noise level on the impedance data is higher with error model 2, due to increased KKR on the imaginary part. Therefore, higher values of the regularization parameter for the DRT calculation are needed to suppress the oscillations
- The results for the variation of the CPE exponents and the inductance are comparable to those achieved with error model 1. The numerical oscillations are caused by CPE effects in the respective frequency range and are only enhanced by statistical errors.
- If no CPE effects are present in a particular frequency range, high degrees of statistical error and inductive effects do not cause numerical instabilities in the DRT calculation.
- Statistical errors simulated with error model 2 cause a shift of the peak location of high-frequency artefacts and change their expression, which complicates the identification of those artefacts. Therefore statistical errors increase the probability of misinterpreting high-frequency peaks in the DRT in case that CPE effects are present.

4.2.3 Simulations with ppd variation

In this chapter the results of the simulation study on variation of the number of points per decade (ppd) in the EIS simulation are presented. The parameters for the ECM in Table 4.2.2 were chosen on basis of the simulation series which were performed in advance. Because of the fact that low values of the CPE exponent are favoring numerical instability, those values are set to 0. 75 for all electrochemical processes. Every EIS spectrum was simulated five times to check the repeatability as a measure of the numerical stability of the DRT calculation. The main objective of the following simulations is to investigate the numerical stability of the DRT calculation depending on the data point density and the influence of this density on the ability of the DRT to achieve a correct peak resolution in case significant CPE behavior is present. All simulations were carried out for three different frequency ranges from 100 mHz to 10 kHz, 100 kHz and 1 MHz.

Table 4.2.2: Simulation parameters for the ECM used for the ppd study

Parameter	Value
Polarization/ Ohmic resistance	12 mΩ
Inductance	$2*10^{-9}$ H
CPE exponent 12.5 Hz process	0. 75
CPE exponent 200 Hz process	0. 75
CPE exponent 2000 Hz process	0. 75
ε0	0. 5 %
points per decade	7/14/28/72

The simulations were conducted for both error models. Because the results are not different from a qualitative point of view and the conclusions which are drawn from the simulations are the same for both error models, only the results of error model 1 are presented in this thesis. The quantitative difference lies in the magnitude of the regularization parameter that is necessary to suppress the oscillations of the DRT. The root cause is the higher error on the imaginary part in EIS spectra simulated with error model 2 compared to error model 1 as shown in the sections before.

The regularization parameters for the calculation of the DRT functions shown in the Figures 4.2.41 to 4.2.42 are set to $\lambda = 8*10^{-3}$. These high values were necessary to suppress the numerical oscillations caused by the addition of statistical error and to point out the principle that the choice of the regularization parameter is a trade-off between a sufficient peak resolution and suppressing undesired numerical oscillations. An important finding of this study is the fact that the proportion between peak resolution and numerical oscillation becomes more beneficial with increasing number of points per decade. This result was achieved for all simulated frequency ranges. While for the simulation with 7 ppd, the peak at 200 Hz is no longer visible with a CPE exponent of 0. 75, it becomes more and more pronounced with increasing value of the points per decade and can be clearly identified for 72 ppd while the degree of numerical oscillations is comparable for all simulations.

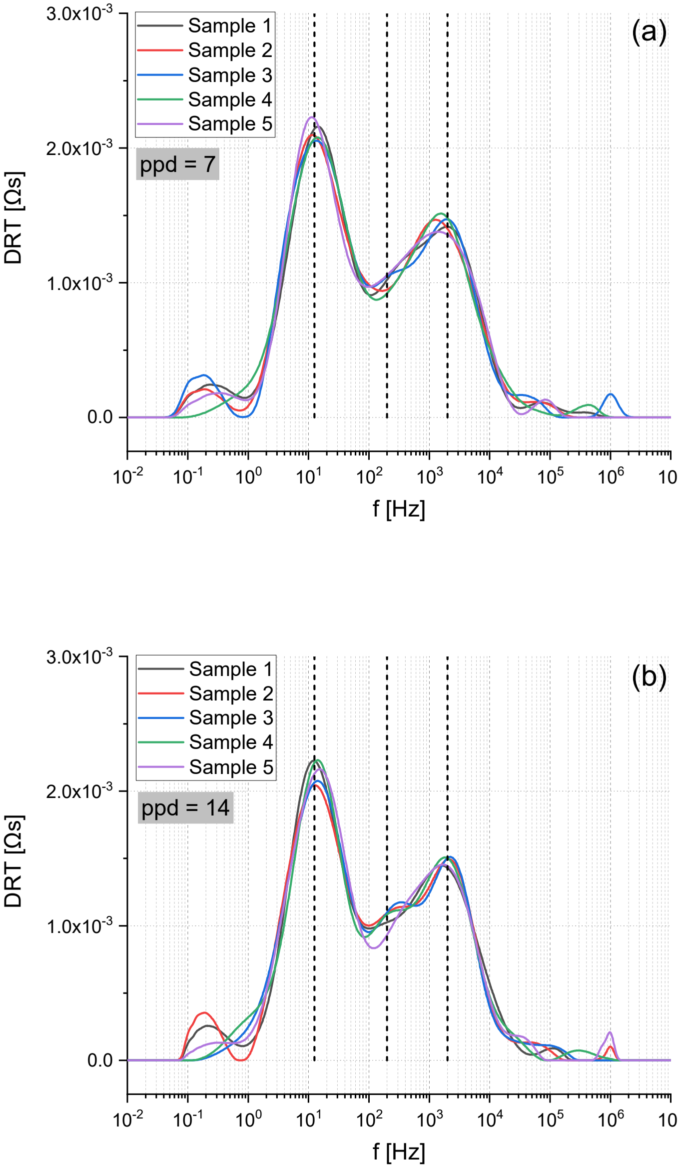
(a)
Sample 1
Sample 2
Sample 3
Sample 4
Sample 5
ppd = 7
DRT [Ωs]
3.0x10-3
2.0x10-3
1.0x10-3
0.0
f [Hz]
10-2
10-1
100
101
102
103
104
105
106
107
(b)
Sample 1
Sample 2
Sample 3
Sample 4
Sample 5
ppd = 14
DRT [Ωs]
3.0x10-3
2.0x10-3
1.0x10-3
0.0
f [Hz]
10-2
10-1
100
101
102
103
104
105
106
107

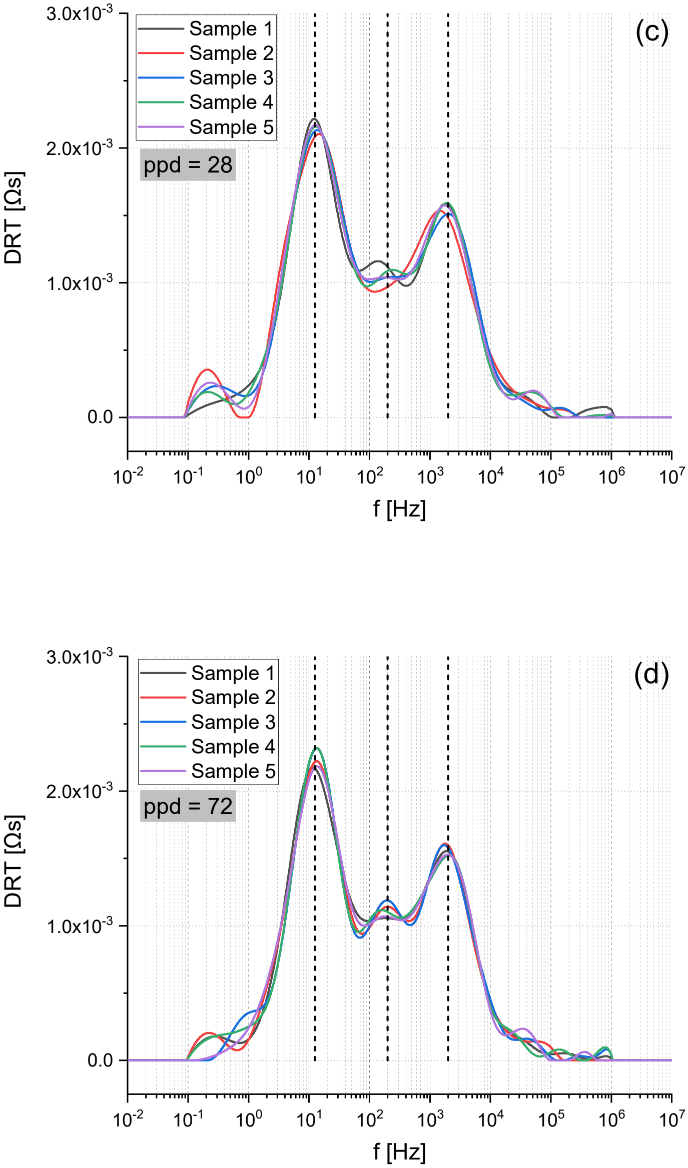

*Figure 4.2.41. DRT graphs for the simulation study on the data density in the frequency range 100 mHz to 1 MHz. The ppd value is increasing from (a) 7 ppd, (b) 14 ppd, (c) 28 ppd to (d) 72 ppd. The regularization parameter is λ=8*10⁻³ in all cases. The total polarization resistance is 10 mΩ.*

Looking at the results for the frequency range 100 mHz to 1 MHz explicitly, there is no systematic influence of the ppd value on the low-frequency and high-frequency artefacts visible. Only for the simulation with 14 ppd, the characteristic peak at the maximum frequency seems to be more pronounced than for the other data point densities. Having the results of the repeatability study in mind, this kind of differences most probably arise from the statistical error. Based on this considerations, the data point density does not seem to have an impact on the expression of artificial peaks at high frequencies in case of a maximum frequency of 1 MHz.

For the simulations in the frequency range 100 mHz to 100 kHz, the characteristic high-frequency peak is most pronounced for the highest ppd value of 72, as shown in Figure 4.2.42. In principle the high-frequency characteristics are more prominent for the simulation to a smaller maximum frequency, which was shown in the chapters before. In comparison to the simulation to 1 MHz maximum frequency, the visibility of the mid frequency peak located at 200 Hz seems to be shifted slightly to lower ppd values as it is already clearly visible for the simulation with 28 ppd.

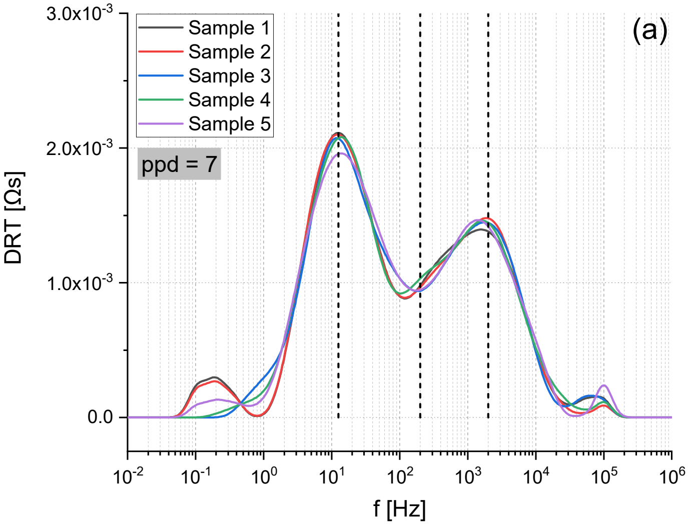
3.0x10-3
2.0x10-3
1.0x10-3
0.0
DRT [Ωs]
Sample 1
Sample 2
Sample 3
Sample 4
Sample 5
ppd = 7
(a)
10-2
10-1
100
101
102
103
104
105
106
f [Hz]

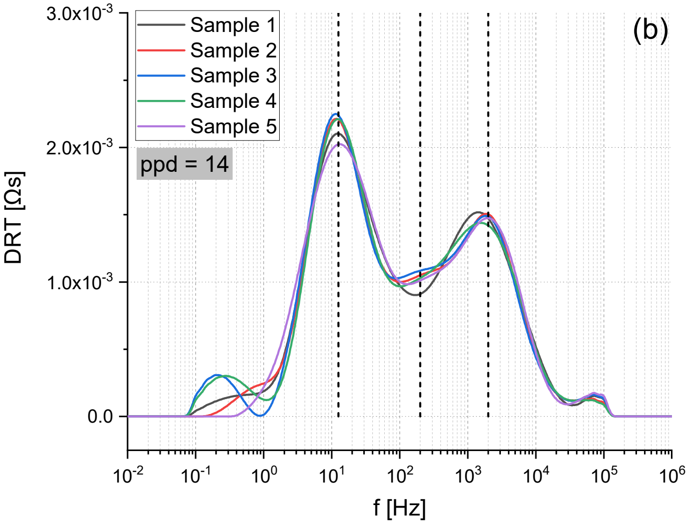
3.0x10-3
2.0x10-3
1.0x10-3
0.0
DRT [Ωs]
Sample 1
Sample 2
Sample 3
Sample 4
Sample 5
ppd = 14
(b)
10-2
10-1
100
101
102
103
104
105
106
f [Hz]

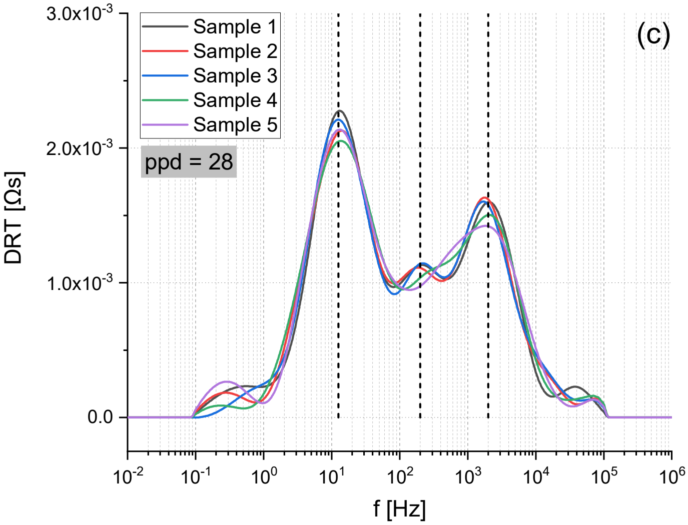

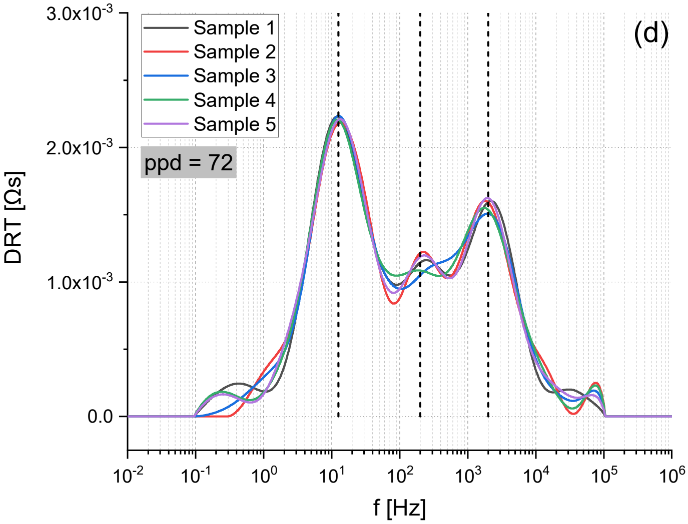

Figure 4.2.42: DRT graphs for the simulation study on the data density in the frequency range 100 mHz to 100 kHz. The ppd value is increasing from (a) 7 ppd, (b) 14 ppd, (c) 28 ppd to (d) 72 ppd. The regularization parameter is $\lambda=8*10^{-3}$ in all cases. The total polarization resistance is 10 mΩ.

Lastly, Figure 4.2.43 shows the results for the frequency range 100 mHz to 10 kHz. A trend to a more pronounced characteristic artificial peak with increasing ppd value and decreasing maximum frequency can be observed. The data point density that is needed to express the mid-frequency peak is shifted to lower ppd values. Here, the peak is already slightly visible at a ppd value as low as 14. In addition, the high-frequency artificial peak exhibits a greater decoupling from the 2000 Hz process if the data point density is increased. This means that not only the inter-peak resolution of real electrochemical processes is increased by increasing the data point density but also the resolution of artificial peaks is increased.

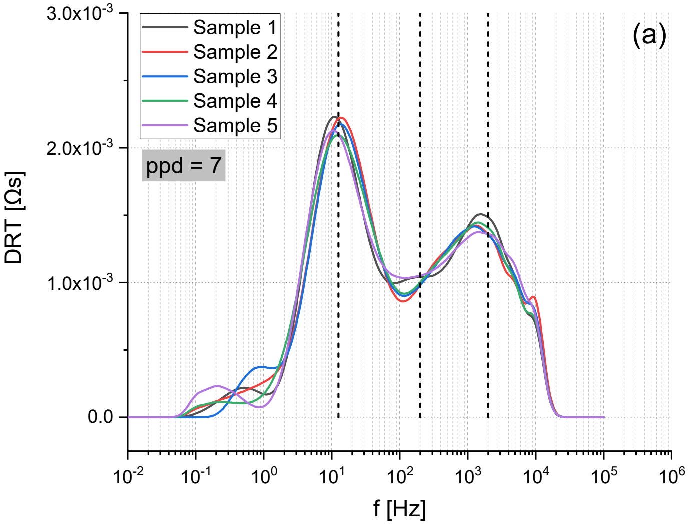
(a)
ppd = 7
Sample 1
Sample 2
Sample 3
Sample 4
Sample 5
DRT [Ωs]
3.0x10^-3
2.0x10^-3
1.0x10^-3
0.0
f [Hz]
10^-2
10^-1
10^0
10^1
10^2
10^3
10^4
10^5
10^6

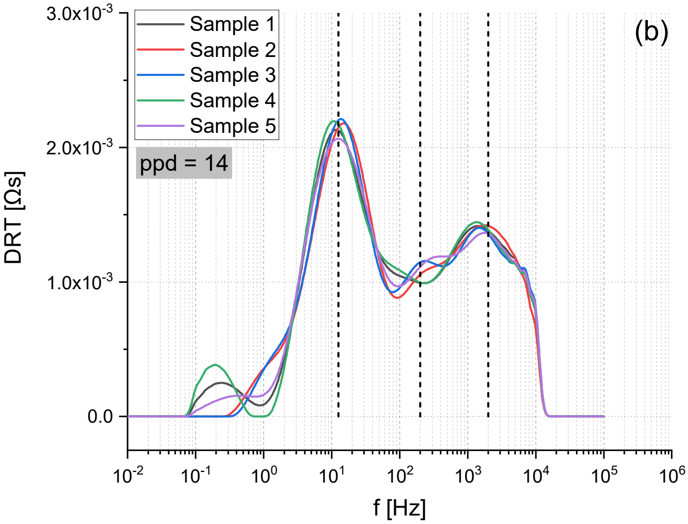
(b)
ppd = 14
Sample 1
Sample 2
Sample 3
Sample 4
Sample 5
DRT [Ωs]
3.0x10^-3
2.0x10^-3
1.0x10^-3
0.0
f [Hz]
10^-2
10^-1
10^0
10^1
10^2
10^3
10^4
10^5
10^6

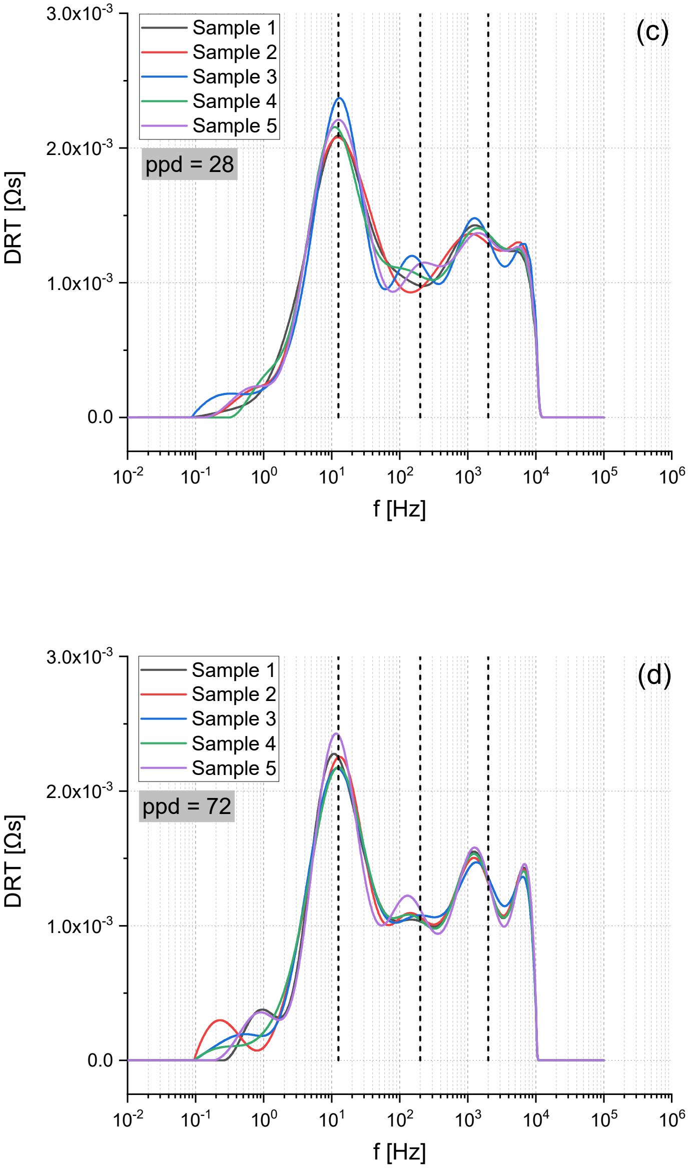

Figure 4.2.43. DRT graphs for the simulation study on the data density in the frequency range 100 mHz to 10 kHz. The ppd value is increasing from (a) 7 ppd, (b) 14 ppd, (c) 28 ppd to (d) 72 ppd. The regularization parameter is $\lambda=8*10^{-3}$ in all cases. The total polarization resistance is 10 mΩ.

The results show that with increasing error level and CPE behavior of the investigated electrochemical processes, the data point density has to be increased to obtain a sufficient peak resolution in parallel with a suppression of numerical oscillations. This finding again emphasizes that it is needed to gain information about the electrochemical system which is investigated when conducting the DRT analysis to achieve a reliable information about the physico-chemical processes in the cell. As stated before, the information about the expected frequency dispersion can be gained from a CNLS-Fit of the EIS data. As another hint, the degree of the depression of semicircles in the Nyquist plot can be used. This can of course be omitted if the measurement error is low and the peak separation is sufficient.

These conclusions which can be drawn from this simulations are of high relevance for the analysis of experimental EIS spectra with DRT. They contradict the statement that the DRT analysis is a pure ab initio method for which no information about the investigated system is necessary in advance. Additionally, it shows that it is necessary to conduct EIS measurements with a higher data point density if significant frequency behavior has to be expected from the processes in the fuel cell. Another important conclusion from the ppd study is that a single EIS measurement seems not to be sufficient to extract a reliable statement about the number of processes in the electrochemical system. As can be observed in the graphs shown in this chapter, single DRT plots would have potentially led to a non-visible mid-frequency peak and therefore to a misinterpretation about the number of processes. Repeated measurements with a higher ppd are recommended to verify the number of peaks in case of peak overlapping, while the possible increased resolution of artificial peak at the highest frequency needs to be considered, too. At this point it should be emphasized that simply decreasing the value of the regularization parameter to increase the peak resolution is not a suitable strategy because this can potentially lead to peak multiplication in frequency ranges with electrochemical processes exhibiting CPE behavior, which was shown in the simulations with varying CPE exponents in all frequency ranges.

4.2.4 Simulations with variation of error level

In this chapter, different error levels are simulated by means of varying the ε_0 to achieve a deeper knowledge on the influence of statistical errors on the DRT result and the choice of a suitable regularization parameter for the DRT calculation, as well as on the interplay of statistical error and CPE behavior. In the study the error level was varied between ε_0 = 0. 01 % to ε_0 = 0. 5 %. The highest value of 0. 5 % is the default for the simulations shown so far. Therefore the error levels are varied in the range between the ideal EIS simulations (see chapter 4.1) and the EIS simulations with error (see chapters 4.2.1 and 4.2.2).

The simulations were conducted with a representative set of simulation parameters, which are summarized in Table 4.2.3. The frequency range of 100 mHz to 100 kHz is used because it is also frequently used for EIS measurements on SOFC stacks at IEK-14 of the Jülich Research Center, which are used later as well for the verification of the simulation results of this thesis.

Table 4.2.3. Circuit parameters for the simulation of EIS spectra used for the simulation study on the influence of the error level on DRT analysis

Parameter	**Value**
Polarization/ Ohmic resistance	10 mΩ
Inductance	$2*10^{-9}$ H
CPE exponent 12.5 Hz process	0. 95
CPE exponent 200 Hz process	0. 95
CPE exponent 2000 Hz process	0. 65 and 0. 75
ε0	0. 01 % / 0. 1 % / 0. 2 % / 0. 5 %
Frequency range	100 mHz - 100 kHz
Points per decade	14

To put light on the link between frequency dispersion and measurement error, the simulations were conducted for different combinations of the CPE exponents and the error level. Main emphasis in terms of CPE behavior is put on the process which is located at 2000 Hz relaxation frequency, denoted as process 3 with CPE-n3. In this chapter, the results for both error models are shown in detail.

In Figure 4.2.44, the Nyquist diagrams for the EIS spectra simulated with error model 1 can be found.

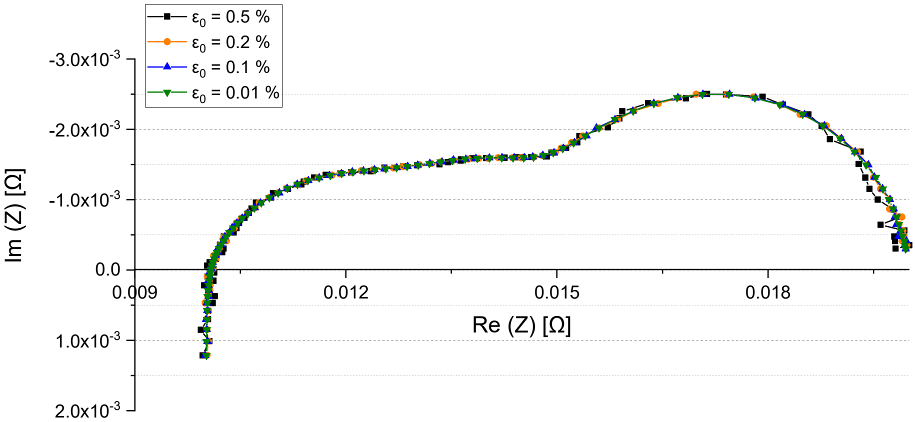

*Figure 4.2.44. Nyquist diagrams for EIS spectra simulated with different error levels with error model 1. The CPE exponents of the low- and mid-frequency processes are 0. 95 and the CPE exponent of the 2000 Hz process is 0. 75. L = 2*10^{-9} H and the total polarization resistance is 10 mΩ.*

In Figure 4.2.45, the KKR of the EIS spectra with different error levels are presented for error model 1. Bringing together the DRT results with the KKR, it can be concluded that the threshold of the KKR for achieving a reasonable extent of numerical oscillation lies below 0. 5 %.

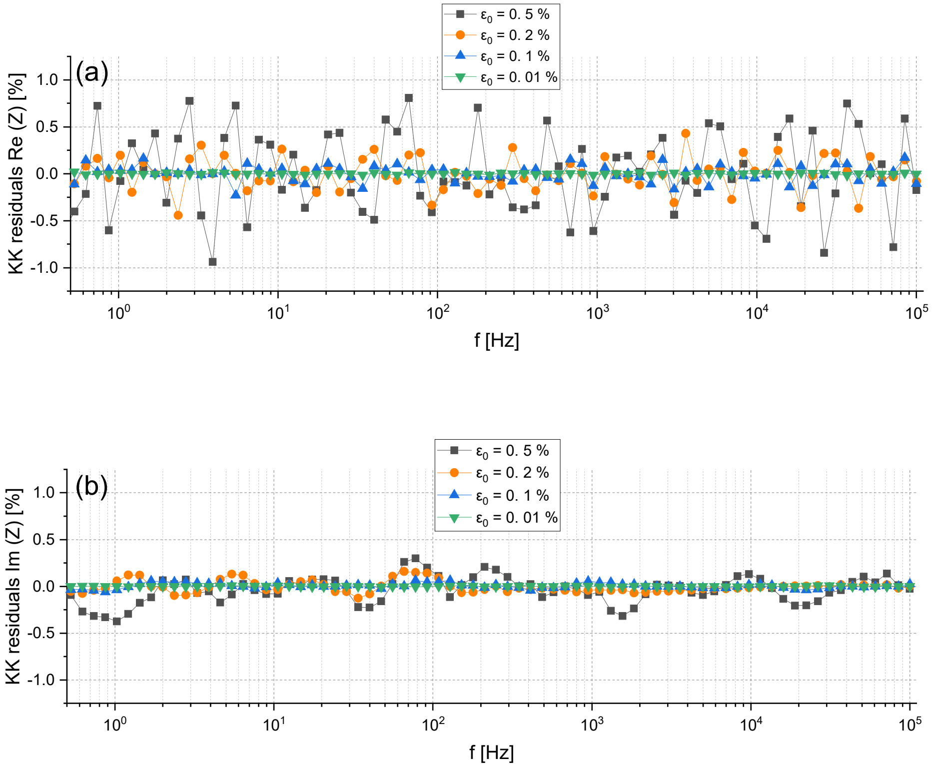

Figure 4.2.45: Kramers - Kronig residuals of the real (a) and imaginary (b) part for the simulations with error model 1. CPE exponents of all electrochemical processes are set to 0. 95. The total polarization resistance is 10 mΩ. (100 mHz – 100 kHz, 14 ppd).

In Figure 4.2.46, the DRT results for the simulations with CPE - n1 and CPE - n2 are set to 0. 95 and different values of the CPE - n3 are shown for the four different error levels on EIS simulations with error model 1. The regularization parameters are chosen to $\lambda=10^{-5}$ and $\lambda=10^{-4}$. The first and important conclusion from the results is the fact that with increasing regularization parameter the differences between the DRT calculated from EIS data with different error levels are decreasing. If λ is decreased to values as low as 10^{-5} the oscillations especially in the high-frequency range are more pronounced for higher error levels.

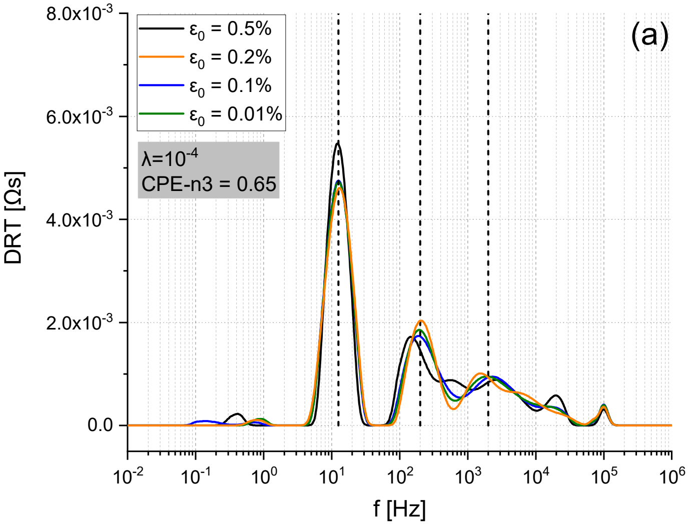

8.0x10-3
6.0x10-3
4.0x10-3
2.0x10-3
0.0
DRT [Ωs]
ε0 = 0.5%
ε0 = 0.2%
ε0 = 0.1%
ε0 = 0.01%
λ=10-4
CPE-n3 = 0.65
(a)
10-2
10-1
100
101
102
103
104
105
106
f [Hz]

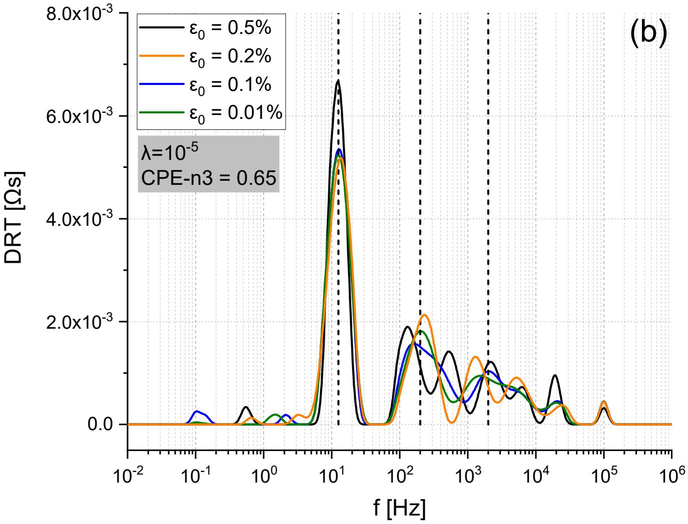

8.0x10-3
6.0x10-3
4.0x10-3
2.0x10-3
0.0
DRT [Ωs]
ε0 = 0.5%
ε0 = 0.2%
ε0 = 0.1%
ε0 = 0.01%
λ=10-5
CPE-n3 = 0.65
(b)
10-2
10-1
100
101
102
103
104
105
106
f [Hz]

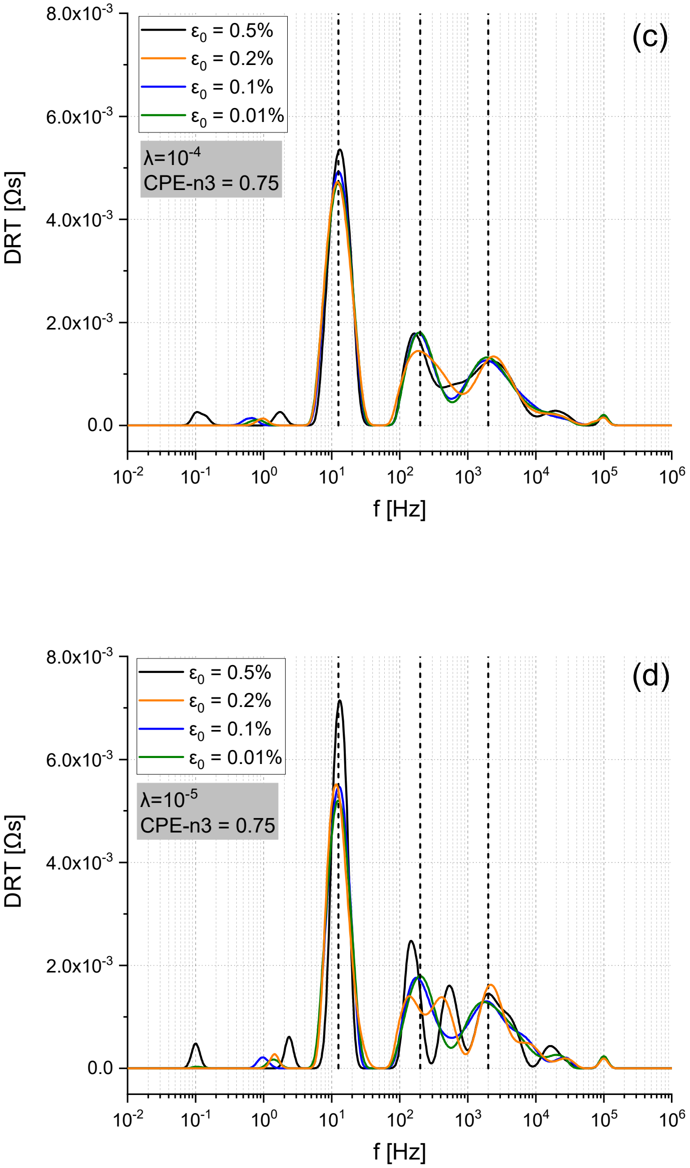

*Figure 4.2.46. DRT spectra for the variation of error level and CPE exponent of the high-frequency process with error model 1. The regularization parameter is λ=10^{-4} for (a) and (c) and 10^{-5} for (b) and (d), while the CPE exponent is 0. 65 for (a) and (b) and 0. 75 for (c) and (d). All other CPE exponents are 0. 95. L = 2*10^{-9} H and the total polarization resistance is 10 mΩ. (100 mHz – 100 kHz, 14 ppd).*

As stated in chapters 4.1, 4.2.1 ad 4.2.2 further investigation on the relationship of the error and the high frequency oscillations especially regarding the characteristic artefact at maximum frequency were necessary. From the results of this study it can be confirmed that the CPE exponents of electrochemical processes in the mid- and high-frequency range are the main contributor to the expression of this peak and not the inductance or the measurement error, as there is no systematic influence of the error level on the expression of the sharp peak.

In order to have a comparison between both error models, the Nyquist diagram for EIS spectra simulated with different error levels with error model 2 are shown in Figure 4.2.47.

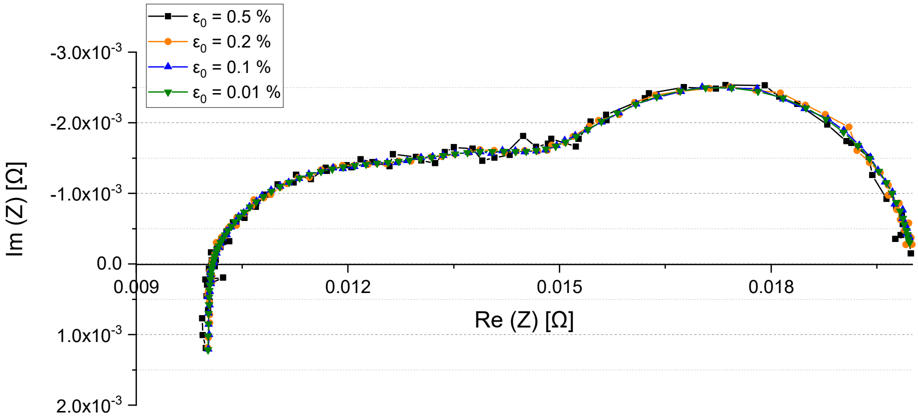

*Figure 4.2.47. Nyquist diagrams for EIS spectra simulated with different error levels with error model 2. The CPE exponents of the low- and mid-frequency processes are 0. 95 and the CPE exponent of the 2000 Hz process is 0. 75. L = 2*10^{-9} H and the total polarization resistance is 10 mΩ.*

The results of the KKR analysis for error model 2 with different values of ε_0 are shown in Figure 4.2.48.

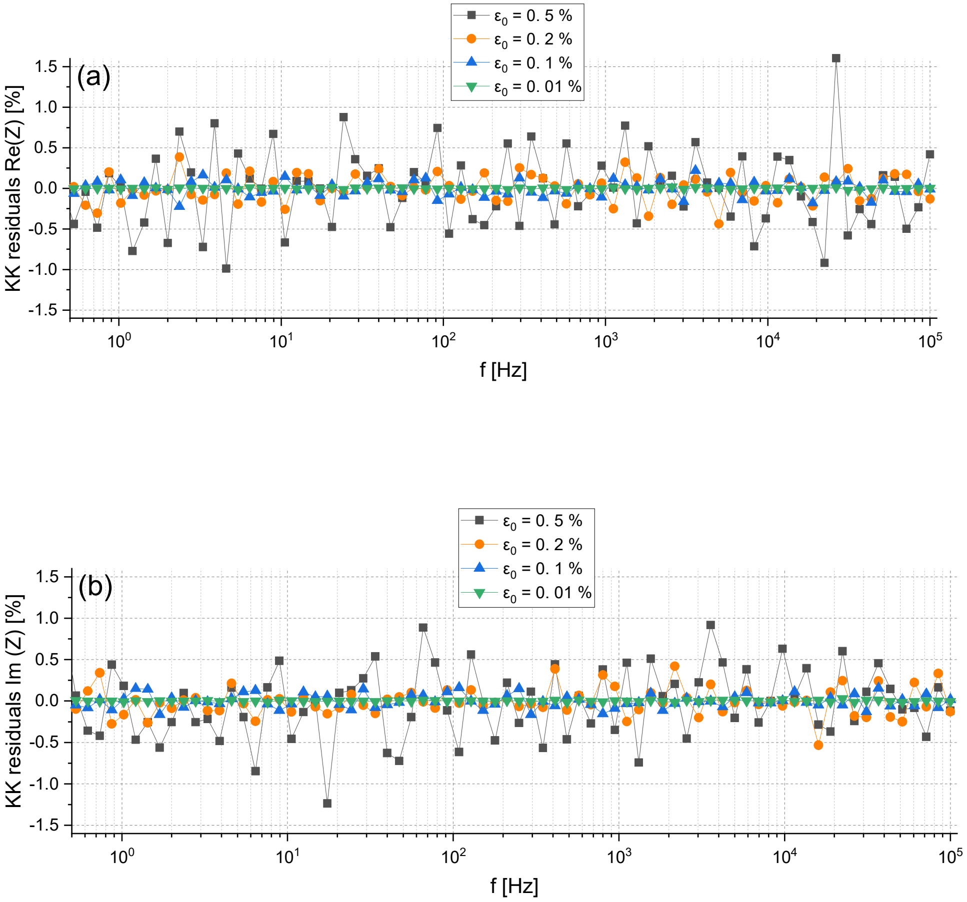

Figure 4.2.48. Kramers - Kronig residuals of the real (a) and imaginary (b) part for the simulations with error model 2. CPE exponents of all electrochemical processes are set to 0. 95. The total polarization resistance is 10 mΩ. (100 mHz – 100 kHz, 14 ppd).

The corresponding DRT results based on EIS simulations with error model 2 are presented in Figure 4.2.49. For the simulations with this error model, there are significant differences visible between the varying error levels also for regularization parameters of 10^{-4}.

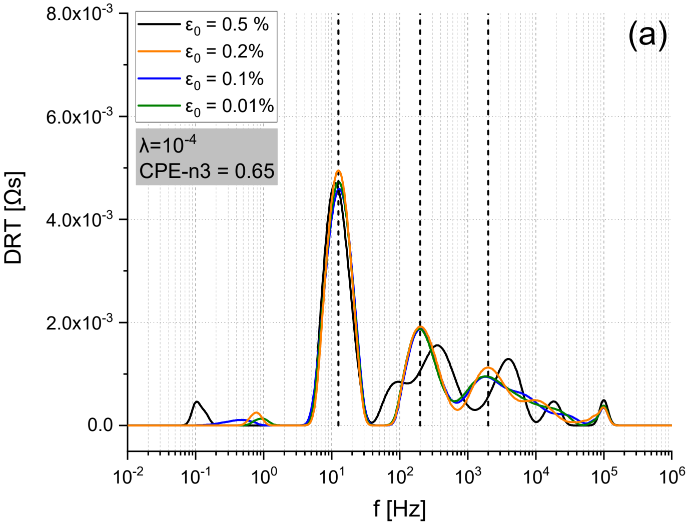
(a)
ε0 = 0.5 %
ε0 = 0.2%
ε0 = 0.1%
ε0 = 0.01%
λ=10-4
CPE-n3 = 0.65
DRT [Ωs]
8.0x10-3
6.0x10-3
4.0x10-3
2.0x10-3
0.0
10-2
10-1
100
101
102
103
104
105
106
f [Hz]

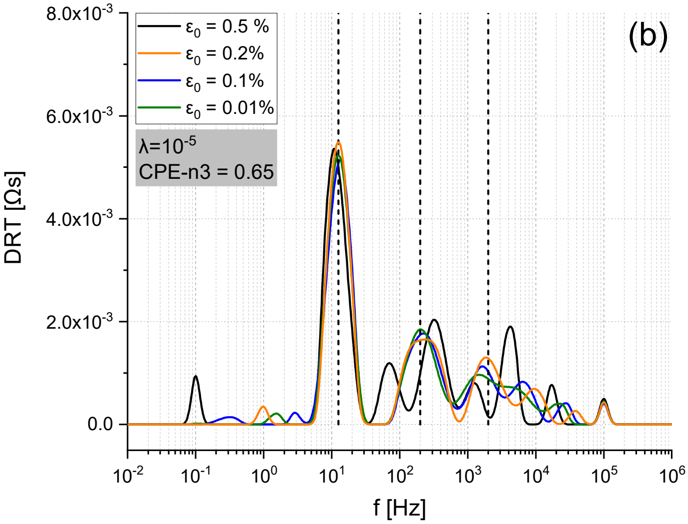
(b)
ε0 = 0.5 %
ε0 = 0.2%
ε0 = 0.1%
ε0 = 0.01%
λ=10-5
CPE-n3 = 0.65
DRT [Ωs]
8.0x10-3
6.0x10-3
4.0x10-3
2.0x10-3
0.0
10-2
10-1
100
101
102
103
104
105
106
f [Hz]

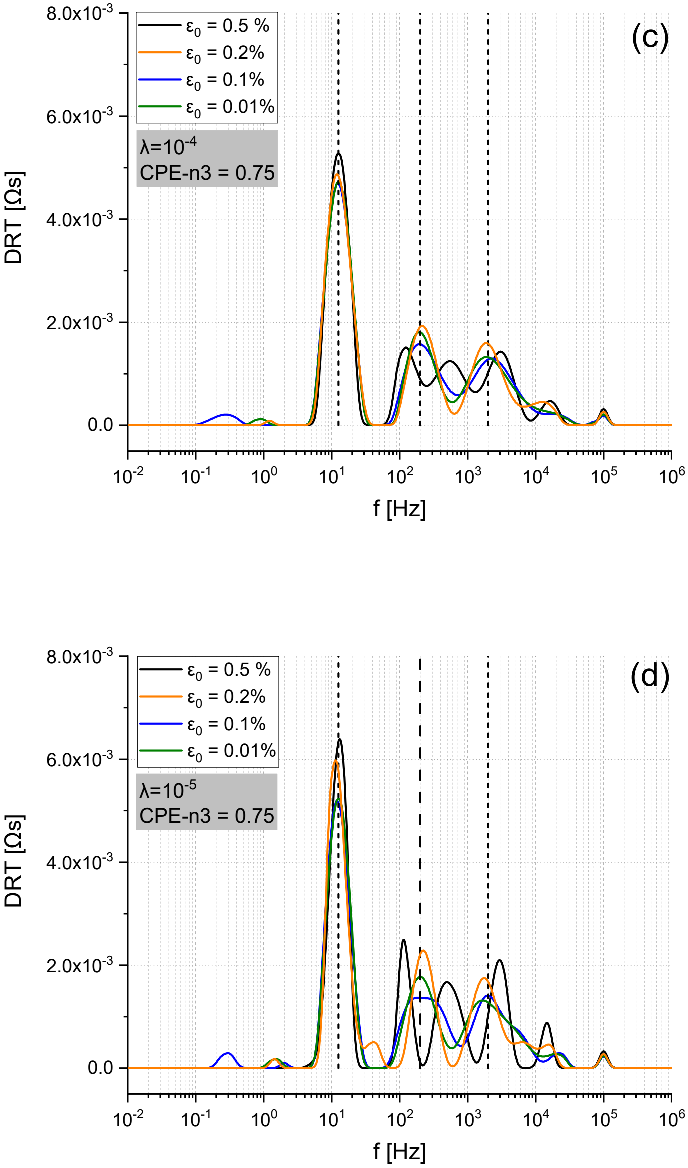

*Figure 4.2.49. DRT spectra for the variation of error level and CPE exponent of the high-frequency process with error model 2. The regularization parameter is λ=10^{-4} for (a) and (c) and 10^{-5} for (b) and (d), while the CPE exponent is 0. 65 for (a) and (b) and 0. 75 for (c) and (d). All other CPE exponents are 0. 95. L = 2*10^{-9} H and the total polarization resistance is 10 mΩ. (100 mHz – 100 kHz, 14 ppd).*

As stated before, the error on the imaginary part is higher than for error model 1 due to the scaling of the error with the modulus of the impedance. Therefore it would need even higher values of λ to balance the differences in the DRT. Nevertheless, the differences mainly occur between the spectra originating from EIS data with $\varepsilon_0 = 0.5$ % and the ones generated with EIS data sets with lower error levels. For error levels of $\varepsilon_0 = 0.2$ % and lower, the differences are already rather low with $\lambda=10^{-4}$. Therefore the critical limit for numerical oscillations seems to be between $\varepsilon_0 = 0.5$ % and $\varepsilon_0 = 0.2$ %, as concluded for error model 1 as well. While there is no influence on the maximum frequency artefact visible, the artefacts between the 2000 Hz process and the maximum frequency are subject to changes with changing error levels, which was expected based on the simulation results shown before.

From these findings and comparison of the KKR, which were shown in Figure 4.2.48, it can be stated the KKRs have to be lower than 0. 5 % to achieve an acceptable level of numerical oscillation in the DRT analysis that is needed for a repeatable DRT calculation. By conducting KK validity tests on experimental EIS data, the fulfilment of this criterion can be verified. In case the KK limit is not reached, the EIS measurement should be repeated with an improved measurement setup to avoid the expression of high-frequency artefacts in the DRT which can potentially lead to a subsequent misinterpretation about the number of electrochemical processes. An increase of the ppd can be useful as well, as this measure offers the possibility of increasing the regularization parameter to suppress the numerical oscillations while reducing the risk of losing physical information.

An additional advantage of EIS measurements with low error level is the fact that the repeatability is increasing with decreasing measurement error. This allows the choice of lower values for the regularization parameter and therefore a better resolution of the electrochemical processes.

The main conclusions from this simulation study are:

- The error level shows no systematic influence on the expression of the artificial peak at the maximum frequency, but a rather high influence on the artefacts between the maximum frequency and the real high-frequency electrochemical process for maximum frequencies of 100 kHz and above.
- The limit for the KKRs of the real and imaginary part is within 0. 5 % to achieve a reasonable degree of numerical oscillations. Below this value the degree of numerical oscillation is almost constant and the regularization parameter has lesser influence on the DRT result.
- Numerical oscillations arising from measurement errors can be suppressed with choosing higher λ-values bearing the risk of losing physical information in case of processes with similar relaxation times. In such cases, the measurement should be repeated with an increased data point density (i.e., ppd).

4.2.5 Simulations with variation of minimum frequency

As shown in the previous chapters, there is a relationship between the maximum frequency of the EIS data set and the high-frequency arteficial peaks in the DRT spectrum. Because there are also artefacts present in the low-frequency range, a simulation study with variation of the minimum frequency was conducted to investigate if similar dependencies on the CPE in the low-frequency range together with the minimum frequency of the EIS data set can be observed. This study is executed on a representative simulation series with frequency dispersion of the electrochemical process located at a relaxation frequency of 12. 5 Hz. DRT results based on EIS simulations with no error, error model 1 and error model 2 will be shown in this chapter to highlight the different behavior of the low-frequency artefacts compared to those observed in the high-frequency range.

In Figure 4.2.50 the results for two different CPE exponents of the low-frequency process (CPE - n1) are shown based on EIS data sets starting at minimum frequencies of 10 mHz, 50 mHz and 100 mHz with no statistical error added. There are no low-frequency artefacts present for neither CPE – n1 = 0. 75 nor CPE – n1 = 0. 65, which already shows that the mechanism of the expression of low-frequency artefacts follows a different mechanism than the expression of high-frequency artefacts.

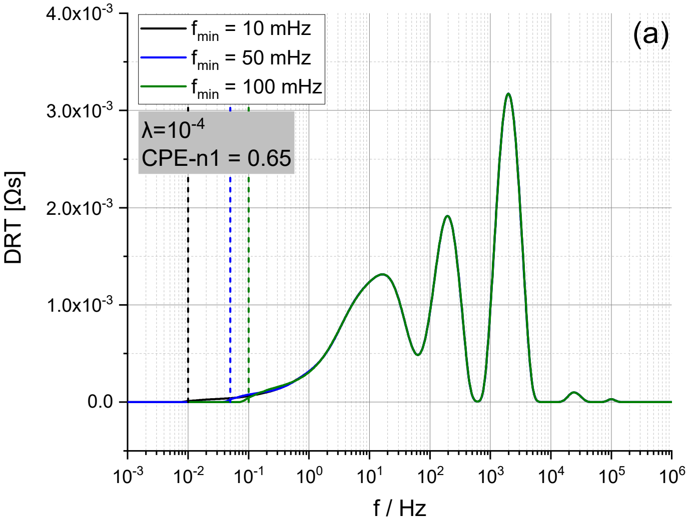

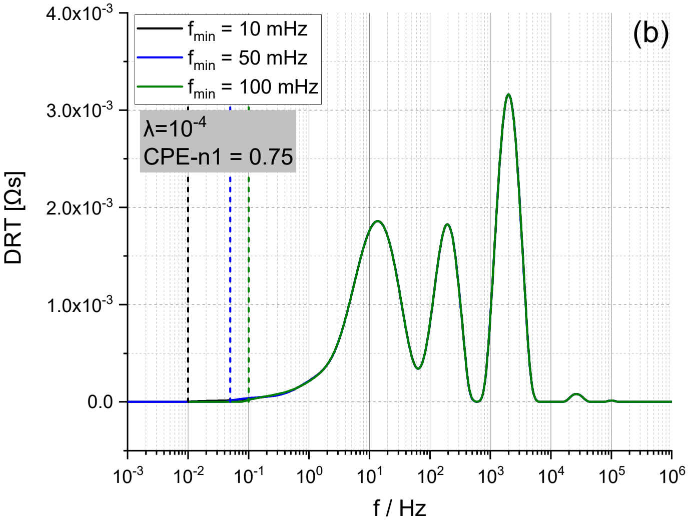

*Figure 4.2.50. DRT results of the simulation study based on ideal EIS spectra with different minimum frequencies. The CPE exponent of the 12. 5 Hz process is set to 0, 65 (a) and 0. 75 (b), the CPE exponents of the remaining processes are 0. 95. L=2*10^{-9} H. The regularization parameter is 10^{-4}. The total polarization resistance is 10 mΩ. (14 ppd).*

In Figure 4.2.51, the results for the simulations with error model 1 are shown. In case of CPE - n1 = 0. 65, there are peaks at the minimum frequency visible for the simulation to 10 mHz and 50 mHz, which is not the case for the simulation beginning from 100 mHz. For the higher CPE exponent of 0. 75 none of the simulations shows a characteristic artificial peak at the minimum frequency.

In Figure 4.2.52, the results for the simulations with error model 2 are shown. Similarly to the results for error model 1, the artificial peaks in the low-frequency range exhibit no systematic dependency on the CPE – n1 or the minimum frequency of the underlying EIS data set. Based on these results it can be concluded that there is no clear relationship between frequency dispersion effects in the low-frequency range and low-frequency artificial peaks in the DRT. Furthermore, the position of the artefacts does not correlate in a systematic way with the minimum frequency of the EIS data set.

The conclusions that can be drawn from the shown simulations is are the following:

- CPE effects in the low-frequency range are not systematically causing artificial peaks in the low-frequency regime of the DRT spectrum, as observed for high-frequency CPE effects.
- There is no clear correlation between the minimum frequency of the EIS data set and the expression of low-frequency artefacts observable.
- For ideal EIS spectra, no low-frequency artefacts are observable at all, while for simulations with error model 1 and 2, artificial peaks can be observed.
- If a statistical error is simulated, the value of CPE – n1 seems to enhance the expression of oscillations in the low-frequency regime, but in an unsystematic way.
- Based on these results, the expression of low-frequency artefacts is caused by a different mechanism compared to the high-frequency artefacts. The latter are mainly caused by CPE effects, while the main contributor to the expression of low-frequency artefacts is the statistical error.

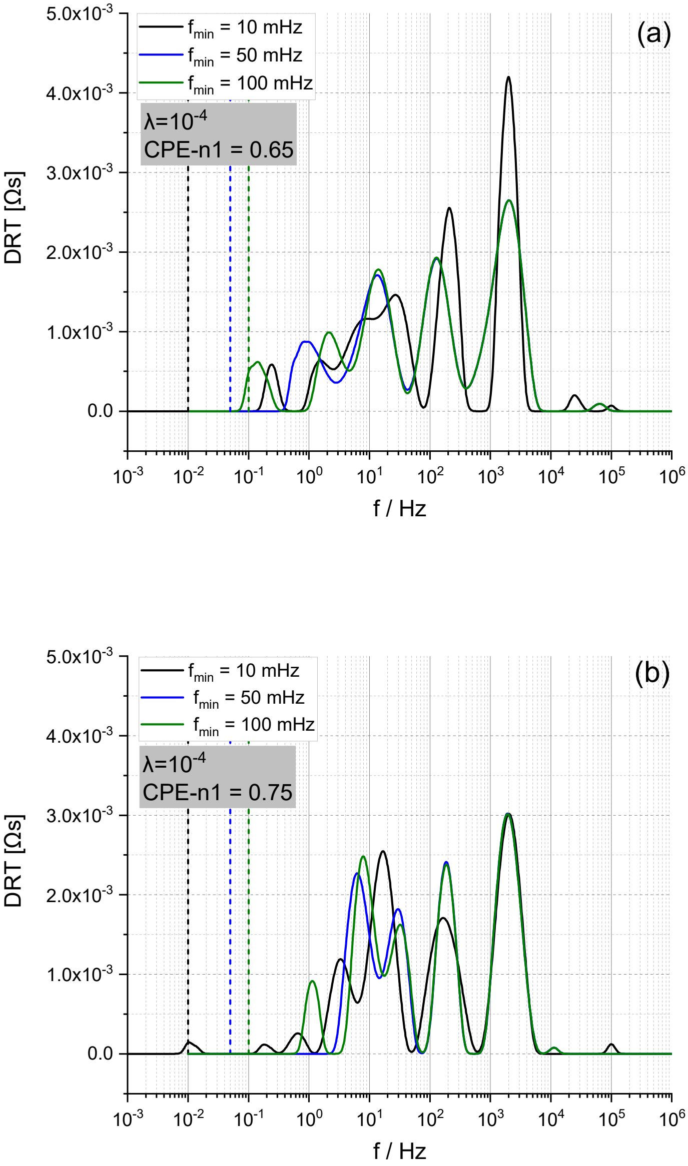

*Figure 4.2.51. DRT results of the simulation study based on EIS spectra with error model 1 and different minimum frequencies. The CPE exponent of the 12. 5 Hz process is set to 0. 65 (a) and 0, 75 (b), the CPE exponents of the remaining processes are 0. 95. L=2*10^{-9} H. The regularization parameter is 10^{-4}. The total polarization resistance is 10 mΩ. (14 ppd).*

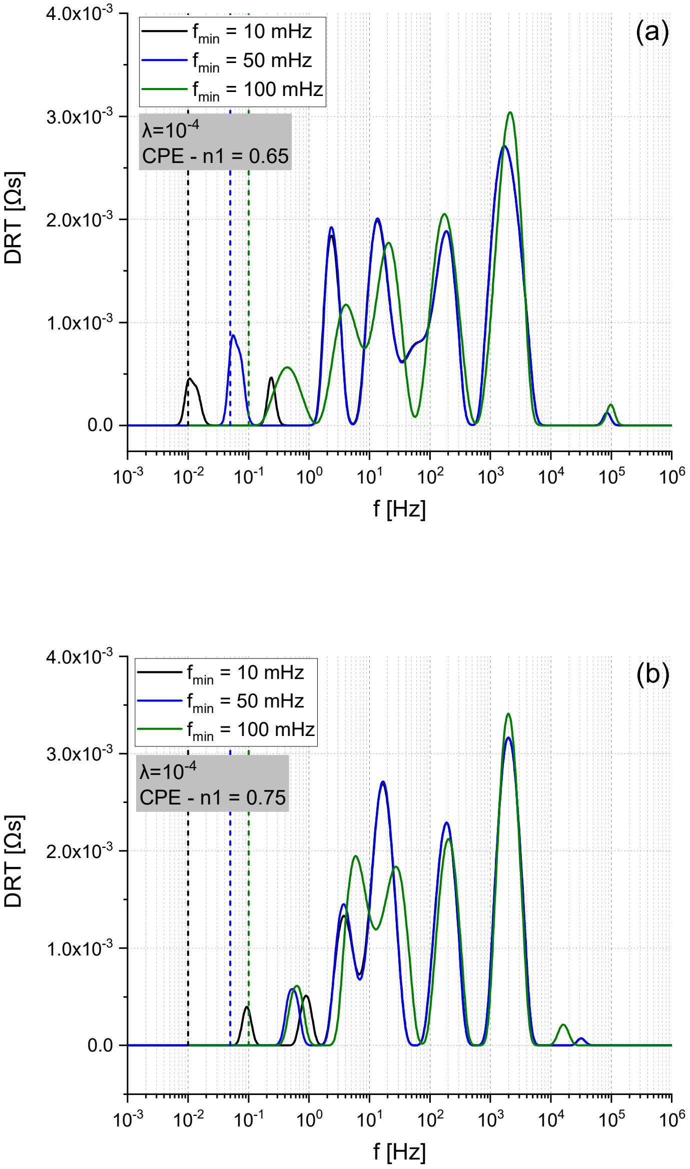

*Figure 4.2.52. DRT results of the simulation study based on EIS spectra with error model 1 and different minimum frequencies. The CPE exponent of the 12. 5 Hz process is set to 0. 65 (a) and 0. 75 (b), the CPE exponents of the remaining processes are 0. 95. L=2*10^{-9} H. The regularization parameter is 10^{-4}. The total polarization resistance is 10 mΩ. (14 ppd).*

4.3 Summary of simulation results

Electrochemical impedance spectra were simulated using an equivalent circuit model consisting of an inductor, an ohmic resistor and three parallel combinations of a resistor and a constant phase element which represent electrochemical processes exhibiting frequency dispersion and thus a deviation from the ideal RC element behavior. To simulate a measurement error, two different error models were applied to the EIS data. In addition, different frequency ranges, data point densities and error levels were analyzed to investigate the influence of those on the accuracy of the DRT calculation with DRTtools.

The objective of these simulations was to gain an increased knowledge on the qualitative and quantitative impact of the parameters mentioned above and also combined influences of those on the DRT result to reveal weaknesses of the DRT calculation with the regularized regression approach and raise awareness of potential risks in terms of misinterpretation of the DRT function. Based on the simulations performed in this study, recommendations can be given for an optimized DRT analysis for SOFCs and SOFC stacks. In the following part, the results of the simulation study are summarized.

Influence of the CPE exponents

By means of a variation of the CPE exponents of the electrochemical processes in different relaxation frequency regimes between 12. 5 Hz and 2000 Hz, it was found that a decreasing value of the CPE - n potentially leads to peak broadening and overlapping of adjacent peaks or artificial peak multiplication in the frequency range in which the respective electrochemical process is located. Whether the peaks are overlapping or multiplied depends on the choice of the regularization parameter and the CPE exponents of the respective adjacent peaks. With a decreasing value of the regularization parameter, the oscillations are spreading from the frequency range of the respective process to the frequency areas beneath. From this it has to be concluded that dependent on the choice of the regularization parameter, the frequency dispersion effect of one electrochemical process can potentially influence other processes in adjacent frequency regimes as well. This effect becomes even more enhanced if adjacent electrochemical processes both exhibit significant CPE behavior. In this case the peak resolution may not be sufficient to make both processes visible in the DRT and in parallel achieve a sufficient suppression of the numerical oscillations. Regarding the

CPE exponent of high-frequency processes, a major impact of the CPE – n3 on the high-frequency artificial peaks was observed. With decreasing CPE exponent, the sharp high-frequency artificial peak located at the maximum frequency of the underlying EIS data set becomes more prominent. Furthermore, with increasing maximum frequency or distance between the high-frequency electrochemical process and the maximum frequency, additional artefacts appear in between them, which bear the risk of misinterpretation of those as distinct processes related to the polarization loss of the fuel cell. While the maximum frequency artefact can easily be identified as such, the correct identification of the additional artefacts is more difficult. In such cases, repeated EIS measurements to different maximum frequencies are recommended to confirm the high-frequency electrochemical processes. Special emphasis should also be put on low measurement errors to suppress the expression of those artefacts, as there was evidence from the simulations that especially the artefacts between the 2000 Hz process and the maximum frequency are affected by statistical errors. However, it could be observed that the peak height of the maximum frequency artefacts is decreasing with increasing distance between the high-frequency process and the maximum frequency.

In general low CPE exponents make it necessary to achieve a good trade-off between peak resolution and the suppression of numerical artefacts in terms of an optimal choice of the regularization parameter. From the simulation study with varying value of points per decade it turned out that this ratio is getting better with an increasing data point density. In case of apparent peak overlapping in the DRT spectrum, it is recommended to repeat the EIS measurement with a higher ppd value to increase the resolution. Based on the results shown in this chapter, it cannot be recommended to directly decrease the regularization parameter to increase the peak resolution as this bears the risk of peak multiplication in frequency regimes in which electrochemical processes with CPE behavior are located. Additionally, it can be recommended to do at least two EIS measurements at the same conditions and compare the DRT results for a reliable statement about the number of processes present in the investigated system and for correct determination of the high-frequency processes. In addition, a CNLS fitting procedure can help to estimate the degree of frequency dispersion of the electrochemical processes in the investigated system.

Influence of the polarization resistance

In general the influence of the polarization resistance on the DRT result was fairly low. Therefore the variation of the polarization resistance was only conducted for ideal EIS spectra and not included in the simulations with statistical error. With increasing polarization resistance, the peak height of the artificial peaks increased as well, but keeping a constant ratio between the peak heights of simulated process peaks and the artefacts. One possible scenario in which a misinterpretation of additional peaks could occur would be that an increasing peak height with varying operation parameters would be interpreted as a reaction of the artificial process peaks on the implemented change. Still this is not very likely as every artefact in the DRT would react in the same extent to the parameter changes. Based on the results, the polarization resistance is not considered to be a contributor to numerical instabilities in the DRT calculation with DRTtools.

Influence of the inductance

Regarding the results for the ideal EIS spectra, there was no impact of varying inductance on the DRT visible at all, as the inductance was included in the DRT model by choosing the option “Fitting with inductance” in DRTtools. To further investigate non-ideal inductances, the same parameter variation was conducted on simulations with two different error models. From these results, no systematic influence of the inductance value on the high-frequency oscillations could be observed. It can therefore be concluded that inductive effects of the measurement setup are only an indirect contributor to the high-frequency by causing a higher level of measurement instability in the high - frequency range. However, it could be shown that numerical artefacts originating from CPE effects can potentially enhanced by high values of the inductance. In reverse, no artefacts were observed in cases in which no CPE effects were present neither in the mid- nor in the high-frequency range. As the inductance itself is therefore not a main contributor to the oscillations, a subtraction from the EIS data alone will not be successful to get rid of the sharp artefacts. Repeating parts of the simulation study on the inductance with the option “Fitting without inductance” confirmed that the inductance is not contributing to the high-frequency oscillations, but is causing a peak shift of the process peaks to lower frequencies.

Influence of the error structure and magnitude

It was found that with increasing statistical error the degree of numerical oscillations increases and the repeatability of the DRT decreases in the same extent. Therefore, with increasing error level the regularization parameter value has to be increased as well to suppress the oscillations. In reverse, the repeatability increased with increasing value of the regularization parameter. Furthermore there is an interplay of statistical errors with the CPE behavior of the electrochemical processes, expressed as an enhancement of the numerical artefacts caused by low CPE exponents with increasing statistical error. With increasing error level, the numerical oscillations increase the most in frequency ranges with CPE-like processes, whereas in frequency ranges with no significant CPE behavior, the errors have only very less impact on the numerical stability. Comparing the differences in the DRT results for different error levels and structures with the Kramers-Kronig validity test of the underlying EIS spectra, a threshold limit of KKR = 0. 5 % was found to ensure a repeatable DRT calculation with only small dependency on the choice of the regularization parameter. This means that high quality of the EIS measurement data is important to decrease the influence of the regularization parameter on the DRT result. These findings lead to the recommendation to use the optimization strategy for the regularization parameter proposed by Schlüter [166] which is based on a minimization of the variance between DRT spectra of EIS data sets at the same operation point. This concept can be extended and improved by taking possible frequency dispersion effects into account, as shown in this thesis.

Influence of the EIS frequency range

Based on the results for different maximum frequencies, it can be stated that there is a clear correlation between the maximum frequency and the position of the sharp high-frequency artificial peak. In the simulations based on ideal EIS spectra, the sharp artificial peak was located exactly at the maximum frequency of the underlying data set, scaling with the CPE exponent of the 2000 Hz process. By increasing the maximum frequency and thereby the distance between the 2000 Hz process and the maximum frequency, the expression of this sharp artefact in terms of its peak heights is reduced. Unfortunately, there is evidence that additional artefacts between the high - frequency electrochemical process and f_{max} arise for simulations up to 100 kHz and 1 MHz which are additionally affected by statistical errors, which is complicating their identification as artefacts, also because there is no clear correlation to measured frequency range. Furthermore, it was observed that the expression of all high-frequency artefacts is increased with decreasing values of the regularization parameter. In order to investigate similar effects in the low-frequency regime, simulations with different minimum frequencies were conducted as well. In this case, no clear correlation was observed between the CPE – n1 of the low-frequency process and the artificial peaks in the low-frequency regime of the DRT. For simulations based on ideal EIS spectra, no artefacts could be observed at all. Based on these results, it can be concluded that the mechanism behind the expression of low-frequency artefacts is different from the one governing the high-frequency artefacts. Further investigation is needed to understand the root cause of the low-frequency artificial peaks, which is outside of the scope of this thesis.

4.4 Verification of results on experiment

In order to verify the simulation results which were stated in the previous chapter on experimental EIS data, measurements were conducted on an SOFC stack in the Jülich F10-Design with two Anode supported Cells (ASC) at the IEK-14 of the Jülich Research Center. The cells consist of an LSC cathode with an LSCF contact coating and a Ni-YSZ anode contacted with a Nickel mesh. The cell area is 80 cm^2. The interconnect material is Crofer 22 APU with a manganese cobalt ferrite (MCF) protective coating on the air side. The stack was sealed with glass with a clamping pressure of 1 kN. The internal number of the stack is F1002-197 and it was installed in the test bench with the number MP04. In Table 4.4.1, the operation parameters of the stack for the conducted EIS measurement are summarized. All EIS spectra were measured starting at high frequencies with 5 A DC current and 2 A AC current, ensuring that the cell does not reach the electrolysis mode.

Table 4.4.1: Operation and measurement parameters for the EIS study on the SOFC stack F1002-197.

Sample	frequency range 100 mHz -	Temperature [°C]	H2 flow [slm]	H2O [vol-%]	Air flow [slm]
EIS 13	**10 kHz**	**800**	**2**	**0**	**8**
EIS 14	**50 kHz**	**800**	**2**	**0**	**8**
EIS 15	**100 kHz**	**800**	**2**	**0**	**8**
EIS 16	**10 kHz**	**650**	**2**	**0**	**8**
EIS 17	**50 kHz**	**650**	**2**	**0**	**8**
EIS 18	**100 kHz**	**650**	**2**	**0**	**8**
EIS 20	**10 kHz**	**700**	**2**	**0**	**8**
EIS 21	**50 kHz**	**700**	**2**	**0**	**8**
EIS 22	**100 kHz**	**700**	**2**	**0**	**8**

Special emphasis was put on the interplay of the maximum frequency of the EIS measurement and the sharp high - frequency peak as well as on the suppression of oscillations with optimized values of the regularization parameter. This optimization was done via minimizing the differences between the DRT spectra based on EIS spectra measured in different frequency ranges – either by different measurement ranges or cutting off the data at certain frequencies. This approach is an extension of the optimization procedure proposed by Schlüter [166]. The purpose of cutting the measurement data was to check if the results of cut-off EIS spectra are comparable to those of EIS spectra measured to the respective maximum frequencies.

After identifying the real electrochemical processes and exclusion of the artificial peaks, the respective single polarization resistances of the real processes are calculated via the approximation formula for the area of Gaussian peaks which is given by:

$$A_p = 1.0645 \cdot FWHM \cdot h \tag{90}$$

with the peak height h and the FWHM of the DRT peak. It has to be emphasized that this approximation is only valid for approximating the polarization resistance if Gaussian functions are used as RBFs in the discretization procedure of the DRT calculation in DRTtools. For the calculation, the MATLAB built-in function *findpeaks* was used to filter the real processes with a position tolerance of +/- 10 % and determine the peak height and FWHM of the single peaks for the calculation of the peak area using equation (90).

Applying this relationship to the DRT spectra in the respective range of optimized regularization parameters, an averaging is done over different λ values and subsequently over the results for different frequency ranges. This means that the polarization resistances have to be treated as averaged estimated values. These values were subsequently used to calculate an Arrhenius plot of the single electrochemical processes. Furthermore, the single polarization resistances were summed up to be compared with the total polarization resistance determined by integrating the DRT spectrum over the entire frequency range. Details on the accuracy of the total polarization determined by means of the integration of the DRT over the entire frequency range can be found in the Appendix/Part B.

In the following chapters, the results of the DRT analysis of EIS measurements at different stack temperatures are presented.

4.4.1 Measurements at 650 °C

In Figure 4.4.1, the Nyquist plots of the EIS measurements for cell 1 (a) and cell 2(b) at 650 °C are shown. Cell 1 thereby refers to the bottom cell and cell 2 to the top cell of the 2-layer stack. A difference concerning the inductive tail at high frequencies is clearly seen between cell 1 and 2.

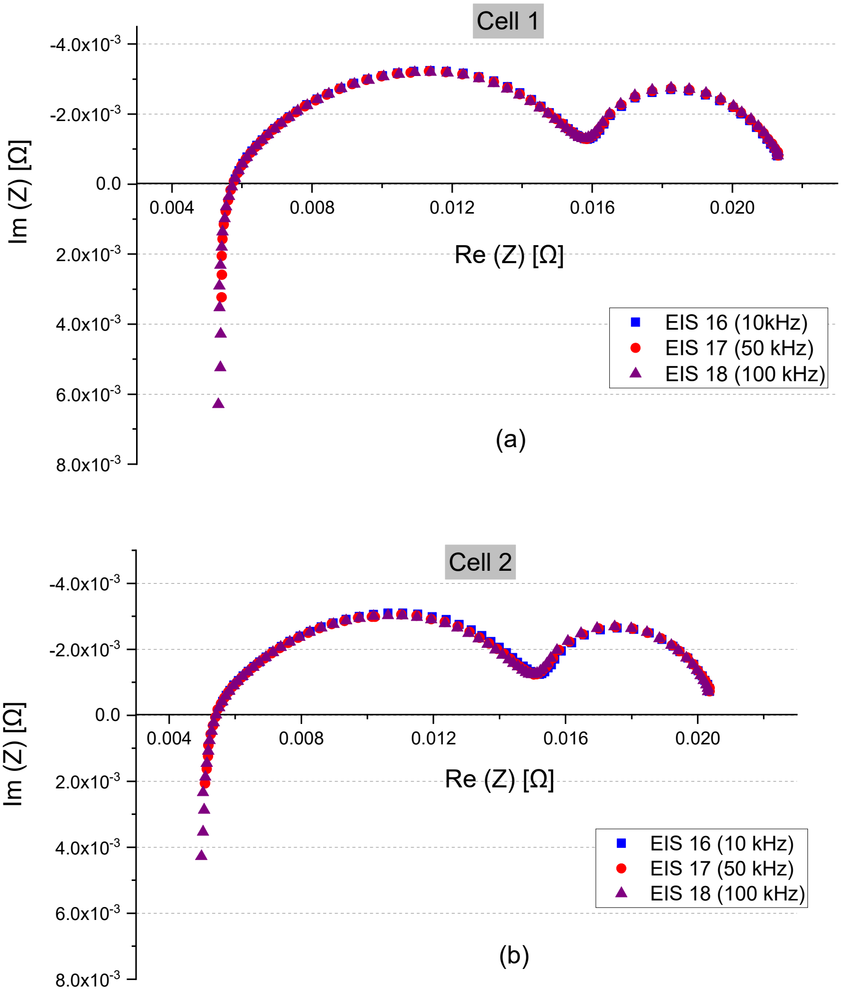

Figure 4.4.1. Nyquist diagrams for EIS 16 – 18 with the bottom cell 1 in (a) and the top cell 2 in (b) measured at 650 °C.

The ohmic resistance for cell 1 is 5. 5 mΩ. By subtracting this value from the (extrapolated) low-frequency intersection with the x-axis, the sum of polarization losses of the electrochemical processes is determined and is roughly 15. 6 mΩ.

In order to investigate the measurement error in more detail, Kramers-Kronig validity tests were performed with the Linear KK-Tool. The results are shown in Figure 4.4.2 for cell 1 and Figure 4.4.3 for cell 2. In the KKR plots it can be observed that the measurements are very accurate, exhibiting a low error level and for measurements except EIS 18, which is starting at 100 kHz, the KKR are well within the previously proposed 0. 5 % limit. Therefore it can be expected that low values for the regularization parameter can be chosen without causing significant oscillation, as long as frequency dispersion effects are not too pronounced.

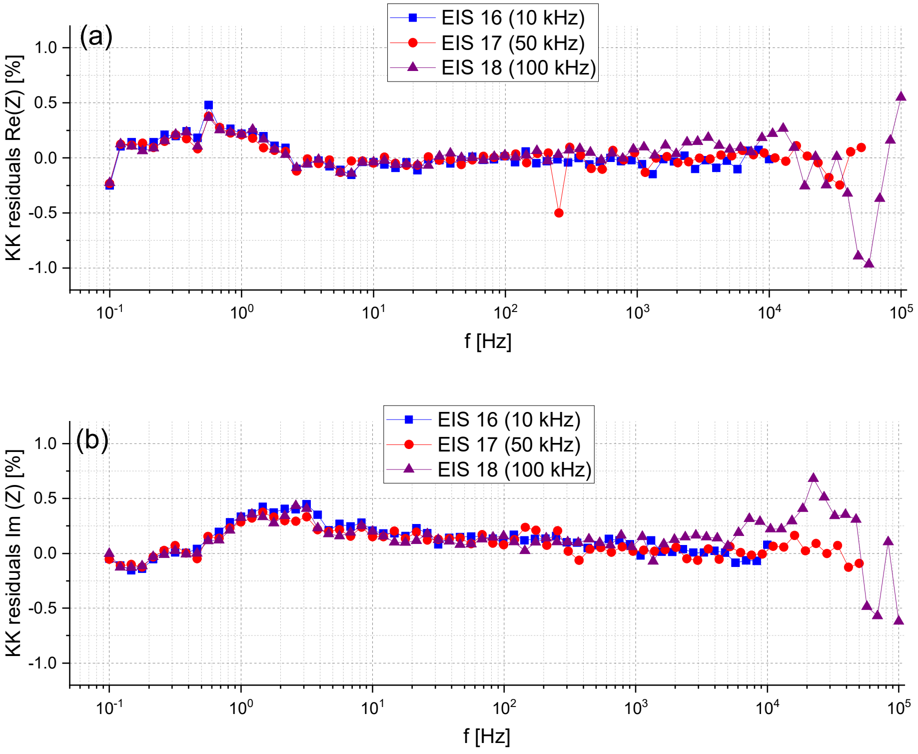

Figure 4.4.2. Kramers-Kronig residuals for EIS 16 – 18 for real (a) and imaginary (b) part for cell 1 at 650 °C.

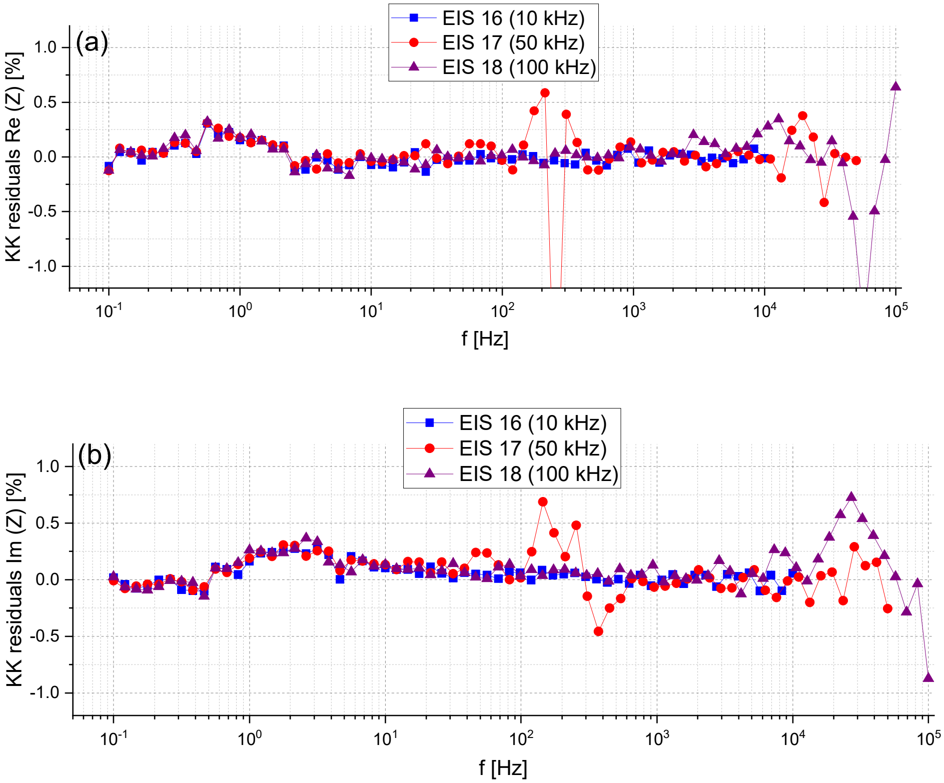

Figure 4.4.3. Kramers-Kronig residuals for EIS 16 – 18 for real (a) and imaginary (b) part for cell 2 at 650 °C.

Looking closer in the high-frequency range, a bias in the KKR, which is increasing with increasing frequency can be observed. This effects is greater the higher the starting frequency of the EIS measurement.

In Figure 4.4.4, the DRT spectra for cell 1 with regularization parameters of $\lambda=10^{-4}$ and $\lambda=10^{-5}$ are shown. As observed in the simulation study, artificial peaks are located at the maximum frequency of the underlying EIS spectrum, except for the EIS measurement starting at 100 kHz. It could be shown in the simulation study that the probability of the expression of the maximum frequency peak is decreases with increasing f_{max} and additionally depends on the statistical error especially for high frequencies. Looking at the frequency range from 5 kHz to 50 kHz, another artificial peak appears at roughly 10 - 20 kHz. This peak was detected as an artefact also in the simulation study. Based on these results, this peak is not treated as an electrochemical process as well.

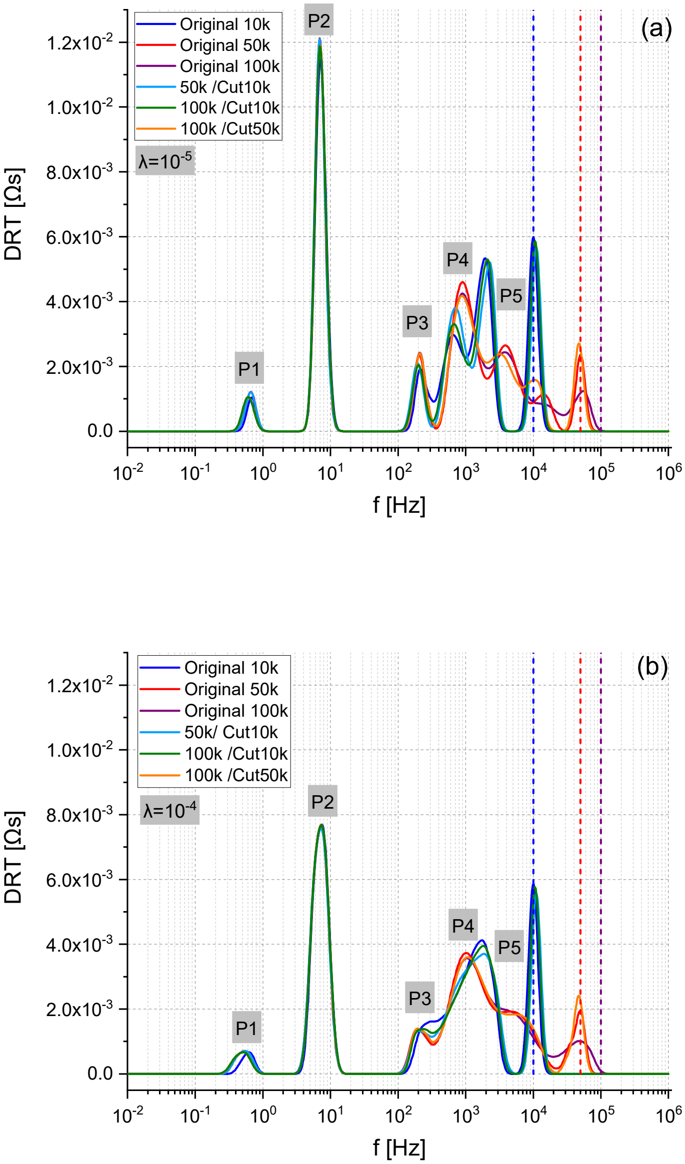

Figure 4.4.4. DRT plots for EIS measurements at 650 °C on different frequency ranges with λ=10^{-5} *(a) and λ=10*$^{-4}$ *(b) for cell 1. The colored dashed lines mark the respective maximum frequency in the underlying EIS data set.*

These experimental results emphasize the relevance of the simulation results and highlight the risk of misinterpretations especially for low values of the regularization parameter, as this additional peak at 10 kHz to 20 kHz only appears for regularization parameters as low as 10^{-5}. If the high-frequency artefacts are cancelled out, five electrochemical processes can be identified in the DRT spectrum. As there was evidence that measurement errors can also cause artefacts in the low-frequency area and peaks in the frequency range between 0. 1 and 1 Hz were observed in the simulation study, the peak at 0. 5 – 0. 7 Hz could potentially be an artefact. However, this peak is observed for all EIS measurements for cell 1 and cell 2 and is therefore considered to be a real electrochemical process. Furthermore, this process has been identified before in [56] to represent a process related to gas transport at the air electrode, but only at low oxygen partial pressure. This may indicate a possible degradation of the air electrode after previous operation.

Another important finding is that the DRT results for cut-off EIS spectra and spectra measured to lower maximum frequency are essentially the same, which means that in theory one measurement to high frequency is sufficient and other EIS data sets with different frequency ranges can be created via cutting off the high frequency data. Additionally, it can be stated that a single measurement to 10 kHz maximum frequency would not have been sufficient to identify all electrochemical processes contributing to the total loss of the cell, because the artificial maximum frequency peak is covering the process at around 4 kHz to 5 kHz relaxation frequency. In terms of optimization of the regularization parameter, a value between $\lambda=10^{-4}$ and $\lambda=10^{-5}$ is suitable to neither have numerical oscillations nor suppressing electrochemical features. This value was found via minimizing the differences between the EIS data sets. Due to the low error level of the measurement, also regularization parameters around 10^{-5} are applicable without causing severe numerical oscillation.

In Table 4.4.2, the identified peaks for cell 1 are summarized with their average relaxation frequency and polarization resistance, averaged over all calculated DRT spectra for regularization parameters between 10^{-5} and 10^{-4}. The sum of the single polarization resistances is compared with the total integral of the DRT over the entire frequency range, depicted as Total area and is calculated with the *trapz*-function in MATLAB.

Table 4.4.2. List of identified electrochemical processes with their single polarization resistances of cell 1 at 650 °C compared to the total area under the DRT curve.

Relaxation frequency	Polarization resistance +/- standard deviation [mΩ]	Comment
0.5 – 0.6 Hz (P1)	0. 5 +/- 0.02	Real
5 – 7 Hz (P2)	5.5 +/- 0.1	Real
200 – 300 Hz (P3)	1.2 +/- 0.04	Real
0.9 – 1. 2 kHz (P4)	6.8 +/- 1.6	Real
3.5 - 4 kHz (P5)	3.1 +/- 0.2	Real
15 – 20 kHz	-	Artefact
10 kHz / 50 kHz / 100 kHz	-	Artefact
SUM	**17.2 +/- 1.6**	**Total area: 16.3 mΩ**

The results for cell 2 are comparable, with the difference of a clearly pronounced sharp artificial peak at 100 kHz, as can be seen in Figure 4.4.5. This finding confirms the statement from the simulation results, that the magnitude of the inductance is not correlating to the expression of the high frequency artefacts, as the inductive tail is more pronounced for cell 1, where the 100 kHz peak is not observed. The difference in the expression of this peak for cell 1 and 2 will be most probably due to measurement error or different extents of CPE behavior in the high-frequency range. For the EIS spectrum starting at 100 kHz for cell 2 another artificial peak at around 20 kHz is observed. Compared to cell 1, this peak is also clearly visible for a higher regularization parameter, see Figure 4.4.5 (b). As for the characterization of cell 1, this peak is not treated as an electrochemical process. In Table 4.4.3, the calculated polarization resistances are given for cell 2. In summary, cell 2 exhibits a slightly lower polarization resistance compared to cell 1, which is mostly due to a lower polarization resistance of the process at 1 kHz.

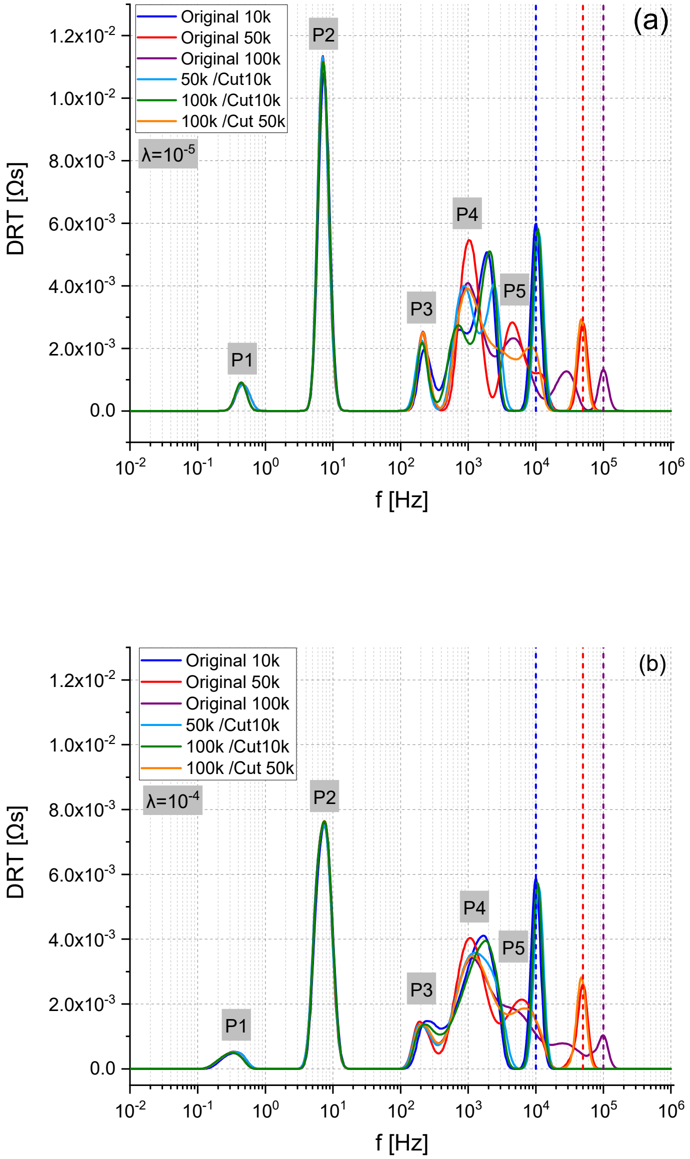

Figure 4.4.5. DRT plots for EIS measurements at 650 °C on different frequency ranges with λ=10^{-5} (a) and λ=10^{-4} (b) for cell 2. The colored dashed lines mark the respective maximum frequency in the EIS dataset.

Table 4.4.3. List of identified electrochemical processes with their single polarization resistances of cell 2 at 650 °C compared to the total area under the DRT curve.

Peak position	Polarization resistance +/- standard deviation [mΩ]	Comment
0.4 – 0.5 Hz (P1)	0.5 +/- 0.04	Real
5 – 7 Hz (P2)	5.4 +/- 0.1	Real
200 – 300 Hz (P3)	1.2 +/- 0.07	Real
1 – 1. 4 kHz (P4)	5.9 +/- 1.5	Real
4 kHz (P5)	3.1 +/- 0.5	Real
15 – 20 kHz	-	Artefact
10 kHz / 50 kHz / 100 kHz	-	Artefact
SUM	**16.6 +/- 1.2**	**Total area: 15.7 mΩ**

4.4.2 Measurements at 700 °C

Visualization of the EIS spectra at 700 °C in the Nyquist diagram are shown in Figure 4.4.6, showing a less pronounced inductance tail compared to the measurements at 650 °C which were shown before. However, it can be observed that the inductive tail is inclined, which was not the case for the measurements at 650 °C.

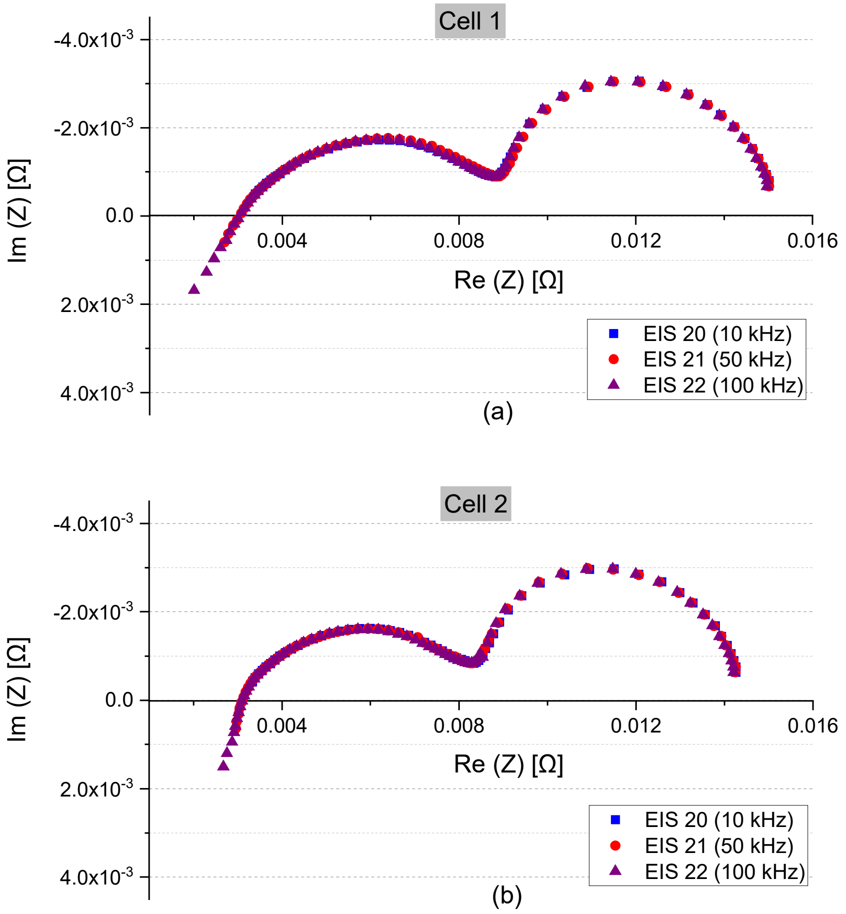

Figure 4.4.6: Nyquist diagrams for EIS 20 – 22 with the bottom cell 1 in (a) and the top cell 2 in (b) measured at 700 °C.

Again, the EIS data were analyzed with the Kramers-Kronig-validity test. The results for cell 1 and 2 are shown in Figure 4.4.7 and 4.4.8 respectively. For the frequency range between 100 mHz and 10 kHz, the KKR lie well within the 0. 5 % limit, with slightly higher deviations between 500 Hz and 10 kHz for Cell 1 compared to Cell 2. It has to be pointed out that for Cell 1 a pronounced bias in the real and to a lesser extent on the imaginary part is seen for measurements starting at 100 kHz maximum frequency. In contrast, the measurement starting at 50 kHz does show a lower level bias. This was also observed for measurements at 650 °C, which were shown before.

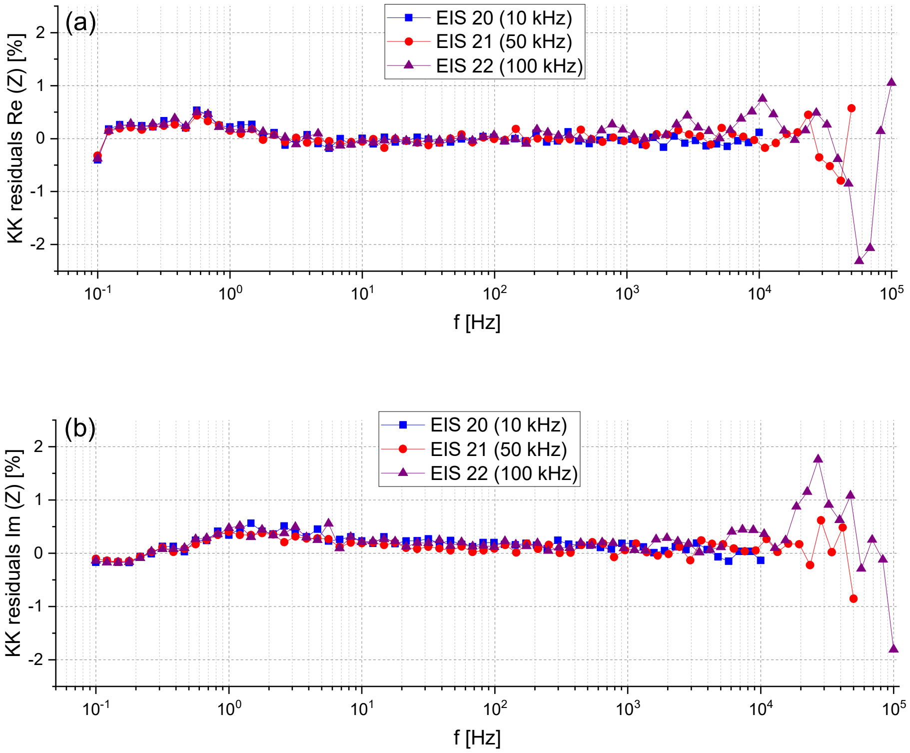

Figure 4.4.7: Kramers-Kronig residuals for EIS 20 – 22 for real (a) and imaginary (b) part for cell 1 at 700 °C.

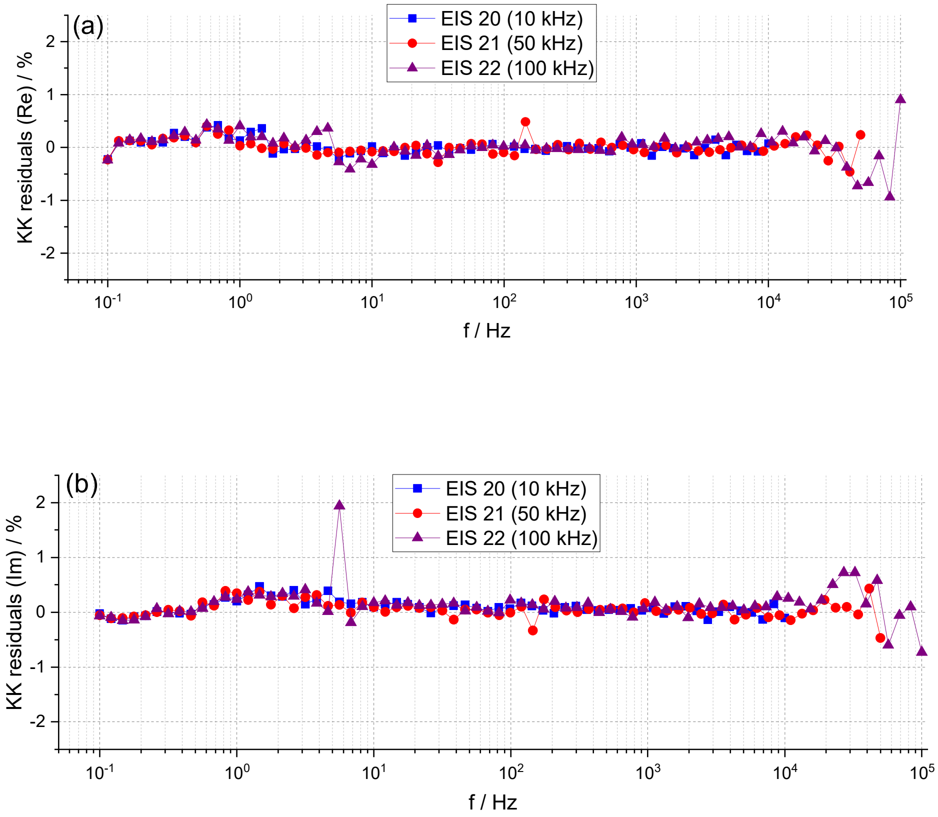

Figure 4.4.8. Kramers-Kronig residuals for EIS 20 – 22 for real (a) and imaginary (b) part for cell 2 at 700 °C.

In the DRT plots for the measurements at 700 °C, which are shown in Figure 4.4.9, the maximum frequency artefacts which were proposed in the simulation study are again clearly pronounced for at all measured maximum frequencies for both cells and can therefore be defined as such and excluded from the interpretation of the electrochemical processes in the cell. Interestingly, the peak at 0. 5 – 0. 7 Hz which was observed in the analysis of the EIS measurements at 650 °C is not existing at 700 °C. From comparison of the differences between the DRT functions, the optimal regularization parameter is again between 10^{-5} and 10^{-4}. Omitting the high-frequency artefacts, four electrochemical processes can be identified in the DRT, namely at around 7 Hz, 300 Hz, 1600 Hz and between 6 kHz and 9 kHz.

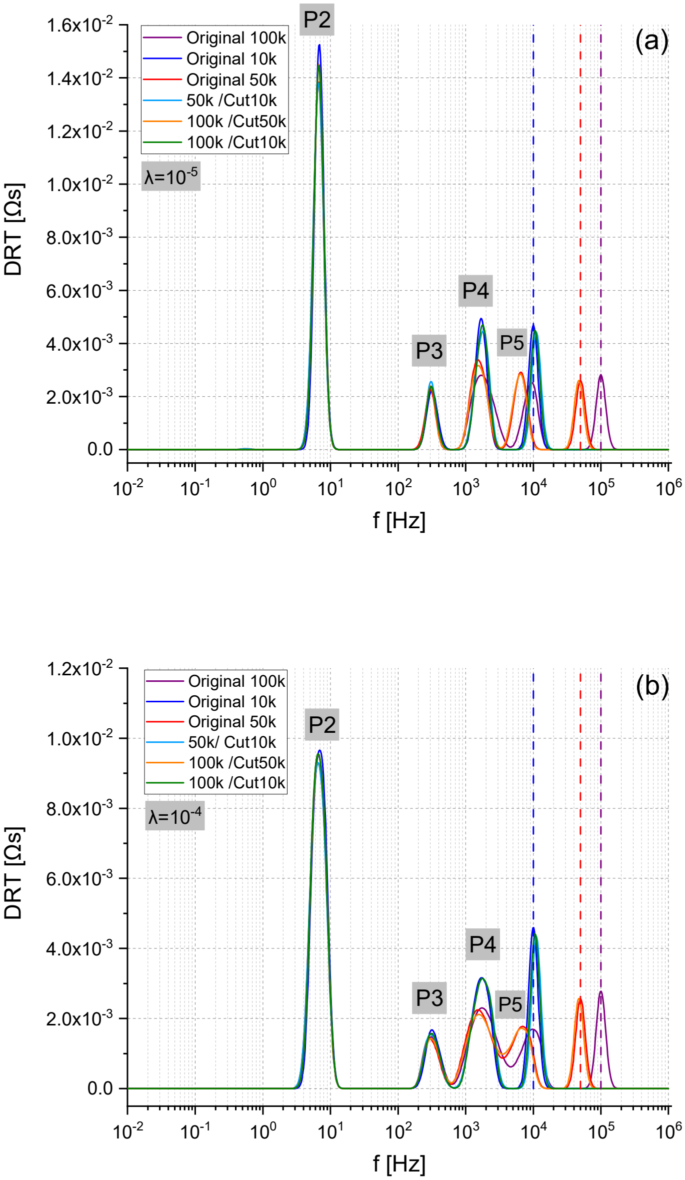

Figure 4.4.9. DRT plots for EIS measurements at 700 °C on different frequency ranges with λ=10⁻⁵ (a) and λ=10⁻⁴ (b) for cell1. The colored dashed lines mark the respective maximum frequency in the EIS data set.

In Table 4.4.4, the calculated relaxation frequencies and estimated single polarization resistances for the identified processes are summarized for cell 1. As for the measurements at 650 °C, the sum of the single polarization resistances calculated from the DRT is matching well to the total polarization calculated by integrating the DRT over the entire frequency range. It is shown in the Appendix/Part B that the integral over the entire frequency range – including the artificial peaks – gives very accurate values of the total polarization. The results shown there are based on the comparison of the total polarization fixed in the ECM and the integral over the entire frequency range for the simulation study.

Table 4.4.4. List of identified electrochemical processes with their single polarization resistances of cell 1 at 700 °C compared to the total area under the DRT curve.

Relaxation frequency	Polarization resistance +/- standard deviation [mΩ]	Comment
6 – 7 Hz (P2)	6.3 +/- 0.1	Real
300– 350 Hz (P3)	1.0 +/- 0.02	Real
1.5– 1.7 kHz (P4)	2.6 +/- 0.1	Real
6 – 9 kHz (P5)	1.7 +/- 0.1	Real
15 – 20 kHz	-	Artefact
10 kHz / 50 kHz / 100 kHz	-	Artefact
SUM	**11.6 +/- 0.2**	**Total area: 12.3 mΩ**

In Figure 4.4.10, the DRT spectra for cell 2 are shown. The results are comparable to cell 1, with a slightly less pronounced peak at around 8 kHz for cell 2. For the simulations starting at 1 MHz, an additional artefacts between the 8 kHz process and the maximum frequency located at roughly 20 kHz is observed.

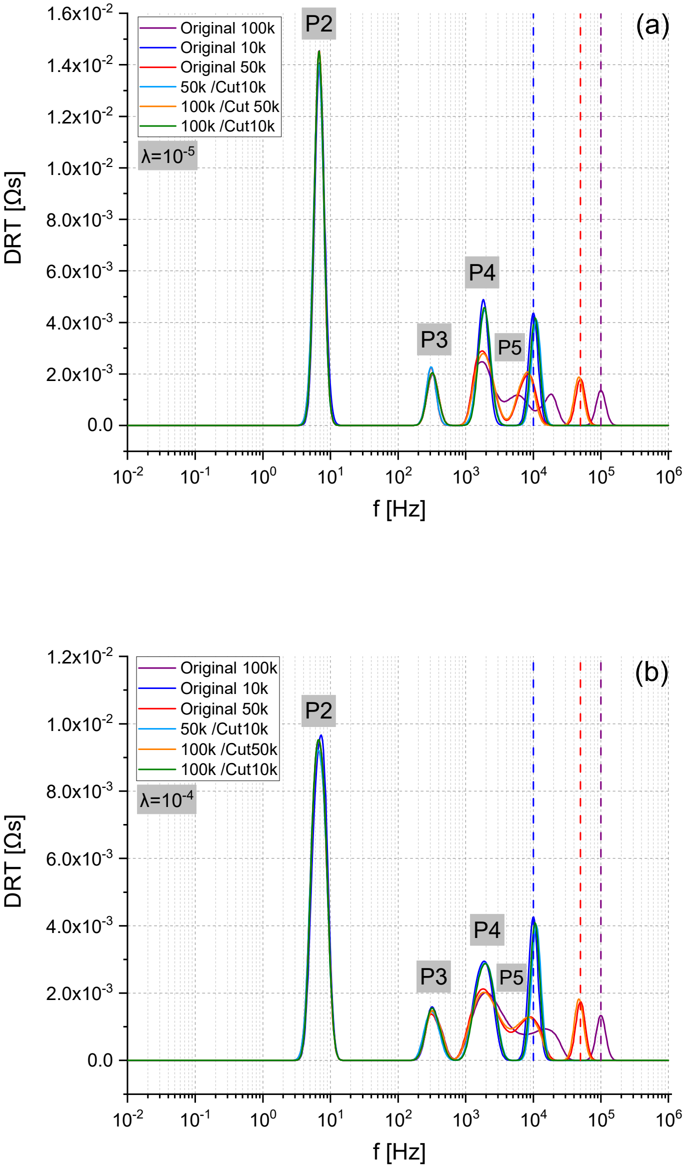

Figure 4.4.10: DRT plots for EIS measurements at 700 °C on different frequency ranges with λ=10^{-5} (a) and λ=10^{-4} (b) for cell 2. The colored dashed lines mark the respective maximum frequency in the EIS dataset.

Based on the findings of the simulation study, this peak can be omitted for the determination of the number of electrochemical processes. Therefore, four distinct electrochemical processes can be identified as well for cell 2. As stated in the last chapter, a single measurement starting at 10 kHz would not have been sufficient to identify all the electrochemical processes involved, as the artefact at the maximum frequency is covering the process located at roughly 8 kHz. The information about the characteristic relaxation frequency of those and an estimation of their polarization resistances can be found in Table 4.4.5.

Table 4.4.5. List of identified electrochemical processes with their single polarization resistances of cell 2 at 700 °C compared to the total area under the DRT curve.

Relaxation frequency	Polarization resistance +/- standard deviation [mΩ]	Comment
6 – 7 Hz (P2)	6.1 +/- 0.1	Real
300– 350 Hz (P3)	0.9 +/- 0.03	Real
1.5– 1.7 kHz (P4)	2.6 +/- 0.3	Real
6 – 9 kHz (P5)	0.8 +/- 0.07	Real
15 – 20 kHz	-	Artefact
10 kHz / 50 kHz / 100 kHz	-	Artefact
SUM	**10.4 +/- 0.7**	**Total area: 11.4 mΩ**

4.4.3 Measurements at 800 °C

In Figure 4.4.11, the Nyquist diagrams for the EIS measurements at 800 °C are shown. The length of the inductive tail at positive values of the imaginary part is comparable to the measurements at 700 °C. Again the inclination of the tail is higher for cell 1 compared to cell 2.

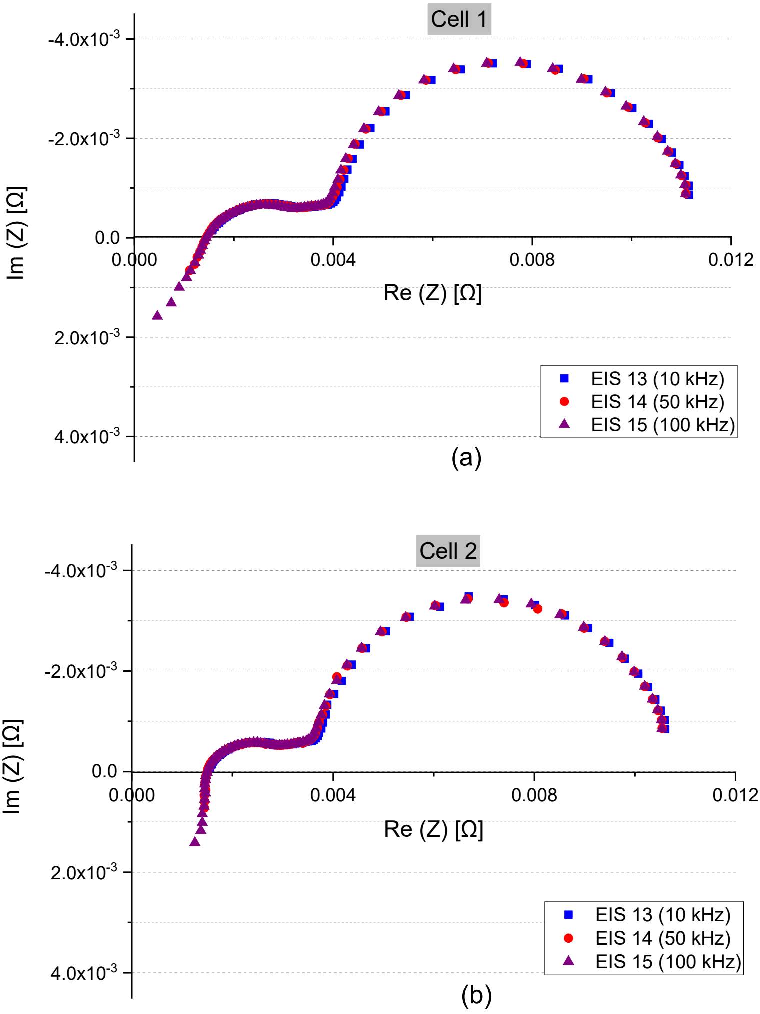

Figure 4.4.11. Nyquist diagrams for EIS 13 – 15 with the bottom cell 1 in (a) and the top cell 2 in (b) measured at 800 °C.

A significant difference to the measurements at lower temperatures is that the measurements at 800 °C exhibit a higher level of KK residuals, as shown in Figure 4.4.12 for cell 1. As observed in the measurements at 650 °C and 700 °C, there is a bias visible in both the KKR of the real and imaginary part of the impedance, which is more pronounced in cases in which the EIS measurement is started at higher frequencies. Additionally, the KKR over the remaining frequency range are higher compared to the results that were obtained at lower temperatures. A possible root cause for the higher instability is a worse signal-to-noise ratio when the total polarization of the cell is reduced by an increased temperature. However, in the range from 100 mHz to roughly 1 kHZ, the KKR are still within the limit of +/- 0. 5 % for both the real and imaginary part.

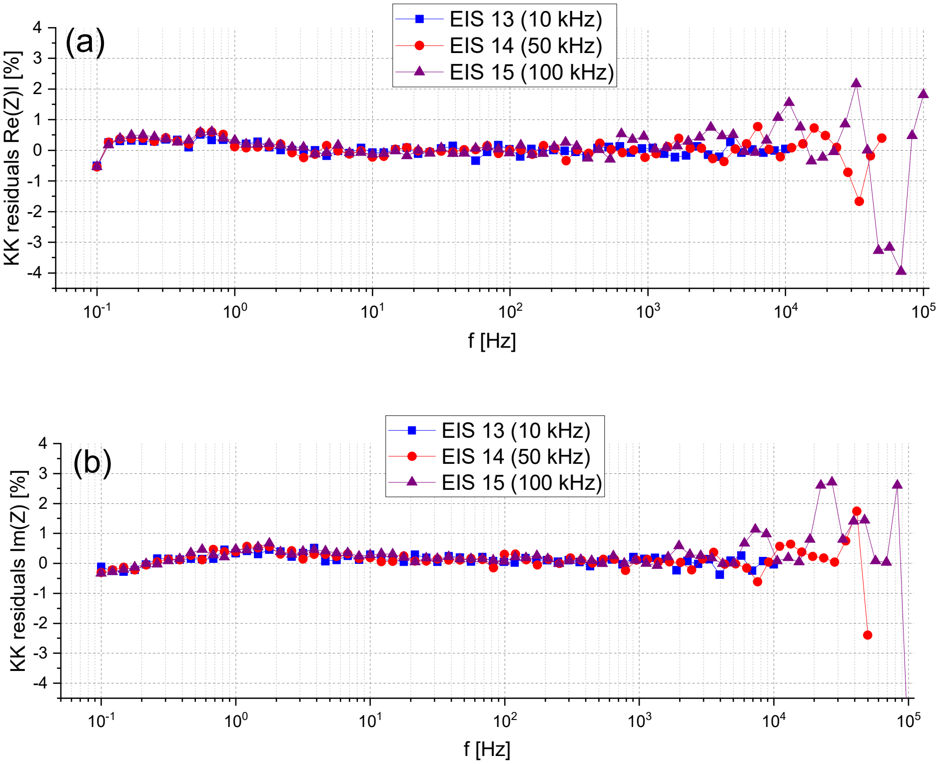

Figure 4.4.12. Kramers-Kronig residuals for EIS 13 – 15 for real (a) and imaginary (b) part for cell 1 at 800°C.

As observed in the measurements at 700 °C, the bias in the KKR for the real and imaginary part is less pronounced for cell 2, resulting in lower residuals in the high-frequency range, as shown in Figure 4.4.13. Regarding the remaining frequency regime, the KKR are comparable to those of cell 1, with some outliers around 1 Hz and 200 Hz in the real part and around 3 Hz in the imaginary part for the measurement starting at 50 kHz maximum frequency.

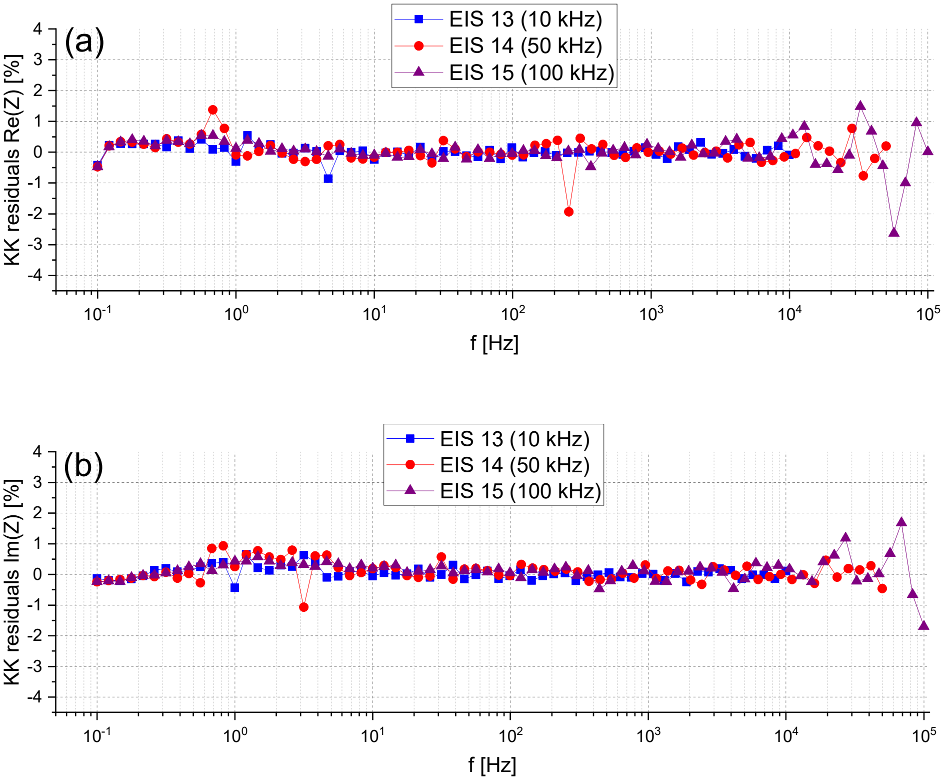

Figure 4.4.13. Kramers-Kronig residuals for EIS 13 – 15 for real (a) and imaginary (b) part for cell 2 at 800°C.

In Figure 4.4.14, the graphical depiction of the DRT spectra calculated for cell 1 can be found. Like for the measurements shown in the previous sections, the artificial maximum frequency peaks are visible at 10 kHz, 50 kHz and 100 kHz and can therefore be declared as numerical artefacts and excluded from the electrochemical characterization of this cell.

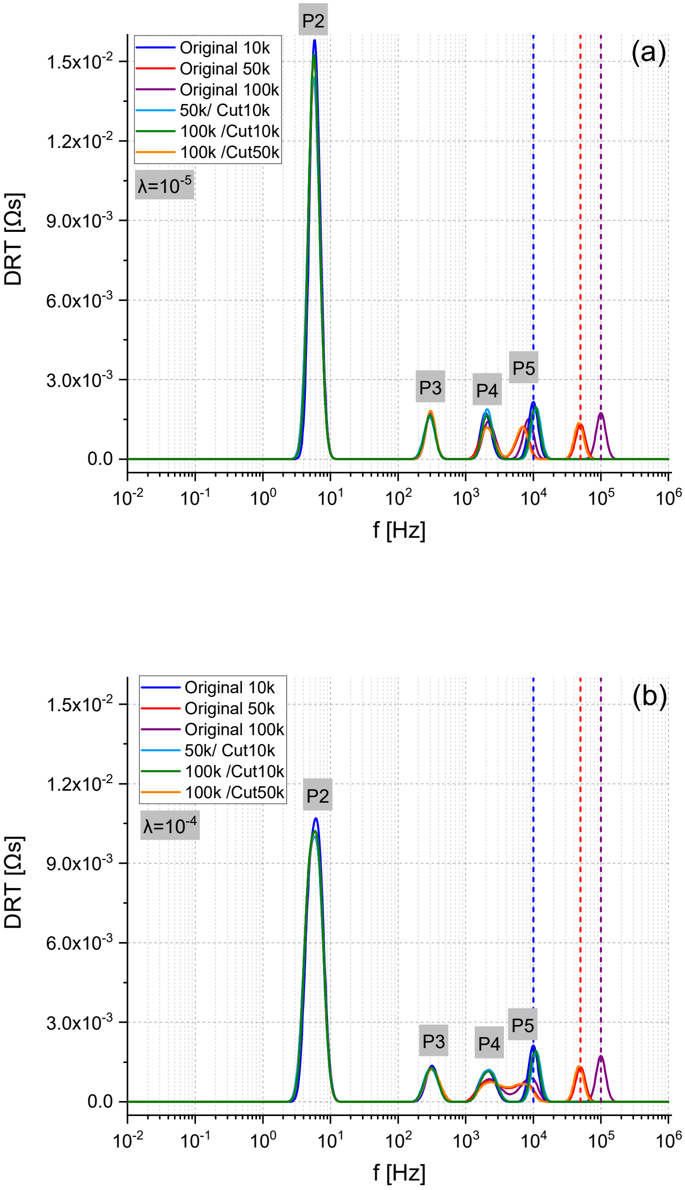

Figure 4.4.14. DRT plots for EIS measurements at 800 °C on different frequency ranges with λ=10^{-5} (a) and λ=10^{-4} (b) for cell 1. The colored dashed lines mark the respective maximum frequency in the EIS dataset.

Compared to the measurements at lower temperatures, no artificial peak at roughly 15 - 20 kHz is visible, regardless of the regularization parameter.

Looking at the measurement starting at 10 kHz, only three peaks are visible besides the artefact because it is covering a high-frequency electrochemical process. Therefore a single EIS measurement starting at 10 kHz would not have been sufficient to identify all processes. For measurements starting at higher frequencies of 50 kHz and 100 kHz, the high-frequency process can be identified leading to a total number of four electrochemical processes as in the measurement at 700 °C. Their estimated relaxation frequencies and respective polarization resistances can be found in Table 4.4.6.

Table 4.4.6. List of identified electrochemical processes with their single polarization resistances of cell 1 compared to the total area under the DRT curve.

Relaxation frequency	**Polarization resistance +/- standard deviation [mΩ]**	Comment
5 – 6 Hz (P2)	7.5 +/- 0.1	Real
300 –320 Hz (P3)	0.8 +/- 0.01	Real
2 – 3 kHz (P4)	0.8 +/- 0.06	Real
7 – 9 kHz (P5)	0.7 +/- 0.02	Real
10 kHz / 20 kHz / 100 kHz	**-**	Artefacts
SUM	**9.7 +/- 0.2**	**Total area: 10.0 mΩ**

In Figure 4.4.15, the results for cell 2 are shown. In this case, the interpretation of the DRT is more challenging, as the process at around 8 kHz is very less pronounced and vanishes for $\lambda = 10^{-4}$. In addition, the maximum frequency peak for the 50 kHz measurement is shifted to the position of the second artificial peak at roughly 20 kHz. The measurements at 800 °C confirm the recommendations that were stated in the summary of the simulation study, that an optimization of the regularization parameter based on purely mathematical principles – such as the minimization of variances between different EIS data sets which would result in $\lambda = 10^{-4}$ - cannot guarantee a correct interpretation of the DRT result. With the additional knowledge gained in the simulation study, the regularization parameter can be reduced to increase the peak resolution in the high-frequency regime while still assuring that the in parallel more enhanced artefacts are not falsely interpreted as additional electrochemical processes. Also the knowledge that additional artefacts between the maximum frequency and the electrochemical process with the highest relaxation frequency may arise can aid the interpretation of the DRT.

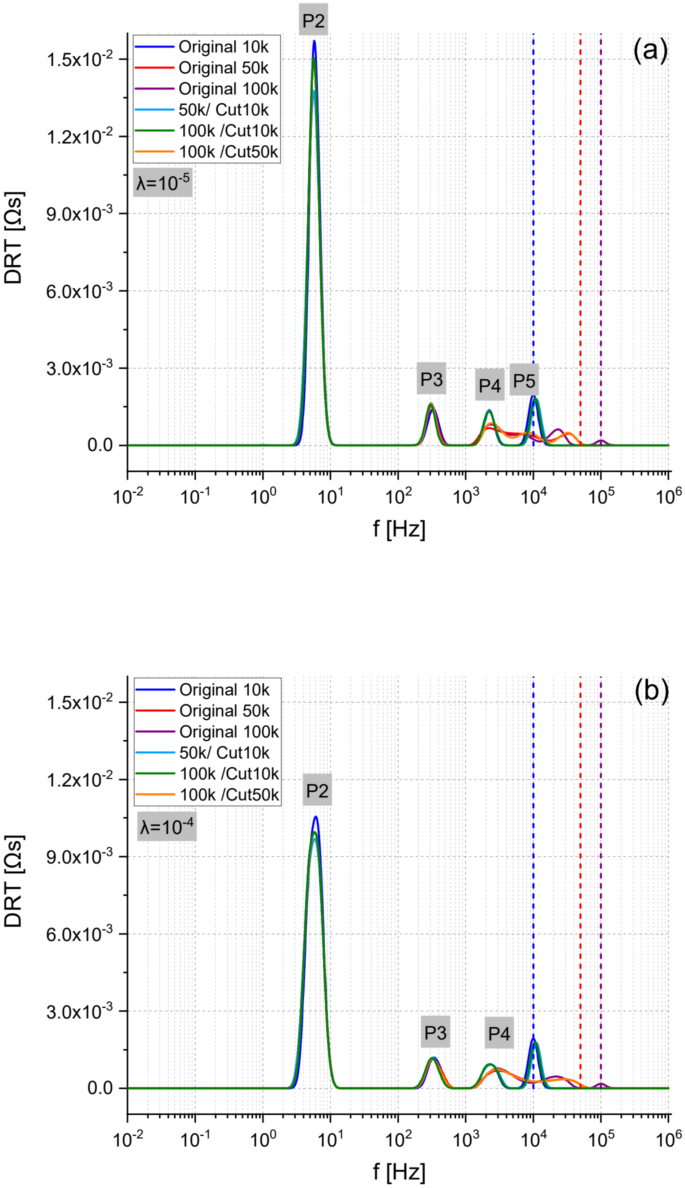

Figure 4.4.15. DRT plots for EIS measurements at 800 °C with different frequency ranges with λ=10^{-5} (a) and λ=10^{-4} (b) for cell 2. The colored dashed lines mark the respective maximum frequency in the EIS dataset.

Furthermore, the results show that the regularization parameter has to be adapted to every operation point separately and should not be kept constant for measurements at different operation conditions by default.

In case of the current measurement for cell, even lower values of the regularization parameter would be beneficial so separate the 8 kHz process from the numerical artefacts, as shown in Figure 4.4.16, in which the DRT calculation was performed with $\lambda = 10^{-6}$.

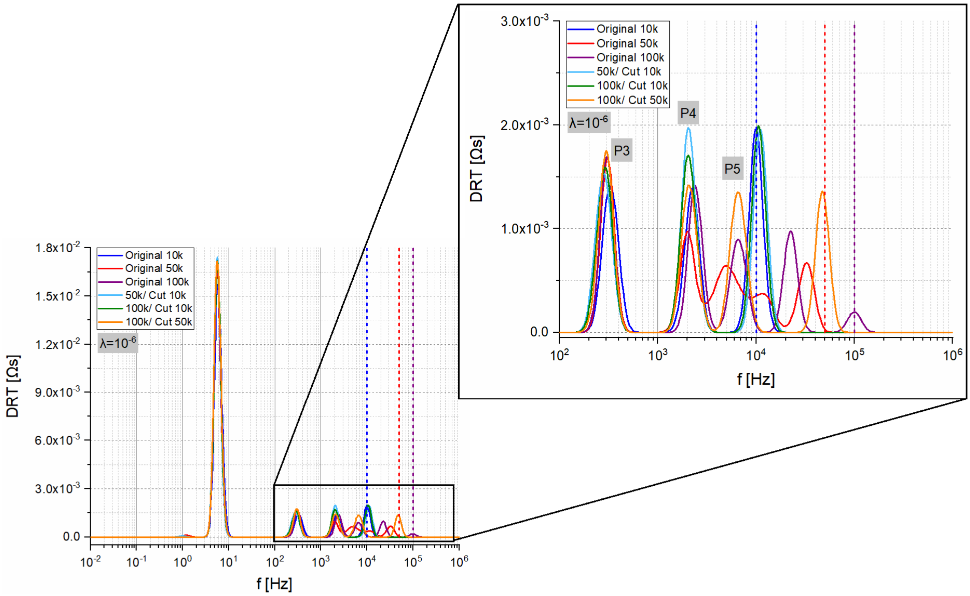

Figure 4.4.16. DRT spectra for cell 2 with a reduced regularization parameter of 10^{-6} to express the electrochemical process at 7-9 kHz relaxation frequency.

Taking all the numerical effects into account, there are four electrochemical processes left. Their relaxation frequencies and respective polarization resistances are summarized in Table 4.4.7.

Table 4.4.7: List of identified electrochemical processes with their single polarization resistances of cell 1 compared to the total area under the DRT curve.

Relaxation frequency	**Polarization resistance +/- standard deviation [mΩ]**	Comment
5 – 6 Hz (P2)	7.3 +/- 0.1	Real
300 –320 Hz (P3)	0.7 +/- 0.01	Real
2 – 3 kHz (P4)	1.1 +/- 0.02	Real
7 – 9 kHz (P5)	1.1 +/- 0.02	Real
10 kHz / 20 kHz / 100 kHz	**-**	Artefacts
SUM	**9.5 +/- 0.5**	**Total area: 9.2 mΩ**

Summary of Verification Results

The important findings of this verification section can be summarized as follows:

1) The high-frequency artificial peaks at the maximum frequency which were identified in the simulation study are also present in the experiment and can therefore be treated as artefacts and excluded from the electrochemical characterization.

2) In case of measurements starting at higher maximum frequencies such as 50 kHz and 100 kHz, also the additional artefacts between 8 kHz and 50 kHz are visible in some cases. Those could also be identified as artefacts based on the simulation study.

3) Excluding the artefacts and only taking into account the real peaks gives a good agreement with the total polarization resistance calculated by integration of the DRT function over the entire frequency range. This comparison could in general aid the DRT analysis to check whether the number of identified processes is correct.

4) The optimization of the regularization parameter as proposed by Schlüter [166] based on the minimization of the variance between DRT spectra calculated with different regularization parameters, is successful in the most cases but has to be extended by the

findings from the presented simulation study to avoid covering electrochemical process by choosing too high values for the regularization parameter. In general, there is the need for an additional physical understanding of the investigated system and knowledge about the numerical instabilities that can potentially occur in the DRT calculation.

5) Different operating parameters such as the temperature will apparently change the properties of the system, such as the polarization resistances of single electrochemical processes. Thereby, the signal-to-noise ratio of the impedance signal and also the relaxation characteristics, such as CPE effects, can be changed leading to a different optimum of the regularization parameter. This means that a purely mathematical approach to optimize the regularization parameter is not sufficient to achieve reliable information from the DRT analysis.

In general it is recommended to perform more EIS measurements starting from different maximum frequencies to confirm the presence of electrochemical processes with high relaxation frequencies. In case of overlapping or less pronounced electrochemical features, a repeated measurement with a higher data point density is recommended based on the simulation results presented in chapter 4.2.3. This approach would have been beneficial for the DRT analysis of cell 2 at 800 °C as well to increase the expression of the process located at 6 – 8 kHz relaxation frequency. Additionally, if there is awareness about the principle characteristics of the high-frequency artefacts, the regularization parameter could be reduced to increase the peak resolution in the desired frequency range. Apparently a change in the regularization parameter can potentially cause an over-regularization in the entire frequency regime, which can lead to undesired peak multiplication in case there are electrochemical processes contributing which exhibit CPE behavior. In case of doubt, a prior CNLS fitting approach is recommended to estimate the degree of frequency dispersion in the investigated system. If all CPE exponents are fairly close to one, an over-regularization is rather improbable, based on the simulation results shown in this thesis.

Bringing all the results of the simulation study and the experimental verification together, there is one major question arising: What is the mechanism behind the expression of high-frequency artificial peaks and why is the constant phase element a main root cause for the expression of those? A possible explanation is elaborated in the following cross-chapter discussion.

5. Cross-chapter discussion

In the simulation studies which were performed in this thesis, it could be shown that the degree of numerical oscillations in the DRT calculation is strongly correlating with the maximum frequency of the underlying EIS data set, the data point density in terms of points per decade and especially the CPE exponent n, which is in general a measure of the broadness of the relaxation frequency distribution of the respective electrochemical process and the deviation of the process from the ideal RC element behavior that equals a CPE – n value of one. It was observed that the expression of the high-frequency artefacts is increasing with decreasing CPE exponent of the high- and to a smaller extent the mid-frequency electrochemical process and that they are mostly located at the maximum frequency. For higher maximum frequencies, additional artefacts appeared between the high-frequency process and f_{max}. Furthermore, the peak height of the sharp artefacts is decreasing with increasing maximum frequency. Parasitic inductances and measurement errors were found to only enhance the numerical instabilities caused by the CPE, but are not the origin of those leaving the CPE as the origin of the observed artefacts. As the observed artificial peaks in the high-frequency are sometimes interpreted as real electrochemical processes in literature, for example in [171] [172], the numerical origin of those needs deeper investigation, which will be presented in the following chapter.

In DRTtools, the DRT function is calculated in two steps, namely the discretization followed by the regularized regression. First, the continuous DRT function is discretized with a sum of N RC elements, each having a characteristic relaxation time τ_n. The mathematical modelling of the single elements can be done with discrete or continuous basis functions, each weighted with a coefficient x_n, as depicted in (90).

$$\gamma\,(\ln\tau) = \sum_{n=1}^{N} x_n \Phi_\mu(|\ln\tau - \ln\tau_n|) \tag{92}$$

In order to achieve a smooth DRT function, radial basis functions are implemented in DRTtools. For this thesis, Gaussian RBFs of the form given in (91) are chosen.

$$\Phi_\mu(x) = \exp(-(\mu x)^2) \tag{93}$$

The shape-parameter μ governs the FWHM of the respective RBFs as FWHM = 1.665 / μ. By default, the shape parameter is twice the distance between adjacent data points, therefore 2 (ln Δτ) and is constant over the entire frequency range. In Figure 5.1, the calculation of the DRT as a sum of weighted basis functions is depicted graphically. Decreasing the CPE exponent of the modeled DRT peak will lead to a broadening of this peak. In this case, there are two possibilities to account for this change. The first one is to enlarge the FWHM of the RBFs by decreasing the shape parameter μ. To account for different extents of CPE behavior in different frequency ranges, a vector or a function of the shape parameter rather than a single value would be needed. Implementing μ as a vector in DRTtools increased the degree of numerical oscillations dramatically. Therefore this approach is not applicable in DRTtools. The second option would be an increase of the number of single RBFs. Unfortunately, the numerical stability of the regularized regression method gets worse with an increasing ratio of the number of RBFs N and the number of experimental collocation points M [159]. In such cases, EIS measurements with higher data point densities would be needed to use more RBFs, as the number of RBFs is fixed to the number of data points in DRTtools. This fact is a possible explanation for the observation that an increased data point density is increasing the accuracy of the DRT result.

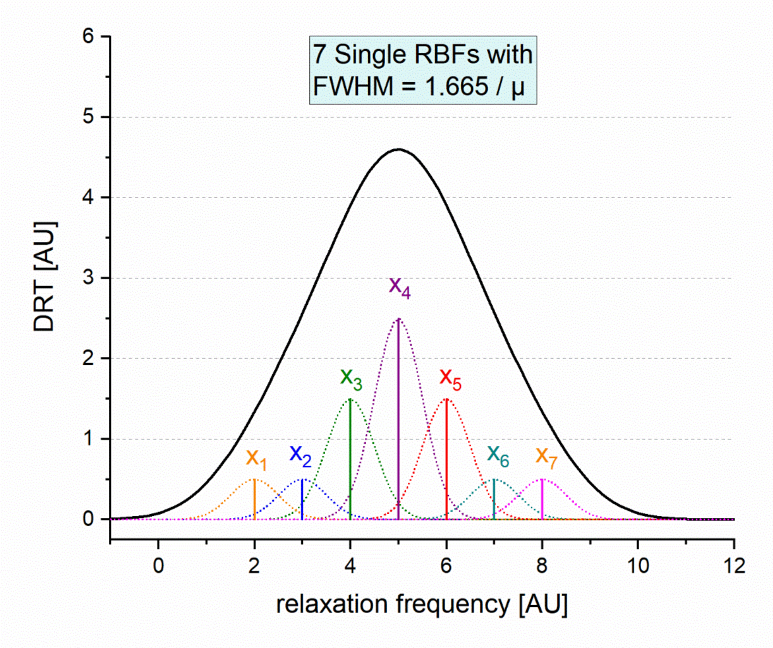

Figure 5.1. Graphical depiction of the modelling of the DRT function as a sum of 7 radial basis functions weighted with coefficients x_1 *to* x_7*.*

If now the number of RBFs is not sufficient and the CPE causes a peak broadening the frequency range of the respective electrochemical process, numerical instabilities may occur leading to a wrong calculation of the weighting coefficients x_n. The potential consequence of this effect is shown graphically in Figure 5.2 as the expression of additional peaks or shoulders on existing peaks, depending on the remaining coefficients and the FWHM. Apparently an additional measurement error will increase numerical instabilities thus enhancing this effect. Based on the simulation results with different CPE exponent in various relaxation frequency ranges, it is obvious that the observed numerical issues are caused by the CPE, as the peak multiplication and the expression of artefacts is closely confined to the frequency range in which the respective simulated process is located. Therefore in principle those effects can arise in the entire frequency range.

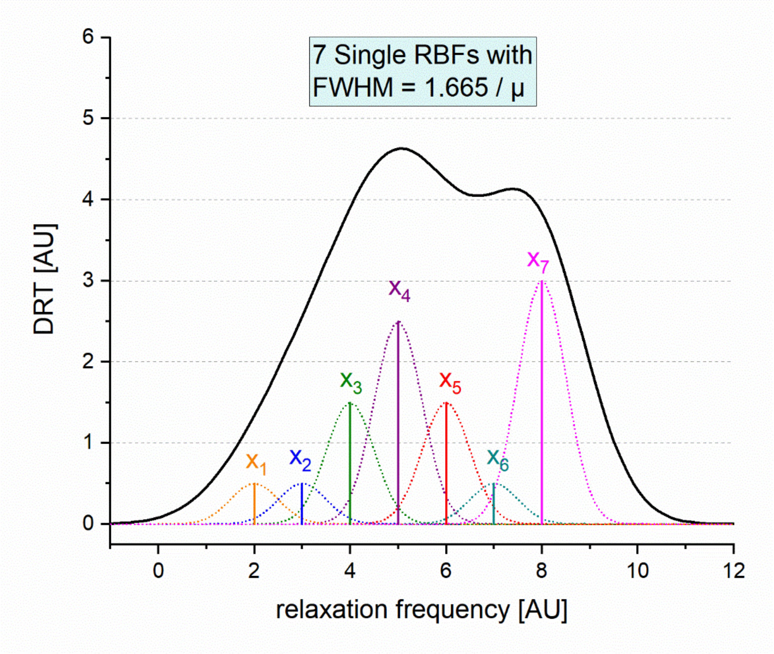

Figure 5.2. Theoretical effect of wrongly determined RBF coefficients xn on the expression of artificial peaks in the DRT spectrum.

However, the most prominent expression of artificial peaks occurred in the high-frequency range and is proven to be caused by CPE effects of electrochemical processes with high relaxation frequencies because the artefacts were also observed in the simulations based on ideal EIS spectra. To investigate the expression of the sharp artefacts located at the maximum frequency and their dependency on the frequency range of the underlying EIS spectrum, the calculated coefficient matrix **x**, which is stored in the variable *x_ridge_combined* in the MATLAB Workspace, was analyzed together with the DRT curve to proof the theoretical hypothesis that was proposed before that fluctuations in the coefficient calculation cause additional artefacts in the DRT spectrum. This analysis was performed on simulated and experimental EIS spectra.

Analysis of simulated EIS spectra

In Figure 5.3, the results of the coefficient analysis for ideal EIS spectra simulated with CPE – n3 = 0. 75 starting at three different maximum frequencies of 10 kHz, 100 kHz and 1 MHz are shown. The regularization parameter is 10^{-4}. The blue curve is the DRT function and the black symbols are the single coefficients x_n. There is a trend visible which shows that the magnitude of the first few x-values decreases with increasing maximum frequency which has then a direct effect on the expression of the sharp artificial peak. It can be clearly observed that the first data point of the EIS input file, which is the measurement point at the highest frequency is causing problems in the regression procedure that is implemented by an interior-point convex optimization algorithm in MATLAB.

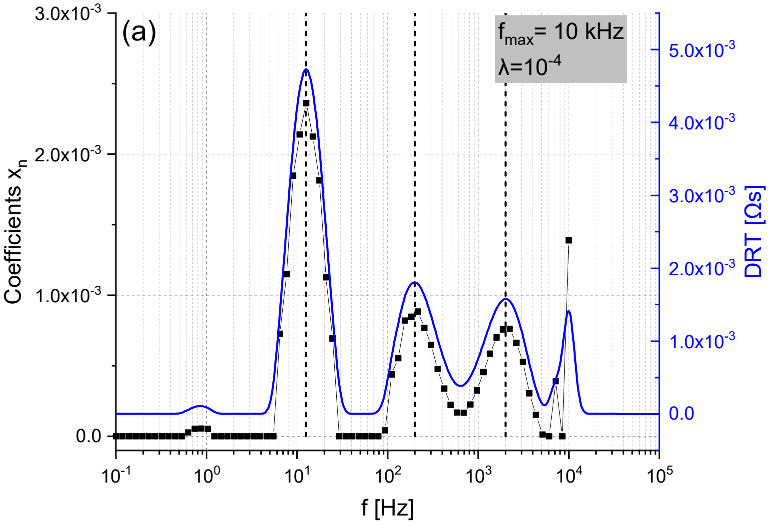

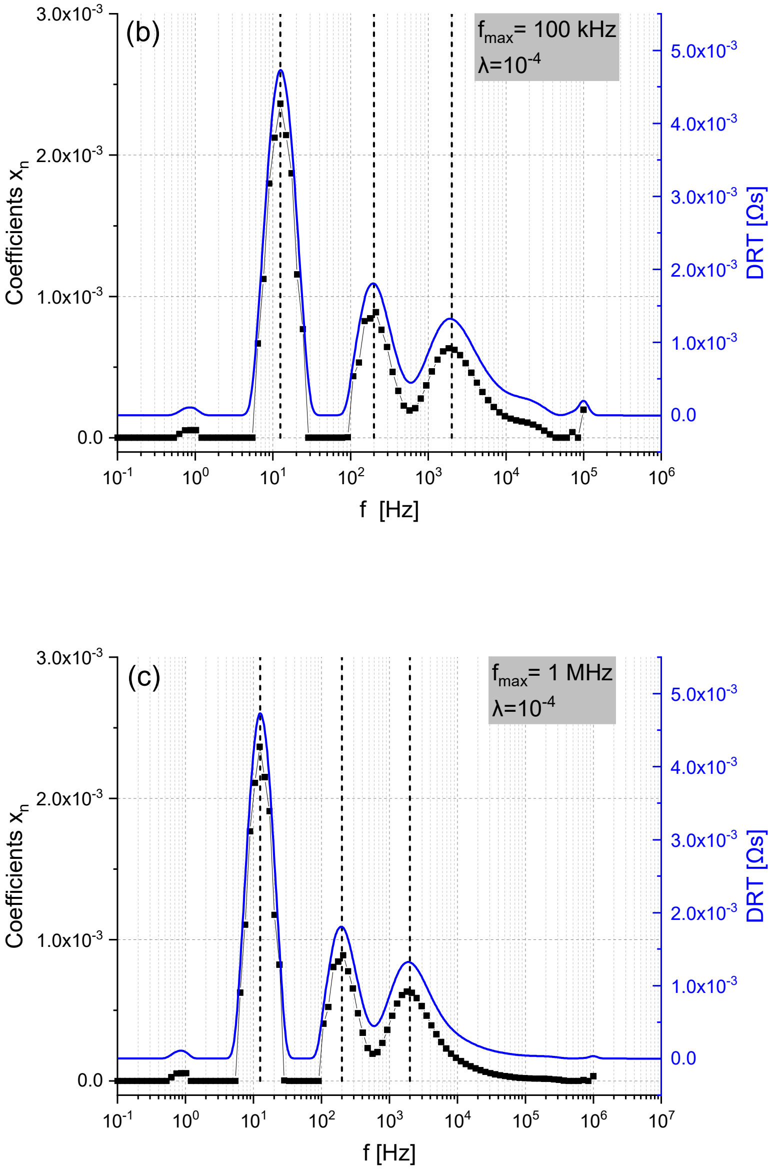

Figure 5.3. Combined analysis of the coefficient matrix ***x*** *(black symbols) and the DRT function (blue line) for ideal EIS simulations starting at 10 kHz in (a), 100 kHz in (b) and 1 MHz in (c) to emphasize the interplay between the constant phase element and the maximum frequency in the expression of high - frequency artefacts. The regularization parameter is* 10^{-4}*. The total polarization resistance is 10 mΩ. L =* $2*10^{-9}$ *H.*

In order to demonstrate the influence of the regularization parameter on the behavior of the numerical oscillations and their interference with the real electrochemical process located at 2000 Hz, the analysis was repeated for a higher regularization parameter of 8*10^{-3}. The results are shown in Figure 5.4.

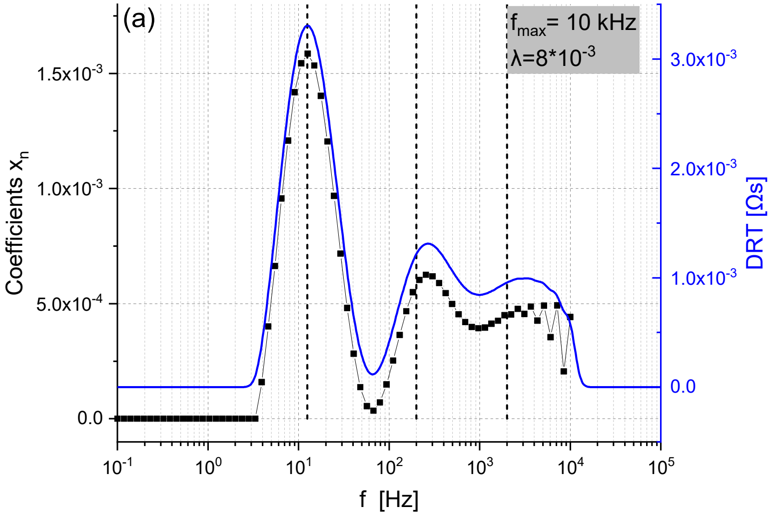

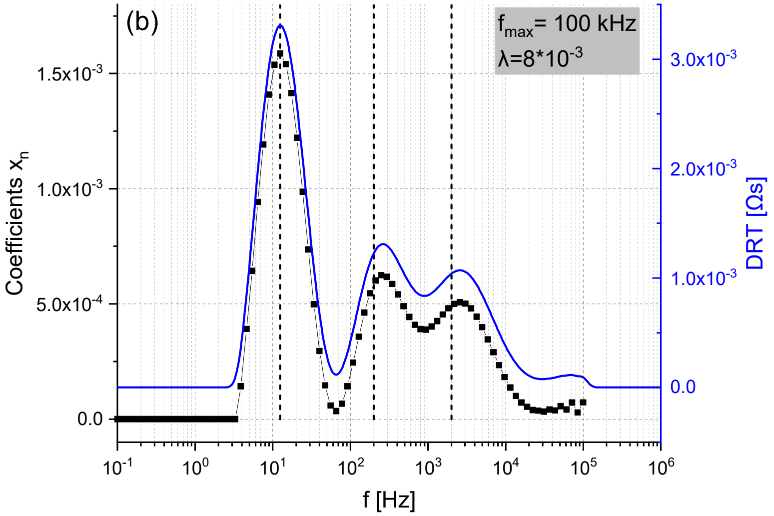

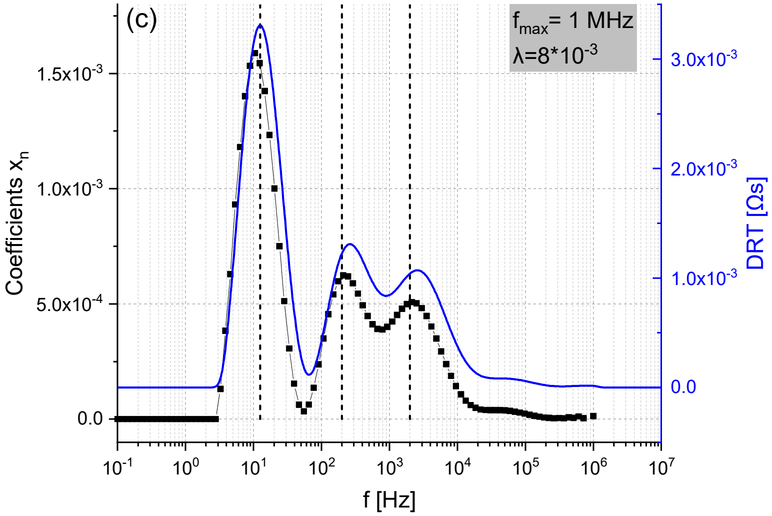

Figure 5.4. Combined analysis of the coefficient matrix ***x*** *(black symbols) and the DRT function (blue line) for ideal EIS simulations starting at 10 kHz in (a), 100 kHz in (b) and 1 MHz in (c) to emphasize the interplay between the constant phase element and the maximum frequency in the expression of high-frequency artefacts. The regularization parameter is 8*10^{-3}. The total polarization resistance is 10 mΩ. L = 2*10^{-9} H.*

It can be observed that depending on the maximum frequency, the instabilities in the coefficient matrix are interfering with the electrochemical process located at 2000 Hz relaxation frequency. While there is a separation between the artefact at 10 kHz and the process for regularization parameters of 10^{-4}, the artefact is already partly covering the electrochemical process if the regularization parameter is increased to 8*10^{-3}. That means that in principle increasing the regularization parameter has a similar effect on the separation of the artefacts from the real processes as increasing the maximum frequency. In order to investigate the role of the CPE exponent in the instability of the calculation of **x** in more detail, the coefficient matrices are plotted for different values of CPE – n3 in Figure 5.5. There a clear correlation between the magnitude of the first coefficient and the CPE – n3 can be observed, as well as a decrease of this value with increasing maximum frequency or distance to the 2000 Hz process. For the simulation starting at 100 kHz, the artificial shoulder between the high-frequency process and the maximum frequency artefact is already seen.

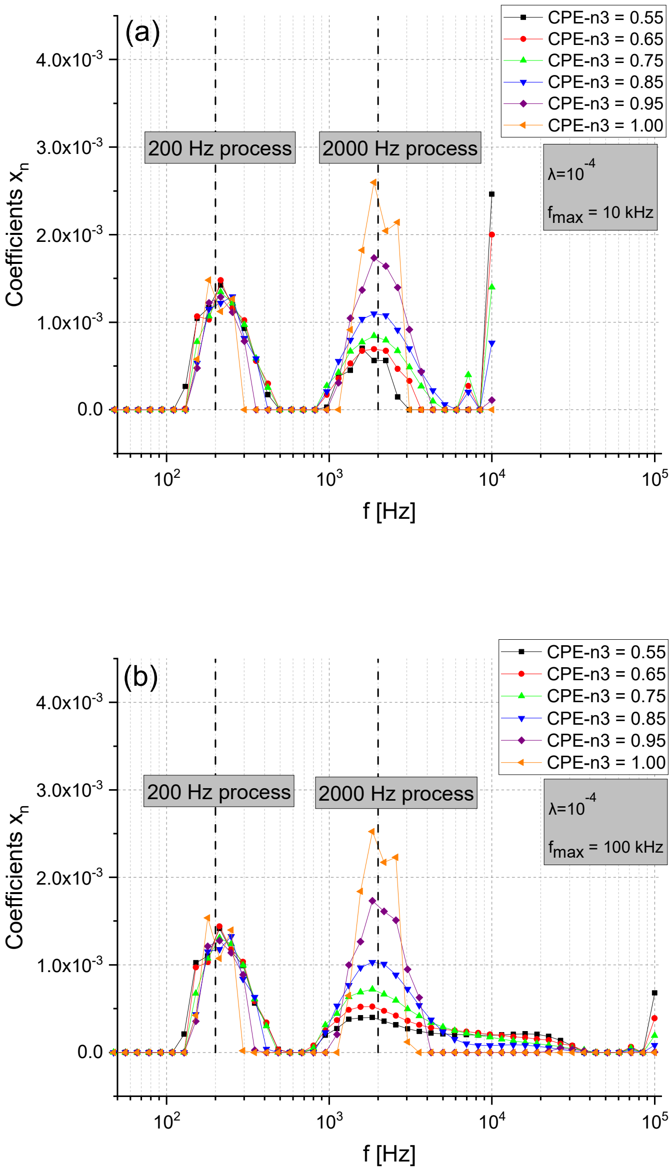

Figure 5.5. Coefficient analysis for different values of CPE – n3 and a maximum frequency of 10 kHz in (a) and 100 kHz in (b). The regularization parameter is 10^{-4}. The total polarization resistance is 10 mΩ. L = $2*10^{-9}$ H.

As there was evidence in the simulation study that those intermediate artefacts are affected by statistical errors, the same CPE analysis was performed for EIS spectra simulated with error model 2. The results are shown in Figure 5.6. While for the simulation starting at 10 kHz, no change in the coefficient characteristics at the highest frequencies can be seen, in the case of simulation starting at 100 kHz the influence of the statistical error is clearly visible as major fluctuations in the frequency range between 2000 Hz and 100 kHz that even lead to the expression of additional peaks, as observed in the simulation study.

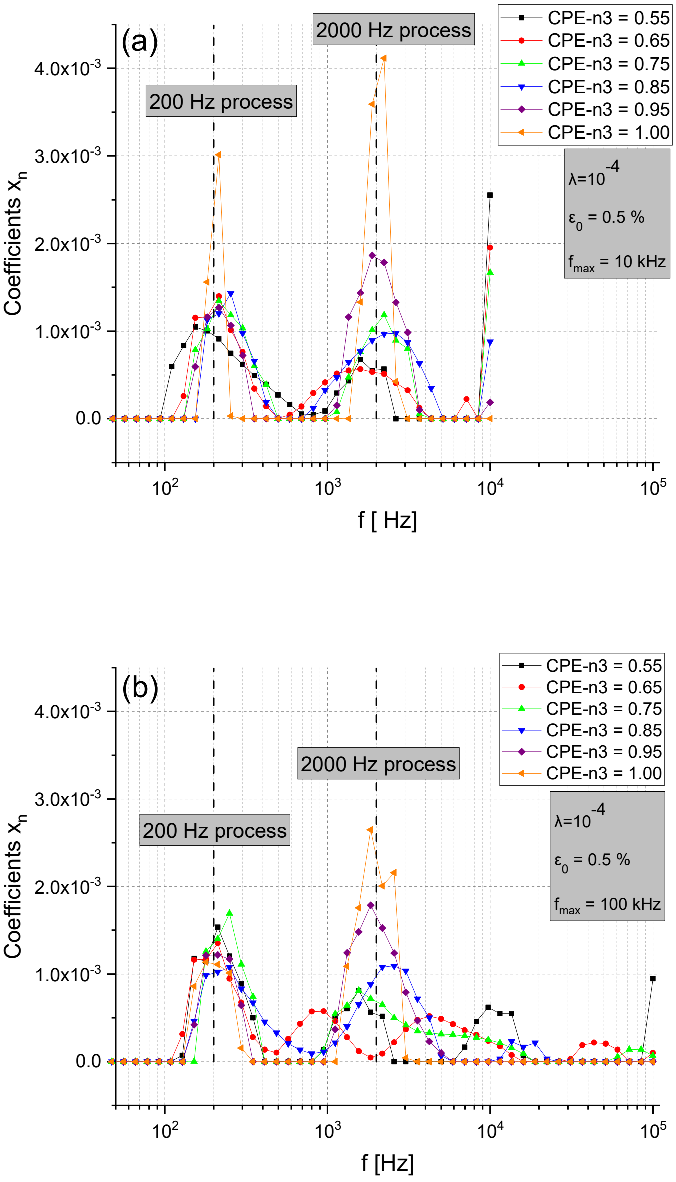

Figure 5.6 Coefficient analysis for different values of CPE – n3 and a maximum frequency of 10 kHz in (a) and 100 kHz in (b) based on EIS spectra simulated with error model 2. The regularization parameter is 10^{-4}. The total polarization resistance is 10 mΩ. L = $2*10^{-9}$ H.

Analysis of experimental EIS spectra

The same analysis that was conducted on the simulated EIS spectra was performed on the experimental EIS spectra to proof the relationships between the maximum frequency, the regularization parameter and the numerical instabilities in the experiment as well. In Figure 5.7, the coefficient matrix is shown together with the DRT function for the measurements at 700 °C starting at 10 kHz, 50 kHz and 100 kHz. The regularization parameter is 10^{-4}. There the same effect is seen that is responsible for the expression of the high-frequency artificial peak, namely a wrong calculation of the first coefficient. To prove the above stated interference of this artefact with high-frequency electrochemical processes, the same analysis was also conducted with a higher regularization parameter of 10^{-3}. The results are shown in Figure 5.8.

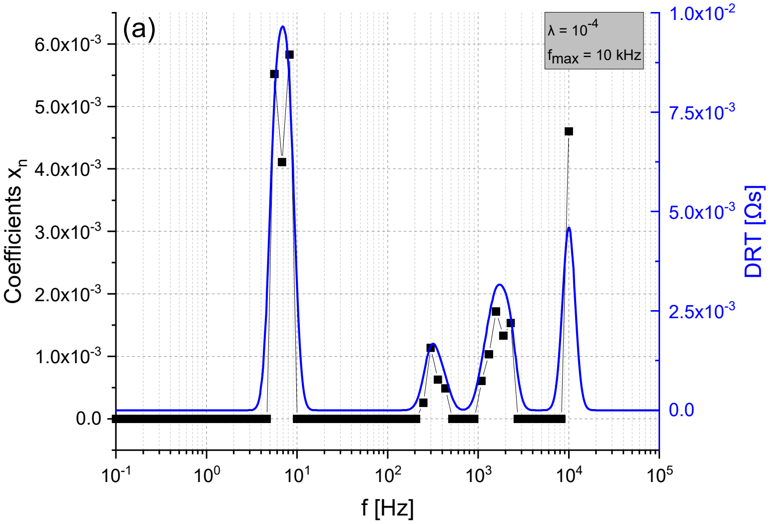

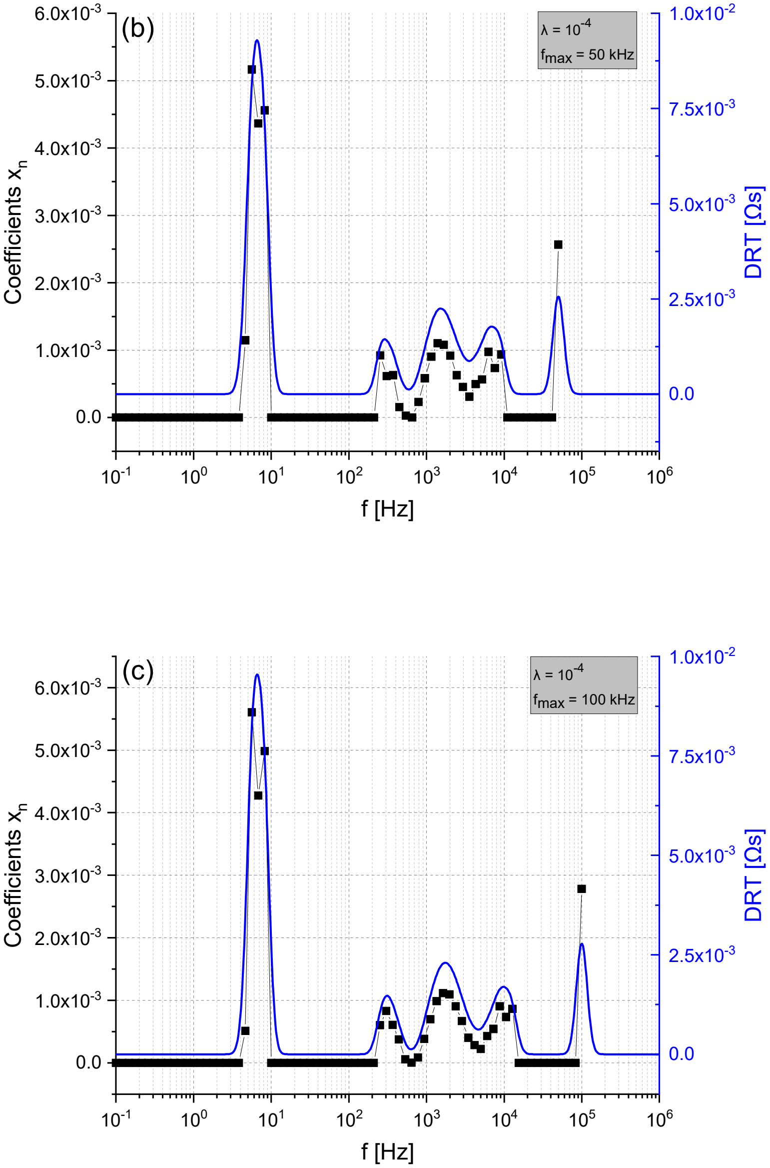

Figure 5.7. Combined analysis of the coefficient matrix x (black symbols) and the DRT function (blue line) for the experimental EIS measurements conducted at 700 °C starting at 10 kHz in (a), 50 kHz in (b) and 100 kHz in (c). The regularization parameter is 10^{-4}.

As expected from the analysis of simulated EIS spectra, the same interference effect is observed in the experimental DRT analysis as well. Similarly to the results shown in advance, there are two possibilities of separating the numerical artefacts from the real electrochemical process, namely decreasing the regularization parameter and/or increasing the maximum frequency. However, there is evidence in the simulation study and also in the analysis of the experimental EIS spectra conducted at 800 °C that an increased maximum frequency can potentially lead to additional artefacts between the electrochemical process with the highest relaxation frequency and the maximum frequency. Therefore, the approach of decreasing the regularization parameter seems to be a promising way to separate the artefacts. Unfortunately this will not only cause a separation of the artefact but also can lead to an over-regularization in the remaining frequency range.

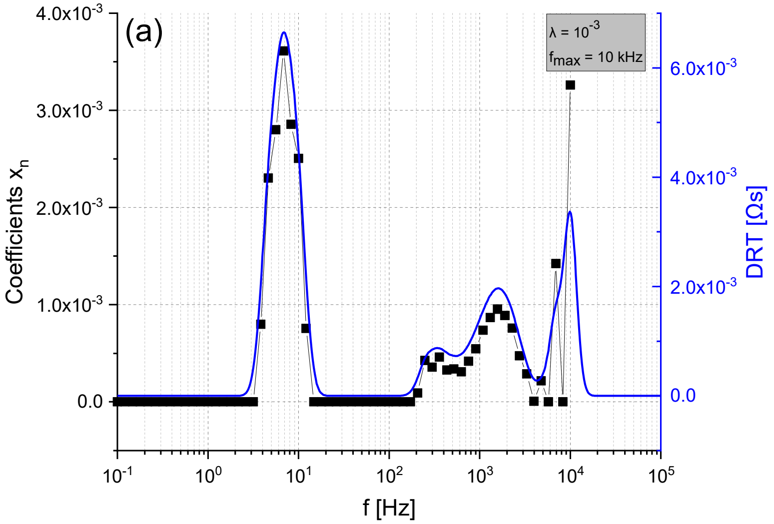

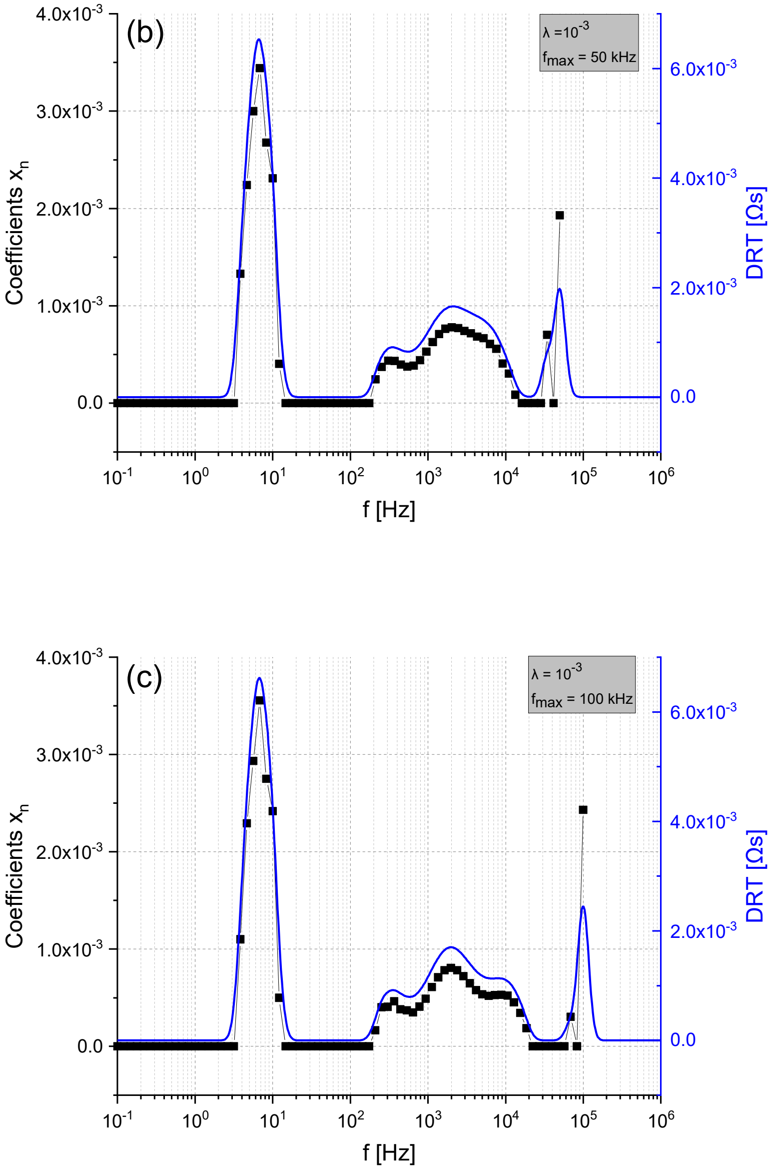

Figure 5.8. Combined analysis of the coefficient matrix x (black symbols) and the DRT function (blue line) for the experimental EIS measurements conducted at 700 °C starting at 10 kHz in (a), 50 kHz in (b) and 100 kHz in (c). The regularization parameter is 10^{-3}.

Optimization Method

Based on the above considerations, the proposal of Zhang [165] to use a vector of regularization parameters instead of a single value to account for different characteristics in different time scales seems a promising approach to account for CPE effects in different frequency ranges on the hand and to separate the high-frequency artefacts from the DRT spectrum on the other hand. To evaluate this method in terms of its power to remove the artefacts, the concept of a vector of regularization parameters was implemented in MATLAB. For the calculations which are shown in what follows, the first five entries of the vector were filled with $\lambda = 10^{-6}$ and the remaining values are set to $\lambda = 10^{-3}$. The purpose of the concept is to move the numerical instability to the point of maximum frequency only and then overwrite the first entry in the coefficient matrix *x_ridge_combined* with zero.

In first place, the approach was tested on simulated EIS spectra with CPE – n3 = 0. 65 starting at maximum frequencies of 10 kHz, 100 kHz and 1 MHz. Subsequently, the experimental EIS spectra were analyzed with the same approach. Figure 5.9 shows an exemplary result of the new approach applied on a simulated EIS spectrum starting at 10 kHz maximum frequency with a CPE – n3 of 0. 65.

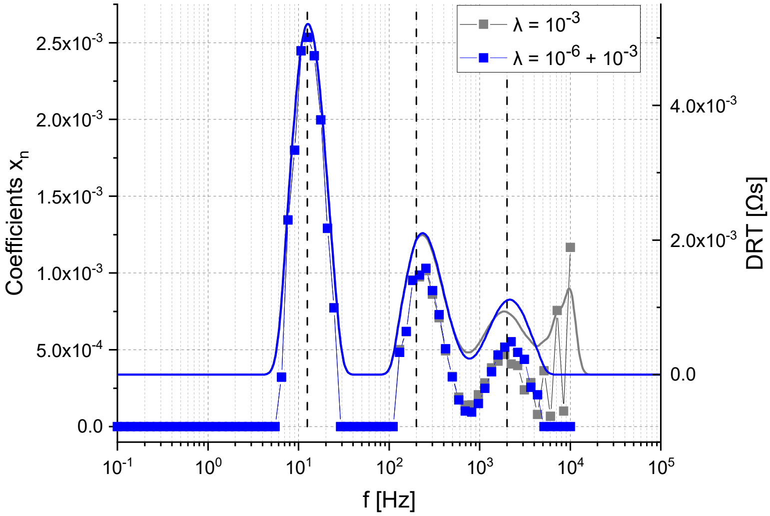

Figure 5.9. Demonstration removing the high-frequency artificial peak with the new approach of defining the regularization parameter as a vector in DRTtools. The blue symbols and solid line mark the coefficients and DRT function calculated with the new approach, the grey symbols and line mark the coefficients and DRT function calculated with the default approach in DRTtools.

The regularization parameter was set to 10^{-3} for the default approach and 10^{-6} for the first five entries in the vector followed by 10^{-3} for the remaining frequency range.

In order to underline the capability of the approach to remove the artefacts in different maximum frequency ranges, the EIS spectra with CPE – n3 = 0. 65 and maximum frequencies of 10 kHz, 100 kHz and 1 MHz were analyzed with the new approach as well. The results can be found in Figure 5.10, showing that the approach is working also for higher maximum frequencies. However, it can be observed that the intermediate artefacts are not suppressed with the mentioned setting of the regularization parameter. Further investigation is needed to figure out the mechanism of their origin in more detail to come up with a suitable method to remove those as well. Anyhow their removal is not that straightforward, as they are affected by measurement errors and exhibit the risk to be mixed up with real electrochemical processes. The investigation of the numerical root cause for this behavior can be the objective of future works dealing with the DRT analysis.

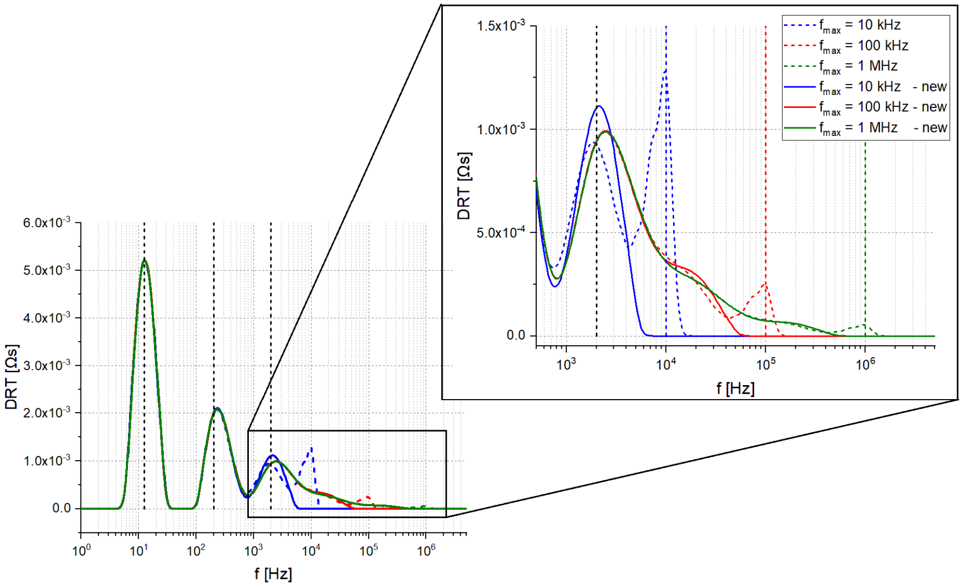

Figure 5.10. Comparison of different maximum frequencies for the default DRTtools settings with one regularization parameter of 10^{-3} (dashed lines) and the new approach with a vector of regularization parameters (solid line), in which the first five entries are set to 10^{-6} followed by 10^{-3} for the remaining frequency range.

Finally, also experimental EIS spectra were analyzed with the new approach and the results for the measurements conducted at 800 °C can be found in Figure 5.11. The artefacts at the maximum frequency can be removed completely with the vector of regularization parameters while leaving the remaining frequency range unchanged.

Based on the analysis that was provided in this chapter, there is clear evidence that CPE effects of electrochemical processes with high relaxation frequencies cause the numerical instabilities in the calculation of the weighting coefficients **x** which give then rise to sharp artificial peaks at the maximum frequency. It was shown that no such artefacts are observed for CPE exponents of one, which equals the ideal RC element behavior. In reverse this means that CPE effects are present in the investigated ASCs as the maximum frequency artefacts are clearly visible for all measurements that were conducted.

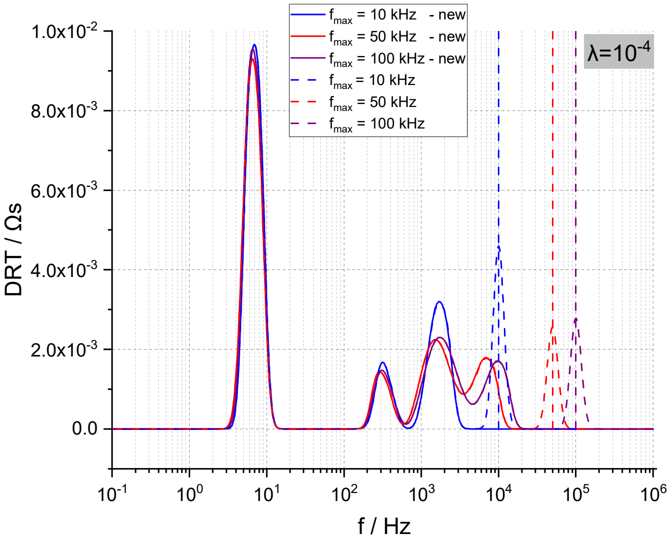

Figure 5.11. DRT spectra calculated with the DRTtools default settings (dashed line) and the new approach with a vector of regularization parameters (solid line) for the EIS measurements conducted at 700 °C.

Based on the findings of the coefficient analysis, an alternative approach based on the idea of Zhang to use different values of the regularization parameter in different frequency ranges, an alternative method to calculate the DRT with DRTtools is proposed and evaluated on synthetic and experimental EIS spectra. By pushing the numerical oscillations to the first frequency point and subsequently replacing the value by zero, the maximum frequency artefacts can be successfully removed. However, the removal of intermediate artefacts is more puzzling and needs further investigation. Although it is now possible to remove the artefacts from the experimental DRT analysis, there is still an information about the presence of high-frequency dispersion effects stored in them. Therefore, it is recommended to first conduct the DRT analysis with the default settings in DRTtools to explore the CPE effects and only remove the artefacts in a subsequent calculation.

Because there is evidence that CPE effects are present in the SOFC, based on the results of this thesis, further experimental investigation on the physical origin of those could be objective of subsequent studies and could help to increase the understanding of high-frequency effects in the SOFC.

6. Summary

In this thesis, an EIS simulation study was performed using an equivalent circuit model to simulate the theoretical impedance response of an anode-supported Solid Oxide Fuel Cell with a subsequent Distribution of Relaxation Times analysis using the freely available MATLAB package DRTtools. The basis of the DRT deconvolution therein is the Tikhonov regularized regression approach, which is a commonly used technique to solve ill-posed mathematical problems numerically. Aim of the simulation study was the investigation of the influence of parasitic inductances, error structures and magnitudes, constant phase element behavior of electrochemical processes, available EIS frequency ranges and data point densities on the accuracy and reliability of the DRT calculation with DRTtools. It could be shown that simulated ideal inductances in the range from 10^{-9} H and $2*10^{-7}$ H are not contributing to the numerical oscillations in the high frequency range in a systematic way. This result could be confirmed also for simulations with added statistical error and for different EIS frequency ranges. Contrarily, frequency dispersion effects are identified as the main contributor to numerical oscillations in the frequency range of the respective electrochemical process. This calculation instability is especially pronounced in the high-frequency range of the DRT spectrum. It could be shown that CPE effects in the high-frequency range lead to the expression of a sharp artificial peak in the DRT which is precisely located at the maximum frequency of the underlying EIS data set. The peak height of these peaks increases with decreasing CPE exponent and decreases with increasing maximum frequency, which means an increased distance between the high-frequency electrochemical process and the maximum frequency. Furthermore, it could be shown that measurement errors are enhancing the effects caused by the constant phase element, whereas the error structure did not cause significant differences. However, higher error magnitudes make it necessary to increase the value of the regularization parameter to suppress the CPE-induced oscillations which are enhanced by statistical errors. Additional peaks could be observed between the 2000 Hz process and the maximum frequency artefact if the simulations are performed up to 100 kHz and 1 MHz. Analyzing the impact of minimum frequencies, no systematic correlation of the same with the size and position of the low-frequency artefacts could be observed, which leads to the conclusion that their formation is due to a different numerical mechanism. Regarding the analysis of the data point density, it could be shown that increasing the ppd value can improve the peak resolution in the DRT in case of closely adjacent peaks exhibiting CPE behavior.

The findings of the simulation results were subsequently verified on experimental EIS measurements performed at different temperatures and in different frequency ranges on a 2-layer ASC stack in the Jülich F10-Design. The high-frequency oscillations could be confirmed in the experiment, leading to an improved DRT analysis by identification of the artefacts and therefore excluding them from the electrochemical characterization of the ASC. For the measurements conducted at 800 °C, the additional artefacts between the maximum frequency and the electrochemical process with the highest relaxation frequency could be observed. These peaks were excluded from the electrochemical characterization as well, based on the findings from the simulation study. In order to confirm the number of identified electrochemical processes, their single polarization resistances were calculated with the Gauss approximation formula and their sum was compared with the total integral of the DRT function over the entire frequency range.

By analyzing the coefficient matrix **x** which contains the RBF weighting coefficients, it could be shown that the maximum frequency is a special vulnerable point of the algorithm used in DRTtools and therefore acts as starting point of the high-frequency oscillations. The closer the maximum frequency is to the electrochemical process with the highest relaxation frequency, the higher the interaction of the numerical instabilities with the process. Furthermore, higher regularization parameters also favor the interaction of the artefacts with the real electrochemical processes with high relaxation frequencies. Based on these findings, an alternative approach for choosing the regularization parameter was proposed which is capable of removing the sharp artificial peak at the maximum frequency. However, this approach was not able to remove the artefacts between f_{max} and the high-frequency process as well. By analyzing the magnitude of the wrongly calculated coefficient x_1, it could be revealed that the peak height of this peak is a measure of the frequency dispersion effects in the investigated system. Therefore, there could be physical information about the high-frequency processes stored in this artefact as well.

Being aware of the numerical weaknesses of the algorithm in DRTtools in case of the presence of frequency dispersion effects and statistical measurement errors, the DRT method is a powerful technique to identify and characterize the electrochemical processes in Solid Oxide Fuel Cells. However, the DRT method cannot be assumed to be a pure a-priori analysis method, as there is a deep knowledge about the processes and their relaxation characteristics and about the calculation method needed to ensure a correct interpretation of the DRT results.

Based on the findings of this study, an investigation of the impact of CPE effects on the DRT calculation with different algorithms and DRT approaches can be subject of subsequent works.

Recommendations for an optimized DRT analysis based on the results of this thesis

- Prior estimation of CPE exponents of the electrochemical processes is beneficial to optimize the regularization parameter and reduce the risk of peak multiplication and misinterpretations in terms of the number of processes.

- In case of overlapping features with high regularization parameters, a repeated EIS measurement with a higher value of points per decade will improve the peak resolution for broadened DRT peaks. Increasing λ only to separate peaks could potentially lead to unwanted oscillations and misinterpretation of the number of processes in case of the presence of CPE effects.

- Sharp peaks observed at the maximum frequency of the EIS have to be treated as artefacts. They are arising from a weakness of the algorithm due to the maximum frequency cut-off. Additional attention has to be paid to artefacts close to the maximum frequency which are changing their position with changing the maximum frequencies. These have to be analyzed in detail and bear the risk of being interpreted as real processes.

- In case of doubt, analysis of the coefficient matrix (*x_ridge_combined*) can reveal numerical oscillations in the high frequency range and their interaction with real processes.

- EIS measurements at different maximum frequencies are required to confirm the high - frequency electrochemical processes. In case of overlapping of the maximum frequency artefact with a real process, separation of those can be achieved by decreasing the regularization parameter in the high-frequency range as proposed in the last chapter of this thesis.

Appendix

A.

In the following part, the derivation of the matrices for the calculation of the DRT function in DRTtools is given, taken from the publication of DRTtools by T. H. Wan [10]. As stated in Chapter 2.2.5, the DRT function can be approximated as a sum of discretization functions as

$$\gamma\,(\ln\tau) = \sum_{n=1}^{N} x_n \Phi_\mu(|\ln\tau - \ln\tau_n|) \tag{A.1}$$

Therefore the model impedance

$$Z_{DRT}(f) = R_O + \int_{-\infty}^{\infty} \frac{\gamma(ln\tau)}{1+i2\pi f\tau} dln\tau \tag{A.2}$$

Can be rewritten as

$$Z_{DRT}\,(f) = R_0 + \sum_{n=1}^{N} x_n \begin{bmatrix} \int_{-\infty}^{\infty} \frac{1}{1+(i2\pi f\tau)^2} \Phi_\mu(|\ln\tau - \ln\tau_n|)dln\tau - \\ i\int_{-\infty}^{\infty} \frac{2\pi f\tau}{1+(i2\pi f\tau)^2} \Phi_\mu(|\ln\tau - \ln\tau_n|)dln\tau \end{bmatrix} \tag{A.3}$$

which is in matrix form

$$Z_{DRT}(f) = R_0 + \sum_{n=1}^{N}[(\boldsymbol{A}')_{nm}\boldsymbol{x}_n + i(\boldsymbol{A}'')_{nm}\boldsymbol{x}_n] \tag{A.4}$$

with

$$(\boldsymbol{A}')_{nm} = \int_{-\infty}^{\infty} \frac{1}{1+4\pi^2 e^{2(y+lnf_n-lnf_m)}} \Phi_u(|y|)dy \tag{A.5}$$

$$(\boldsymbol{A}'')_{nm} = \int_{-\infty}^{\infty} \frac{2\pi e^{2(y+lnf_n-lnf_m)}}{1+4\pi^2 e^{2(y+lnf_n-lnf_m)}} \Phi_u(|y|)dy \tag{A.6}$$

Where $y = \ln\tau - \ln\tau_m$. In case of logarithmically spaced frequencies **A’** and **A’’** are diagonal constant matrices.

The penalty which is added to stabilize the DRT result is the square norm of the first derivative of the DRT function

$$\frac{d\gamma(\ln\tau)^2}{d\ln\tau} = \boldsymbol{x^T M x} = \sum_{\boldsymbol{n=1}}^{\boldsymbol{N}}\sum_{\boldsymbol{l=1}}^{\boldsymbol{N}} \boldsymbol{x_l x_m (M)_{lm}} \tag{A.7}$$

By implementing the RBF, one obtains

$$\frac{d\gamma(ln\tau)}{dln\,\tau} = \sum_{\boldsymbol{n=1}}^{\boldsymbol{N}}\sum_{\boldsymbol{l=1}}^{\boldsymbol{N}} \boldsymbol{x_l x_m} \frac{\boldsymbol{d\Phi_u}(|\boldsymbol{ln\,\tau - ln\,\tau_l}|)\boldsymbol{d\Phi_u}(|\boldsymbol{ln\,\tau - ln\,\tau_n}|)}{\boldsymbol{dln\,\tau}} \tag{A.8}$$

Combining the above equations, yields the expression for **M** as

$$(\mathbf{M})_{lm} = \int_{-\infty}^{\infty} \frac{\boldsymbol{d\Phi_u}(|\boldsymbol{ln\,\tau - ln\,\tau_l}|)\boldsymbol{d\Phi_u}(|\boldsymbol{ln\,\tau - ln\,\tau_n}|)}{\boldsymbol{dln\,\tau}}\, dln\,\tau \tag{A.9}$$

Again it has to be noted that $(\mathbf{M})_{lm}$ is a diagonal constant matrix if the frequency points are logarithmically spaced.

The expressions for **Ω**’ and **Ω**’’ are given as

$$(\boldsymbol{\Omega}')_{n,m} = \delta_{n,m}\sqrt{w'_{n,m}} \tag{A.10}$$

$$(\boldsymbol{\Omega}'')_{n,m} = \delta_{n,m}\sqrt{w''_{n,m}} \tag{A.11}$$

B.

As mentioned in the beginning of this thesis, attempts were made to achieve a quantitative measure for the accuracy of the DRT result. For this purpose, the single polarization resistances were calculated via the peak area in the DRT with the Gauss approximation formula

$$A_p = 1.0645 \cdot FWHM \cdot h \tag{B.1}$$

and compared with the polarization resistances which were placed in the underlying ECM. By searching for the least differences between the set value and the calculated value, it was tried to find an optimal value for the regularization parameter. This procedure did not result in a continuous trend of the differences in dependence of the CPE or the regularization parameter due to the observed numerical oscillations which are hindering a correct calculation of the single polarization resistances at low CPE exponents, as shown in Figure B.1.

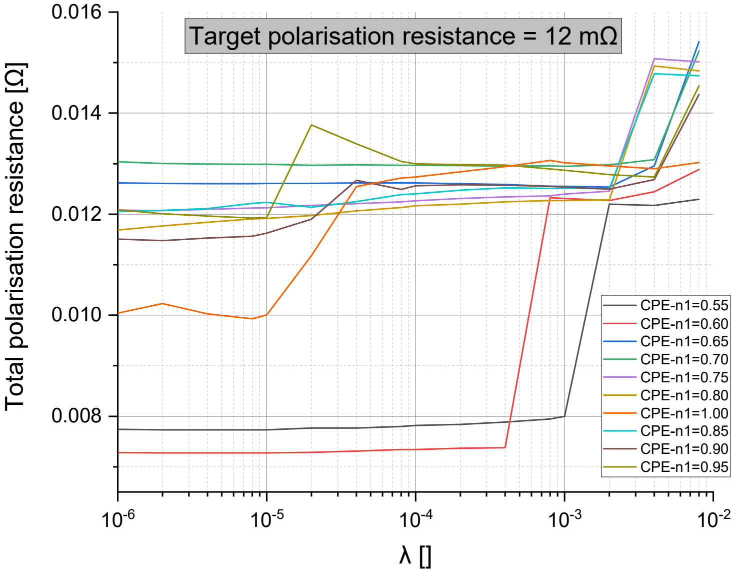

Figure B.1. Calculated total polarization for different values of CPE-n1 plotted against the regularization parameter.

Correlating the differences between calculated polarization resistances and set values in the ECM with the regularization parameter, only general statistical statements could be achieved –such as that the optimal regularization parameter increases with decreasing CPE exponent - and no quantitative information about the degree of oscillations could be gained with this approach.

Another approach was to compare the cumulative integral over the whole frequency range with the sum of the single polarizations calculated with the Gauss formula. When comparing the sum of single polarizations P_{sum} with the set polarization P_{ECM} and the cumulative integral P_{cum} with

$$P_{sum} = \sum_{i=1}^{3} P_i \tag{B.2}$$

$$\Delta P_{sum} = P_{sum} - P_{ECM} \tag{B.3}$$

and

$$\Delta P_{cum} = P_{cum} - P_{sum} \tag{B.4}$$

and plotting ΔP_{sum} against ΔP_{cum}, it was observed that the sum of them was zero for all the CPE exponents.

From this result it can be derived that P_{cum} equals the set value of the ECM:

$$Total\ sum = \Delta P_{sum} + \Delta P_{cun} = (P_{sum} - P_{ECM}) + (P_{cum} - P_{sum}) = 0 \tag{B.5}$$

which leads to

$$P_{cum} = P_{ECM} \tag{B.6}$$

This could be a possible explanation why CPE behavior leads to artificial peaks at the frequency edges as the overlapping areas are not contributing to the cumulative integral and therefore are potentially compensated by additional peaks. To verify this thesis, another study on the correlation of overlapping peak area and area of artificial peaks would be needed.

As the quantitative approaches described here were not satisfying to investigate the oscillations, they were omitted in the later course of this thesis.

References

[1] M. Talawar, R. Sivabalan, T. Mukundan, H. Muthurajan, A. Sikder, B. Gandhe and A. S. Rao, "Environmentally compatible next generation green energetic materials (GEMs)," *Journal of Hazardous Materials,* vol. 161, no. 2-3, pp. 589-607, 2009.

[2] T. Franco, M. Haydn, A. Weber, W. Schafbauer, L. Blum, U. Packbier, D. Roehrens, N. Menzler, J. Rechberger and A. Venskutonis, "The status of metal-supported SOFC development and industrialization at Plansee," *ECS Transactions,* vol. 57, no. 1, pp. 471-480, 2013.

[3] D. Roehrens, F. Han, M. Haydn, W. Schafbauer, D. Sebold, N. Menzler and H. Buchkremer, "Advances beyond traditional SOFC cell designs," *International Journal of Hydrogen Energy,* vol. 40, no. 35, pp. 11538-11542, 2015.

[4] M. Rüttinger, R. Mücke, T. Franco, O. Büchler, N. Menzler and A. Venskutonis, "Metal-supported Cells with Comparable Performance to Anode-supported Cells in Short-Term Stack Environment," *ECS Transactions,* vol. 35, no. 1, pp. 259-268, 2011.

[5] H. Yokokawa, H. Tu, B. Iwanschitz and A. Mai, "Fundamental mechanisms limiting solid oxide fuel cell durability," *Journal of Power Sources,* vol. 182, no. 2, pp. 400-412, 2008.

[6] S. Badwal, "Zirconia-based solid electrolytes: microstructure, stability and ionic conductivity," *Solid State Ionics,* vol. 4, no. 3-4, pp. 23-32, 1992.

[7] P. Blennow, J. Hjelm, T. Klemenso, S. Ramousse, A. Kromp, A. Leonide and A. Weber, "Manufacturing and characterization of metal-supported solid oxide fuel cells," *Journal of Power Sources,* vol. 196, no. 17, pp. 7117-7125, 2011.

[8] V. Sonn, A. Leonide and E. Ivers-Tiffée, "Combined Deconvolution and CNLS Fitting Approach Applied on the Impedance Response of Technical Ni/8YSZ Cermet Electrodes," *Journal of the Electrochemical Society,* vol. 155, no. 7, pp. B675-B679, 2008.

[9] M. Orazem and B. Tribollet, Electrochemical Impedance Spectroscopy, New Jersey: John Wiley & Sons, 2011.

[10] T. Wan, M. Saccoccio, C. Chen and F. Ciucci, "Influence of the Discretization Methods on the Distribution of Relaxation Times Deconvolution: Implementing Radial Basis Functions with DRTtools," *Electrochimica Acta,* vol. 184, no. 1, pp. 483-499, 2015.

[11] Y. Yan, PhD thesis: Degradation study of SOC stacks with Impedance Spectroscopy, Aachen: Rheinisch-Westfälische Technische Hochschule Aachen, 2018.

[12] F. Barbir, "PEM Fuel Cells: Theory and Practice," in *PEM Fuel Cells*, London, Academic Press, 2013, pp. 33-72.

[13] E. Konysheva, H. Penkalla, E. Wessel, J. Mertens, U. Seeling, L. Singheiser and K. Hilpert, "Chromium Poisoning of Perovskite Cathodes by the ODS Alloy Cr5Fe1Y2O3 and the High Chromium Ferritic Steel Crofer22APU," *Journal of the Electrochemical Society,* vol. 153, no. 4, pp. A765-A773, 2006.

[14] R. Budiman, K. Bagarinao, S. Liu, D. Cho, T. Ishiyama, H. Kishimoto, K. Yamaji, T. Horita and H. Yokokawa, "Time-Dependence of Surface Composition, Transport Properties Degradation, and Thermodynamic Consideration of La0.6Sr0.4Co0.2Fe0.8O3-d under Chromium Poisoning," *Journal of the Electrochemical Society,* vol. 165, no. 14, pp. F1206-F1216, 2018.

[15] M. Kornely, A. Neumann, N. Menzler, A. Leonide, A. Weber and E. Ivers-Tiffée, "Degradation of anode-supported cell (ASC) performance by Cr-poisoning," *Journal of Power Sources,* vol. 196, no. 17, pp. 7203-7208, 2011.

[16] S. Badwal, "Materials for solid oxide fuel cells," *Materials Science,* vol. 21, pp. 187-224, 1997.

[17] O. Yamamoto, Y. Arachi, H. Sakai, Y. Takeda, N. Imanishi, Y. Mizutani, M. Kawai and Y. Nakamura, "Zirconia based oxide ion conductors for solid oxide fuel cells," *Ionics,* vol. 4, pp. 403-408, 1998.

[18] T. Ishihara, H. Matsuda and Y. Takita, "Effects of rare earth cations doped for La site on the oxide ionic conductivity of LaGaO3-based perovskite type oxide," *Solid State Ionics,* vol. 79, pp. 147-151, 1995.

[19] S. Badwal, "Stability of solid oxide fuel cell components," *Solid State Ionics,* vol. 143, no. 1, pp. 39-46, 2001.

[20] K. Huang, R. Tichy and J. Goodenough, "Superior Perovskite Oxide-Ion Conductor; Strontium- and Magnesium-Doped LaGaO3: I, Phase Relationships and Electrical Properties," *Journal of the American Ceramic Society,* vol. 81, no. 10, pp. 2565-2575, 1998.

[21] A. Petric, P. Huang and F. Tietz, "Evaluation of La-Sr-Co-Fe-O perovskites for solid oxide fuel cells and gas separation membranes," *Solid State Ionics,* vol. 135, no. 1-4, pp. 719-725, 2000.

[22] X. Li, D. Wilkinson and J. Zhang, Solid Oxide Fuel Cells: Materials Properties and Performance, London: CRC Press, 2016.

[23] H. S. Spacil, "Electrical device including nickel-containing stabilized zirconia electrode". United States Patent US3503809A, 31 March 1970.

[24] S. Singhal and K. Kendall, High-temperature Solid Oxide Fuel Cells: Fundamentals, Design and Application, Amsterdam: Elsevier, 2003.

[25] T. Iwata, "Characterization of Ni-YSZ Anode Degradation for Substrate-Type Solid Oxide Fuel Cells," *Journal of the Electrochemical Society,* vol. 143, no. 5, pp. 1521-1525, 1996.

[26] K. Nikooyeh, R. Clemmer, V. Alzate-Restrepo and J. Hill, "Effect of hydrogen on carbon formation on Ni/YSZ composites exposed to methane," *Applied Catalysis A: General,* vol. 347, no. 1, pp. 106-111, 2008.

[27] J. F. B. Rasmussen and A. Hagen, "The effect of H2S on the performance of Ni-YSZ anodes in solid oxide fuel cells," *Journal of Power Sources,* vol. 191, no. 2, pp. 534-541, 2009.

[28] F. Wang, W. Wang, R. Ran, M. Tade and Z. Shao, "Aluminum oxide as a dual-functional modifier of Ni-based anodes of solid oxide fuel cells for operation on simulated biogas," *Journal of Power Sources,* vol. 268, pp. 787-793, 2014.

[29] X. Song, X. Dong, M. Li and H. Wang, "Effects of adding alumina to the nickel-zirconia anode materials for solid oxide fuel cells and a two-step sintering method for half-cells," *Jorunal of Power Sources,* vol. 308, pp. 58-64, 2016.

[30] X. Wu, Y. Tian, J. Zhang, W. Zuo, X. Kong, J. Wang, K. Sun and X. Zhou, "Enhanced electrochemical performance and carbon anti-coking ability of solid oxide fuel cells with silver modified nickel-yttrium stabilized zirconia anode by electroless plating," *Journal of Power Sources,* vol. 301, pp. 143-150, 2016.

[31] S. Sengodan, "Enhancing Sulfur Tolerance of a Ni-YSZ Anode through BaZr0.1Ce0.7Y0.1Yb0.1O3-d Infiltration," *Journal of the Electrochemical Society,* vol. 161, no. 5, pp. F668-673, 2014.

[32] W. Quaddakers and V. Shermet.USA Patent 2,003,059,335, 2003.

[33] P. Piccardo, P. Gannon, S. Chavalier, M. Viviani, A. Barbucci, G. Caboche, R. Amendola and S. Fontana, "ASR evaluation of different kinds of coatings on a ferritic stainless steel as SOFC interconnects," *Surface and Coatings Technology,* vol. 202, no. 4-7, pp. 1221-1225, 2007.

[34] Z. Yang, G.-G. Xia, G. Maupin and J. Stevenson, "Conductive protection layers on oxidation resistant alloys for SOFC interconnect applications," *Surface and Coatings Technology,* vol. 201, no. 7, pp. 4476-4483, 2006.

[35] L. Blum, L. de Haart, J. Malzbender, N. Menzler, J. Remmel and R. Steinberger-Wilckens, "Recent results in Jülich solid oxide fuel cell technology development," *Journal of Power Sources,* vol. 241, pp. 477-485, 2013.

[36] E. Barsoukov and J. Macdonald, Impedance Spectroscopy: Theory, Experiment and Applications, New Jersey: John Wiley & Sons, 2005.

[37] P. Agarwal, O. Moghissi and L. Garcia-Rubio, "Application of Measurement Models for Analysis of Impedance Spectra," *Corrosion,* vol. 49, no. 4, pp. 278-289, 1993.

[38] G. Popkirov and R. Schindler, "Validation of experimental data in electrochemical impedance spectroscopy," *Electrochimica Acta,* vol. 38, no. 7, pp. 861-867, 1993.

[39] H. Kramers, "La diffusion de la lumiere par les atomes," *Transactions of Volta Centenary Congress,* vol. 2, pp. 545-557, 1927.

[40] R. d. L. Kronig, "On the theory of Dispersion of X-rays," *Journal of the Optical Society of America,* vol. 12, no. 6, pp. 547-557, 1926.

[41] B. Boukamp, "A linear Kronig-Kramers Transform Test for Immitance Data Validation," *Journal of the Electrochemical Society,* vol. 142, no. 6, pp. 1885-1894, 1995.

[42] P. Bruzzoni, R. Carranza, J. Lacoste and E. Crespo, "Kramers-Kronig transforms calculation with a fast convolution algorithm," *Electrochimica Acta,* vol. 48, no. 4, pp. 341-347, 2002.

[43] M. Schönleber, "A Method for Improving the Robustness of linear Kramers-Kronig Validity tests," *Electrochimica Acta,* vol. 131, pp. 20-27, 2014.

[44] [Online]. Available: http://www.iam.kit.edu/wet/Lin-KK.php.

[45] J. Illig, J. Schmidt, M. Weiss, A. Weber and E. Ivers-Tiffée, "Understanding the impedance spectrum of 18650 LiFePO4-cells," *Journal of Power Sources,* vol. 239, pp. 670-679, 2013.

[46] D. Klotz, A. Weber and E. Ivers-Tiffée, "Practical Guidelines for Reliable Electrochemical Characterization of Solid Oxide Fuel Cells," *Electrochimica Acta,* vol. 227, pp. 110-126, 2017.

[47] E. Warburg, "Ueber das Verhalten sogenannter unpolarisierbarer Elektroden gegen Wechselstrom," *Annalen der Physik und Chemie,* vol. 67, no. 3, pp. 493-499, 1899.

[48] R. Armstrong, "The metal-solid electrolyte interphase," *Journal of Electroanalytical Chemistry and Interfacial Electrochemistry,* vol. 52, no. 3, pp. 413-419, 1974.

[49] H. Gerischer, "Zum Mechanismus der kathodischen Wasserstoffabscheidung an Quecksilber, Silber und Kupfer," *Zeitschrift für Elektrochemie,* vol. 59, pp. 1049-1060, 1955.

[50] R. Armstrong and M. Henderson, "Impedance plane display of a reaction with an adsorbed intermediate," *Journal of Electroanalytical Chemistry and Interfacial Electrochemistry,* vol. 39, no. 1, pp. 81-90, 1972.

[51] O. Shamardina, "A simple transient model for a high temperature PEM fuel cell impedance," *International Journal of Hydrogen Energy,* vol. 39, no. 5, pp. 2224-2235, 2014.

[52] E. Schouler, "In situ study of the sintering process of yttria stabilized zriconia by impedance spectroscopy," *Solid State Ionics,* Vols. 9-10, no. 2, pp. 989-996, 1983.

[53] J. H. Sluyters and J. Oomen, "On the impedance of galvanic cells: II. Experimental Verifications," *Recueil des Travaux Chimiques des Pays-Bas,* vol. 79, pp. 1101-1110, 1960.

[54] J. Randles, "Kinetics of rapid electrode reactions. Part 2 - Rate constants and activation energies of electrode reactions," *Transactions of the Faraday Society,* vol. 48, p. 828, 1952.

[55] R. Armstrong, R. Firman and H. Thirsk, "The ac impedance of complex electrochemical reactions," *Chemical Society Specialist Periodical Reports,* vol. 56, pp. 244-263, 1973.

[56] A. Leonide, V. Sonn, A. Weber and E. Ivers-Tiffée, "Evaluation and Modelling of the Cell Resistance in Anode-Supported Solid Oxide Fuel Cells," *Journal of the Electrochemical Society,* vol. 155, no. 1, pp. B36-B41, 2007.

[57] J. Llopis, "Study of the Impedance of a Platinum Electrode Acting as Anode," in *Proc. 8th meeting of the CITCE*, Madrid, 1956.

[58] J. R. Macdonald, "Theory of a.c. Space Charge Polarization Effects in Photoconductors, Semiconductors, and Electrolytes," *Physical Review Journals,* vol. 92, pp. 4-17, 1953.

[59] J. R. Macdonald, "Electrical Response of Materials Containing Space Charge with Discharge at Electrodes," *The Journal of Chemical Physics,* vol. 54, pp. 2026-2050, 1971.

[60] J. R. Macdonald, "Binary Electrode Small-Signal Frequency Response," *Journal of Electroanalytical Chemistry,* vol. 53, pp. 1-55, 1974.

[61] J. R. Macdonald, "Simplified Impedance/Frequency Response Results for Intrinsically Conducting Solids and Liquids," *Journal of Chemical Physics,* vol. 61, pp. 3977-3996, 1974.

[62] J. Macdonald and D. Franceschetti, "Theory of Small-Signal A-C Response of Solids and Liquids with Recombining Mobile Charge," *Journal of Chemical Physics,* vol. 68, pp. 1614-1637, 1978.

[63] H. Gerischer, "Wechselstrompolarisation von Elektroden mit einem potentialbestimmenden Schritt beim Gleichgewichtspotential I.," *Zeitschrift für Physikalische Chemie,* vol. 198, no. 1, pp. 268-313, 1951.

[64] J. R. Macdonald and J. Garber, "Analysis of Impedance and Admittance Data for Solids and Liquids," *Journal of the Electrochemical Society,* vol. 124, p. 1022, 1977.

[65] K. Levenberg, "A method for the solution of certain non-linear problems in least squares," *Quarterly Applied Mathematics,* vol. 2, pp. 164-168, 1944.

[66] D. Marquardt, "An Algorithm for Least-Squares Estimation of Nonlinear parameters," *Journal of the Society for Industrial and Applied Mathematics,* vol. 11, no. 2, pp. 431-441, 1963.

[67] J. Moré, The Levenberg-Marquardt algorithm: Implementation and theory. In: Watson G.A. (eds) Numerical Analysis. Lecture Notes in Mathematics Vol. 630, Berlin, Heidelberg: Springer, 1978.

[68] P. Debye, "Polar molecules," *Chemical Catalogue Company,* p. 94, 1929.

[69] K. Wapenaar, H. Koekkoek and J. Van Turnhout, "Low-temperature ionic conductivity and dielectric relaxation phenomena in fluorite-type solid solutions," *Solid State Ionics,* vol. 7, no. 3, pp. 225-242, 1982.

[70] K. Cole and R. Cole, "Dispersion and Absorption in Dielectrics. I. Alternating Current Characteristics," *Journal of Chemical Physics,* vol. 9, pp. 341-351, 1941.

[71] D. Davidson and R. Cole, "Dielectric Relaxation in Glycerol, Propylene Glycol, and n-Propanol," *Journal of Chemical Physics,* vol. 19, pp. 1484-1490, 1951.

[72] L. Onsager, "Theory of Electrolytes, I," *Physikalische Zeitschrift,* vol. 27, pp. 388-392, 1926.

[73] L. Onsager, "Theory of Electrolytes, II," *Physikalische Zeitschrift,* vol. 28, pp. 277- 298, 1927.

[74] P. Debye and H. Falkenhagen, "Dispersion of the conductivity and dielectric constants of strong electrolytes," *Physikalische Zeitschrift,* vol. 29, p. 121, 1928.

[75] A. K. Jonscher, "The 'universal' dielectric response," *Nature,* vol. 267, pp. 673-679, 1977.

[76] A. K. Jonscher, "The Universal Dielectric Response: A Review of Data and their New Interpretation," *Physics of Thin Films,* vol. 11, pp. 205-317, 1980.

[77] K. Funke, "Debye-Hückel-type relaxation processes in solid ionic conductors: The model," *Solid State Ionics,* Vols. 18-19, no. 1, pp. 183-190, 1986.

[78] K. Funke, R. Banhatti, S. Brückner, C. Cramer, C. Krieger, A. Mandanici, C. Martiny and I. Ross, "Ionic motion in materials with disordered structures: conductivity spectra and the concept of mismatch and relaxation," *Physical Chemistry Chemical Physics,* vol. 4, no. 14, p. 3155, 2002.

[79] P. Hetjans and J. Kärger, Diffusion in condensed matter: methods, materials, models, Berlin Heidelberg: Springer, 2005.

[80] M. Abouzari, F. Berkemeier, G. Schmitz and D. Wilmer, "On the physical interpretation of constant phase elements," *Solid State Ionics,* vol. 180, no. 14-16, pp. 922-927, 2009.

[81] B. McNealy and J. Hertz, "On the use of the constant phase element to understand variation in grain boundary properties," *Solid State Ionics,* vol. 256, pp. 52-60, 2014.

[82] C. Peters, A. Weber, B. Butz, D. Gerthsen and E. Ivers-Tiffée, "Grain size effects in YSZ Thin-Film Electrolytes," *Journal of the American Ceramic Society,* vol. 92, no. 9, pp. 2917-2024, 2009.

[83] B. Hirschorn, M. E. Orazem, B. Tribollet, V. Vivier, I. Frateur and M. Musiani, "Constant-Phase-Element Behavior Caused by Resistivity Distributions in Films, I. Theory," *Journal of the Electrochemical Society,* vol. 157, no. 12, pp. C452-C457, 2010.

[84] B. Hirschorn, M. E. Orazem, B. Tribollet, V. Vivier, I. Frateur and M. Musiani, "Constant-Phase-Element Behavior Caused by Resistivity Distributions in Films, II. Applications," *Journal of the Electrochemical Society,* vol. 157, no. 12, pp. C458-C463, 2010.

[85] P. Córdoba-Torres, "Relationship between constant-phase element (CPE) parameters and physical properties of films with a distributed resistivity," *Electrochimica Acta,* vol. 225, pp. 592-604, 2017.

[86] P. Córdoba-Torres, "A generalized expression for the resistivity distribution in films: from the Young model to constant-phase element (CPE) behavior," *Electrochimica Acta,* vol. 241, pp. 535-543, 2017.

[87] P. Bottelberghs and G. Broers, "Interfacial Impedance Behavior of Polished and Paint Platinum Electrodes at Na2WO4-Na2MoO4 Solid Electrolytes," *Journal of Electroanalytical Chemistry,* vol. 67, no. 2, pp. 155-167, 1976.

[88] D. Raistrick, C. Ho, Y. Hu and R. Huggins, "Ionic Conductivity and Electrode Effects on beta-PbF5," *Journal of Electroanalytical Chemistry,* vol. 77, pp. 319-337, 1977.

[89] R. Leek and N. Hampson, "The dispersion of double-layer capacitance with frequency i. smooth solid electrodes," *Surface Technology,* vol. 7, no. 2, pp. 151-155, 1978.

[90] G. Brug, A. van den Eeden, M. Sluyters-Rehbach and J. Sluyters, "The analysis of electrode impedances complicated by the presence of a constant phase element," *Journal of Electroanalytical Chemistry,* vol. 176, no. 1-2, pp. 275-295, 1984.

[91] C. Alexander, B. Tribollet and M. Orazem, "Contribution of Surface Distributions to Constant-Phase-Element (CPE) Behavior: 2. Capacitance," *Electrochimica Acta,* vol. 188, pp. 566-573, 2016.

[92] B. Hirschorn, M. Orazem, B. Tribollet, V. Vivier, I. Frateur and M. Musiani, "Determination of effective capacitance and film thickness from constant-phase element parameters," *Electrochimica Acta,* vol. 55, pp. 6218-6227, 2010.

[93] S. Wu, M. Orazem, B. Tribollet and V. Vivier, "The influence of Coupled Faradaic and Charging Currents on Impedance Spectroscopy," *Electrochimica Acta,* vol. 131, pp. 3-12, 2014.

[94] B. Kurtyka and R. de Levie, "Frequency dispersion associated with a non-homogeneous interfacial capacitance," *Journal of Electroanalytical Chemistry,* vol. 322, pp. 63-77, 1992.

[95] U. R. G. Rammelt, "On the applicability of a constant phase element (CPE) to the estimation of roughness of solid metal electrodes," *Electrochimica Acta,* vol. 35, no. 6, pp. 1045-1049, 1990.

[96] J. C. Wang, P. King and R. Huggins, "Model for the interfacial impedance between a solid electrolyte and a blocking metal electrode," *Solid State Ionics,* Vols. 18-19, no. 1, pp. 224-228, 1986.

[97] Z. Kerner and T. Pajkossy, "On the origin of capacitance dispersion of rough electrodes," *Electrochimica Acta,* vol. 46, no. 2-3, pp. 207-211, 2000.

[98] Z. Kerner and T. Pajkossy, "Impedance of rough capacitive electrodes: the role of surface disorder," *Journal of Electroanalytical Chemistry,* vol. 448, no. 1, pp. 139-142, 1998.

[99] P. Cordoba-Torres, T. Mesquita and R. Nogueira, "Relationship between the Origin of Constant-Phase Element Behavior in Electrochemical Impedance Spectroscopy and Electrode Surface Structure," *Journal of Physical Chemistry C,* vol. 119, no. 8, pp. 4136-4147, 2015.

[100] C. Alexander, B. Tribollet and M. Orazem, "Contribution of Surface Distributions to Constant-Phase-Element (CPE) Behavior: 1. Influence of Roughness," *Electrochimica Acta,* vol. 173, pp. 416-424, 2015.

[101] P. Córdoba-Torres and T. N. R. Mesquita, "Influence of geometry-induced current and potential distributions on the characterization of constant-phase element behavior," *Electrochimica Acta,* vol. 87, pp. 676-685, 2013.

[102] C. Hsu and F. Mansfeld, "Technical Note: Concerning the Conversion of the Constant Phase Element Parameter Y0 into a Capacitance," *Corrosion,* vol. 57, no. 9, pp. 747-748, 2001.

[103] M. S. Abouzari, PhD thesis: Ion-Conductivity of Thin-Film Li-borate Glasses, Münster: Westfälische Wilhelms-Universität , 2007.

[104] M. Carpanese, D. Clematis, A. Bertei, A. Giuliano, E. Mercadelli, C. Nicolella and A. Barbucci, "Understanding the electrochemical behavior of LSM-based SOFC cathodes. Part I - Experimental and electrochemical," *Solid State Ionics,* vol. 301, pp. 106-115, 2017.

[105] M. Drüschler, B. Huber, S. Passerini and B. Roling, "Hysteresis Effects in the Potential-Dependent Double Layer Capacitance of Room Temperature Ionic Liquids at a Polycrystalline Platinum Interface," *Journal of Physical Chemistry C,* vol. 114, no. 8, pp. 3614-3617, 2010.

[106] D. Lee and K. Yong, "ZnO-based Nanostructuring Strategy Using an Optimized Solution Process in CuInS2 Superstrate Photovoltaics," *Journal of Physical Chemistry C,* vol. 118, no. 15, pp. 7788-7800, 2014.

[107] V. M.-W. Huang, V. Vivier, M. Orazem, N. Pébère and B. Tribollet, "The Apparent Constant-Phase Element Behavior of a Disk Electrode with Faradic reactions: A Global and Local Impedance Analysis," *Journal of the Electrochemical Society,* vol. 154, no. 2, pp. C99-C107, 2007.

[108] B. Hirschorn, M. Orazem, B. Tribollet, V. Vivier, I. Frateur and M. Musiani, "Determination of effective capacitance and film thickness from constant-phase-element parameters," *Electrochimica Acta,* vol. 55, no. 21, pp. 6218-6227, 2010.

[109] J. Macdonald, "Relaxation in systems with exponential or Gaussian distributions of activation energies," *Journal of Applied Physics,* vol. 61, no. 2, p. 700, 1987.

[110] C. Alexander, B. Tribollet, V. Vivier and M. Orazem, "Contribution of Surface Distributions to Constant-Phase-Element (CPE) Behavior: 3. Adsorbed Intermediates," *Electrochimica Acta,* vol. 251, pp. 99-108, 2017.

[111] C. Alexander, B. Tribollet and M. Orazem, "Influence of micrometric-scale electrode heterogeneity on electrochemical impedance spectroscopy," *Electrochimica Acta,* vol. 201, pp. 374-379, 2016.

[112] J. Newman, "Frequency dispersion in capacity measurements at a disk electrode," *Journal of the Electrochemical Society,* vol. 117, pp. 198-203, 1970.

[113] C. Blanc, M. Orazem, N. Pébère, B. Tribollet, V. Vivier and S. Wu, "The origin of the complex character of the ohmic impedance," *Electrochimica Acta,* vol. 55, pp. 6313-6321, 2010.

[114] K. Davis, A. Dizon, C. Alexander and M. Orazem, "Influence of geometry-induced frequency dispersion on the impedance of rectangular electrodes," *Electrochimica Acta,* vol. 283, pp. 1820-1828, 2018.

[115] O. Gharbi, A. Dizon, M. Orazem, M. Tran and B. Tribollet, "From frequency dispersion to ohmic impedance: A new insight on the high-frequency impedance analysis of electrochemical systems," *Electrochimica Acta,* vol. 320, p. 134609, 2019.

[116] J. Bisquert, G. Garcia-Belmonre, F. Fabregat-Santiago, F. N.S, P. Bogdanoff and E. Pereira, "Doubling Exponent Models for the Analysis of Porous Film Electrodes by Impedance. Relaxation of TiO2 Nanoporous in Aqueous Solution," *Journal of Physical Chemistry B,* vol. 104, no. 10, pp. 2287-2298, 2000.

[117] A. Lasia, "Impedance of Porous Electrodes," *Journal of Electroanalytical Chemistry,* vol. 397, no. 1-2, pp. 27-33, 1995.

[118] C. Hitz and A. Lasia, "Experimental study and modeling of impedance of the her on porous Ni electrodes," *Journal of Electroanalytical Chemistry,* vol. 500, no. 1-2, pp. 213-222, 2001.

[119] H.-K. Song, H.-Y. Hwang, K.-H. Lee and L. Dao, "The effect of pore size distribution on the frequency dispersion of porous electrodes," *Electrochimica Acta,* vol. 45, no. 14, pp. 2241-2257, 2000.

[120] S. M. R. Niya and M. Hoorfar, "On a possible physical origin of the constant phase element," *Electrochimica Acta,* vol. 188, pp. 98-102, 2016.

[121] S. Ricciardi, J. Ruiz-Morales and P. Nunez, "Origin and quantitative analysis of the constant phase element of a platinum SOFC cathode using the state-space model," *Solid State Ionics,* vol. 180, no. 17-19, pp. 1083-1090, 2009.

[122] D. Klotz, J. Schmidt, A. Kromp, A. Weber and E. Ivers-Tiffée, "The Distribution of Relaxation Times as Beneficial Tool for Equivalent Circuit Modelling of Fuel Cells and Batteries," *ECS Transactions,* vol. 41, no. 28, pp. 25-33, 2012.

[123] D. Papurello, D. Menichini and A. Lanzini, "Distributed relaxation times technique for the determination of fuel cell losses with an equivalent circuit model to identify physicochemical processes," *Electrochimica Acta,* vol. 258, pp. 98-109, 2017.

[124] S. Khan, S. Rivzi and S. Urooj, "Equivalent Circuit modelling using electrochemical impedance spectroscopy for different materials of SOFC," in *3rd International Conference on Computing for Sustainable Global Development (INDIA Com)*, New Delhi, 2016.

[125] J.-B. Jorcin, M. Orazem, N. Pébère and B. Tribollet, "CPE analysis by local electrochemical impedance spectroscopy," *Electrochimica Acta,* vol. 51, no. 8-9, pp. 1473-1479, 2006.

[126] S. Niya, R. Phillips and M. Hoorfar, "Dependency of the power of the constant phase element to operating conditions in Proton Exchange Membrane Fuel Cells," in *13th International Conference on Fuel Cell Science, Engineering and Technology*, San Diego, 2015.

[127] M. Saccoccio, "Optimal Regularization in Distribution of Relaxation Times applied to Electrochemical Impedance Spectroscopy: Ridge and Lasso Regression Methods - A Theoretical and Experimental Study," *Electrochimica Acta,* vol. 147, pp. 470-482, 2014.

[128] F. Ciucci and C. Chen, "Analysis of Electrochemical Impedance Spectroscopy Using the Distribution of Relaxation Times," *Electrochimica Acta,* vol. 167, pp. 439-454, 2015.

[129] Y. Zhang, Y. Chen, M. Yan and F. Chen, "Reconstruction of relaxation time distribution from linear electrochemical impedance spectroscopy," *Journal of Power Sources,* vol. 283, pp. 464-477, 2015.

[130] J. R. Macdonald, "Impedance Spectroscopy: Old Problems and New Developments," *Electrochimica Acta,* vol. 35, no. 10, pp. 1483-1492, 1990.

[131] F. Dion and A. Lasia, "The use of regularization methods in the deconvolution of underlying distributions in electrochemical processes," *Jorunal of Electroanalytical Chemistry,* vol. 475, no. 1, pp. 28-37, 1999.

[132] A. Tesler, D. Lewin, S. Baltianski and Y. Tsur, "Analyzing results of impedance spectroscopy using novel evolutionary programming techniques," *Journal of Electroceramics,* vol. 24, pp. 245-260, 2010.

[133] S. Hershkovitz, S. Baltianski and Y. Tsur, "Harnessing evolutionary programming for impedance spectroscopy analysis: A case study of mixed ionic-electronic conductors," *Solid State Ionics,* vol. 188, no. 1, pp. 104-109, 2011.

[134] S. Hershkovitz, S. Tomer, S. Baltianski and Y. Tsur, "ISGP: Impedance Spectroscopy Analysis Using Evolutionary Programming Technique," *ECS Transactions,* vol. 33, no. 40, pp. 67-73, 2011.

[135] E. Tuncer and S. Gubanski, "On dielectric data analysis. Using the Monte Carlo method to obtain relaxation time distribution and comparing non-linear spectral function fits," *IEEE Transactions on Dielectrics and Electrical Insulation,* vol. 8, no. 3, pp. 310-320, 2001.

[136] E. Tuncer and J. Macdonald, "Comparison of methods for estimating continuous distributions of relaxation times," *Journal of Applied Physics,* vol. 99, p. 074106, 2006.

[137] B. Boukamp, "Fourier transform distribution function of relaxation times; application and limitations," *Electrochimica Acta,* vol. 154, pp. 35-46, 2015.

[138] T. Hörlin, "Deconvolution and maximum entropy in impedance spectroscopy of noninductive systems," *Solid State Ionics,* vol. 107, no. 3-4, pp. 241-253, 1998.

[139] A. Mikonis, J. Banys, R. Grigalaitis, A. Matulis, S. Lapinskas and G. Völkel, "Determination of the two dimensional distribution of the attempt relaxation times and activation energies from temperature dependence of dielectric dispersion," *Central European Journal of Physics,* vol. 11, pp. 206-212, 2013.

[140] R. A. Renault, R. Baker, M. Horst, C. Johnson and D. Nasir, "Stability and error analysis of the polarization estimation inverse problem for microbial fuel cells," *Inverse Problems,* vol. 29, no. 4, p. 045006, 2013.

[141] P. C. Hansen, "Regularization Tools: A Matlab Package for analysis and solution of discrete ill-posed problems," *Numerical Algorithms,* vol. 6, pp. 1-35, 1994.

[142] P. C. Hansen, "Regularization Tools version 4.0 for Matlab 7.3," *Numerical Algorithms,* vol. 46, pp. 189-194, 2007.

[143] A. Hoerl and R. Kennard, "Ridge regression: biased estimation of Nonorthogonal problems," *Technometrics,* vol. 12, pp. 55-67, 1970.

[144] R. Tibshirani, "Regression Shrinkage and Selection Via the Lasso," *Journal of the Royal Statistical Society: Series B,* vol. 58, no. 1, pp. 267-288, 1996.

[145] A. Altmann and J. Gondzio, "Regularized symmetric indefinite systems in interior point methods for linear and quadratic optimization," *Optimization Methods and Software,* vol. 11, no. 1-4, pp. 275-302, 1999.

[146] MathWorks, "Quadratic Programming Algorithms," [Online]. Available: https://de.mathworks.com/help/optim/ug/quadratic-programming-algorithms.html#bvj25y3-1. [Accessed 03 January 2021].

[147] N. Gould and P. Toint, "Preprocessing for quadratic programming," *Mathematical Programming, Series B,* vol. 100, pp. 95-132, 2004.

[148] J. Nocedal and S. Wright, Numerical Optimization, Second Edition, New York: Springer-Verlag, 2006.

[149] S. Mehrotra, "On the Implementation of a Primal-Dual Interior Point Method," *SIAM Journal on Optimization,* vol. 2, pp. 575-601, 1992.

[150] J. Gondzio, "Mulitple centrality corrections in a primal dual method for linear programming," *Computational Optimization and Applications,* vol. 6, no. 2, pp. 137-156, 1996.

[151] R. Kohn, M. Smith and D. Chan, "Nonparametric regression using linear combinations of basis functions," *Statistics and Computing,* vol. 11, pp. 313-322, 2001.

[152] O. Christensen and K. Christensen, Approximation Theory: From Taylor Polynomials to Wavelets, Boston: Birkhauser, 2012.

[153] B. Fornberg and N. Flyer, "Accuracy of radial basis function interpolation and derivative approximations on 1-D infinite grids," *Advances in Computational Mathematics,* vol. 23, pp. 5-20, 2005.

[154] B. Fornberg, N. Flyer and J. Russell, "Comparisons between pseudospectral and radial basis function derivative approximations," *IMA Journal of of Numerical Analysis,* vol. 30, no. 1, pp. 149-172, 2010.

[155] B. Fornberg and J. Zuev, "The Runge phenomenon and spatially variable shape parameters in RBF interpolation," *Computers & Mathematics with Applications,* vol. 54, no. 3, pp. 379-398, 2007.

[156] A. Tikhonov and V. Arsenin, Methods for Solving Ill-Posed Problems, Moscow: Nauka, 1979.

[157] J. Honerkamp and J. Weese, "Tikhonovs regularization method for ill-posed problems," *Continuum Mechanics and Thermodynamics,* vol. 2, pp. 17-30, 1990.

[158] J. Weese, "A reliable and fast method for the solution of Fredhol integral equations of the first kind based on Tikhonov regularization," *Computer Physics Communications,* vol. 69, no. 1, pp. 99-111, 1992.

[159] J. Winterhalter, D. Ebling, D. Maier and J. Honerkamp, "Analysis of Admittance Data: Comparison of a Parametric and a Nonparametric Method," *Jorunal of Computational Physics,* vol. 153, no. 1, pp. 139-159, 1999.

[160] G. H. Golub, M. Heath and G. Wahba, "Generalized Cross-Validation as a Method for Choosing a Good Ridge Parameter," *Technometrics,* vol. 21, no. 2, pp. 215-223, 1979.

[161] V. A. Morozov, Methods for Solving Incorrectly Posed Problems, New York: Springer, 1984.

[162] P. C. Hansen, "Analysis of Discrete Ill-Posed Problems by Means of the L-Curve," *SIAM Review,* vol. 34, no. 4, pp. 561-580, 1992.

[163] T. Hesterberg, N. Choi, L. Meier and C. Fraley, "Least angle an l1 penalized regression: A review," *Statistic Surveys,* vol. 2, pp. 61-93, 2008.

[164] A. Arlot and A. Celisse, "A survey of cross-validation procedures for model selection," *Statistic Surveys,* vol. 4, pp. 40-79, 2010.

[165] Y. Zhang, Y. Chen, M. Li, M. Yan, M. Ni and C. Xia, "A high-precision approach to reconstruct distribution of relaxation times from electrochemical impedance spectroscopy," *Journal of Power Sources,* vol. 308, pp. 1-6, 2016.

[166] N. Schlüter and S. Ernst, "Finding the Optimal Regularization Parameter in Distribution of Relaxation Times Analysis," *ChemElectroChem,* vol. 6, pp. 6027-6037, 2019.

[167] C. R. Vogel, "Non-convergence of the L-Curve regularization parameter selection method," *Inverse Problems,* vol. 12, no. 4, pp. 535-547, 1996.

[168] J. T. Kent and M. Mohammadzadeh, "Global optimization of the generalized cross-validation criterion," *Statistics and Computing,* vol. 10, pp. 231-236, 2000.

[169] B. W. Rust and D. P. O'Leary, "Residual periodograms for choosing regularization parameters for ill-posed problems," *Inverse Problems,* vol. 24, no. 3, p. 034005, 2008.

[170] A. L. Gavriluk, D. A. Osikin and D. Bronin, "The Use of Tikhonov Regularization Method for Calculating the Distribution Times in Impedance Spectroscopy," *Russian Journal of Electrochemistry,* vol. 53, no. 6, pp. 575-588, 2017.

[171] Y. Kikuchi, J. Matsuda, Y. Tachikawa, Y. Shiratori, S. Taniguchi and K. Sasaki, "Degradation of SOFCs by Various Impurities: Impedance Spectroscopy and Microstructural Analysis," *ECS Transactions,* vol. 78, no. 1, pp. 1253-1260, 2017.

[172] G. DiGiuseppe, A. Hunter and F. Zhu, "Combined equivalent circuits and distribution of relaxation times analysis and interfacial effects of (La0.60S0.40)0.95Co0.20Fe0.80O3-x," *Electrochimica Acta,* vol. 350, p. 136252, 2020.

Acknowledgements

I want to thank Prof. Dr. Lehnert for the continuous and extraordinarily engaged support during the challenging time in which I conducted this thesis. His interest in my investigation and my ideas was a strong motivation throughout the last years and made the completion of the work possible in first place. I also appreciated the regular discussions on my work and the qualified input. My gratefulness to Prof. Dr. Lehnert for making this project possible will last throughout my entire life.

My special gratitude also goes to Dr. Fang, who supported the conduction of this thesis with high personal effort and great engagement. He also found time to answer my questions and support me in the process of writing my publications and my thesis, even if he actually didn’t have much time left in most cases. I always appreciated his experienced input to my work.

Another person I want to thank is Mrs. De Haart, who supported me with experimental stack measurements at the IEK-14 in the challenging times of the COVID-19 pandemic and inspired my work in many fruitful discussions about my results and their application in SOFC analysis. Without her help, this thesis couldn’t have been conducted.

Furthermore, I want to thank my team at my company for the mental support during my PhD time and for bearing me at work when I was tired and/or grumpy. They always met me with understanding of my situation and accepted some personal weaknesses that aroused from the double burden over a long time. Sometimes I needed someone to tell me that everything is too much and that I have to rest and in these situations I could always count on my colleagues and for this I am very grateful now and also in future.

Band / Volume 545
Potential depletion of ozone in the mid-latitude lowermost stratosphere in summer under geoengineering conditions
S. Robrecht (2021), 185 pp
ISBN: 978-3-95806-563-5

Band / Volume 546
Two-phase Flow in Porous Transport Layers of Polymer Electrolyte Membrane Electrolysers
D. Borah (2021), xi, 196 pp
ISBN: 978-3-95806-564-2

Band / Volume 547
Effects of root temperature on food quality of horticultural crops
F. He (2021), V, 143 pp
ISBN: 978-3-95806-565-9

Band / Volume 548
Verhalten und Kontrolle von Schlacken des bioliq®-Vergasers
K. Mielke (2021), 162, XXXV pp
ISBN: 978-3-95806-566-6

Band / Volume 549
Gravity waves resolved in Numerical Weather Prediction products
C. Strube (2021), iii, 139 pp
ISBN: 978-3-95806-567-3

Band / Volume 550
Experimental study of the chemical degradation of biogenic volatile organic compounds by atmospheric OH radicals
M. Rolletter (2021), XIII, 199 pp
ISBN: 978-3-95806-568-0

Band / Volume 551
Infiltrated Positive Electrodes for All-Solid-State Sodium Batteries
T. Lan (2021), vi, 104 pp
ISBN: 978-3-95806-576-5

Band / Volume 552
Trajectory Analysis on the Asian Tropopause Aerosol Layer (ATAL) based on Balloon Measurements at the Foothills of the Himalayas
S. Hanumanthu (2021), xiv, 147 pp
ISBN: 978-3-95806-578-9

Schriften des Forschungszentrums Jülich
Reihe Energie & Umwelt / Energy & Environment

Band / Volume 553
Field assisted sintering of yttria ceramics for plasma etching applications
M. Kindelmann (2021), VI, 122, XXX pp
ISBN: 978-3-95806-579-6

Band / Volume 554
Characterisation of the effect of redox potential on the emission of greenhouse gases using wireless sensing techniques
J. Wang (2021), XIV, 104 pp
ISBN: 978-3-95806-581-9

Band / Volume 555
Stability assessment of variably saturated hillslopes using coupled hydromechanical models
S. Moradi (2021), xxxii, 123 pp
ISBN: 978-3-95806-583-3

Band / Volume 556
Catalytic-doping of Silicon Alloys for the Use in Silicon Heterojunction Solar Cells
Y. Liu (2021), 126 pp
ISBN: 978-3-95806-591-8

Band / Volume 557
Formation of highly oxygenated organic molecules from α-pinene photochemistry
S. Kang (2021), xvii, 156 pp
ISBN: 978-3-95806-596-3

Band / Volume 558
Synthese von Cr_2AlC MAX-Phasen Kompositen und Bestimmung ihrer oxidativen Eigenschaften
T. Go (2021), ii, 119 pp
ISBN: 978-3-95806-598-7

Band / Volume 559
Distribution of Relaxation Times for Analysis of Solid Oxide Fuel Cell Stacks
K. Fitzek (2021), 237 pp
ISBN: 978-3-95806-599-4

Weitere ***Schriften des Verlags im Forschungszentrum Jülich*** unter
http://wwwzb1.fz-juelich.de/verlagextern1/index.asp

Energie & Umwelt / Energy & Environment
Band / Volume 559
ISBN 978-3-95806-599-4

Mitglied der Helmholtz-Gemeinschaft

JÜLICH
Forschungszentrum